

# Numerical Approximation of Optimal Microstructures in Elastic Shape Optimization

DISSERTATION

zur Erlangung des Doktorgrades (Dr. rer. nat.)  
der Mathematisch-Naturwissenschaftlichen Fakultät  
der Rheinischen Friedrich-Wilhelms-Universität Bonn

vorgelegt von

**Benedict Gei**

geboren in Dormagen

Bonn im Dezember 2022



---

Angefertigt mit Genehmigung der Mathematisch-Naturwissenschaftlichen Fakultät  
der Rheinischen Friedrich-Wilhelms-Universität Bonn  
am Institut für Numerische Simulation

1. Gutachter: Prof. Dr. Martin Rumpf
2. Gutachter: Prof. Dr. Sergio Conti

Tag der Promotion: 2. Mai 2023  
Erscheinungsjahr: 2023



---

## Summary

---

We develop and analyze a numerical two-scale optimization scheme for structural shape optimization. Whenever cost functionals, such as the elastic energy, are subject to minimization, while meeting a constraint on the available material, the emergence of microstructures can be observed. The costs are constantly reduced by fine-scale structures on a decreasing length scale  $\delta$ . For an optimum, a generalized notion is required in the limiting case  $\delta \rightarrow 0$ , where materials are macroscopically characterized by an effective density  $\theta \in [0, 1]$  and an effective behavior only. These are governed by the concrete realization of the underlying microstructure and there are provable optimal, yet nonunique, constructions. Being mostly of theoretical interest, they lack a physical counterpart, which could serve as guidance for manufacturing real materials. The goal of this work is to establish a flexible algorithmic method, that can assess the approximation quality of alternative, simple microstructure models.

A numerical simulation and optimization can only be computationally feasible when distinct length scales are treated in a coupled but separated manner. This work builds upon the intuitive idea of pointwise probing the reaction of the underlying microstructure. A linearization of the macroscopic displacement serves as an affine-periodic boundary condition for a locally attached cell problem, whose solution is used as the microscopic correction. The intuitive approach is rigorously derived and linked to well-known concepts of homogenization, two-scale convergence and the heterogeneous multiscale method (HMM). This allows to adopt results on the approximation quality of the two-scale approach and its discretization.

The deformation of the elastic bodies is modeled via the partial differential equations of linearized elasticity. Within the microscopic cells, the shapes of perforations, parametrized by few degrees of freedom, will be subject to optimization. For this purpose, the shape derivative will be computed analytically in the two-scale context via an adjoint approach. Upon discretization, a finite dimensional optimization problem with constraints on the microscopic geometries and the globally available amount of material is achieved. The numerical scheme uses a finite element discretization on the macroscale and a boundary element method on the microscale. For the optimization problem, an SQP-algorithm of the software `Ipopt` is employed.

At first we consider synthetic problems that allow to study the behavior of optimized microstructures and identify their limits with respect to optimality. On the basis of classical shape optimization problems, we then compare various microstructures among each other and study the gap towards optimality, realized by the analytically optimal sequential lamination model. Furthermore we discuss the influence of numerical parameters and algorithmic speed-up measures.

Next the two-scale scheme is applied to problems in risk averse stochastic optimization, where multiple loads with different probabilities of occurrence need to be taken into account in an appropriate manner. In view of the appearing highly nonlinear functionals, the scheme proves to be robust. Furthermore the concept of stochastic dominance is introduced, which allows to compare results with single-scale optimized shapes.

Finally we derive a posteriori error estimates for the two-scale scheme, following the dual weighted residual (DWR) approach. They are employed to adaptively refine the macroscopic computational grid, which allows to achieve results comparable to uniform refinement with drastically reduced computational cost. The adaptive scheme is used both with the analytical sequential lamination model and the numerical two-scale approach. Furthermore an error estimator is developed, which allows to locally assess the modeling error of the simple microstructures with respect to optimal materials.

Parts of this work have already been published in:

S. Conti, B. Geihe, M. Lenz, and M. Rumpf. “A posteriori modeling error estimates in the optimization of two-scale elastic composite materials.” In: *ESAIM: Mathematical Modelling and Numerical Analysis* 52.4 (2018), pp. 1457–1476. DOI: [10.1051/m2an/2017004](https://doi.org/10.1051/m2an/2017004).

B. Geihe and M. Rumpf. “A posteriori error estimates for sequential laminates in shape optimization.” In: *Discrete and Continuous Dynamical Systems - Series S* 9.5 (2016), pp. 1377–1392. DOI: [10.3934/dcdss.2016055](https://doi.org/10.3934/dcdss.2016055).

S. Conti, B. Geihe, M. Rumpf, and R. Schultz. “Two-Stage Stochastic Optimization Meets Two-Scale Simulation.” English. In: *Trends in PDE Constrained Optimization*. Ed. by G. Leugering et al. Vol. 165. International Series of Numerical Mathematics. Springer International Publishing, 2014, pp. 193–211. DOI: [10.1007/978-3-319-05083-6\\_13](https://doi.org/10.1007/978-3-319-05083-6_13).

B. Geihe, M. Lenz, M. Rumpf, and R. Schultz. “Risk averse elastic shape optimization with parametrized fine scale geometry.” In: *Mathematical Programming* 141.1-2 (2013), pp. 383–403. DOI: [10.1007/s10107-012-0531-1](https://doi.org/10.1007/s10107-012-0531-1).

---

# Contents

---

<b>Summary</b>	<b>v</b>
<b>Notation</b>	<b>xi</b>
<b>1. Introduction</b>	<b>1</b>
<b>2. Literature study on shape optimization</b>	<b>9</b>
2.1. Analytical results on optimal shapes . . . . .	9
2.2. Numerical shape optimization approaches . . . . .	11
2.3. Multiscale methods . . . . .	21
2.4. Error estimation . . . . .	23
2.5. Stochastic optimization . . . . .	27
<b>3. Fundamentals in elasticity</b>	<b>31</b>
3.1. Derivation of a linearized model . . . . .	31
3.2. Properties of elastic materials . . . . .	34
3.3. Solution of the elasticity problem . . . . .	36
3.4. Periodic boundary conditions . . . . .	39
3.5. Periodic homogenization . . . . .	40
3.5.1. Derivation of the homogenized equation . . . . .	41
3.5.2. Properties of the homogenized elasticity tensor . . . . .	43
3.5.3. Remarks as to rigorous justifications . . . . .	44
3.6. Numerical solution . . . . .	46
3.6.1. Finite element method . . . . .	46
3.6.2. Boundary element method . . . . .	50
<b>4. Fundamentals in shape optimization</b>	<b>53</b>
4.1. PDE constrained optimization . . . . .	53
4.1.1. Shape calculus . . . . .	53
4.1.2. Lagrangian calculus . . . . .	55
4.1.3. Shape derivative of cost functionals . . . . .	57
4.1.4. Application to the compliance cost functional . . . . .	57
4.2. Optimal shapes . . . . .	59
4.2.1. Relaxation . . . . .	60
4.2.2. Bounds on the elastic energy . . . . .	62
4.2.3. Sequential lamination model . . . . .	63
4.2.4. Further results on optimal microstructures . . . . .	66

<b>5. A two-scale approach</b>	<b>71</b>
5.1. Derivation of the two-scale model . . . . .	71
5.1.1. Motivation . . . . .	71
5.1.2. Intuitive idea . . . . .	72
5.1.3. Formal description . . . . .	73
5.2. Application of the two-scale model . . . . .	75
5.2.1. Solving of the elasticity problem . . . . .	75
5.2.2. Optimization of microscopic geometries . . . . .	77
5.2.3. Numerical treatment . . . . .	78
5.3. Relation to other approaches . . . . .	79
5.3.1. Periodic homogenization . . . . .	79
5.3.2. Heterogeneous multiscale method . . . . .	80
5.3.3. Works by Barbarosie and Toader . . . . .	81
5.4. Investigated microstructure models . . . . .	82
5.4.1. Ellipsoidal shaped perforations . . . . .	82
5.4.2. Rods with fixed orientation . . . . .	84
5.4.3. Rotating orthogonal rods . . . . .	85
5.5. Aspects of practical realization . . . . .	86
5.5.1. Discrete spaces . . . . .	86
5.5.2. Implementation of the two-scale elasticity problem . . . . .	87
5.5.3. Implementation of the optimization algorithm . . . . .	88
5.5.4. Implementation of the sequential lamination algorithm . . . . .	88
5.6. Computational speedup . . . . .	89
5.6.1. Exploitation of matrix structure . . . . .	89
5.6.2. Exploitation of linearity . . . . .	90
5.6.3. Parallelization . . . . .	90
5.6.4. Microstructure look-up table . . . . .	91
5.6.5. Notes on the microscopic problem . . . . .	91
<b>6. Numerical experiments for the two-scale model</b>	<b>93</b>
6.1. Results for prescribed constant strains . . . . .	93
6.1.1. Setting of the problem . . . . .	93
6.1.2. Numerical results . . . . .	94
6.1.3. Numerical issues . . . . .	101
6.2. Results for a classical shape optimization problem . . . . .	104
6.2.1. Numerical results . . . . .	104
6.2.2. Asymptotic analysis of macroscopic discretization . . . . .	109
6.2.3. Influence of microscopic discretization . . . . .	111
6.3. Inspection of speed-up measures . . . . .	112
6.3.1. Parallelization . . . . .	112
6.3.2. Microstructure look-up table . . . . .	113
6.4. Conclusion . . . . .	115
<b>7. Stochastic Shape Optimization</b>	<b>117</b>
7.1. Preliminaries . . . . .	117
7.2. Stochastic optimization . . . . .	118
7.2.1. Definition of stochastic cost functionals . . . . .	119



---

7.2.2. Practical aspects . . . . .	120
7.2.3. Numerical results for optimization of stochastic cost functionals . . . . .	123
7.3. Stochastic dominance . . . . .	129
7.3.1. Definition of stochastic dominance . . . . .	130
7.3.2. Practical aspects . . . . .	132
7.3.3. Numerical example . . . . .	132
7.4. Conclusion . . . . .	136
<b>8. Adaptive schemes for optimal microstructures</b>	<b>137</b>
8.1. Derivation of weighted error estimates . . . . .	137
8.1.1. Practical aspects . . . . .	141
8.2. Application to the sequential lamination model . . . . .	141
8.2.1. A priori estimation of weights . . . . .	142
8.2.2. Numerical approximation of weights . . . . .	145
8.2.3. Numerical results . . . . .	147
8.3. Application to the two-scale microstructure model . . . . .	158
8.4. Modeling error estimation . . . . .	164
8.5. Conclusion . . . . .	176
<b>9. Conclusion</b>	<b>177</b>
<b>A. Adaptive schemes using triangular meshes</b>	<b>181</b>
<b>B. Variation of the two-scale functional</b>	<b>183</b>
B.1. Two-scale variational framework . . . . .	183
B.2. Error estimation . . . . .	183
B.3. Shape derivative . . . . .	185
B.4. Application to the compliance functional . . . . .	186
B.4.1. Adjoint problem . . . . .	186
B.4.2. Error estimates . . . . .	186
B.4.3. Shape derivative . . . . .	186
<b>C. Software design</b>	<b>187</b>
<b>Acknowledgements</b>	<b>189</b>
<b>Bibliography</b>	<b>191</b>



### Symbols

$\mathbb{N}$	natural numbers, including 0
$\mathbb{Z}$	integers
$\mathbb{R}$	real numbers
$\mathbb{R}^+$	positive real numbers, including 0
$\mathbb{C}$	complex numbers
$\text{Re}$	real part of a complex number
$d$	dimension, mostly $d = 2$ unless otherwise noted
$\delta_{ij}$	Kronecker delta, $\delta_{ij} = 1$ if $i = j$ , $\delta_{ij} = 0$ else
$\mathbb{R}^d$	Euclidean vector space of dimension $d$
$v_i$	$i$ -th component of a vector $v \in \mathbb{R}^d$
$ v $	$l^2$ norm of a vector $v \in \mathbb{R}^d$ : $ v  = \sqrt{\sum_{i=1}^d v_i^2}$
$e_i$	$i$ -th canonical basis vector of $\mathbb{R}^d$ , $(e_i)_j = \delta_{ij}$
$\mathbf{1}$	vector $v \in \mathbb{R}^d$ with $v_i = 1$ for $i = 1, \dots, d$
$\mathbb{R}^{d \times d}$	square matrices of dimension $d \times d$
$\mathbb{R}_{\text{sym}}^{d \times d}$	symmetric matrices in $\mathbb{R}^{d \times d}$
$M_{ij}$	entry of matrix $M$ in $i$ -th row and $j$ -th column
$\ M\ _F$	Frobenius norm of matrix $M$ : $\ M\ _F = \sqrt{\sum_{i,j} M_{ij}^2}$
$SO(d)$	special orthogonal group
$Q$	rotation matrix in $SO(d)$
$\mathcal{O}$	domain used for elastic objects, subset of $\mathbb{R}^d$
$\Gamma$	boundary of $\mathcal{O}$
$\Gamma_D, \Gamma_N, \Gamma_F$	Dirichlet, Neumann, and free part of $\Gamma$ , see Section 3.1
$n$	outer normal of $\mathcal{O}$
$D$	circumjacent working domain, subset of $\mathbb{R}^d$
$\mathcal{Y}$	unit cell used for microscale problem, possibly with holes, see Section 3.5
$D\mathcal{Y}$	circumjacent working domain for cells, mostly the unit cell $[0, 1]^2$
$\delta$	microscopic scale, see Section 3.5
$\theta$	volume of $\mathcal{Y}$ , see Section 3.4, equals local material density, see Section 4.2
$\mathcal{V}$	universal function space
$\vartheta$	universal function from a space depending on context
$\frac{d^m}{dx^m}$	total derivative of order $m$ w. r. t. $x$ ( $m$ omitted for $m = 1$ )
$\partial_x^m$	partial derivative of order $m$ w. r. t. $x$ ( $m$ omitted for $m = 1$ )

$D$	Jacobian, $D\vartheta = \left(\partial_{x_j} \vartheta_i\right)_{ij} \in \mathbb{R}^{n \times m}$ for $\vartheta: \mathbb{R}^m \rightarrow \mathbb{R}^n$
$L^p$	space of functions with Lebesgue integrable $p$ -th power of absolute value
$W^{m,p}$	Sobolev space of $L^p$ integrable functions with mixed weak partial derivatives up to degree $m$ in $L^p$
$\ \vartheta\ _{m,p,\mathcal{O}}$	$W^{m,p}$ -norm of a function $\vartheta$ : $\ \vartheta\ _{m,p,\mathcal{O}} = \begin{cases} \left(\sum_{ \alpha  \leq m} \int_{\mathcal{O}}  \partial^\alpha \vartheta ^p\right)^{\frac{1}{p}}, & \text{for } 1 \leq p < \infty \\ \max_{ \alpha  \leq m} \text{ess sup}_{x \in \mathcal{O}}  \partial^\alpha \vartheta(x) , & \text{for } p = \infty \end{cases}$ with multi-index $\alpha \in \mathbb{N}^d$ , $\partial^\alpha = (\partial_{x_1}^{\alpha_1}, \dots, \partial_{x_d}^{\alpha_d})$ , $ \alpha  = \sum_{i=1}^d \alpha_i$
$ \vartheta _{m,p,\mathcal{O}}$	$W^{m,p}$ -seminorm of a function $\vartheta$ , involving only derivatives of highest order, i. e. $ \alpha  = m$ in previous definition
$H^m$	shortcut for $W^{m,2}$
$H_{\Gamma_D}^1$	space of functions in $H^1$ with vanishing trace on $\Gamma_D$ , see Section 3.3
$H_{\text{per}}^1$	space of functions in $H^1$ , periodic on given domain, see Section 3.4
$H_{\text{per},0}^1$	space of functions in $H^1$ , periodic on given domain with vanishing integral mean, see Section 3.4
$\mathcal{C}^m$	space of functions with smooth derivatives up to order $m$
$F_{,\vartheta}[\vartheta](v)$	Gâteaux derivative of functional $F$ in direction $v$ : $F_{,\vartheta}[\vartheta](v) = \lim_{\delta \rightarrow 0} \delta^{-1}(F[\vartheta + \delta v] - F[\vartheta])$
$u$	solution of elasticity problem, see (3.10)
$\varepsilon_x[u]$	strain tensor $\frac{1}{2}(Du + Du^\top)$ with derivatives w. r. t. $x$ , see Section 3.1
$\varepsilon_{ij}$	symmetric basis matrix with $(\varepsilon_{ij})_{kl} = \frac{1}{2}(\delta_{ik}\delta_{jl} + \delta_{jk}\delta_{il})$
$\sigma$	stress tensor, see Section 3.1
$C$	elasticity tensor, see Section 3.1
$C^*$	effective elasticity tensor, see (3.26)
$p$	dual solution, see Section 4.1.2
$\mathcal{R}$	reconstruction operator for microscopic quantities, see Section 5.1.3
$q$	vector of coefficients defining microstructure, see Section 5.2.2
$l$	number of coefficients
$\varrho, m, \theta$	parameters of sequential lamination model, see Section 4.2.3
$\chi_A$	characteristic function of set $A$ : $\chi_A: A \rightarrow \{0, 1\}$ , $\chi_A(x) = 1$ if $x \in A$ , $\chi_A(x) = 0$ otherwise
$H$	Heaviside function: $H: \mathbb{R} \rightarrow \{0, 1\}$ , $H(x) = \chi_{\{x > 0\}}(x)$ , see Section 7.2.1
$d_{\mathcal{O}}$	shape derivative w. r. t. domain $\mathcal{O}$ , see Section 4.1.1
$\mathbf{J}$	arbitrary cost functional, see (4.1)
$\mathbf{J}^c$	compliance cost functional, see (4.11)
$\mathbf{J}^{\text{total}}$	total free energy, see (3.12)
$\mathcal{L}$	Lagrangian, see (4.2)
$\mathbf{Q}$	stochastic cost functionals, see Section 7.2.1
$\mathcal{M}_h$	computational grid with mesh width $h$ , see Section 3.6.1
$E$	finite element $E \in \mathcal{M}_h$ , see Section 3.6.1
$\mathcal{P}_k$	space of polynomials of maximum degree $k$ , see Section 3.6.1

---

$\mathcal{V}_h^{(k)}$	finite element space of globally continuous, piecewise polynomials of order $k$ , see Definition 3.20
$\mathcal{I}_h^{(k)}$	Lagrange interpolating polynomial of order $k$ (in each dimension), see Definition 3.21
$\mathcal{N}_h$	degrees of freedom: set of nodes on which discrete values are prescribed
$N$	number of degrees of freedom $N :=  \mathcal{N}_h $ , see Section 3.6.1
$\mathcal{U}_{\text{ad}}$	set of admissible shapes, see Section 4.1.2

## Sub- and superscripts

$h$	discretized quantity on grid $\mathcal{M}_h$ with mesh size function $h$ , see Section 3.6.1
$\delta$	quantity with multiple, fully resolved scales, see Section 3.5
$*$	macroscopic, effective part of a multiscale quantity, see Section 3.5
$\sim$	microscopic, periodic part of a multiscale quantity, see Section 5.1.3
$\hat{\phantom{x}}$	fundamental solutions, see Section 3.6.2
L	quantity in context of the sequential lamination model, e. g. $u^{\text{L}}$
M	quantity in context of the two-scale microstructure model, e. g. $u^{\text{M}}$
opt	optimized quantity

## Operators

$\cdot$	scalar product of two vectors $a, b \in \mathbb{R}^d$ : $a \cdot b = \sum_{i=1}^d a_i b_i$
$:$	inner product of two matrices $A, B \in \mathbb{R}^{d \times d}$ : $A : B = \sum_{i,j=1}^d A_{ij} B_{ij}$



---

# CHAPTER 1

## Introduction

---

SHAPE optimization is a very natural, yet highly complex phenomenon that can be witnessed in various facets of everyday life. Whenever a body is subject to any kind of outer forcing, it often has a beneficially adapted shape in order to withstand. At the same time, consuming as few material as possible comes in as a natural constraint, for saving on weight and material, or functional reasons. Out of these contradictory goals, fascinating structures emerge. They can be seen in diverse environments and on highly varying length scales. Examples include advanced engineering, as in bridges, ogives in classical architecture, patterns in nature and biology, as in bones or vascular tissue, and self-similar microscopic arrangements of atoms in crystalline grids.

From a mathematical point of view, shape optimization is by no means less interesting or complex. An early instance is the Dido problem dating back to antiquity. Told in Virgil's Aeneid, Dido was allowed to buy as much land as she could enclose with a bull's hide. Phrased mathematically, the task was to find a shape with largest enclosed area among all with a given, fixed perimeter. The solution being a circle was already proven by the Greek in an accepted way at that time. However it lasted until the 19th century and the advent of the calculus of variations that a rigorous proof was available [86]. This historical example is meant to give evidence that shape optimization problems are often easily comprehensible but hard to tackle mathematically.

**Motivation.** The special nature of shape optimization lies in the variability of the domain itself. This comes along with lacking regularity in the space of the degrees of freedom. In addition, practical shape optimization problems, governed by a state equation and a constraint on the amount of material, turn out ill-posed. An optimal shape does not exist and instead, microstructures, formed on infinitesimally small length scales, allow to incessantly decrease typically chosen target functionals. This is the practical manifestation of lacking compactness in theory and has fostered novel research areas and methods. By virtue of relaxation, the classical notion of a shape comprising bulk and void regions is left behind and intermediate material densities are allowed as limiting cases of infinitesimally small microstructures. The theory of *homogenization* allows to eliminate scales and define corresponding effective material properties on the macroscale. Here an intriguing fact is that the set of effective tensors, known as *G-closure*, lacks an algebraic description. As such it cannot be easily searched for minimizers of specific functionals. Moreover optimal candidates are not unique and can possibly be obtained via different microscopic constructions.

A numerical scheme for shape optimization will naturally adopt the creation of fine-scale structures, but is practically limited by the resolution of the computational grid. An illustrating example is shown in Figure 1.1. Here a two dimensional domain serves as a model of an

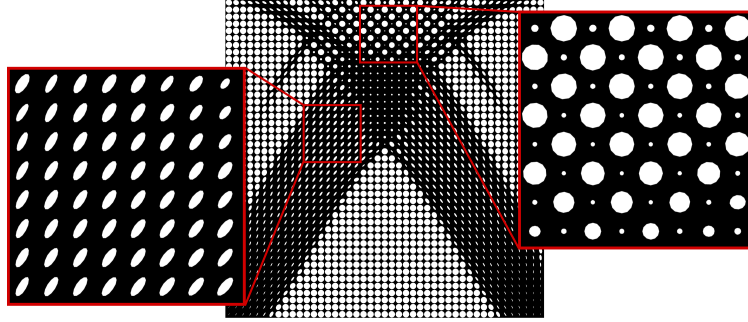


Figure 1.1.: Shape optimization of  $45 \times 45$  ellipsoidal perforations in an elastic plate subject to shearing loads, from [183].

elastic plate, fixed at the bottom and subject to a horizontal shearing load at the top. Its rigidity is to be optimized and a numerical scheme adapts the elongation and orientation of the ellipsoidal perforations while maintaining a constraint on the overall area cut out. From the result two fundamental insights can be drawn. First, the distribution of invested material demarcates different areas. The resulting global shape is reminiscent of a supporting structure. Second, within the identified areas the perforations establish diverse periodic patterns. A further numerical optimization, with more ellipsoidal perforations allotted, changes the result in two aspects. First, the interfaces between the identified areas become sharper. Second, the periodic patterns remain, but on a smaller scale, corresponding to the refinement w. r. t. the allotted perforations. Both consequences improve the shape in terms of the optimization problem.

The fundamental idea of the two-scale shape optimization model developed in this work is to decouple the observed behaviors. Thereby shapes, characterized by distinct amounts of invested material, and their demarcating interfaces are realized on a macroscopic scale. Fine perforations are considered and optimized on a separate microscopic scale, where periodicity and scale invariance allow to remove the limitation by the computational grid. The established numerical scheme is easily parallelized and makes use of simple geometries, where only the boundaries need to be discretized. This results in an efficient and highly versatile framework for the exploration of optimal microstructures. In contrast to purely theoretical constructions, realistic material models are obtained, which could actually be manufactured.

**The two-scale approach.** Starting on the macroscopic scale, a linearized elasticity problem for given boundary conditions is to be solved. Its weak solution can be characterized as the unique minimizer of the total free energy

$$\begin{aligned} \mathbf{J}^{\text{total}}[\mathcal{O}; u] &:= \frac{1}{2}a(\mathcal{O}; u, u) - l(\mathcal{O}; u) \\ &:= \frac{1}{2} \int_{\mathcal{O}} C\varepsilon[u] : \varepsilon[v] \, dx - \int_{\mathcal{O}} f \cdot v \, dx - \int_{\Gamma_N} g \cdot v \, da(x), \end{aligned} \quad (1.1)$$

where  $\mathcal{O}$  is the domain,  $f$  and  $g$  denote volume forces on  $\mathcal{O}$  and surface loads on a part  $\Gamma_N$  of the boundary,  $u$  is the unknown *displacement*,  $\varepsilon[u] = \frac{1}{2}(Du + Du^\top)$  the *strain tensor*, and  $C$  the *elasticity tensor*, characterizing material properties and linearly relating the strain



to a stress  $\sigma = C\varepsilon[u]$ . The microstructures to be investigated are made of perforations placed on a regular lattice, as seen in Figure 1.1. Their length scale  $\delta$  should possibly be small, leading to rapid oscillations in the corresponding tensor field  $C^\delta$  and consequently in the elastic solution  $u^\delta$ . At this point a fully resolving numerical scheme would become computationally infeasible. Instead, purely macroscopic and smoothly varying quantities  $C^*$  and  $u^*$  are considered, which are enriched by microscopic corrections on demand. In particular the macroscopic problem is discretized using the *finite element method (FEM)*, where integrals of the weak problem are computed via numerical quadrature. Whenever the bilinear form  $a(\mathcal{O}; u^\delta, u^\delta)$  needs to be evaluated at a fixed macroscopic point  $x$ , a locally attached cell  $\mathcal{Y}(x)$ , carrying a representative of the perforation pattern, is considered. On this domain the weak linearized elasticity *corrector problem*

$$\int_{\mathcal{Y}(x)} C(x, y) \varepsilon_y[\tilde{u}](x, y) : \varepsilon_y[\vartheta](y) \, dy = - \int_{\mathcal{Y}(x)} C(x, y) \varepsilon_x[u^*](x) : \varepsilon_y[\vartheta](y) \, dy \quad \forall \vartheta$$

is solved for a periodic displacement  $\tilde{u}$  in the decoupled microscopic variable  $y$ , where  $\vartheta$  is an appropriate test function. The right hand side is fixed and can be interpreted as inhomogeneous Dirichlet boundary conditions, deforming the cell by the linear mapping  $(\mathbf{1} + \varepsilon_x[u^*])(x)$ . This intuitive idea is sketched exemplarily in Figure 1.2. Practically we solve the cell problems

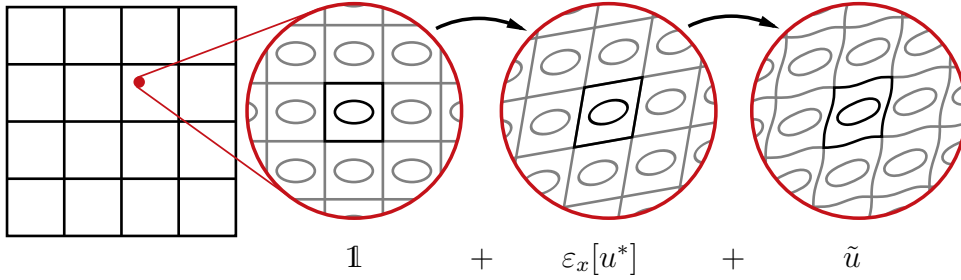


Figure 1.2.: Macroscopic domain with computational grid and magnified locally periodic lattice with perforation. Upon applying a linear deformation, the solution of an elasticity cell problem provides the microscopic displacement correction.

using the *boundary element method (BEM)*, which requires a discretization of the boundaries of the perforations only. The initially considered bilinear form is finally evaluated using the corrected displacement as an approximation of the true, fully resolved solution, i. e.

$$(C^\delta \varepsilon[u^\delta] : \varepsilon[u^\delta])(x) \approx \text{Vol}(\mathcal{Y})^{-1} \int_{\mathcal{Y}(x)} C(x, y) \varepsilon_y[\mathcal{R}[u](x, y)] : \varepsilon_y[\mathcal{R}[u](x, y)] \, dy$$

with  $\varepsilon_y[\mathcal{R}[u](x, y)] = \varepsilon_x[u^*](x) + \varepsilon_y[\tilde{u}](x, y)$ .

We elaborate on this intuitive idea and rigorously derive the sketched correction operation. Thereby links to well-known concepts of *periodic homogenization*, *two-scale convergence*, and the *heterogeneous multiscale method (HMM)* are established.

In view of optimization, the classical choice of the *compliance* functional is adopted, which serves as a measure of rigidity. It is defined by

$$\mathbf{J}^c[\mathcal{O}; u[\mathcal{O}]] := \int_{\mathcal{O}} f \cdot u[\mathcal{O}] \, dx + \int_{\Gamma_N} g \cdot u[\mathcal{O}] \, da(x) \quad (1.2)$$

and is related to the total free energy via  $\mathbf{J}^c[\mathcal{O}; u[\mathcal{O}]] = -2\mathbf{J}^{\text{total}}[\mathcal{O}; u]$ . However, the methodology developed in this work is in no way restricted to this special instance. The degrees of freedom to be optimized are parameters  $q$  of the microscopic perforations. To this end we focus on simple geometries like ellipsoidal and rectangular holes. The optimization is driven by the external software `Ipopt`, a *sequential quadratic programming (SQP)* type algorithm for constrained finite dimensional optimization. It is able to handle equality and inequality constraints on the parameters, which are required to impose a global constraint on the amount of material and to maintain intact cell geometries, respectively. Besides the constraints, the target functional and its first derivative need to be provided. For the latter we compute the analytical *shape derivative*.

Shape calculus is a fully established theory on its own. The aim is to rigorously obtain a directional derivative, i. e.  $d_{\mathcal{O}}\mathbf{J}[\mathcal{O}](V)$ , where  $V$  describes the variation of the shape. Ultimately it can be calculated explicitly for certain functionals. A common difficulty is that the considered objective functionals typically involve the solution  $u$  of the elasticity problem, which in turn depends on the shape itself. This nested dependence is solved by Lagrangian calculus and the introduction of an adjoint problem, which is routinely used for single-scale problems. We show that, due to linearity of the corrector problem, an application within the proposed two-scale framework is straightforward.

The developed two-scale approach was presented in [138] and the employed geometries were already used in [184] in the single-scale context.

**Applications.** The devised numerical two-scale scheme is applied to a range of shape optimization problems, starting with synthetic benchmarks and ultimately leading to multi-load stochastic programming. In a first step the macroscopic strain tensor  $\varepsilon_x[u^*]$  is assumed constant, which allows to check corner cases for optimizing microstructures. When e. g. a uniaxial compression is imposed, the perforations align with the forcing, see Figure 1.3(a). The shape realized by rectangular holes seems better suited than the elongated ellipsoidal perforation. In fact it creates a simple laminate, which is provable optimal in this situation. When shearing is imposed, there is no dominant axis and both models create a lattice, see Figure 1.3(b). The overall rotation in case of the rectangular holes allows for a better adaptation, but nevertheless both models fall short of an optimal microstructure, which is e. g. achieved by sequential lamination. This construction, however, requires several successive limiting processes, each on a distinct scale. In total we examine four microstructure models obtained from simple perforations. We apply the two-scale approach to classical shape optimization problems and constantly compare to optimal results given by the sequential lamination model. These results were partly published in [138].

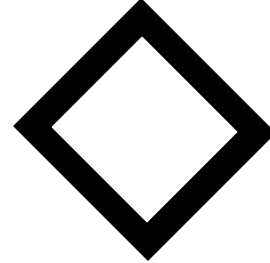
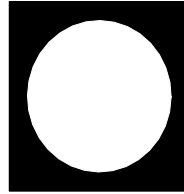
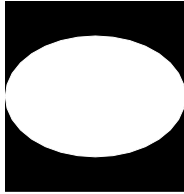
Next we embark on a stochastic perspective, a highly relevant topic for real world applications where often a lack of full data needs to be faced. In this context we do not consider a single macroscopic loading anymore, but a great many, each associated with a probability of occurrence. As concrete events cannot be predicted, all possibilities need to be taken into account a priori in a suitable manner. We therefore transfer concepts of *two-stage stochastic programming*, an established field in operations research, to our two-scale shape optimization model. A critical aspect is the choice of an objective functional, which initially takes the form

$$\mathbb{E} [r(\mathbf{J}[\omega, \mathcal{O}; u])],$$

where  $\omega$  denotes possible events. Simply computing the expected value of individual cost functionals turns out negligent, as events with low probability but critical impact are not

$$u^*(x, y) = (x, 0), \quad \varepsilon[u^*] = \begin{pmatrix} 1 & 0 \\ 0 & 0 \end{pmatrix}$$

$$u^*(x, y) = (y, 0), \quad \varepsilon[u^*] = \begin{pmatrix} 0 & \frac{1}{2} \\ \frac{1}{2} & 0 \end{pmatrix}$$



(a) Uniaxial compression.

(b) Shearing.

Figure 1.3.: Representative cell of optimized periodic microstructures using ellipsoidal and rectangular perforations for two types of loading.

adequately taken into account. Therefore the choice of the *ranking function*  $r$  is important. We consider  $r(t) = \max\{t - \eta, 0\}$  and  $r(t) = H(t - \eta)$ , with the *Heaviside* function  $H$ , leading to the *expected excess* and *excess probability* functionals. Both include a threshold parameter  $\eta$ , which allows to steer the perception of critical events. Its influence can be seen in Figure 1.4 for the excess probability functional and ellipsoidal perforations in the two-scale scheme. Depending on its value the amount of material invested to support the upper right or left hand varies. These results were partly published in [138].

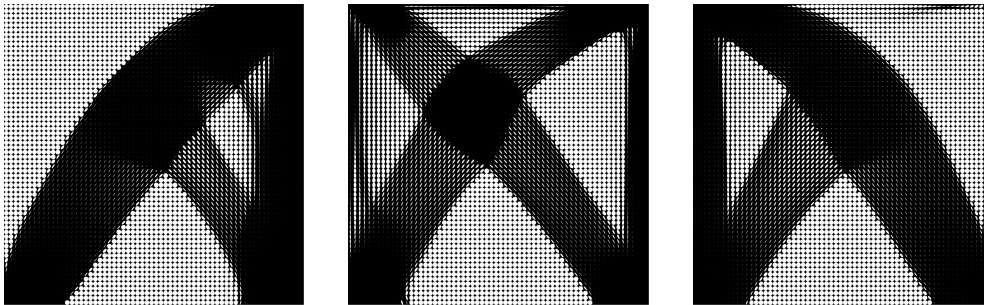


Figure 1.4.: Results of stochastic optimization using the excess probability functional with increasing threshold parameter  $\eta$  from left to right. The macroscopic domain is subject to strong loadings with low probability on the upper left boundary, and weak loadings with high probability on the upper right part. Ellipsoidal perforations are used in the two-scale scheme and a representative of the underlying microstructure is shown within each macroscopic grid cell.

A new application is *stochastic dominance*, a concept where an already existing shape serves as a benchmark. Competing candidates with less material are searched, while they need to perform comparable to the benchmark for each loading scenario. The choice of ranking functions leads to different order relations in this comparison, which possibly allow for flexibility by balancing a budget of exceeding costs.

The advanced applications come at the price of more intricate, initially non-smooth functionals, which need to be taken care of. In view of the many possible events, the computational costs can still be kept low, again by virtue of linearity. In the end the devised two-scale scheme turns out efficient and remarkably robust.

**A posteriori error estimates and grid adaptivity.** With an optimization scheme for microstructures at hand, the improvement of the macroscopic numerical model is approached next. As motivated before via Figure 1.1, interfaces can be identified across which the effective amount of spent material jumps. In consequence these interfaces should be resolved sharply, which can be achieved efficiently via grid adaptivity. To select cells in the computational mesh that are eligible for refinement, suitable error indicators need to be computed. To this end we pick up the *dual weighted residual (DWR)* approach for optimal control problems. Based on Lagrangian calculus it yields an *a posteriori error estimate* of the form

$$\begin{aligned}
 |\mathbf{J}[q; u^*] - \mathbf{J}[q_h; u_h^*]| &\leq \sum_E \left( \eta_E^u + \eta_{\partial E}^u + \frac{1}{2} \eta_E^q \right) (q_h; u_h^*) + \mathcal{R} \quad \text{with} \\
 \eta_E^u &:= \left| \int_E \operatorname{div} \{ C^*[q_h] \varepsilon[u_h^*] \} \cdot (u^* - \vartheta_{u_h^*}) \, dx \right|, \\
 \eta_{\partial E}^u &:= \left| \int_{\partial E} j(C^*[q_h] \varepsilon[u_h^*]) \cdot (u^* - \vartheta_{u_h^*}) \, da(x) \right|, \\
 \eta_E^q &:= \left| \frac{d}{dq_h} \left( \int_E C^*[q_h] \varepsilon[u_h^*] : \varepsilon[u_h^*] \, dx \right) (q - \vartheta_{q_h}) \right|.
 \end{aligned}$$

Here  $u^*$  and  $q$  denote the unknown, continuous displacement field and optimal microstructure parameters,  $u_h^*$  and  $q_h$  their discretized counterparts, and  $\vartheta$  appropriate test functions.  $\mathcal{R}$  is a remainder term of higher order and  $j$  defines the jump of normal stresses across edges of cells  $E$  in the computational mesh. The error estimator is *goal-oriented*, which means it controls the error in the target functional, rather than the discretization error in the PDE solution, as done by traditional residual based estimators. Thereby another term  $\eta_E^q$  comes into play, measuring the sensitivity of the local elastic energy density w. r. t. the optimization parameters.

We transfer the concept to our two-scale shape optimization approach. For terms still involving unknown continuous quantities, suitable approximations are defined, based on interpolation to higher order polynomials. Taking a macroscopic point of view, the gained adaptive scheme can directly be applied to the sequential lamination construction and our microscopic perforations. Hereby macroscopic, effective elastic properties stem from analytical formulae or numerical optimization, respectively. In case of sequential lamination, an explicit dependence of the parameters on the elasticity solution furthermore allows to derive rigorous a priori estimates. In Figure 1.5 results using sequential lamination for a bridge type scenario are shown. Sharp interfaces are established, separating void, solid, and regions with intermediate amounts of material. These results were partly published in [185].

Likewise, results are obtained for the two-scale scheme with numerically optimized microscopic perforations. In this context the comparison to the functional  $\mathbf{J}[q^M; u^*]$  however is fallacious. It comprises the continuous, optimized parameters  $q^M$ , but the employed model is already known to partly produce suboptimal results. Instead we consider  $\mathbf{J}[q^L; u^*]$  with optimal sequential lamination parameters  $q^L$ . To maintain efficiency, these are approximated on the

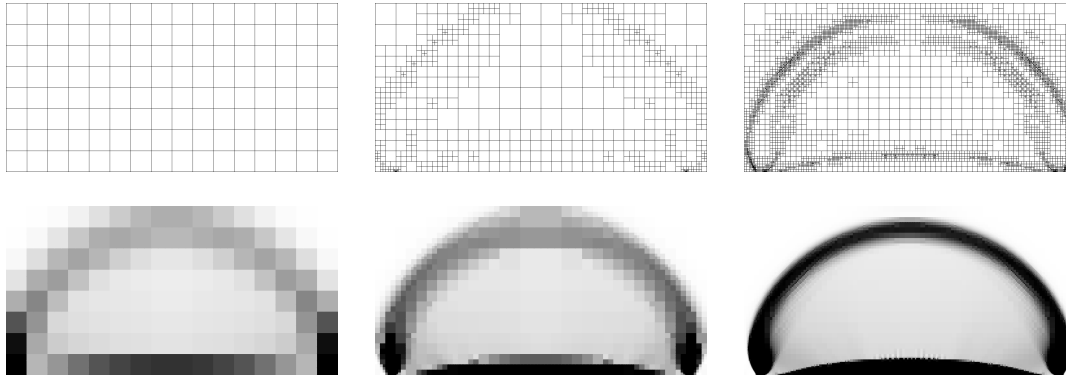


Figure 1.5.: Results of the adaptive scheme using sequential lamination as microstructure model for a bridge fixed at the lower left and right hand side and subject to a downwards pointing load in between. Refined meshes and corresponding effective amounts of material after 0, 8, and 16 refinement steps are shown.

fly via a truncated iterative algorithm. In Figure 1.6 outcomes of the resulting scheme for a cantilever type scenario are shown. A crucial insight is that the error  $|\mathbf{J}[q^L, u^*] - \mathbf{J}[q_h^M; u_h^M]|$

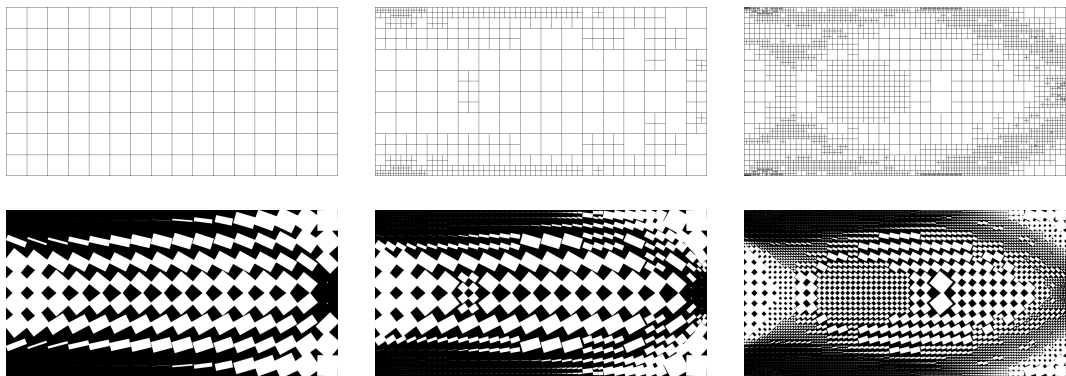


Figure 1.6.: Results of the adaptive scheme steered by modeling error estimation and using rectangular perforations as microstructure for a cantilever fixed at the left hand side and subject to a downwards pointing load on the right hand side. Adaptively refined meshes and corresponding optimized microscopic perforations after 0, 4, and 8 refinement steps are shown.

cannot be driven to zero anymore. Still the algorithm allows to asses the remaining global error due to the suboptimal microstructure modeling and its spatial distribution. These results were partly published in [137].

**Overview.** This thesis is structured as follows. In Chapter 2 an extensive study of literature on research fields linked to the method developed in this work is presented. The theory of linearized elasticity, which is used as the state model throughout this work, is recapitulated

in Chapter 3. Fundamental aspects of shape optimization, covering the shape derivative, Lagrangian calculus in PDE constrained optimization, the concept of relaxation and optimizing microstructures, and especially explicit formulae for sequential lamination, are summarized in Chapter 4. The two-scale approach is motivated and derived rigorously in Chapter 5. Fundamental shape optimization concepts are applied in the two-scale context and the approach is linked to well-known theory. Moreover practical aspects are covered, namely the concrete construction of investigated microstructures, the implementation of the numerical scheme, and employed speed-up measures. Chapter 6 presents results of the two-scale approach for synthetic benchmarks and classical shape optimization problems. Optimal results obtained from sequential lamination are constantly considered for comparison. Numerical issues, the influence of numerical parameters, and the effectiveness of speed-up measures are analyzed. Chapter 7 is devoted to stochastic optimization. Basic principles from mathematical programming are introduced and related to PDE constrained shape optimization. For several stochastic cost functionals and stochastic dominance the practical realizations are discussed and extensive results based on two microstructure models are presented. Chapter 8 deals with a posteriori error estimation and grid adaptivity in the context of two-scale shape optimization. For a macroscopic, effective formulation the dual weighted residual approach is adopted and applied to the sequential lamination and the two-scale model. Furthermore an approach to modeling error estimation with regard to non-optimal microstructures is devised. Finally Chapter 9 draws conclusions and hints at further research perspectives.

---

## CHAPTER 2

### Literature study on shape optimization

---

RESEARCH results in fields close to the topics of the present work are surveyed in this chapter. Shape optimization problems typically comprise a geometry description, a state equation modeling physical behavior, and a quantity of interest to be optimized. As such, they are special instances of optimal control problems, constrained by partial differential equations, which is a well-established field [260, 398, 228]. However, with the domain itself being the control, typical regularity results of the control-to-state mapping do not exist. Shape optimization is therefore a topic on its own and has received a lot of scientific attention. Comprehensive material can be found in the textbooks [52, 375, 79, 218, 121, 18, 217].

This work deals with structural optimization, where the domain is regarded as an elastic body. The most classical setting is considered, where the deformation is modeled via the partial differential equations of linearized elasticity and the compliance cost functional is used as a measure of rigidity. However, the range of applications for shape optimization is huge. The following literature survey thus focuses on established results and techniques rather than applications. Further fundamental concepts, which appear as building blocks in the developed two-scale approach, are detailed in the respective chapters along with corresponding references.

#### 2.1. Analytical results on optimal shapes

Naturally, a fundamental question in shape optimization is whether a provably optimal shape can be found. In contrast to purely geometric settings, as for the Dido problem in the introduction, such rigorous results are limited in the context of PDE constraints. For general expositions, see the textbook chapters [331, Chapter 3] and [97, Chapter 5].

**Ill-posedness.** As hinted in the introduction, optimal solutions for common problems in shape optimization often do not exist. Instead, microstructures appear on infinitesimally small length scales. Such counter examples were first given by Murat [298, 299] for a scalar state equation and coefficients subject to optimization. A vectorial equivalent is described by Kohn and Strang in [256, Example 8.3]. As a remedy it is either possible to restrict the set of admissible shapes by adding further constraints, or to enlarge the set by relaxation, which amounts to allow for generalized, possibly non-physical, designs.

**Restriction.** An early reference is Cherepanov [118]. Here the state  $u$  solves a Neumann problem on the domain  $\mathcal{O}$  and a tracking functional  $\mathbf{J}[\mathcal{O}] = \|u - u_0\|_{\mathcal{O},0,2}$  with prescribed state  $u_0$  is minimized. Admissible domains are required to satisfy a uniform cone property, which

is equivalent to uniform Lipschitz continuity for the boundary. Under this assumption the existence of a minimizer is proven, based on continuity of the cost functional and compactness of the set of admissible shapes. Šverák [390] proves existence in two space dimensions under the assumption that the complement of  $\mathcal{O}$  has a limited number of connected components. This is sufficient to deduce continuity of the state for limiting domains. In [109] Chambolle shows an analogous result for linearized elasticity. Thereby the existence of solutions to the cantilever shape optimization problem and the time-continuous fracture evolution model by Francfort and Marigo [177] is proven. Ambrosio and Buttazzo [32] impose a penalization of the perimeter  $\text{Per}(\mathcal{O})$  of the domain by extending the cost functional to  $\mathbf{J}[\mathcal{O}] + c\text{Per}(\mathcal{O})$ . In the scalar setting for conductivity and under a growth assumption for  $\mathbf{J}[\mathcal{O}]$ , they prove a compactness property which implies the existence of an optimal solution. Chambolle and Larsen [110] prove  $C^\infty$ -regularity of the free boundary of a shape minimizing the compliance and penalizations for the volume and the perimeter. The result holds in the scalar setting and, with some limitation, for linearized elasticity as well.

**Relaxation.** The idea of relaxation, which goes back to Hilbert [226], is to re-enable the direct method of the calculus of variations by defining an appropriate closure of the space of admissible designs, and corresponding extensions of the state equation and objective functionals. First rigorous results are attributed to McShane [282] and Young [423]. Textbooks on the subject are e. g. [424, 142, 168].

In the context of optimal design, homogenization turned out to be an essential tool for relaxation. It is the mathematical foundation for accurately describing the effect of mixing materials on a microscopic scale and, as such, is closely related to the study of composite materials. Kohn and Strang comprehensively describe the interplay of structural optimization and relaxation by either homogenization or convexification [254, 255, 256].

Apart from the homogenization approach, Buttazzo and Dal Maso [103] use relaxation of a Dirichlet problem with a general cost functional to show existence of minimizers and derive optimality conditions. In [104] Buttazzo and Dal Maso study target functionals which are monotonic w. r. t. set inclusion and lower semicontinuous w. r. t.  $\Gamma$ -convergence. An elliptic PDE with Dirichlet boundary conditions is considered and the objective is optimized among all domains with a prescribed volume. No additional regularity is assumed, but admissible shapes are allowed to be quasi-open, i. e. they are allowed to differ from open sets by an infinitesimal capacity. Under these conditions the existence of minimizers is proven.

**Composite materials.** The goal of the study of composite materials is to define an appropriate notion of an averaging process, which allows to predict the effective macroscopic behavior. It is thus highly relevant for physical and engineering applications. In this context, often *representative volume elements* (RVE) are investigated as samples of a material, whose microscopic arrangement is typically only given by a stochastic modeling assumption. A first reference is Maxwell [281] from 1873, who considers the effective conductivity of a material including spherical particles. Exhaustive expositions on composites can be found in the survey article by Hashin [214] and the textbooks by Sendeckyj [366] and Milton [285].

**Homogenization.** From the mathematical point of view, homogenization is a notion of convergence for the solution operator of the state equation. It allows to derive a limiting problem on the scale of interest for a sequence of problems associated with a sequence of



composite material domains. The development started in the 1970s, see [393, 305, 158, 257, 190, 297, 269] for early references and the collection [124] for some English translations.

Textbooks on the subject are, among others, [81, 48, 314, 239, 93, 132, 130]. The idea of employing homogenization to obtain solutions to optimal design problems first appears in works by Lurie [266], Tartar [393], and Raitums [337]. In the context of bars and plates early references are Lurie et al. [270, 271] and Cheng and Olhoff [117]. The full elasticity setting is treated by Suquet [388] and Francù [180].

**G-closure and optimal bounds.** The search for optimal microstructures later became more systematic by studying the *G-closure*, which is the set of all effective tensors obtained via homogenization. It can be fully described by algebraic formulae in case of the scalar conductivity problem, but not for elasticity. Instead, bounds are derived for important quantities defined on the set. The elastic energy density, which appears in the state equation (1.1) as well as in the compliance objective (1.2) in our work, received a lot of attention. We present the most important results in Section 4.2.2 and our employed relaxation procedure in Section 4.2.1.

**Optimal microstructures.** With the optimal bounds at hand, microscopic constructions have been proposed that actually attain the bounds, thereby reducing the full G-closure to subsets of simpler structure. The most universal one is sequential lamination. It will be covered in detail in Section 4.2.3 and serve as a benchmark for our numerical approach. Further, at least partially, optimal constructions are presented in Section 4.2.4.

Apart from these constructions, considered in the course of relaxation via homogenization, many other interesting results were obtained under specialized conditions. Focussing on shape optimization as considered in this work, an early famous example is the Michell truss construction from 1904 [283]. Finitely many joints, connected by elastic rods, are considered. It is assumed that the thickness of the rods is proportional to the stresses they can withstand. For a given external load, a framework with least volume of material is sought that is capable of sustaining the inner stresses, and esthetical results are obtained. Buttazzo and Aze [102] consider periodic frameworks of infinitesimally thin lower dimensional layers with infinite conductivity and analyze their optimal potential based on  $\Gamma$ -convergence results. Kohn and Wirth [250, 251] study compliance optimization under volume and perimeter penalization for uniaxial and shearing loads. They focus on the limiting case of very small perimeter penalization, thereby allowing for tiny structures. Based on a triangular truss construction, a hierarchical branching pattern is proposed. Boundary layer estimates are used where the construction has to be fitted to geometric constraints. Finally an optimal scaling law in the perimeter penalization parameter is obtained.

## 2.2. Numerical shape optimization approaches

Shape optimization is highly relevant from a practical point of view. However, as seen in the previous survey, rigorous results are limited to special, often unphysical, settings. Therefore numerical approaches received a lot of attention as soon as they became available. They differ in the degrees of freedom allocated for admissible shapes and the way the shapes are represented. A rough categorization distinguishes *sizing*, *shape*, and *topology optimization*.

In sizing optimization, shapes are a priori fixed and only a small set of parameters is varied. For structural optimization, e. g. the thickness of rods or the location of joints could

be controlled. Often the state, e.g. the elastic response of the rods, can directly be evaluated in terms of the parameters via an appropriate modeling. The associated optimization problem is inherently discrete and techniques from mathematical programming can be applied. An early reference is [359] by Schmit. Problems of this type are often well-posed, an existence result is e.g. proven by Bendsøe [76]. In works by Rozvany et al. [353, 352] *optimality criteria methods* are explored, which are based on continuum-type state models and discretizations by large finite element systems. There is a lot of classical literature available on the subject, see e.g. the textbooks [427, 355]. A more recent example is [155], dealing with branching patterns in metallurgy.

In contrast to the discrete setting, the shape is regarded as a continuum for shape and topology optimization. Here admissible domains are usually arbitrary subsets of a given working domain. An evident approach is to start from an initial shape  $\mathcal{O}$  and apply slight variations to improve its performance w.r.t. a defined measure  $\mathbf{J}[\mathcal{O}]$ . This leads to the *perturbation of identity* technique. Considering a vector field  $\vartheta$  and the perturbed shape  $\mathcal{O}_t$ , a *shape derivative* can be defined as

$$d_{\mathcal{O}} \mathbf{J}[\mathcal{O}] := \lim_{t \searrow 0} \frac{1}{t} (\mathbf{J}[\mathcal{O}_t] - \mathbf{J}[\mathcal{O}]), \quad \mathcal{O}_t = (\text{Id} + t\vartheta) \mathcal{O}.$$

Early references are [300, 373] by Murat and Simon. The resulting formulae for integral quantities were already given before by Hadamard [208]. They can be used to compute sensitivities and steer optimization schemes. Later on, the more general *velocity method* was introduced by Zolésio [431, 432]. In special situations both concepts coincide. We follow the later approach and give further details in Section 4.1.1. By now, important results for second order shape derivatives are available as well, but will not be employed in this work.

Classical results show that the shape derivative only depends on variations of the boundary of the shape. Naturally, such variations leave the topology mostly fixed. Opposing parts of the boundary might merge, but there will not be any spontaneous creation of holes, which however play a crucial role for optimal shapes. Apart from the rigorous result already presented above, the formation of microstructures was observed in numerical approaches as well. Early indications can be found in [108] by C ea et al., or in [117] by Cheng and Olhoff in the context of plates.

In summary, a numerical approach should on the one hand be able to flexibly represent the shape and allow for changes in its topology. On the other hand, as shape optimization is ill-posed, arbitrary fine structures must be avoided or handled in an appropriate manner. Of course, a natural limitation is induced by the finite discretization, but such a mesh dependence is to be avoided for a stable numerical scheme. In the following we list different numerical techniques.

**Boundary variation technique.** A straightforward application of the shape derivative concept leads to boundary tracking methods. Here the computational domain is fully resolved and discretized to allow the evaluation of the derivative for certain variations of the boundary. These could directly stem from moving nodes of the computational grid or indirectly from varying parameters, e.g. control points of spline functions or properties of fixed shapes as in sizing problems. When a profitable variation is found, the domain is updated. Early references with several examples are [330, 127, 147, 148]. To maintain the quality of the computational grid, remeshing is typically required after several steps, which has to be integrated in an automated manner, see e.g. [88]. Using the boundary element method significantly reduces

the algorithmic workload as only the boundary is discretized, see e. g. [98, 245]. Still the initial topology is fixed throughout and fundamental changes, such as constricting domains, are difficult to handle. More recent applications of the boundary variation technique can e. g. be found in [219, 60], dealing with optimization of microstructures for conductivity and elasticity problems, or [140], investigating branching patterns in metallurgy.

**Level set method.** An entirely different approach is offered by the level set method. It uses an implicit representation via a scalar function  $\phi: D \subset \mathbb{R}^d \rightarrow \mathbb{R}$ , defining the actual shape as  $\mathcal{O} = \{x \in D: \phi(x) < 0\}$ , i. e. the boundary is the zero level set of  $\phi$ . The method was originally introduced by Osher and Sethian in [317] in the context of mean curvature motion. Since then it has been used extensively in many disciplines, like image processing, computational geometry, and optimization. The evolution of the level set function  $\phi$  is given by a Hamilton-Jacobi-type equation

$$\frac{d}{dt} \phi + v_n |\nabla \phi| = 0.$$

By this the level set function changes along its gradient, which is precisely the normal to its level sets. The normal velocity  $v_n$  needs to be given and the level set equation advanced via a suitable numerical scheme. A famous first application to shape optimization is [367] by Sethian and Wiegmann. The aim is to remove as much material as possible from a given structure while meeting a constraint on the compliance. The von Mises stresses are computed on the boundary and used as an ad hoc criteria for the evolution. For reasons of efficiency, a narrow band technique is used in [7]. It allows to compute the required quantities and the evolution of the level set function only within a small surrounding of the zero level set.

A more systematic approach is to employ the shape derivative and define the normal velocity as the solution of the variational problem  $d_{\mathcal{O}} \mathbf{J}[\mathcal{O}] \vartheta = g(v_n, \vartheta)$  for a given metric  $g$ . This is done by Osher and Santosa [316] to solve a constrained eigenvalue optimization problem within a two dimensional domain with two phases. Burger [99] sets out an abstract framework based on gradient flows and studies different choices for the metric  $g$ .

Shape optimization as considered in this work is approached with the level set method by Allaire et al. [27, 28]. They study linearized and nonlinear elasticity problems in two and three space dimensions under the compliance or tracking objective functional. An adjoint problem has to be solved to compute the shape derivative, which is then used to define the normal velocity via a smoothing  $H^{-1}$ -metric. Furthermore, design dependent loads, different schemes for the solution of the Hamilton-Jacobi equation, and time step size control are investigated. The same problem was independently studied by Wang et al. [414]. They prove that their choice of the normal velocity actually leads to a decrease in the objective functional.

In these works the boundary is not explicitly represented. In order to solve the state equation, interpolation is used or the complement is assumed to contain a material with negligible rigidity, thereby reducing the problem to a two-phase design on the whole working domain. In contrast, Conti et al. [136, 139] combine the level set approach with composite finite elements [206] to resolve the interfaces. Abe et al. [6] do so by explicitly constructing the interface and employing the boundary element method.

The level set method remains of practical importance until today. In [145] a framework oriented towards application in architecture is presented with emphasis on constraints related to the mechanical performance or aesthetic requirements. Its drawback is the inability to

generate additional holes in a purposive way. As such the results of optimization significantly depend on the initial topology, cf. [28, Figure 11].

**Topology optimization.** Owing to the structures observed in optimal shapes, the importance of altering the topology rather than the shape was recognized early. In a naive approach one could discretize the domain and decide for each cell whether to place material or void. This leads to a large scale integer programming problem, which however is highly mesh sensitive and was found to suffer from poor convergence. As workarounds, reformulations are proposed, see e. g. [387].

Alternatively void regions could be identified based on suitable criteria derived from the state. This approach, also called *hard-kill*, is used in *evolutionary structural optimization (ESO)*, e. g. by Xie and Steven [420], based on heuristic criteria aiming at removing regions of understressed material. Enhancements by adaptively modifying the mesh, termed *reverse adaptivity*, are presented by Reynolds et al. [344]. Also genetic algorithm can be employed, see e. g. Jensen [237].

A rigorous concept is the *topological derivative*, introduced by Eschenauer et al. [169] and Schumacher [364] as the *bubble method*. It is defined as

$$d_{\text{topo}} \mathbf{J}[\mathcal{O}](x) := \lim_{\delta \searrow 0} \text{Vol}^{-1}(\overline{B_\delta(x)}) \left( \mathbf{J}[\mathcal{O} \setminus \overline{B_\delta(x)}] - \mathbf{J}[\mathcal{O}] \right)$$

and measures the sensitivity of a cost functional w. r. t. the insertion of a tiny hole  $B_\delta$ . Generalizations to a wider class of shape functionals [376], three space dimensions [377], and arbitrarily shaped holes [181] were obtained later. For a comprehensive overview see also the textbook [309].

The concept met with significant reception, especially in combination with establish numerical methods. Feijó et al. [171] work out a connection between the topological and the shape derivative, such that established results from shape sensitivity analysis can be reused. Sokółowski and Żochowski [374] formulate optimality conditions based on applying the shape derivative on the boundary and topological derivative in the interior. Burger et al. [100] incorporate the topological derivative in an additional source term in the evolution equation for the level set function based on heuristic considerations. Thereby the inability of the level set method to introduce new holes is compensated. The approach is generalized in [220] to a wide range of objective functionals. Also Allaire et al. [26] combine both approaches, generating new holes after a specified number of gradient descent steps based on the shape derivative. Amstutz and Andrä [34] alter the evolution equation as well, this time by using a projection of the topological gradient onto the orthogonal complement of the level set function, i. e.  $\frac{d}{dt} \phi = P_{\phi^\tau}(d_{\text{topo}} \mathbf{J}[\mathcal{O}])$ . This implies that, upon convergence, the level set function equals the normalized topological gradient and therefore the obtained shapes fulfill topological optimality conditions. In [33] the approach is pursued to generate microstructures leading to optimal homogenized coefficients. The same problem is addressed by Barbarosie and Toader [60], here by combining the boundary variation technique with the topological derivative.

**Phase field method.** Phase fields are another way to implicitly represent a shape. Unlike level set functions, they are not governed by an evolution equation, but defined as minimizers of a scalar Ginzburg-Landau-type energy. Their origin is the study of phase separation in liquids by Cahn and Hilliard [105]. For a phase field function, again denoted by  $\phi: \mathbb{R}^d \rightarrow \mathbb{R}$ ,

the energy is given by

$$\frac{1}{2} \int_D \epsilon |\nabla \phi|^2 + \frac{1}{\epsilon} \Psi(\phi),$$

where  $\Psi$  is a potential function that forces  $\phi$  to attain discrete values. Typically  $\{-1, 1\}$  are considered, representing the different phases, and the smooth double-well potential,  $\Psi[\phi] = (1 - \phi^2)^2$ , or the non-smooth obstacle potential,  $\Psi[\phi] = (1 - \phi^2)$  for  $|\phi| \leq 1$  and  $\Psi = \infty$  else. The first term  $|\nabla \phi|^2$  favors constant values of  $\phi$ , but additionally penalizes steep transitions where they occur. Balancing the two conflicting terms is enabled by the parameter  $\epsilon > 0$ , leading to diffuse interfaces. In fact, a classical result by Modica and Mortola [290] asserts that the gradient term, with some scaling,  $\Gamma$ -converges to the perimeter for  $\epsilon \searrow 0$ . As such, phase field approaches directly incorporate a regularization.

Bourdin and Chambolle [89] consider compliance minimization for linearized elasticity under design-dependent loads. They introduce three phases, namely void, solid, and liquid, a corresponding triple-well potential, and allow for transitions in between. The existence of minimizers is proven for the sharp interface model, i. e. when  $\epsilon \searrow 0$ . Numerical experiments are conducted using a decreasing interface parameter  $\epsilon$  and a semi-implicit optimization scheme. Wang and Zhou [415] adopt the phase field model for the classical shape optimization problem aiming at identifying solid and void regions. They consider a Tikhonov regularization by an initially arbitrary function  $g(|\nabla \phi|)$  and point out the relation to image segmentation problems and the Cahn-Hilliard theory. For the numerical examples, different regularization terms, including edge-preserving ones, are tested. Burger and Stainko [101] consider the minimization of volume under stress constraints. They pick up the reformulation of Stolpe and Svanberg [387] and additionally relax the 0-1-constraints by introducing a phase field and adding a Cahn-Hilliard term to the objective. For the resulting continuous problem the existence of a minimizer is proven and for the discretized problem the linear inequality constraint qualification condition is shown. Blank et al. [85] solve the phase field optimization problem by a gradient descent method using different metrics. In case of an  $H^{-1}$ -flow, a volume-conserving, fourth-order Cahn-Hilliard-type equation is obtained. In case of an  $L^2$ -flow, a second order Allen-Cahn-type equation is obtained instead. The latter leads to a variational inequality and an additional volume constraint but is cheaper to solve using a primal-dual active set method. Moreover by using an obstacle potential, the phase field only needs to be computed in the interface region. The numerical experiments show similar final results, but the observed evolutions differ. In [84] also the sharp interface limit is studied. Penzler et al. [325], in contrast to linearized elasticity, assume a nonlinear elastic state equation. In consequence, different formulations of the compliance objective no longer coincide, optimal shapes under symmetric loading conditions are no longer symmetric, and the elastic deformation, e. g. when buckling occurs, is no longer unique. This may result in non-existence of optimal shapes when the deformation yielding the worst compliance is chosen. On the contrary, existence is proven both for the diffuse and the sharp interface model when the least compliant deformation is used. The numerical algorithm is based on the phase field model and a trust region and quasi-Newton scheme. Figure 13 in their work impressively illustrates the effect of varying the weighting parameters for surface and volume penalizations.

**Further regularizing approaches.** Belytschko et al. [68] also use an implicit representation by applying the Heaviside function to a level set function. The Heaviside function is then regularized to obtain a smooth functional, which amounts to a regularization of the shape

as well, similar to the phase field setting. A heuristic update scheme is used to optimize the nodal values of the implicit function. Guo et al. [203] follow the same approach. They observe that the regularization of the Heaviside function induces a boundary layer where holes can be created. Moreover they argue that the topological derivative is governed by the same terms as in their sensitivities of the implicit function. Eventually the regularization parameter is chosen large such that topological changes can occur globally. Wei and Wang [416] propose an alternative to the level set method by constraining its values to piecewise constant integers for connected components. Sensitivities are evaluated based on variation of an augmented Lagrangian functional including a total variation term. As such the method resembles the phase field approach in that the function is forced to attain discrete values and jumps and the perimeter are controlled. The level set function is advanced using an implicit scheme. Thereby reinitialization and the typical restriction by the CFL condition are circumvented. Yamada et al. [421] also use a level set function, but constrain its values to the interval  $[0, 1]$ . Furthermore the objective is supplemented with a fictitious interface energy  $|\nabla\phi|$ , similar to the phase field setting. The evolution is steered based on the gradient of the Lagrangian, which is observed to be related to the topological derivative. Consistent numerical results are obtained for different initializations and mesh resolutions, and an additional scaling factor of the fictitious interface energy allows to control the geometric complexity of optimized shapes.

**Homogenization.** The other way to overcome the ill-posedness of shape optimization is relaxation. To this end, homogenization was early adopted for numerical computations, see e. g. [45, 46, 47, 92]. A first application to optimal design is by Goodman et al. [194]. They consider a composite of two elastic materials for the cross-section of a rod maximizing its torsional rigidity and solve a discretized relaxed problem. Rozvany et al. [354] similarly investigate least-weight perforated plates with prescribed compliance, using first and second order lamination, which they call *ribs*. Żochowski [429] assumes the domain to contain perforations on a regular lattice. The behavior of the full domain is then approximated using local *substitute material coefficients*, which are in fact the homogenized coefficients. Sensitivities of cost functionals w. r. t. parameters describing the local perforations and entering via the homogenized coefficients are computed. The presented numerical examples employ circles and ellipsoidal holes, just as in the present work.

In view of the general topology optimization problem, a breakthrough is however mostly attributed to Bendsøe and Kikuchi [78]. They also consider periodically distributed, infinitesimally small holes, this time of rectangular shape, also employed in this work. Via homogenization, a relation between the local fraction of used material and the macroscopic material coefficients is established. Thereby the topology optimization problem is transformed to a sizing problem, where the *density* is the local design variable taking values in the interval  $[0, 1]$ . In practice, the homogenized coefficients are computed in advance for several samples of the parameter space and interpolated. The algorithm is based on an iterative scheme for solving the optimality criteria. In the experiments, the authors conclude that the resulting density is most crucial and therefore resort to square holes, which require less parameters. On the other hand, optimized rotations of the local cells are identified as influential as well. The approach with slight modification is pursued by Suzuki and Kikuchi [389], showing a lot of numerical examples and verifications. In [73, 77] the meanwhile established results on optimal sequential lamination composites are discussed. By taking these microstructures into account, a full relaxation is achieved. The simple periodic constructions are only sometimes

optimal and therefore amount to a partial relaxation. However the focus is on obtained local densities only and it is concluded that it be more economical to use simple microstructures. The situation changes around [80]. In [240] Jog et al. present the relaxation process for the full shape optimization problem. Using a saddle point theorem by Lipton [262], a result on optimal alignment of orthotropic materials by [323], and explicit formulae for the optimal parameters of rank-2 sequential laminates, stepwise analytical optimizations are performed for the state and the design variables, thus termed *self-adaptive materials*. The elasticity problem is treated both based on displacements and stresses, and the former is pursued numerically. It results in an inf-sup mixed variational formulation for the density and displacement fields and is solved in alternation using a mixed finite element method, very close to the one employed in this work, cf. Section 5.5. The stress based formulation is found to coincide with that of Allaire and Kohn [15]. It had been developed in parallel, based on earlier results concerning optimal bounds [29, 30], and ultimately results in a single optimization over admissible stress fields only. The remaining functional however is non-differentiable. For the purpose of demonstration a regularization is used and piecewise cubic, globally smooth Clough-Tocher finite elements.

Cherkaev and Palais [119] show the first numerical results in three space dimensions. They follow the same program, but build upon the independently discovered optimality results of Gibiansky and Cherkaev [190]. Díaz and Lipton [153] consider the three dimensional problem using two phases based on results in [263, 262, 264]. In [12] Allaire et al. give an exhaustive treatise. The relaxation result is proven for arbitrary spatial dimensions based on quasiconvexification and explicit formulae for the three dimensional setting are given, based on [17]. Furthermore technical aspects of the algorithmic realization are discussed.

Following up on this groundbreaking results, several further applications were investigated. For multiple loadings the method of Bendsøe and Kikuchi [78] was generalized in [151]. Sequential lamination was considered by Allaire et al. [21]. The relaxation results can mostly be carried over, however there are no explicit formulae for the optimal parameters anymore, see also Remark 4.22. They are therefore determined numerically in the course of the alternating algorithm. For eigenvalue optimization, Díaz and Kikuchi [152] present numerical examples based on their established method. Allaire et al. [20] derive another relaxation result, based on a variational characterization of the eigenvalues and a saddle-point theorem. However, when a sum of eigenvalues is considered, there are again no explicit formulae for optimal sequential laminates. For other objective functionals there are no corresponding rigorous results. Sequential laminates can still be employed, as e.g. done in [19], but then merely amount to a partial relaxation.

Another extension is the inclusion of strains or stresses in the objective or constraints. This is highly relevant from a practical point of view as structures are supposed to fail first where the local stresses are high. From the mathematical point of view it complicates matters because local microscopic concentrations are not captured by the homogenized macroscopic quantities. This is reflected by the weak and not pointwise convergence of homogenization. Duysinx and Bendsøe [159] to this end explicitly calculate the von Mises criterion in terms of macroscopic stresses and parameters for a rank-2 laminate. For their algorithmic realization they furthermore implement a relaxation of the stress constraint to circumvent discontinuities. Lipton [265] considers maximization of the torsional rigidity with a constraint on the mean square stress. The microscopic quantity is defined via a *corrector matrix*, leading to a relaxed formulation involving a *covariance tensor*. Allaire et al. [14] approach minimum stress design using the objective  $\int_{\mathcal{O}} |\sigma|^2 dx$ , possibly localized to subdomains  $\omega \subset \mathcal{O}$ . To pass to a limit with

homogenized quantities, *corrector tensors*  $P^\delta$  are required. In particular,  $\sigma^\delta - P^\delta \sigma$  converges strongly and the term is used in approximating the objective, corresponding to the approach by Lipton [265]. For sequential laminates the correctors can be computed explicitly.

In the discussed numerical realizations often checkerboard instabilities were observed, cf. [77, Figure 20], [12, Figure 4]. Jog et al. [240] suggest it be a numerical artifact similar to patterns observed in the pressure field for Stokes flow. As a remedy they consider a checkerboard-free function space on patches of four neighboring elements, according to Johnson and Pitkäranta [242]. Jouve and Bonnetier [243] look into this phenomenon by an explicit investigation of the alternating sequential lamination algorithm, applied to a small test problem with known optimal solution. They linearize the update procedure around the optimal state and show by an eigenvalue analysis that checkerboard errors are amplified when the degenerate homogenized elasticity tensor is regularized and the principle stresses are of equal magnitude. This could explain why instabilities were not observed in the three dimensional setting where rank-3 laminates in general do not yield degenerate tensors.

**Recovery of classical designs.** Intermediate densities produced by algorithms based on homogenization are at the core of the relaxation process and enable unrestricted topology optimization in the first place. Still they are difficult to interpret in real life design applications and a lot of effort has therefore been put into regaining classical designs, made from material and voids, which could actually be manufactured.

As a general concept results can provide initial guesses for a subsequent optimization, e. g. based on the boundary variation technique as in [315]. Allaire et al. [12] propose a penalization of intermediate densities as a post processing step, i. e. instead of updating to the optimal local densities  $\theta^{\text{opt}}$  in the alternating algorithm, penalized values  $\theta^{\text{pen}} := \frac{1}{2}(1 - \cos(\pi \theta^{\text{opt}}))$  are used. Bourdin and Kohn [91] take a different approach by resorting to single-scale laminates. Instead of the recursive layering on successive length scales, a superposition on a single scale is proposed. They prove that, to leading order, the construction performs equally well and has a simple explicit formula, which scales linearly with weight. Thus they argue that for low overall volume, or *high porosity*, the influence of the intersections on the same scale is negligible. An entirely novel approach is introduced by Pantz and Trabelsi [319], based on the idea of projecting the underlying microscopic information onto the macroscale. In a first step the optimal sequential laminate is substituted pointwise by a locally periodic microstructure made from cells  $\mathcal{Y}(x)$  containing rectangular holes. It is assumed that the field of orientations is regular. A smooth function  $\phi: D \rightarrow \mathbb{R}^2$  is then introduced, yielding a perforated domain  $\mathcal{O}^\delta = \{x \in D: \delta^{-1}x \in \phi^{-1}(\mathcal{Y}(x))\}$ , where the parameter  $\delta$  allows to control the fineness of reconstructed structures. The mapping  $\phi$  is optimized to locally reproduce the underlying orientation. This is in fact the most delicate step as it requires an orientation of the eigenvector field and fails when more than one singularity occurs.

Spurred by additive manufacturing techniques, the approach has been adopted and extended. Groen and Sigmund [201] directly optimize microstructures given by rectangular holes. They use interpolation of precomputed samples, as in [78], a coarse scale for computational speed, and project the result onto a fine mesh. The spatial variation of the sizing parameters is represented using cosine waves, and reconstruction uses a Heaviside function and thresholding. For the local orientation, the mapping  $\phi$  is picked up, however based on a different optimization approach. Among other things, the local alignment is enforced only in regions with intermediate density via a weighting term, a consistent orientation is achieved using the *connected component labeling*



approach from image processing, a scaling is used to obtain a desired averaged projected cell size, and some heuristics prevent overly small structures. Allaire et al. [25] consider the same microstructure, but pay special attention to the local alignment. The mapping  $\phi$  is required to be conformal, which is equivalent to the orientation field being harmonic. This is enforced via an additional constraint and regularization during the alternating algorithm. It is moreover required to preserve the proportions of the rectangular holes by optimizing a dilation factor. The final mapping can be constructed provided the rotation field is coherent. In contrast to [201] this is handled via an abstract manifold, which basically amounts to two instances of the rotation field with flipped orientations and a corresponding discontinuous Galerkin discretization. Finally, in a post processing step, thresholding is applied and disconnected components are removed. In [187] the three dimensional case is considered. Here the microstructure is made of cubes perforated with rectangular shaped holes from side to side. Instead of local angles, symmetric matrices corresponding to the local principle stresses are regularized.

**Material distribution schemes.** In [73] Bendsøe sketches a “naive” approach to topology optimization by defining the effective material properties via a blending function, i. e.

$$C^* = \theta^p C, \quad \theta \in [0, 1], \quad p \in \mathbb{N}.$$

This has a physical interpretation when considering variable thickness sheet problems, where  $\theta$  would be the thickness, see e. g. [351]. In the full elasticity setting, however, there is no such justification. Nonetheless the approach later became enormously popular under the name *SIMP*, mostly understood as *simple isotropic material with penalization*. Penalization here refers to inhibiting intermediate values of  $\theta$  and is achieved by choosing the exponent  $p$  significantly larger than 1. This leads to sublinear increase of material stiffness for increasing  $\theta$ , whereas the material costs scale linearly, thus rendering intermediate values uneconomical. Similar relations were observed for the effective coefficients obtained from periodic microstructures or sequential lamination, cf. [78, Figure 6] or [77, Figures 4, 5], however based on solid grounds of homogenization.

Applications of the method can be seen in [77, 422, 79]. Bendsøe et al. [77] also compare to results based on homogenization. In [75] some physical justification is provided by showing that tensors generated by the SIMP model, under some conditions on the exponent  $p$ , satisfy the Hashin-Shtrikman bounds.

Like the homogenization approach, the method is prone to checkerboard instabilities. In [154, 241] it is asserted that these patterns result from an unphysical overestimation of the strain energy when using bilinear finite elements. In consequence a lot of effort was put into finding remedies. Haber et al. [205] introduce perimeter penalization based on an approximation of the total variation of the artificial density. The approach was later improved by Petersson [326]. Petersson and Sigmund [327] impose slope constraints, which limit the rate of change for the artificial density on neighboring cells. Local filtering techniques are surveyed in [370]. Bourdin [90] and Borrvall and Petersson [87] independently propose a regularization of the density by means of a convolution operator. It allows to prove existence of solutions and convergence of the finite element approximation. Matsui and Terada [279] propose to keep a continuous density field and instead employ appropriate finite element functions.

**Free material optimization.** Instead of considering parameters yielding effective material properties, one can directly optimize the coefficients of the macroscopic elasticity tensor. The

idea goes back to Ringertz [346], where the compliance is minimized in two dimensions. A constraint on the available material is imposed via  $\int_D j(C) dx \leq \theta \int_D \|\bar{C}\|_F dx$ , where the cost function  $j$  is chosen as the tensor trace. Moreover  $C \preceq \bar{C}$  needs to hold pointwise, i. e.  $\bar{C} - C$  must be positive semidefinite, with  $\bar{C}$  corresponding to an isotropic solid. The constraints are incorporated using a logarithmic barrier function and a convex optimization problem is obtained. Bendsøe et al. [74] investigate the same approach. Via analytical optimization they reduce the problem to a single variable.

More recent works are e. g. [386, 385] by Stingl et al. with a focus on optimization techniques. The sequential convex programming approach is generalized to matrix valued variables by constructing a sequence of subproblems with block separable convex first-order approximations. Local stress and displacement constraints are additionally considered by Haslinger et al. [216]. This requires a different proof of the existence of optimal solutions based on H-convergence.

**Microstructure identification problem.** The crux of free material optimization is that the generated materials might not have a physical equivalent. Thus, in a post processing step, a best approximating realization is searched, referred to as *inverse homogenization*. To this end, Milton and Cherkaev [287] show that in fact all possible tensors are attainable as effective elasticity tensors of a two-phase composite when sufficiently weak and stiff materials are assumed. A numerical approach is used by Sigmund [371], where trusses or continuous plates with varying thickness are considered in base cells. They are optimized for minimum weight while matching their homogenized tensor with the target. Haslinger and Dvořák [219] investigate the problem in the conductivity setting. They consider star-shaped inclusions parametrized in polar coordinates and prove the existence of optimal solutions. For the computation of homogenized properties, upper and lower bounds given by the potential and the complementary energy are used to ensure reliability. Barbarosie [56] considers conductivity as well as linearized elasticity. The numerical approach uses a periodic finite element mesh with arbitrary generators. A fixed number of holes is optimized using the boundary variation technique and remeshing. The approach was pursued in [59, 60] and extended by incorporating the topological derivative to allow for the nucleation of new holes.

**Multiscale optimization.** Because of the significance of multiple scales in shape optimization, it is natural to handle all of them simultaneously in a numerical scheme. Dvořák et al. [160] consider the conductivity problem in a two-scale context. They thoroughly work out the relaxation process based on periodic homogenization, H-convergence, and correctors in case of gradients in the cost functional, and prove the existence of solutions. For numerical experiments the conductivity field is approximated by piecewise constant homogenized coefficients stemming from periodic problems with star-shaped inclusions as in [219]. Likewise sensitivities are obtained to optimize tracking functionals for the state and its gradient. The full relaxation using optimal rank-2 laminates is described by Haslinger et al. [215] and applied to a torsional rigidity and a tracking problem. The same approach is followed by Rodrigues et al. [349] in the elasticity setting under the name *hierarchical optimization*. They obtain homogenized coefficients from local microscopic cell problems employing the SIMP model and investigate the compliance problem under multiple loads. An extension to three dimensions is developed by Coelho et al. [135]. Also Barbarosie and Toader extend their work to a two-scale setting [61]. It is in fact very close to the approach developed in this work, see the discussion in Section 5.3.3. Within this framework Tölkes [397] uses a phase field approach for the microscopic cell

problems. Applications also include stochastic optimization under dominance constraints. Aiming at the reduction of computational costs, especially for three dimensional problems, Valentin et al. [399] revisit the idea of Bendsøe and Kikuchi [78] to compute effective elasticity tensors for samples of the design parameter space beforehand in an *offline* phase and use interpolation during optimization in the *online* phase. To overcome the curse of dimensionality when several parameters are used in the construction of the microstructure, an adaptive sparse grid approach is employed. Hierarchical B-splines are used for interpolation, which are smooth and allow to use exact continuous gradients for optimization. For numerical experiments simple microstructures are considered, among others rotating orthogonal rods as in [78] and the present work.

Schury et al. [365] combine free material optimization, to obtain optimal effective elasticity coefficients on the macroscale, and subsequent inverse homogenization via the SIMP method, to obtain microscopic realizations. Motivated by rapid prototyping techniques, they incorporate manufacturability constraints, thereby achieving *graded materials*. On the one hand, only tensors should be considered that can actually be attained by a periodic composite. This is ensured by deriving reference values from maximally stiff isotropic materials with prescribed relative densities and allowing for some deviation. On the other hand, the macroscopic variation of the microstructure is limited by slope constraints, i. e.  $\|\partial_x C^*\|_F \leq c$ . Finally additional transition cells are introduced and optimized to guarantee continuity across neighboring cells.

The advent of low-cost high-resolution additive manufacturing techniques has lately fostered the adoption of the two-scale framework to produce optimized shapes that can directly be turned into real life workpieces. Milton et al. [286] showcase theoretical constructions to show which effective elasticity tensors are actually realizable. In practice one would however resort to subsets generated from more realistic setups.

Zhu et al. [426] consider isotropic, cubic, orthotropic, or virtual materials given by the SIMP model, as candidates and realizable by microstructures made from  $16^d$  micro cells carrying materials or void. In a preprocessing phase, attainable tensors are explored by a stochastic Monte Carlo method and subsequent optimization to obtain extremal structures. The whole set is encoded via a level set function, which is used in the global optimization to formulate a realizability constraint. Finally microstructures matching optimized material properties and being topologically similar to their neighbors are placed on the macroscopic domain to generate high-resolution printable structures. Examples include tracking for mechanical devices and compliance optimization. Conti et al. [141] use phase fields to find periodic microstructures realizing given bulk and shear moduli. They enforce material bridges at preselected parts of the fundamental cell's boundary. With each candidate a cost is associated, taking into account the used amount of material and its perimeter. That way samples are generated and interpolated by cubic B-splines in a preprocessing step. A macroscopic problem can then be considered, optimizing a compliance or tracking functional and the interpolated costs.

## 2.3. Multiscale methods

The multiscale nature of shape optimization requires numerical methods to appropriately handle the involved scales. While homogenization eventually eliminates the microscopic components in favor of averaged quantities, a fully resolving discretization, on the other hand, is prohibitive due to the computational cost, even if a finite separation of the length scales is assumed. Consequently several techniques have been developed to adequately capture the

microscopic contributions while remaining efficient.

**Multiscale finite element method (MsFEM).** The multiscale finite element method was introduced by Hou et al. [232, 233], see also the textbook [165]. It relies on precomputed basis functions, specially crafted for resolving local microscopic effects, a concept that can already be found in [44]. For the scalar elliptic model problem,  $\nabla a(\frac{x}{\delta})\nabla u^\delta = f$ , nodal finite element basis functions  $\psi_i$  are numerically determined as solutions of  $\nabla a(\frac{x}{\delta})\psi_i = 0$  on each element  $E \in \mathcal{M}_h$ . Here the discretization size  $h$  is assumed larger than the microscale  $\delta$ . Convergence analysis yields the sharp error estimate

$$\|u^\delta - u_h\|_{1,2,\mathcal{O}} \leq c_1 h \|f\|_{0,2,\mathcal{O}} + c_2 \left(\frac{\delta}{h}\right)^{\frac{1}{2}}$$

and a corresponding  $L^2$  estimate using the Aubin-Nitsche trick. This is in contrast to standard estimates, which would yield  $\frac{h}{\delta}$  terms and dictate a fully resolving scheme, i.e.  $h < \delta$ . In particular, convergence of the method is assured also for  $\delta \searrow 0$ . Problematic is the case  $h \sim \delta$ , termed *resonance*, which could e.g. happen for continuously varying scales. It is found to be caused by the boundary layer and can be remedied by imposing specialized boundary conditions or using a supersampling technique with enlarged discretization  $h' > h + \delta$ . In [166] multiple separated scales are considered. Allaire and Brizzi [22] develop a generalized version, where standard conformal finite element base functions are concatenated with solutions of cell problems. It allows to use higher order elements and obtain corresponding error estimates in the classical framework, but reduces to the original approach for linear elements. Buck et al. [96] consider the method for linearized elasticity.

**Generalized finite element spaces.** Matache et al. [274, 275] construct and analyze generalized finite element spaces based on the Fourier-Bochner representation

$$u^\delta(x) = (2\pi)^{-\frac{d}{2}} \int_{\mathbb{R}^d} \hat{f}(t) e^{ixt} \psi\left(\frac{x}{\delta}, \delta, t\right) dt$$

from [291, 292], where the kernel  $\psi$  solves a microscopic cell problem. From an approximating finite Fourier series a well-conditioned basis is extracted via singular value decomposition. Under the assumption of a locally periodic microstructure and further requirements for the input data, an exponential convergence rate is proven. Both the error and the computational work thereby do not depend on the microscale  $\delta$ . In [277] the concept is extended to nonhomogeneous periodic media using Bloch waves. A different approach is taken in [278, 276]. Both scales are handled simultaneously by considering a Bochner space, like  $H^1(D; H^1_{\text{per}}(\mathcal{Y}; \mathbb{R}^d))$  in the notation of the present work. This is closely related to the concept of *periodic unfolding* by Cioranescu et al. [131]. Matache and Schwab [278] establish two-scale regularity results. Discretization is then achieved using a two-scale tensor product space and again convergence rates independent of  $\delta$  are shown. Due to the interacting scales, an efficient implementation is more complicated. To this end, [278] suggests parallel computation based on a moment formulation, whereas [276] introduces a sparse grid approximation. Several scales are addressed in [230].

**Heterogeneous multiscale method (HMM).** The heterogeneous multiscale method, introduced by E et al. [163, 161], initially depicts a very general paradigm for coupling multiple

scales. In particular it takes into account possibly different schemes on the individual scales and suitable *compression* and *reconstruction* operators to pass data among one another. In the setting of variational homogenization problems an in-depth analysis is presented in [162, 164]. A critical comparison w. r. t. accuracy and performance of the heterogeneous multiscale method and the multiscale finite element method is done in [289]. Additional major contributions are made by Abdulle [2], considering the fully discrete setting. In contrast to [164], the computation of the effective tensor is not assumed exact. Hence in addition to the macroscopic error, the approximation error in the numerical solution of cell problems and its influence on the macroscale, as well as a modeling error is analyzed. The latter accounts for the coupling procedure and depends on assumptions such as periodicity or sampling domain size. A key finding is that the resolution of the macroscopic and microscopic computational meshes need to be linked. Based on these results, linearized elasticity is considered in [3] and numerical experiments are presented in [236]. The approach taken in this work is completely in line with the heterogeneous multiscale method and thus the error analysis directly applies, see Section 5.3.2.

**Further approaches.** Another class are *variational multiscale methods* introduced by Hughes [234]. They also build upon an additive decomposition of the solution  $u^\delta = u^* + \tilde{u}$ . A variational formulation is considered and the *subgrid scale* solution  $\tilde{u}$  is expressed analytically via a Green's function and in dependence of the *coarse scale* residual  $\mathcal{L}u^* - f$ . Thereby an equation depending on  $u^*$  only is obtained, which can be solved numerically. In [234, 235] the connections to stabilized methods and bubble function used for enriching finite element spaces are pointed out.

More generally, *multigrid* methods can be employed to efficiently resolve the different scales, see e. g. Fish and Belsky [174, 173] and Neuss et al. [304]. Also *wavelets* have been considered, see e. g. Dorobantu and Engquist [157].

## 2.4. Error estimation

Error estimates and their incorporation into adaptive numerical schemes provide the theoretical and practical foundations to break computational complexity by focussing on the most relevant parts of the employed model for the desired output. An often-quoted early contribution is the *hypercircle* method of Prager and Synge [332], which describes errors in function spaces based on geometrical intuition. Extensive modern introductions can be found in the textbooks [402, 8, 342].

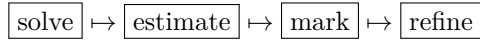
**Basic concepts.** Most classical error estimates are *residual based*. In the canonical setting of a scalar second order partial differential equation, the finite element discretization error  $e_u = u - u_h$  is estimated as

$$\|e_u\|_{1,2,\mathcal{O}} \leq c \left( \sum_E h_E^2 \eta_E^2 + h_{\partial E} \eta_{\partial E}^2 \right)^{\frac{1}{2}},$$

$$\eta_E := \|\operatorname{div}(a \nabla u_h) + f\|_{0,2,E},$$

$$\eta_{\partial E} := \|j(\nabla u_h \cdot n)\|_{0,2,\partial E},$$

where  $\eta_E$  measures the residual within each element and  $\eta_{\partial E}$  the jump discontinuity across element edges. This idea goes back to Babuška and Rheinboldt [41, 40]. Bank and Weiser [55] propose to solve various local Neumann problems on each element, with  $\eta_E$  and  $\eta_{\partial E}$  acting as right hand sides, and use the solutions as error estimators. They prove that they are bounded by a multiple of the norm of the true error. Zienkiewicz and Zhu [428] develop *recovery methods* to produce improved approximations of derivatives of the state. When comparing these to the directly differentiated state, the difference can be used as an error indicator. In these early works the computed quantities are already utilized for selecting cells of the computational mesh that should be refined in order to improve the approximation. The iterative procedure



remains standard to the present day. Although less popular, there is a rich theory for error estimation and adaptivity in the framework of the boundary element method as well, see e. g. the early reference [339] and the survey article [172].

Further research considers the convergence and computational efficiency of adaptive methods, the extension to other sources of errors and the quality of error bounds. Concerning convergence analysis, a major contribution is the marking strategy by Dörfler [156], which amounts to finding a subset of all cells, on which the accumulated estimates make up for a fixed fraction of the total estimated error. Initial restrictions on properties of the mesh have subsequently been lifted, cf. [295, 106]. The case of hanging nodes, as occurring in the present work, is considered as well, see [425]. Concerning computational efficiency, see e. g. the recent contribution [328] on the complexity of optimal marking strategies. Besides discretization errors, modeling errors are e. g. considered by Stein and Ohnibus [381]. *Goal-oriented* error estimates in derived quantities are discussed below. Concerning the quality of error bounds, a natural requirement is that an error estimate  $\eta$  provides an upper bound for the error, i. e.  $c\|e\| \leq \eta$  with  $c$  being independent of the exact solution and the computational mesh. This is mostly referred to as being *reliable*. A further desirable property is a lower bound, i. e.  $\eta \leq C\|e\|$ , which assures that the true error is not overestimated. This is sometimes referred to as being *efficient*. When the constants are exactly computable, the bounds are termed *guaranteed*. At best, the ratio of the estimator and the error, called *effectivity index*, should be close to unity, at least asymptotically for decreasing grid size. Furthermore *robustness* is considered, i. e. insensitivity to regularity of the solution or the mesh and variations of parameters. An early example for fully explicit bounds is [150] by Destuynder and Métivet for the Poisson problem. The starting point is the identity by Prager and Synge

$$\|\nabla u - \nabla \vartheta\|^2 + \|\nabla u - p\|^2 = \|\nabla \vartheta - p\|^2 \quad \forall \vartheta \in H_{\Gamma_D}^1(\mathcal{O}; \mathbb{R}), p \in H(\text{div}, \mathcal{O}),$$

where  $H(\text{div}, \mathcal{O}) := \{p \in L^2(\mathcal{O}; \mathbb{R}^2) : \text{div } p + f = 0\}$  is the set of vector fields fulfilling the dual equilibrium equation. From this

$$\|\nabla u - \nabla u_h\| \leq \inf_{p \in H(\text{div}, \mathcal{O})} \|p - \nabla u_h\|$$

follows and hence, for a good estimate,  $p$  has to be as close to  $\nabla u_h$  as possible. This is referred to as *equilibrated flux reconstruction* and has attracted much attention, especially in view of efficient local approaches. A lot of further results are contributed by Repin, collectively called *functional a posteriori estimates* to stress that they are purely based on functional analytical properties and do not involve any approximation or numerical method, see e. g. [341, 340]. Fully

robust and guaranteed estimates are derived by Vohralík [407], using Raviart-Thomas-Nédélec elements for the post processed flux fields and a local conservation property of the finite element method on dual meshes.

**Goal-oriented error estimates.** From a practical point of view, a numerical simulation is often employed to obtain the solution or a certain derived quantity on parts of the computational domain only. In such a situation it not useful to estimate the global discretization error as it might be largely irrelevant for the actual goal. This motivates *goal-oriented* error estimates, which measure the error in a *quantity of interest*  $\mathbf{J}[u]$ . An early example is [39] by Babuška and Miller.

A major contribution is the *dual weighted residual* (DWR) method by Becker and Rannacher, see the early reference [66], applications to optimal control problems [65, 67], and the textbook [50]. The approach is based on a Lagrangian, coupling the quantity of interest and the state equation. Residual type estimates then get weighted by the solution of an adjoint problem, reflecting local sensitivities w. r. t. the considered functional. Since its introduction the approach has found wide application. We pick it up in the present work as well and apply it to our two-scale shape optimization model, see Chapter 8.

Alternative techniques are proposed by Prudhomme and Oden [334, 310] and Paraschivoiu et al. [320], focussing on output functionals depending linearly on the state, such as averages of the solution on subdomains or mollified pointwise stresses. Here the adjoint problem is considered as well. Prudhomme and Oden refer to its solution  $p$  as *influence function*. With the errors in the primal and adjoint solution,  $e_u$  and  $e_p$ , it follows from Galerkin-orthogonality and the polarization identity that

$$\mathbf{J}[e_u] = a(e_u, e_p) = \frac{1}{4} \|\nabla(se_u + s^{-1}e_p)\|_a^2 - \frac{1}{4} \|\nabla(se_u - s^{-1}e_p)\|_a^2,$$

where  $\|\vartheta\|_a^2 = a(\vartheta, \vartheta)$  denotes the energy norm. The introduction of the *balancing factor*  $s$  extends ideas of [43]. It can be obtained by explicit optimization, but is approximated in practice. From this point on, classical estimates are used to derive exact lower and upper bounds. They can be split into contributions on cells of the computational mesh, though the balancing factor is a global quantity.

Nochetto et al. [307] revisit the dual weighted residual approach. As the weighting terms involve approximations of the incomputable continuous adjoint solution, the method hinges on the assumption that the numerical error in the computation of the discrete adjoint solution is negligible. A counter example is given, which demonstrates underestimation of the true error. As a remedy, the usual method is enhanced by a *safeguarding* term. While the usual weighting is realized with quadratic finite elements, the additional term estimates the approximation error of the adjoint solution. Asymptotically the combined estimate coincides with the usual one.

Ainsworth and Rankin [9] further improve the approach by deriving guaranteed bounds on the error in the quantity of interest, which do not involve any unknown multiplicative constants. To this end, higher order finite elements are employed for the primal problem as well. In the numerical experiments the estimators are found to provide tight upper bounds with efficiency indices approaching unity.

**Error estimates for multiscale methods.** Error estimates for methods involving several scales were of interest in the context of *hierarchical modeling*, cf. Zohdi et al. [430], Babuška

and Schwab [42], and Stein and Ohnibus [382]. In this setting different models are available on varying length scales with associated level of details and computational complexity. An adaptive selection thus requires a concept for *modeling error estimation*. In a series of works [311, 312, 401, 400] Oden and Vemaganti employ their goal-oriented error estimation technique to analyze elastic bodies with possibly complex microstructure. In the beginning, material properties are given on the coarsest scale, e. g. obtained via homogenization. The difference in a quantities of interest based on the homogenized and the fully resolved solution is then estimated and regions are determined where the modeling should be refined. Subsequently the fully resolved elasticity tensor is directly employed there, or local problems are solved to enrich the homogenized solution.

In [313] the discretization of the heterogeneous multiscale method is considered as well, but based on a direct finite element discretization of the two-scale homogenized equation, which is essentially (5.6) in our context. Results include an a-priori estimate, in line with (5.13),

Henning and Ohlberger [313, 223] derive a posteriori error estimates for elliptic homogenization problems with fine-scale diffusion. They employ the heterogeneous multiscale method and a direct finite element discretization of the associated two-scale homogenized equation, which is close to the setting in the present work, see Section 5.3.2. The resulting estimates yield separate terms for errors in the macroscopic and the microscopic discretization, respectively. Nonlinear problems are approached in [224].

The fully discrete setting, investigated by Abdulle, is pursued in the context of adaptivity by Abdulle and Nonnenmacher [1]. A posteriori lower and upper bounds are derived following classical constructions. Thereby the jump of the multiscale flux  $\text{Vol}(\mathcal{Y})^{-1} \int_{\mathcal{Y}} a \nabla \tilde{u}_h \, dy$  is considered, where  $\tilde{u}_h$  is the solution of a microscopic cell problem as in the present work. Additionally data approximation terms appear, from which local relations of the macroscopic and the microscopic cell sizes can be deduced. Although the analysis is initially not restricted to separated scales, periodicity, or sampling domain sizes, explicit results are derived for the periodic setting.

In [4] goal-oriented error estimates are derived, based on the dual weighted residual concept for the macroscopic problem, similar to the approach taken in this work. The error in a quantity of interest is represented using the macroscopic bilinear form as usual. This however also includes the underlying approximation by the heterogeneous multiscale method, which is subsequently treated as a variational crime. Estimation follows the earlier works, yielding residual and data approximation terms. The latter can be made explicit under further assumptions on the spatial structure of the tensor field and the employed quadrature. In case the microscopic solution is assumed exact, the classical DWR results are recovered.

Regarding adaptivity in the framework of other multiscale methods, the variational multiscale method was considered by Larson and Målqvist [258], the multiscale finite element method by Henning et al. [225], and in the goal-oriented context by Chamoin and Legoll [111].

**Error estimates in shape optimization.** Adaptive schemes have already been employed for shape optimization. An early reference is [248] by Kikuchi et al. Here the optimization of the maximum of a local performance measure, like the van Mises stress, under a volume constraint is considered. A boundary variation technique is used and combined with automatic mesh generation based on relocation of nodes and refinement. It is triggered by an error indicator based on explicitly calculated approximation errors of the used finite elements. Banichuk et al. [53] account both for the error due to discretization of the state equation and the



approximation of the geometry. Therefore they employ the Zienkiewicz and Zhu estimator and additionally the norm of the residual for the necessary optimality condition w. r. t. the design. In numerical examples, weight optimization under displacement constraints is considered with explicitly parametrized shape boundaries as degrees of freedom. Bartels and Carstensen [63] consider optimal distributions of two materials in the cross-section of an infinite bar to maximize its torsional rigidity. They devise an error estimate for the approximation of the stress and prove convergence of the adaptive scheme. Wollner [419] addresses free material optimization as studied by Zowe et al. [433]. He derives a goal-oriented error estimate based on the dual weighted residual approach. Although the degrees of freedom are reduced to a single variable in the end, the derivation is close to the present work in case of the sequential lamination model, cf. Section 8.2. In the full elasticity setting, an adaptive finite element method for shape optimization via boundary tracking, remeshing and perimeter penalization is established by Morin et al. [293, 294]. Here the dual weighted residual approach is used as well, but only to assess the error in the elasticity solution. A separate geometric term is estimated based on the Laplace-Beltrami operator to account for errors in the boundary variation field. Giacomini et al. [189] introduce the *certified descent algorithm* for shape optimization via boundary variation. They consider the error in the shape gradient as quantity of interest  $E$  and aim for descent directions  $\vartheta$  fulfilling

$$d_{\mathcal{O}} \mathbf{J}[\mathcal{O}] \vartheta + |E| < 0.$$

Such directions guarantee a decrease of the objective functional, notwithstanding any numerical approximation errors. The error  $E$  is estimated using the linearized shape gradient, following Oden and Prudhomme [310] and the complementary energy principle according to Repin [341]. In particular additional flux and corresponding dual variables are introduced, and the dual complementary energy is derived. The result is a computable upper bound without unknown constants, which is used as a reliable stopping criterion and localized to steer adaptive mesh refinement. Numerical experiments are presented for inverse shape identification in electrical impedance tomography. In [188] the program is pursued, this time with error estimators based on the equilibrated fluxes method, cf. [8, 9]. Thereby only small local problems need to be solved. In the numerical examples efficiency indices approaching unity can be seen.

## 2.5. Stochastic optimization

The study of uncertainties and their effect on mathematical models has lead to the emergence of *uncertainty quantification* (UQ) as an entire research field. Its practical relevance stems from the fact that influencing factors are often not exactly known or measurable. Examples include atmospheric turbulence, material properties of porous or inhomogeneous media, imprecise knowledge of very large or very small working domains, and inaccurate modeling parameters. These uncertainties enter governing equations via the domain, coefficients, or data and therefore directly distort solutions with in general unknown variability.

**Finite dimensional background.** In mathematical programming the study of uncertainties is an established field, see [144] for an early reference. A wide range of applications can be found in mathematical finance and operations research. In case merely range information of uncertain parameters is available, *robust optimization* considers worst case outcomes, see e.g. [70, 72] and the textbook [71]. On the other hand, in case randomness is fully described by probability

distributions, *stochastic optimization* provides an appropriate mathematical framework. It has been largely studied for linear [357], linear mixed-integer [361] or nonlinear models [383, 324] and for continuous time [175, 112]. See [369] for a recent textbook. *Two-stage* stochastic programming, which is closely connected to the stochastic shape optimization problems investigated in this work, additionally brings into play the concept of *nonanticipativity*, see [333, 83, 244]. Here a first-stage decision must be taken without knowledge of the concrete outcome of a random variable. Upon commencing of the realization, a second-stage decision can be made as *recourse* action. The scheme can naturally be extended to multiple stages, see [350]. A recent overview can be found in [411]. To take into account all possible outcomes of randomness simultaneously, a natural choice is to consider the expectation of desired output functional. Termed *risk neutral*, this approach might lead to negligence of scenarios with a low probability but critical impact. Therefore *risk averse* models have been developed, see [167, 347, 358], and also combined with expectation based approaches, leading to *mean-risk* models, see [329, 362, 369]. In the present work the expected excess and the excess probability functional, see [395], are considered. The latter leads to an optimization problem with binary variables, cf. [345] and [222] for applications to stochastic networks. An alternative approach is *stochastic dominance*, which entails an ordering of candidates based on their performance when solving an optimization problem under uncertain realizations. It is popular in portfolio optimization and was gradually extended from a mere comparison of cumulative distribution functions to more flexible models, see [336, 209, 417]. It can also be used as a constraint in stochastic optimization, see [149]. An overview can be found in the textbooks [296, 368].

**Application to shape optimization.** The discussed concepts have already been applied to structural optimization, see the early study for beam models by Banichuk [51] and the textbooks [273, 54, 280]. In general approaches differ in the way stochasticity enters, which could be via the right hand side data, material coefficients, or the domain itself.

For multiple loadings  $f_i$  and corresponding solutions  $u_i$  a weighted sum of objective values  $\sum_i w_i \mathbf{J}[\mathcal{O}; u_i]$  can be optimized, which amounts to the risk neutral expectation approach. This setting is already included in the seminal work on the optimality of the sequential lamination construction by Avellaneda [37], and in many subsequent applications, e. g. [12]. Also the recently emerging approaches for the recovery of classical designs from homogenized solutions have adopted it, see [238]. The microstructure identification problem based on the SIMP model is extended in [202], level sets are e. g. used in [13], and the free material optimization approach in [386]. A full adoption of the stochastic setting is presented by Conti et al. [136] with a focus on approximating continuous probability distributions. Arbitrary quadratic objective functionals are admitted and linearity of the state equation is exploited to reduce computations to a set of basis solutions. For the representation of the shape the level set method is used with a discretization by composite finite elements. The work is extended in [139] to allow for risk averse measures in terms of the expected excess and excess probability functionals. Dambrine et al. [143] propose an entirely different approach based on the *two-point correlation* of the state. It is obtained as the solution of a tensor-product-type boundary value problem with the two-point correlation of the random loads as right hand side. Thereby no full knowledge of the probability distribution is required. The initially high-dimensional problem is solved efficiently by applying a low-rank approximation.

Robust optimization has received a lot of interest as well. In case of the sequential lamination construction, Cherkaev et al. [125] suggest rank-3 laminates to obtain *stable* optimal designs,

in contrast to rank-2 laminates, which are optimal but degenerate and would thus fail in case small variations occurred. Later, Cherkaev and Cherkaev [122] introduce the *principle compliance*. For unknown loadings, which are only limited by an integral constraint, it amounts to the maximal possible stored energy. Depending on the constraints, explicit expressions are obtained and the optimization problem then takes a min-max structure. Numerical examples include a beam model and continuous optimization with sequential lamination. For a continuous change of the loading constraint, a bifurcation of the solution is studied. Free material optimization in the worst case setting is considered in [69]. Here a reformulation of the problem is developed, the existence of solutions is shown, and interior point algorithms are employed. The setting is also included in [386]. Level sets are used by Gournay et al. [195]. In their work unknown but constrained perturbations of a given load are considered. They prove that a, possibly nonunique, worst perturbation leading to maximal compliance exists. It is characterized as the maximizer of a nonlinear energy and computed numerically. Based on this reformulation, the shape derivative for steering the level set evolution is computed. Kogioso et al. [249] investigate robust optimization of compliant mechanisms by considering a combination of the expectation and variance of the output deformation. They use a two-scale approach with hexagonal microstructures leading to isotropic homogenized material. Takezawa et al. [391] employ the SIMP approach and formulate the optimization problem as the minimization of the maximal eigenvalue of a reduced linear system of equations. Amstutz and Ciligot-Travain [35] revisit the work by Gournay et al. [195]. They approach robust optimization in a general theoretical framework and show the existence of critical loads in the infinite dimensional setting. Furthermore they consider maximization of the *stability radius*. This amounts to finding a shape which tolerates the highest variations of loading while still meeting a constraint on the compliance. In contrast to worst case optimization, not the magnitude of variations but an acceptable tolerance for the objective has to be specified. For numerical demonstrations, they apply their level set approach of [34].

Kharmanda et al. [247] consider *reliability based* topology optimization using the SIMP model. In this approach the compliance is minimized subject to a volume limit and an additional constraint measuring the probability of failure in terms of critical states. Banichuk and Neittaanmäki [54] include material properties and arisen damages as uncertain influence factors. They consider the worst case approach and present transformations to conventional structural optimization problems for several examples. Rumigny et al. [356] optimize the location of prescribed holes in an elastic domain subject to an uncertainty on the actual placement, i. e. an unknown but constrained variation is allowed for the design variable itself. The topological derivative is investigated for varying material properties and right hand side data in [229]. It is shown to continuously depend on the input and is therefore regarded as stable. Chen et al. [114] employ the level set method for varying material properties and loadings. They use a combination of expectation and variance as objective and to this end approximate moments of continuous random fields by the Karhunen-Loève expansion. In [113] the same approach is used to handle uncertainty in the geometry, given by a random perturbation field on the boundary. This additionally requires to maintain point correspondences between the original and the perturbed boundaries. Shape sensitivities are then computed and mapped back to the original domain. Geometric uncertainty is also tackled by Wang et al. in [413] and subsequent works. They employ the SIMP method and obtain classical designs by thresholding. The thresholding parameter is then randomly perturbed to yield variations of the shape. Alexandersen and Lazarov [10] likewise approach a two-scale problem, but with finite separation of length scales. They use the multiscale finite element

approach and prescribe a fixed fine mesh in every macroscopic cell, where a modified SIMP model is employed. The base functions are then obtained from solutions of eigenvalue problems and can be utilized as a multigrid-like preconditioner to efficiently solve the elasticity problem. Constraints are used to enforce connectivity of the periodic fine-scale structures. Allaire and Dapogny [23] consider uncertainties in the loading, the material properties, and the geometry in the worst case setting via linearization. Maximization of the linearized functional can be done explicitly and results in an objective consisting of the unperturbed functional and a penalization of the perturbations, expressed via an adjoint state. The general framework is applied to optimization of a plate and shape optimization via the level set method. In [24] optimization of expectation, variance and failure probability is investigated for a similar set of problems. Under the assumption of small perturbations, first and second order Taylor expansions are derived, from which moments and probabilities can be calculated explicitly. The uncertainties are generated from a small set of random variables, which allow to obtain efficient numerical schemes with computational costs comparable to multiple load problems.

---

## CHAPTER 3

### Fundamentals in elasticity

---

FUNDAMENTAL concepts in linearized elasticity will be revised in this chapter. We present the derivation of the partial differential equations of linearized elasticity, governing the deformation behavior of an elastic body when exposed to loadings. Existence and uniqueness results for classical boundary value problems and periodic cell problems are given. As microstructured materials loom large in this thesis the theory of periodic homogenization will be recapitulated. Finally basic concepts for the discretization of the elasticity problem by conforming finite elements and the boundary element method are discussed.

#### 3.1. Derivation of a linearized model

To model the behavior of a deformable solid under loading we take the viewpoint of continuum mechanics. In contrast to an atomistic perspective the material under consideration is regarded as a continuous substance filling the whole occupied space. Applied forces cause stresses inside the material maintaining an equilibrium, which can be described in a linearized fashion by an elliptic partial differential equation. A series of assumptions will help in deriving such a simplified model. First we restrict ourselves to elastic deformations, which means that a deformed shape will return to its original configuration if the loads hold off again. Secondly we are only interested in small deformations that rather give a tendency of the deformation and will allow for linearization. Lastly we only consider two dimensional objects, although the presented theory and modeling are valid in three dimensions as well. In the following we will briefly sketch the derivation of the partial differential equations of linearized elasticity. For a more detailed and rigorous exposition we refer to the textbooks [129, 272].

Let  $\mathcal{O} \subseteq D \subset \mathbb{R}^2$  be a domain with possibly several path-components representing the elastic object and  $D$  a surrounding, simply connected working domain. In the setting of interest for shape optimization the complement  $D \setminus \mathcal{O}$  represents void regions. To ease the mathematical analysis this region is sometimes assumed to comprise a weak substitute material. That way no interior boundaries within  $D$  and no additional extension operators have to be considered. In general we will consider the perforated setting, unless otherwise noted. We require a minimal, strictly positive volume of the remaining domain to rule out exceptionally large deformations. Both  $\mathcal{O}$  and  $D$  are assumed to have a Lipschitz boundary  $\Gamma := \partial\mathcal{O}$  and  $\partial D$  respectively. On a part  $\Gamma_D \subset \Gamma \cap \partial D$  of positive measure a displacement  $u^\partial \in H^1(D; \mathbb{R}^2)$  is prescribed. Here  $H^1$  denotes the Sobolev space of  $L^2$ -measurable functions with weak first partial derivatives in  $L^2$ . Setting  $u^\partial = 0$  allows to fixate the body along  $\Gamma_D$ . Mathematically  $u^\partial$  takes on a Dirichlet boundary condition. On another part  $\Gamma_N \subset \Gamma \cap \partial D$ , likewise of positive measure, surface loads  $g \in H^1(D; \mathbb{R}^2)$  are applied. The vector field can be interpreted as the density of forces acting on the surface  $\Gamma_N$ . Mathematically these forces constitute Neumann

boundary conditions. We require the two boundary parts  $\Gamma_D$  and  $\Gamma_N$  to be disjoint with the exception of finitely many one dimensional contact points. Furthermore they are fixed in the context of optimization as they could simply be eliminated otherwise. On the contrary the remaining part  $\Gamma_F := \Gamma \setminus (\Gamma_D \cup \Gamma_N)$  is allowed to evolve freely by specifying homogeneous Neumann boundary conditions, i. e.  $g \equiv 0$ . Finally body forces, again specified by a density vector field  $f \in L^2(D; \mathbb{R}^2)$  are given to model forces acting on volumetric elements of the elastic body, like e. g. gravity. Usually one is interested in values of  $u$  and  $f$  restricted to  $\mathcal{O}$ , and  $u^\partial$  and  $g$  restricted to  $\Gamma_D$  and  $\Gamma_N$ , respectively. Due to the requirements, the latter have traces on  $\Gamma$  in  $H^{\frac{1}{2}}(\Gamma; \mathbb{R}^2)$ . For convenience we assume all quantities to have an extension, usually by zero, to the whole domain  $D$ .

Let  $\phi: D \rightarrow \mathbb{R}^2$  denote the deformation caused by the loadings defined above. We assume that  $\phi$  is smooth enough for the definitions to follow, injective, and orientation-preserving, i. e.  $\det D\phi > 0$ . Quantities superscripted by  $\phi$  shall refer to the deformed configuration, e. g.  $\mathcal{O}^\phi = \phi(\mathcal{O})$  is the body in its deformed state, see also Figure 3.1. To relate the deformation

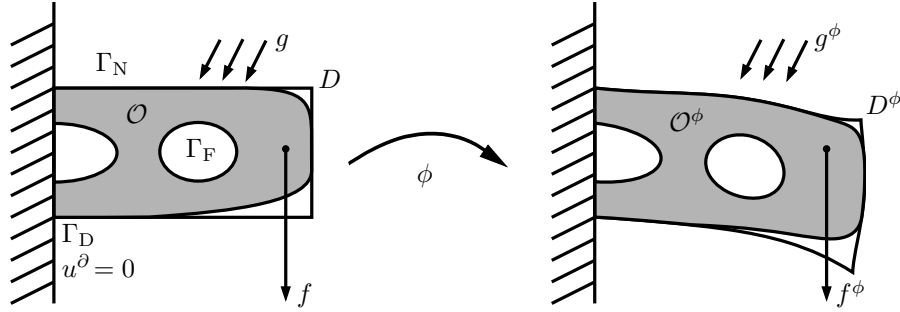


Figure 3.1.: Sketch of elastic domain with boundary conditions in reference and deformed configuration.

to the acting loadings, balancing equations are considered for arbitrary, smoothly bounded test volumes  $V^\phi \subseteq \mathcal{O}^\phi$ . In particular the *Cauchy-Euler stress principle* demands existence of a vector field  $t^\phi(x^\phi, n^\phi): \overline{\mathcal{O}^\phi} \times S^1 \rightarrow \mathbb{R}^2$ , the *stress vector*, s. t.

$$\begin{aligned} t^\phi(x^\phi, n^\phi) &= g^\phi(x^\phi) \quad \text{on } (\Gamma_N^\phi \cup \Gamma_F^\phi) \cap \partial V^\phi, \\ \int_{\partial V^\phi} t^\phi(x^\phi, n^\phi) \, da(x^\phi) + \int_{V^\phi} f^\phi \, dx^\phi &= 0, \\ \int_{\partial V^\phi} t^\phi(x^\phi, n^\phi) \times x^\phi \, da(x^\phi) + \int_{V^\phi} f^\phi \times x^\phi \, dx^\phi &= 0. \end{aligned} \tag{3.1}$$

Here  $S^1$  denotes the unit sphere in  $\mathbb{R}^2$  and  $n^\phi \in S^1$  the normalized outer normal of  $V^\phi$ . This axiom requires that the stress vector exists for any surface within the elastic body, depends, besides the position  $x^\phi$ , on the local normal  $n^\phi$  only and fits to the prescribed surface loads on the real outer boundary. Moreover any test volume is in static equilibrium, i. e. there is a balance of internal surface and body forces resulting in a vanishing force vector and vanishing angular momentum. The latter is expressed by the cross product, which is defined for two

vectors  $a, b \in \mathbb{R}^3$  as  $a \times b = (a_2b_3 - a_3b_2, a_3b_1 - a_1b_3, a_1b_2 - a_2b_1)^\top$ . Altogether acting external forces get transmitted from point to point throughout the whole elastic body.

*Cauchy's stress theorem* now states important consequences from the stress principle. Under the assumption that  $f^\phi$  is continuous and  $t^\phi(x^\phi, n^\phi)$  smooth in  $x^\phi$  and continuous in  $n^\phi$  the dependence of the stress vector on the normal is linear, given by a smooth tensor field  $T^\phi: \overline{\mathcal{O}}^\phi \rightarrow \mathbb{R}^{2 \times 2}$ , called *Cauchy stress tensor*. In particular  $T^\phi(x^\phi)n^\phi = t^\phi(x^\phi, n^\phi)$  for all  $(x^\phi, n^\phi) \in \mathcal{O}^\phi \times S^1$ . Plugging into (3.1), using the divergence theorem and force balance yields the partial differential equations

$$\begin{cases} -\operatorname{div}^\phi T^\phi = f^\phi & \text{in } \mathcal{O}^\phi \\ T^\phi n^\phi = g^\phi & \text{on } \Gamma_N^\phi \cup \Gamma_F^\phi \\ \phi = \operatorname{Id} & \text{on } \Gamma_D^\phi \end{cases}$$

in the deformed configuration. Moreover, by balance of momentum, the tensor turns out to be symmetric, i. e.  $T^\phi(x^\phi) = T^\phi(x^\phi)^\top$ . Pulling back to the undeformed reference configuration results in the transformed quantities

$$\begin{aligned} T(x) &:= T^\phi(x^\phi) \operatorname{cof}(D\phi(x)), \\ g(x) &:= g^\phi(x^\phi) |\operatorname{cof}(D\phi(x)) n(x)|, \\ f(x) &:= f^\phi(x^\phi) \det(D\phi(x)), \end{aligned}$$

where  $\operatorname{cof}(D\phi(x)) = \det(D\phi(x)) D\phi(x)^{-\top}$  denotes the cofactor matrix. The newly obtained tensor  $T$  is known as the *first Piola-Kirchhoff stress tensor*. To regain symmetry one furthermore defines the *second Piola-Kirchhoff stress tensor*  $\Sigma := (D\phi)^{-1} T$ . For the forces often the dead load assumption is used, stating that the loads actually do not change under deformation, and allowing a direct identification of  $f$  and  $g$  with  $f^\phi$  and  $g^\phi$  respectively. The partial differential equations in reference configuration thus read

$$\begin{cases} -\operatorname{div}(D\phi \Sigma) = f & \text{in } \mathcal{O}, \\ D\phi \Sigma n = g & \text{on } \Gamma_N \cup \Gamma_F, \\ \phi = \operatorname{Id} + u^\partial & \text{on } \Gamma_D. \end{cases}$$

At this point a relation of the deformation and the stresses has to be given via constitutive equations. A fundamental postulate is to consider *elastic* materials, where the stress tensor is fully determined by the gradient of the deformation in the reference configuration for all admissible deformations. To be more precise, a material is called elastic if there is a *response function*  $\hat{\Sigma}: \overline{\mathcal{O}} \times \mathbb{R}_{\det>0}^{2 \times 2} \rightarrow \mathbb{R}_{\operatorname{sym}}^{2 \times 2}$ , s. t.  $\Sigma(x) = \hat{\Sigma}(x, D\phi)$ . Here  $\mathbb{R}_{\det>0}^{2 \times 2}$  denotes the set of  $2 \times 2$  matrices with positive determinant and  $\mathbb{R}_{\operatorname{sym}}^{2 \times 2}$  the set of symmetric  $2 \times 2$  matrices. Further simplification results from demanding frame indifference, which constitutes the intuitive requirement that the behavior of the material should not depend on the chosen coordinate frame. For this, consider another deformation  $\tilde{\phi} = Q\phi + b$  obtained via a rigid body transformation of  $\phi$ , i. e.  $Q \in SO(2)$  is a rotation matrix and  $b \in \mathbb{R}^2$  a translation vector. Then  $t^{\tilde{\phi}}(x^{\tilde{\phi}}, n^{\tilde{\phi}}) = Qt^\phi(x^\phi, n^\phi)$  should hold. As a consequence one can show that the response function has an even simpler form, namely there exists another mapping  $\bar{\Sigma}: \overline{\mathcal{O}} \times \mathbb{R}_+^{2 \times 2} \rightarrow \mathbb{R}_{\operatorname{sym}}^{2 \times 2}$ , defined for positive-definite matrices, s. t.  $\hat{\Sigma}(x, D\phi) = \bar{\Sigma}(x, D\phi^\top D\phi)$ . Thus the stresses only depend on the symmetric *right Cauchy-Green strain tensor*  $D\phi^\top D\phi$ .

The establishment of a linear model now occurs in three steps. If a deformation is a rigid body transformation, which is insignificant for an elastic deformation, its associated strain tensor becomes  $\mathbb{1}$ . Therefore one considers the deviation of strain tensors from the identity, i. e.  $\mathcal{E}[\phi] = \frac{1}{2} (\mathbf{D}\phi^\top \mathbf{D}\phi - \mathbb{1})$ . Let  $\phi = \text{Id} + u$  with  $u$  being the *displacement* and define the *linearized strain tensor* as  $\varepsilon[u] := \frac{1}{2} (\mathbf{D}u + \mathbf{D}u^\top)$ . Then  $\mathcal{E}[\phi] = \frac{1}{2} \mathbf{D}u^\top \mathbf{D}u + \varepsilon[u]$  and by neglecting terms of higher order one approximates  $\mathcal{E}[\phi]$  by  $\varepsilon[u]$ . Secondly one chooses a linear relation to couple the stress tensor  $\bar{\Sigma}$  to the linearized strain tensor. This relation is initially given by a fourth order tensor  $C \in \mathbb{R}^{2^4}$ , mapping  $\varepsilon[u]$  to  $\sigma := C\varepsilon[u]$ . From now on we refer to  $\sigma$  as the *stress tensor*. The third step is a Taylor expansion around the origin  $u = 0$  under the assumption that the reference configuration is a natural state, i. e.  $\bar{\Sigma}(x, \mathbb{1}) = 0$ , cf. [129, Theorem 6.2-1]. This assumption guarantees a stress free reference state and makes  $u = 0$  a solution to the elasticity problem in absence of any loading. Ultimately an elliptic system of partial differential equations of second order is obtained, reading

$$\left\{ \begin{array}{ll} -\operatorname{div} \sigma = f & \text{in } \mathcal{O}, \\ \sigma n = g & \text{on } \Gamma_N \cup \Gamma_F, \\ u = u^\partial & \text{on } \Gamma_D, \\ \sigma = C\varepsilon[u] & \text{in } \mathcal{O}. \end{array} \right. \quad (3.2)$$

**Remark 3.1.** It is important to emphasize that the derived simple equations are the result of linearization and can therefore only provide an approximation of the elastic behavior for the applied loadings close to the reference state. Fundamental properties, that were used in the derivation, such as frame indifference, are actually violated by the linearized model. Furthermore large deformations are not adequately modeled. In fact a scaling of the forces merely results in a scaling of the displacement, which is obviously not realistic. Ciarlet, in [129, p. 286], even states “Elasticity cannot be linear!”. Still, despite its shortcomings, the approach has been widely adopted and proven to yield sensible results. Especially for shape optimization the reaction of the material to loadings by trend seems sufficient for a qualitative appraisal of the structure.

**Remark 3.2.** The theory presented in the referenced textbooks is set up for the three dimensional case. It can be reduced to the two dimensional case by dropping the third components of deformations, stresses, and related operators, as done here. One can however not fully justify these omissions by the elastic behavior. Even if there is no strain in a principle direction, stresses in this direction can very well occur and are indeed required to let the strain vanish, and vice versa. Therefore one selected quantity has to be set to zero by assumption and the other has to be neglected. In this work we take the *plane strain* perspective, i. e. we assume that no strain occurs in direction of the third spatial component and ignore stresses in this direction. This assumption leads to a linear stress-strain relation looking familiar to the fully three dimensional case and can be motivated by workpieces that are very long in a certain direction, compared to the others. The deformation in this direction is therefore neglected and only a cross section considered.

## 3.2. Properties of elastic materials

In the derivation of the elastic model a linear mapping was ultimately chosen as the constitutive equation. As such it is a forth order tensor operating on the space of square matrices. Initially



we assume its coefficients to be bounded, i. e.  $C \in L^\infty(\mathcal{O}; \mathbb{R}^4)$ , making it a bounded operator with associated operator norm  $\|C\|$ . Furthermore we assume that *very strong ellipticity* holds, i. e. for a universal constant  $c > 0$

$$CX : X \geq c X : X, \quad \forall X \in \mathbb{R}_{\text{sym}}^{2 \times 2} \quad (3.3)$$

should hold. This assumption is crucial for the existence theory described in the next section. Further motivation of the less strict *strong ellipticity condition* is given in [129, p. 255].

By coupling stresses and linearized strains, the elasticity tensor fundamentally characterizes the material behavior. Initially there are  $2^4 = 16$  degrees of freedom, but most of them are actually interdependent.

**Lemma 3.3.** *The entries of the elasticity tensor  $C$  satisfy the symmetries*

$$C_{ijkl} = C_{jikl}, \quad C_{ijkl} = C_{ijlk}, \quad C_{ijkl} = C_{klij}, \quad i = 1, 2. \quad (3.4)$$

As to the proof, the first relation follows from the fact that  $\sigma$  has to be symmetric by virtue of Cauchy's stress theorem. The third relation requires a more intricate reasoning based on the theory of hyperelasticity. Here entries of the elasticity tensor appear as second derivatives of a hyperelastic energy density and symmetry follows from permutability of differentiation under smoothness assumptions. See e. g. [272, Proposition 4.4, p. 209] for further details. The second relation finally results from combining the first and the third. As an immediate consequence of symmetry there holds

$$C \varepsilon[u] = C D u. \quad (3.5)$$

For providing a better overview of the remaining 6 degrees of freedom of  $C$ , it is common to express the stress-strain relation using *Voigt notation*. It reads

$$\begin{pmatrix} \sigma_{11} \\ \sigma_{22} \\ \sigma_{12} \end{pmatrix} = \begin{pmatrix} c_{11} & c_{12} & c_{14} \\ c_{12} & c_{22} & c_{24} \\ c_{14} & c_{24} & c_{44} \end{pmatrix} \begin{pmatrix} \varepsilon_{11}[u] \\ \varepsilon_{22}[u] \\ 2 \varepsilon_{12}[u] \end{pmatrix}, \quad (3.6)$$

where  $c_{11} = C_{1111}$ ,  $c_{12} = C_{1122}$ ,  $c_{14} = C_{1112}$ ,  $c_{22} = C_{2222}$ ,  $c_{24} = C_{2212}$ , and  $c_{44} = C_{1212}$ . Further simplifications arise from special material properties. *Orthotropic* materials feature different properties along two orthogonal axes of symmetry, e. g. due to an atomistic lattice, and one can deduce  $c_{14} = c_{24} = 0$ . If the behavior in both directions is furthermore identical we have  $c_{22} = c_{11}$ , referred to as *cubic symmetry* for the three dimensional case. A final simplification is the fully *isotropic* case where the material reaction is uniform for every direction, resulting in  $c_{11} = c_{12} + 2c_{44}$ .

**Remark 3.4.** Under the assumption of isotropy it is in fact possible to directly establish the stress-strain relation

$$\sigma = \lambda \operatorname{tr}(\varepsilon[u]) \mathbf{1} + 2\mu \varepsilon[u]. \quad (3.7)$$

This coincides with the afore mentioned simplifications of (3.6) when setting  $\lambda = c_{12}$  and  $\mu = c_{44}$ . However it is important to remark that this is not just a specific choice for the constitutive relation, but a result of rigorous mathematical derivation. See [129, pp. 104 sqq.] for details.

The elasticity coefficients  $\lambda$  and  $\mu$  are known as *Lamé parameters* and can be determined for real materials by experiment. As they are known to be positive, the ellipticity condition follows as  $CX : X \geq 2\mu X : X$  from (3.7). The second parameter  $\mu$  is also known as the *shear modulus*. Further important coefficients are *Young's modulus*  $E$ , *Poisson's ratio*  $\nu$ , and the *bulk modulus*  $\kappa$ , given by

$$E = \frac{\mu(3\lambda + 2\mu)}{\lambda + \mu}, \quad \nu = \frac{\lambda}{2(\lambda + \mu)}, \quad \kappa = \lambda + \frac{2\mu}{d}. \quad (3.8)$$

Roughly speaking  $\mu$  measures the material reaction to shearing,  $\nu$  its lateral contraction, i. e. the decrease in width perpendicular to an applied traction force,  $E$  its change in length due to tensile loads, and  $\kappa$  its compressibility under hydrostatic loads, i. e. uniform normal loads on the surfaces. Of these coefficients only the bulk modulus depends on the dimension  $d \in \{2, 3\}$ .

In this work we usually have isotropic materials in mind, that can be characterized by the constants above. As the concrete values do not have significant influence on the qualitative outcome of shape optimization, we will mostly use normalized parameters  $\lambda = \mu = 1$ . This choice does not reflect properties of a realistic material, but simplifies computations. The two-scale construction, which is the main aspect of this thesis, will however not produce isotropic materials in general anymore.

### 3.3. Solution of the elasticity problem

Throughout this work we will rely on the calculus of variations for the analysis of the shape optimization problem. Accordingly a weak formulation of the elasticity problem (3.2) will be considered. Let the bilinear form  $a: H^1(\mathcal{O}; \mathbb{R}^2) \times H^1(\mathcal{O}; \mathbb{R}^2) \rightarrow \mathbb{R}$  and the linear form  $l: H^1(\mathcal{O}; \mathbb{R}^2) \rightarrow \mathbb{R}$  be defined by

$$\begin{aligned} a(\mathcal{O}; u, \vartheta) &:= \int_{\mathcal{O}} C\varepsilon[u] : \varepsilon[\vartheta] \, dx, \\ l(\mathcal{O}; \vartheta) &:= \int_{\mathcal{O}} f \cdot \vartheta \, dx + \int_{\Gamma_N} g \cdot \vartheta \, da(x), \end{aligned} \quad (3.9)$$

for  $u, \vartheta \in H^1(\mathcal{O}; \mathbb{R}^2)$ . By convention we separate variables which possibly enter nonlinearly by a semicolon from the linear dependencies in the definition of functionals. Let  $H_{\Gamma_D}^1$  denote the space of functions in  $H^1$  with vanishing trace on  $\Gamma_D$ , i. e.  $u(x) = 0$  for  $x \in \Gamma_D$ .

**Theorem 3.5** (Weak formulation of the elasticity problem). *The partial differential equations of linearized elasticity (3.2) are formally equivalent to the following weak formulation.*

Find  $u^0 \in H_{\Gamma_D}^1(\mathcal{O}; \mathbb{R}^2)$ , s. t.  $u = u^0 + u^\vartheta$  satisfies

$$a(\mathcal{O}; u, \vartheta) = l(\mathcal{O}; \vartheta) \quad \forall \vartheta \in H_{\Gamma_D}^1(\mathcal{O}; \mathbb{R}^2). \quad (3.10)$$

*Proof.* For any  $u$ , assumed to be smooth enough, we start from (3.2), multiply both sides by a test function  $\vartheta \in H_{\Gamma_D}^1(\mathcal{O}; \mathbb{R}^2)$  and integrate over  $\mathcal{O}$ . Next we apply partial integration row

wise on the matrix  $\sigma$ , yielding

$$\begin{aligned}
 \int_{\mathcal{O}} f \cdot \vartheta \, dx &= \int_{\mathcal{O}} -\operatorname{div}(\sigma) \cdot \vartheta \, dx \\
 &= \int_{\mathcal{O}} \sigma : D\vartheta \, dx - \int_{\Gamma_N} \sigma n \cdot \vartheta \, da(x) \\
 &= \int_{\mathcal{O}} C\varepsilon[u] : \varepsilon[\vartheta] \, dx - \int_{\Gamma_N} g \cdot \vartheta \, da(x)
 \end{aligned} \tag{3.11}$$

Replacing  $D\vartheta$  by  $\varepsilon[\vartheta]$  is possible due to symmetry of  $C$ , cf. (3.5). Furthermore we have  $\sigma n = g$  on  $\Gamma_N \cup \Gamma_F$ , and especially  $g = 0$  on  $\Gamma_F$ , in virtue of the prescribed boundary conditions. Rearranging then yields (3.10).

Conversely starting from (3.10) and using partial integration in reverse gives

$$\int_{\mathcal{O}} -\operatorname{div}(\sigma) \cdot \vartheta \, dx + \int_{\Gamma_N \cup \Gamma_F} \sigma n \cdot \vartheta \, da(x) = \int_{\mathcal{O}} f \cdot \vartheta \, dx + \int_{\Gamma_N} g \cdot \vartheta \, da(x).$$

Restricting the trial space to compactly supported functions on  $\mathcal{O}$  yields the identity  $-\operatorname{div}(\sigma) = f$  inside  $\mathcal{O}$  by virtue of the fundamental lemma of the calculus of variations, see e. g. [186] as a text book reference. The remaining identity for the boundary integrals over  $\Gamma_N \cup \Gamma_F$  again has to hold for all possible functions  $\vartheta$ . So likewise choosing appropriate functions with traces on  $\Gamma_N \cup \Gamma_N$  establishes  $\sigma n = g$  on  $\Gamma_N$ , and  $\sigma n = 0$  on  $\Gamma_F$ . Finally  $u = u^\vartheta$  on  $\Gamma_D$  is immediately fulfilled due to the definition of the weak problem.  $\square$

**Remark 3.6.** The introduction of  $u^0 \in H_{\Gamma_D}^1(\mathcal{O}; \mathbb{R}^2)$  in Theorem 3.5 above reflects the usual procedure of reducing an inhomogeneous Dirichlet boundary condition to a homogeneous one.

Due to its importance for the existence result, we now restate Korn's inequality.

**Theorem 3.7** (Korn's inequality). *There exists a constant  $c > 0$ , s. t. for all  $\vartheta \in H^1(\mathcal{O}; \mathbb{R}^2)$*

$$\|\vartheta\|_{1,2,\mathcal{O}} \leq c(|\vartheta|_{0,2,\mathcal{O}} + |\varepsilon[\vartheta]|_{0,2,\mathcal{O}}).$$

*Consequently the term on the right hand side defines a norm equivalent to the full  $H^1$ -norm.*

The result is especially remarkable as only the symmetric part of the Jacobian appears on the right hand side. The proof is delicate, but numerous variants have been given throughout the years, see [129, p. 291] for a list of references. We have now gathered all ingredients to give the existence and uniqueness result for the weak elasticity problem.

**Theorem 3.8** (Existence and uniqueness of a weak solution). *Under the assumptions set up so far, there exists a unique solution  $u^0 \in H_{\Gamma_D}^1(\mathcal{O}; \mathbb{R}^2)$ , s. t.  $u = u^0 + u^\vartheta$  satisfies the weak problem of linearized elasticity (3.10).*

*Proof.* The proof is done by applying the Lax-Milgram lemma to the weak problem  $a(\mathcal{O}; u^0, \vartheta) = l(\mathcal{O}; \vartheta) - a(\mathcal{O}; u^\vartheta, \vartheta) \forall \vartheta \in H_{\Gamma_D}^1(\mathcal{O}; \mathbb{R}^2)$ . Therefore note first that the right hand side is linear

in  $\vartheta$ . It is moreover bounded because

$$\begin{aligned}
 & |l(\mathcal{O}; \vartheta) - a(\mathcal{O}; u^\vartheta, \vartheta)| \\
 & \leq \left| \int_{\mathcal{O}} f \cdot \vartheta \, dx + \int_{\Gamma_N} g \cdot \vartheta \, da(x) + \int_{\mathcal{O}} C \varepsilon[u^\vartheta] : \varepsilon[\vartheta] \, dx \right| \\
 & \leq \|f\|_{0,2,\mathcal{O}} \|\vartheta\|_{0,2,\mathcal{O}} + \|g\|_{0,2,\Gamma_N} \|\vartheta\|_{0,2,\Gamma_N} + \|C\| \|u^\vartheta\|_{1,2,\mathcal{O}} \|\vartheta\|_{1,2,\mathcal{O}} \\
 & \leq (\|f\|_{0,2,\mathcal{O}} + \|g\|_{1,2,\mathcal{O}} + \|C\| \|u^\vartheta\|_{1,2,\mathcal{O}}) \|\vartheta\|_{1,2,\mathcal{O}}.
 \end{aligned}$$

Here the Cauchy-Schwartz inequality, the continuity property of the trace operator, and the definitions of the full and semi Sobolev norms were used. The bilinear form on the left hand side is likewise bounded. Furthermore we have

$$a(\mathcal{O}; \vartheta, \vartheta) \geq c \int_{\mathcal{O}} \varepsilon[\vartheta] : \varepsilon[\vartheta] \, dx$$

due to the ellipticity assumption (3.3). To show coerciveness on the space  $H_{\Gamma_D}^1(\mathcal{O}; \mathbb{R}^2)$ , i. e.  $a(\mathcal{O}; \vartheta, \vartheta) \geq c \|\vartheta\|_{1,2,\mathcal{O}}$ , one has to check that  $\vartheta \mapsto \int_{\mathcal{O}} \varepsilon[\vartheta] : \varepsilon[\vartheta] \, dx$  defines a norm, equivalent to the  $H^1$ -norm. For this Korn's inequality, see Theorem 3.7, is the crucial point. Moreover one finds that  $\varepsilon[\vartheta] = 0$  implies  $\vartheta = 0$  if  $\text{Vol}(\Gamma_D) > 0$ . The detailed calculations can be found in [129, pp. 292 sqq.]. This completes the prerequisites of the Lax-Milgram lemma and the result follows.  $\square$

**Remark 3.9.** When proving the norm properties one finds that  $\varepsilon[\vartheta] = 0$  actually implies  $\vartheta(x) = a + Sx$  with  $a \in \mathbb{R}^2$  and  $S \in \mathbb{R}^{2 \times 2}$  skew symmetric, i. e.  $S^\top = -S$ . The mapping by a skew symmetric matrices can be interpreted as an infinitesimal rotation. Thereby, in the linearized setting,  $\vartheta$  corresponds to a translation and rotation, i. e. a rigid body motion. As described in Section 3.1 such deformations are ruled out in the modeling and in fact they are here precluded by requiring  $\text{Vol}(\Gamma_D) > 0$ . From an intuitive point of view this simply means that a fixation of the domain on a strip prevents translations and rotations.

**Remark 3.10.** The existence and uniqueness result stated here in fact demands less regularity of  $u$  than needed for the derivation of the strong formulation (3.2) and the formal calculation in the proof of Theorem 3.5. Under certain assumptions it is furthermore possible to show that weak solutions are also strong solutions, see [129, Theorem 6.3-6] for details. Throughout this thesis we will refer to the weak solution of (3.10) as *the* elasticity solution. Moreover the regularity requirements for  $f$  and  $g$  can be weakened, cf. [129, Theorem 6.3-5], but this is not essential for our exposition.

From the Lax-Milgram lemma we additionally gain a characterization of the elasticity solution as the unique minimizer of an energy functional, which will reappear in the shape optimization context.

**Corollary 3.11.** *The weak elasticity solution of (3.10) is the unique solution of the minimization problem*

$$\min_{\vartheta \in H_{\Gamma_D}^1(\mathcal{O}; \mathbb{R}^2)} \mathbf{J}^{\text{total}}[\mathcal{O}; \vartheta + u^\vartheta], \quad \text{where } \mathbf{J}^{\text{total}}[\mathcal{O}; u] := \frac{1}{2}a(\mathcal{O}; u, u) - l(\mathcal{O}; u) \quad (3.12)$$

is the total free energy. Note that in accordance to (3.10) the candidates are taken from the trial space of functions with vanishing trace on  $\Gamma_D$ .

This result follows from considering variations of the energy functional and checking the necessary and sufficient conditions for a minimizer. We will come across this procedure in the two-scale context.

### 3.4. Periodic boundary conditions

Later on we will be required to solve elasticity problems with periodic boundary conditions, a special setting that was not discussed so far. To this end we consider the domain  $\mathcal{Y} \subseteq D^{\mathcal{Y}} = [0, 1]^2$ , also referred to as *unit cell*. A proper subset is obtained if the domain has holes, which are admitted here but required to keep a distance to the cell boundary. Let  $\theta := \text{Vol}(\mathcal{Y}) \in [c, 1]$ ,  $c > 0$  denote the volume of the unit cell. The elasticity tensor field  $C$  is required to be  $\mathcal{Y}$ -periodic, i. e. the tensors given on the boundary of  $\mathcal{Y}$  have to coincide with their counterparts on the opposing boundary. We furthermore assume the right hand side  $f$  to be  $\mathcal{Y}$ -periodic and consequently look for a solution  $u$ , which is likewise periodic. Therefore we define the spaces  $H_{\text{per}}^1 := \{\vartheta \in H^1 : \vartheta \text{ } \mathcal{Y}\text{-periodic}\}$  and  $L_{\text{per}}^2 := \{\vartheta \in L^2 : \vartheta \text{ } \mathcal{Y}\text{-periodic}\}$  of  $\mathcal{Y}$ -periodic functions from  $H^1$  and  $L^2$  respectively. The elasticity problem, in strong formulation, now reads

$$\begin{cases} -\operatorname{div} C \varepsilon[u] = f & \text{in } \mathcal{Y}, \\ u \in H_{\text{per}}^1(\mathcal{Y}; \mathbb{R}^2), \end{cases} \quad (3.13)$$

for  $f \in L_{\text{per}}^2(\mathcal{Y}; \mathbb{R}^2)$ . The associated weak problem is

$$a(\mathcal{Y}; u, \vartheta) = \int_{\mathcal{Y}} f \cdot \vartheta \, dx \quad \forall \vartheta \in H_{\text{per}}^1(\mathcal{Y}; \mathbb{R}^2). \quad (3.14)$$

One might also think of the problem being defined on the unit torus, leading naturally to the postulated periodic identifications. In any case there is no real boundary delimiting the problem domain anymore, where e. g. Dirichlet boundary conditions could be prescribed. In the context of the preceding section  $\text{Vol}(\Gamma_{\text{D}}) = 0$  holds and the existence result is not applicable. It is however regained by an instance of the *Fredholm alternative*, cf. [322, Theorem 7.9].

**Theorem 3.12** (Fredholm alternative). *Under the hitherto assumptions for the elasticity tensor, exactly one of the following statements holds:*

1. For every  $f \in L_{\text{per}}^2(\mathcal{Y}; \mathbb{R}^2)$  there exists a unique solution of (3.14).
2. The homogeneous equation

$$a(\mathcal{Y}; u, \vartheta) = 0 \quad \forall \vartheta \in H_{\text{per}}^1(\mathcal{Y}; \mathbb{R}^2) \quad (3.15)$$

has a nontrivial solution.

In the latter case problem (3.14) has a solution if and only if

$$\int_{\mathcal{Y}} f \cdot u \, dx = 0 \quad \forall u \text{ solving (3.15)}. \quad (3.16)$$

With respect to the elastic periodic cell problems, that we consider here, the second statement applies. As noted in Remark 3.9 nonuniqueness is related to rigid body transformations in

the linearized setting. In the preceding section these were ruled out by virtue of the Dirichlet boundary conditions on  $\Gamma_D$ . In the current setting rotations are precluded by the periodic identification of displacements on opposing boundaries. Translations are however permitted and lead to a one dimensional family of solutions to the homogeneous equation (3.15). Consequently, for existence of a solution to the cell problem, we need to require that

$$\int_{\mathcal{Y}} f \cdot u \, dx = 0 \quad \forall u \equiv c, \quad c \in \mathbb{R}.$$

Furthermore we can identify a unique solution by restricting the trial space to displacements with vanishing component wise integral mean, defined as

$$H_{\text{per},0}^1 := \left\{ u \in H_{\text{per}}^1 : \theta^{-1} \int_{\mathcal{Y}} u \, dx = 0 \right\}. \quad (3.17)$$

The following property of  $\mathcal{Y}$ -periodic functions will be used later on.

**Lemma 3.13.** *In the mean the divergence of a  $\mathcal{Y}$ -periodic vector field  $\vartheta \in H_{\text{per}}^1(\mathcal{Y}; \mathbb{R}^2)$  vanishes on the unit cell  $\mathcal{Y}$ , i. e.  $\int_{\mathcal{Y}} \text{div } \vartheta \, dx = 0$ .*

*Proof.* By Gauss's theorem

$$\int_{\mathcal{Y}} \text{div } \vartheta \, dx = \int_{\partial \mathcal{Y}} \vartheta \cdot n \, da(x).$$

As  $\vartheta$  is  $\mathcal{Y}$ -periodic it has equal values on opposing sides of  $\mathcal{Y}$ . Due to the opposite sign of the normal, the contributions cancel each other and the assertion follows.  $\square$

### 3.5. Periodic homogenization

Periodic microstructures are at the core of this thesis and homogenization techniques will be used to decouple the strongly separated macroscopic and microscopic scales. We therefore recapitulate the theory of homogenization for an elasticity problem with a periodic material. As reference e. g. the textbooks [81, 314] can be consulted. Often a two-phase setting with a substitute material in  $D \setminus \mathcal{O}$  is considered to simplify the analysis but the results remain valid for the real perforated setting as well, cf. [133, 130].

To be precise let  $\delta \ll 1$  denote the microscopic scale and consider the possibly perforated unit cell  $\mathcal{Y} \subseteq D^{\mathcal{Y}} = [0, 1]^2$ . By scaling and placing copies of this cell on a discrete lattice, we obtain the full, microstructured domain  $\mathcal{O}^\delta := \bigcup_{c_i \in \mathbb{Z}^2} \delta(c_i + \mathcal{Y})$ , cf. Figure 1.2. In this situation the working domain  $D$  simply corresponds to the unperforated domain. The elasticity tensor is assumed to be  $\mathcal{Y}$ -periodic, s. t. it is enough to specify its values on  $\mathcal{Y}$ . We denote it by  $C^\delta(x) := C(\frac{x}{\delta})$  to explicitly state the microscopic dependence. The scaled argument is now used as a new distinct variable  $y := \frac{x}{\delta}$ , called *fast* variable. It reflects the rapid oscillations, in contrast to the *slow* variable  $x$ , acting on the macroscale. At this point the assumption of scale separation justifies an independent treatment of the algebraically related variables.

The setting of the elasticity problem laid out in the preceding sections is not substantially altered by the introduction of the microscopic dependence. In particular, for fixed  $\delta$ , there exists a unique solution  $u^\delta$ , which now inherits the microscopic dependence. By virtue of the Lax-Milgram lemma the solution is bounded. Considering a sequence of scaling parameters

$\delta \rightarrow 0$  thus leads to a sequence of problems with a corresponding sequence of solutions, still denoted by  $u^\delta$  to keep the notation simple. For once assume that due to boundedness a weakly converging subsequence, still denoted by  $u^\delta$ , can be extracted s. t.  $u^\delta \rightharpoonup u^*$ . In the two-phase setting this is straightforward, whereas in the perforated case some extra reasoning is required as each member of the sequence lives in its own space due to the varying domains. Furthermore observe that  $C^\delta \rightharpoonup \bar{C} := \theta^{-1} \int_{\mathcal{Y}} C^\delta dy$  by components. In general this however does not imply convergence of the product  $C^\delta \varepsilon[u^\delta] \rightharpoonup \bar{C} \varepsilon[u^*]$ . The challenging task therefore is to find an equation which is actually solved by  $u^*$ . This will then allow to extract material properties not depending on  $\delta$  anymore and to properly define a corresponding effective elasticity tensor  $C^*$ .

### 3.5.1. Derivation of the homogenized equation

To get an idea of how the solution behaves for  $\delta \rightarrow 0$ , an asymptotic analysis is done using a power series approach for  $u^\delta$ , i. e.

$$u^\delta(x) = \sum_{m=0}^{\infty} \delta^m u^{(m)}(x, y). \quad (3.18)$$

Here we assume that the solution depends on both  $x$  and  $y$  and inherits the  $\mathcal{Y}$ -periodicity in  $y$ . We are going to plug the series into the elasticity PDE (3.13). Therefore first observe that for components  $u_i$ ,  $i \in \{1, 2\}$ , of any displacement vector

$$\nabla_x (u_i(x, y)) = (\nabla_x u_i + \delta^{-1} \nabla_y u_i)(x, y)$$

holds due the definition of  $y$ . Here  $\nabla_x$  and  $\nabla_y$  denote the gradient vector w. r. t. the first and the second argument respectively. Therefore

$$\begin{aligned} C^\delta(x) \varepsilon[u^\delta(x)] &= \sum_{m=0}^{\infty} C(y) \delta^m \left( D_x u^{(m)} + \delta^{-1} D_y u^{(m)} \right)(x, y) \\ &= \delta^{-1} C(y) \varepsilon_y[u^{(0)}](x, y) \\ &\quad + \sum_{m=0}^{\infty} \delta^m C(y) \left( \varepsilon_x[u^{(m)}] + \varepsilon_y[u^{(m+1)}] \right)(x, y) \end{aligned}$$

holds with Jacobians  $D_x$ ,  $D_y$ , and linearized strain tensors  $\varepsilon_x$ ,  $\varepsilon_y$ , referring likewise to the first and the second argument respectively. We now take the divergence and obtain

$$\begin{aligned} \{\operatorname{div} C^\delta \varepsilon[u^\delta]\}(x) &= -\delta^{-2} \left\{ \operatorname{div}_y C \varepsilon_y[u^{(0)}] \right\}(x, y) \\ &\quad - \delta^{-1} \left\{ \operatorname{div}_y C \left( \varepsilon_x[u^{(0)}] + \varepsilon_y[u^{(1)}] \right) + \operatorname{div}_x C \varepsilon_y[u^{(0)}] \right\}(x, y) \\ &\quad - \sum_{m=0}^{\infty} \delta^m \left\{ \operatorname{div}_y C \left( \varepsilon_x[u^{(m+1)}] + \varepsilon_y[u^{(m+2)}] \right) \right. \\ &\quad \left. + \operatorname{div}_x C \left( \varepsilon_x[u^{(m)}] + \varepsilon_y[u^{(m+1)}] \right) \right\}(x, y). \end{aligned}$$

Due to the main equation of the periodic elasticity problem (3.13), the above expression must be equal to  $f(x)$ . We equate equal  $\delta$ -powers and focus on dominant powers for  $\delta \rightarrow 0$ . For  $\delta^{-2}$  we get

$$-\operatorname{div}_y C \varepsilon_y [u^{(0)}] (x, y) = 0 \quad \text{in } \mathcal{Y}, \quad (3.19)$$

which is a periodic cell problem in  $y$  only, with  $x$  acting as a parameter. From Theorem 3.12 in the preceding section we know that constant displacements, which may now depend on  $x$ , are solutions. Thus  $u^{(0)}(x, y) \equiv u^*(x)$  with some function  $u^*$  independent of  $y$  solves (3.19). Plugging this into the  $\delta^{-1}$ -equation and using  $\varepsilon_y[u^*] = 0$  yields

$$-\operatorname{div}_y C(y) \varepsilon_y [u^{(1)}(x, y)] = \operatorname{div}_y C(y) \varepsilon_x [u^*(x)] \quad \text{in } \mathcal{Y}. \quad (3.20)$$

This again is a periodic cell problem in  $y$ , but this time with a nontrivial, yet known, right hand side. In virtue of Theorem 3.12 the equation has a solution if the solvability condition (3.16) is satisfied. Therefore we take the  $y$ -constant test function  $\vartheta(x) \equiv c$  and obtain

$$\int_{\mathcal{Y}} \operatorname{div}_y C(y) \varepsilon_x [u^*(x)] \cdot \vartheta(x) \, dy = c \int_{\mathcal{Y}} \operatorname{div}_y C(y) \varepsilon_x [u^*(x)] \cdot \mathbf{1} \, dy = 0. \quad (3.21)$$

Here the second integral vanishes component wise in virtue of Lemma 3.13. Thus equation (3.20) has a solution, which is unique when taken from  $H_{\text{per},0}^1(\mathcal{Y}; \mathbb{R}^2)$ . We use an approach with separated variables, reading

$$u^{(1)}(x, y) = \sum_{i,j=1}^2 (\varepsilon_x [u^*(x)])_{ij} \omega_{ij}(y), \quad (3.22)$$

where each entry of  $\varepsilon_x [u^*(x)]$  acts as a coefficient in front of unknown displacement vectors  $\omega_{ij}: \mathcal{Y} \rightarrow \mathbb{R}^2$  in  $y$ . Plugging into (3.20) yields

$$\operatorname{div}_y C(y) \sum_{i,j=1}^2 (\varepsilon_x [u^*(x)])_{ij} (\varepsilon_{ij} + \varepsilon_y [\omega_{ij}(y)]) = 0 \quad \text{in } \mathcal{Y},$$

where  $\varepsilon_{ij} := \frac{1}{2} (e_i \otimes e_j + e_j \otimes e_i)$ . Here  $e_i, e_j$  are canonical basis vectors in  $\mathbb{R}^2$  and the tensor product for two vectors  $v, w \in \mathbb{R}^d$  is defined via  $(v \otimes w)_{ij} = v_i w_j$ . As such,  $\varepsilon_{ij}$  constitute a basis of the matrix space  $\mathbb{R}_{\text{sym}}^{2 \times 2}$ . To solve the problem in  $\mathcal{Y}$ , independent of  $x$ , thus the set of problems

$$\left\{ \begin{array}{l} \operatorname{div}_y C(y) (\varepsilon_{ij} + \varepsilon_y [\omega_{ij}(y)]) = 0 \quad \text{in } \mathcal{Y}, \\ \omega_{ij} \in H_{\text{per},0}^1(\mathcal{Y}; \mathbb{R}^2), \end{array} \right\} \quad i, j = 1, 2 \quad (3.23)$$

has to be solved. These problems are often referred to as *cell problems* in homogenization and  $\omega_{ij}$  are called *first order correctors*. Finally the  $\delta^0$ -equation reads

$$\begin{aligned} -\operatorname{div}_y C(y) \varepsilon_y [u^{(2)}(x, y)] &= \operatorname{div}_y C(y) \varepsilon_x [u^{(1)}(x, y)] \\ &\quad + \operatorname{div}_x C(y) \left( \varepsilon_x [u^*(x)] + \varepsilon_y [u^{(1)}(x, y)] \right) \\ &\quad + f(x). \end{aligned}$$



Again, for solvability the right hand side has to vanish when integrated against a  $y$ -constant test function  $\vartheta(x)$ . For the first term the same argumentation as in (3.21) applies and the condition simplifies to

$$-\operatorname{div}_x \left( \int_{\mathcal{Y}} C(y) \left( \varepsilon_x[u^*(x)] + \varepsilon_y[u^{(1)}(x, y)] \right) dy \right) = \int_{\mathcal{Y}} f(x) dy. \quad (3.24)$$

We now insert (3.22) and obtain the *homogenized equation*

$$-\operatorname{div}_x C^* \varepsilon_x[u^*(x)] = \theta f(x) \quad \text{in } D \quad (3.25)$$

with the *homogenized elasticity tensor*

$$C_{ijkl}^* := \int_{\mathcal{Y}} C_{ijkl}(y) + C(y) \varepsilon_y[\omega_{kl}(y)] : \varepsilon_{ij} dy. \quad (3.26)$$

The homogenized equation (3.25) is a purely macroscopic problem for the macroscopic displacement part  $u^*$ , which can be equipped with typical boundary conditions as discussed in Section 3.1. It is well-posed as long as the assumptions of Section 3.2 are not violated for the elasticity tensor  $C^*$ , which will be discussed in the next section. Note that (3.25) is defined on the whole domain  $D$  because  $C^*$  is constant, in contrast to the perforated problem on  $\mathcal{O}^\delta$  involving  $C^\delta$ . For  $f$  the assumed extension to  $D$  is used. The additional scaling factor  $\theta$  reflects the fact that volume forces only affect the volumetric part of the full domain. Microscopic influence enters only implicitly via the homogenized elasticity tensor  $C^*$ , whose coefficients can be computed self-containedly from the correctors  $\omega_{ij}$ , solving microscopic cell problems. Note that  $C^*$  does not depend on the macroscopic domain, the source term  $f$ , and the macroscopic boundary conditions. Using  $\omega_{ij}$  and  $u^{(0)} = u^*$  allows to set up  $\tilde{u} := u^{(1)}$  via (3.22), which means that in view of the power series approach (3.18) an approximation of  $u^\delta$  up to first order was established.

### 3.5.2. Properties of the homogenized elasticity tensor

The obtained homogenized elasticity tensor is defined by its entries given in (3.26). They can be written equivalently as

$$C_{ijkl}^* := \int_{\mathcal{Y}} C(y) (\varepsilon_{ij} + \varepsilon_y[\omega_{ij}(y)]) : (\varepsilon_{kl} + \varepsilon_y[\omega_{kl}(y)]) dy \quad (3.27)$$

by observing that the additional term  $\int_{\mathcal{Y}} C(y) (\varepsilon_{kl} + \varepsilon_y[\omega_{kl}(y)]) : \varepsilon_y[\omega_{ij}(y)] dy$  is in fact a weak formulation of the periodic cell problem (3.23) and therefore vanishes. From (3.27) one can immediately read off the symmetry of  $C^*$  w. r. t. interchanging the index pairs  $(i, j)$  and  $(k, l)$ . The basis matrices  $\varepsilon_{ij}$  are symmetric by construction which leads to coinciding correctors  $\omega_{ij} = \omega_{ji}$  of (3.23). Therefore  $C^*$  is also symmetric w. r. t. interchanging  $i, j$  and  $k, l$  respectively. The entries of  $C^*$  are moreover bounded as in view of (3.26)  $\omega_{ij} \in H_{\text{per},0}^1(\mathcal{Y}; \mathbb{R}^2)$  are bounded solutions of cell problems and the entries of  $C$  are bounded by assumption, thus  $C^* \in L^\infty(D; \mathbb{R}^{2^4})$ . Finally also ellipticity is preserved for  $C^*$ . To this end let  $X \in \mathbb{R}_{\text{sym}}^{2 \times 2}$  be given. Then  $C^* X : X = \int_{\mathcal{Y}} C(y) \tilde{X} : \tilde{X} dy$  with  $\tilde{X} := \sum_{ij} X_{ij} (\varepsilon_{ij} + \varepsilon_y[\omega_{ij}(y)])$  and by ellipticity properties of  $C$  we have  $C^* X : X \geq c \int_{\mathcal{Y}} \tilde{X} : \tilde{X} \geq 0$ . In case  $C^* X : X = 0$ , it follows that

$\tilde{X} = \varepsilon_y \left[ \sum_{ij} X_{ij} (\varepsilon_{ij} y + \omega_{ij}(y)) \right] = 0$ , which implies  $\sum_{ij} X_{ij} \varepsilon_{ij} y - S y = - \sum_{ij} X_{ij} \omega_{ij}(y) + b$  with a skew symmetric matrix  $S \in \mathbb{R}^{2 \times 2}$  and a constant vector  $b \in \mathbb{R}^2$ . The right hand side is  $\mathcal{Y}$ -periodic. On the left hand side a linear mapping is spanned by appropriate basis matrices, which can only be  $\mathcal{Y}$ -periodic in the trivial situation when  $S = 0$  and  $X = 0$ . This proves positive definiteness of  $C^*$  from which ellipticity can be deduced.

### 3.5.3. Remarks as to rigorous justifications

The heuristic power series approach sketched above produces well-posed and decoupled microscopic and homogenized macroscopic elasticity problems. However it does not provide a rigorous justification as to whether the obtained homogenized problem coincides with the limiting problem for  $\delta \rightarrow 0$ . Several techniques have been established to prove this fact. We focus on the concept of two-scale convergence here as it fits to the framework of the two-scale shape optimization model and only touch on further more general methods.

**Two-scale convergence.** The framework of two-scale convergence was introduced in [306] and is presented clearly laid out in [16]. It is specifically tailored to study functions with a periodic, high frequency oscillatory part and is able to handle perforated domains. In addition to defining the limiting function, important properties like compactness and error estimates can be proven. Furthermore the technique allows to derive the homogenized equation in a self-contained way.

**Definition 3.14** (Two-scale convergence). *A sequence of functions  $u^\delta \in L^2(D; \mathbb{R}^2)$  is said to two-scale converge to a limit  $u \in L^2(D \times \mathcal{Y}; \mathbb{R}^2)$  if for any test function  $\vartheta \in C_c^\infty(D; C_{\text{per}}^\infty(\mathcal{Y}; \mathbb{R}^2))$  there holds*

$$\lim_{\delta \rightarrow 0} \int_D u^\delta(x) \vartheta(x, \frac{x}{\delta}) dx = \int_D \int_{\mathcal{Y}} u(x, y) \vartheta(x, y) dy dx.$$

Here  $C_c^\infty$  and  $C_{\text{per}}^\infty$  denote the spaces of smooth functions with compact support or periodicity, respectively. The following statement gives an eligible compactness property. Namely bounded sequences in  $L^2$  are relatively compact w. r. t. the notion of two-scale convergence.

**Theorem 3.15** (Compactness). *Let  $u^\delta \in L^2(D; \mathbb{R}^2)$  be a bounded sequence. Then there is a subsequence, still denoted by  $u^\delta$ , and a limit  $u \in L^2(D \times \mathcal{Y}; \mathbb{R}^2)$ , s. t.  $u^\delta$  two-scale converges to  $u$ .*

Based on this result the following statement is the important point in view of the microstructured elasticity problem studied here.

**Theorem 3.16.** *Let  $u^\delta \in H^1(\mathcal{O}^\delta; \mathbb{R}^2)$  be a bounded sequence. Then there are extensions of  $u^\delta$  and  $\varepsilon[u^\delta]$ , that, up to a subsequence, two-scale converge to limits  $u^*(x) \chi_{\mathcal{Y}}(y)$  with  $u^* \in H^1(D; \mathbb{R}^2)$  and  $(\varepsilon_x[u^*(x)] + \varepsilon_y[\tilde{u}(x, y)]) \chi_{\mathcal{Y}}(y)$  with  $\tilde{u} \in L^2(D; H_{\text{per},0}^1(\mathcal{Y}; \mathbb{R}^2))$ .*

Now the concept of two-scale convergence can be applied to the homogenization problem in elasticity. Due to boundedness of the solution  $u^\delta$  to the usual elasticity problem (3.10), and by virtue of Theorem 3.16, there are subsequences of  $u^\delta$  and  $\varepsilon[u^\delta]$ , extended to the whole domain  $D$ , that two-scale converge to limits  $u^*(x) \chi_{\mathcal{Y}}(y)$  and  $(\varepsilon_x[u^*(x)] + \varepsilon_y[\tilde{u}(x, y)]) \chi_{\mathcal{Y}}(y)$

respectively. Starting from the governing equations (3.2) again a weak formulation is derived, but this time using a special test function. Similar to the approximation of  $u^\delta$  at hand, we choose  $\vartheta^*(x) + \delta\tilde{\vartheta}(x, \frac{x}{\delta})$  with  $\vartheta^* \in C_c^\infty(D; \mathbb{R}^2)$  and  $\tilde{\vartheta} \in C_c^\infty(D; C_{\text{per}}^\infty(\mathcal{Y}; \mathbb{R}^2))$ , which after multiplication and integration by parts yields

$$\begin{aligned} & \int_{\mathcal{O}^\delta} C(\frac{x}{\delta}) \varepsilon[u^\delta(x)] : (\varepsilon_x[\vartheta^*(x)] + \varepsilon_y[\tilde{\vartheta}(x, \frac{x}{\delta})] + \delta\varepsilon_x[\tilde{\vartheta}(x, \frac{x}{\delta})]) \, dx \\ &= \int_{\mathcal{O}^\delta} f(x) \cdot (\vartheta^*(x) + \delta\tilde{\vartheta}(x, \frac{x}{\delta})) \, dx. \end{aligned}$$

The term  $C(\frac{x}{\delta}) (\varepsilon_x[\vartheta^*(x)] + \varepsilon_y[\tilde{\vartheta}(x, \frac{x}{\delta})])$  can be regarded as an admissible test function for two-scale convergence of  $\varepsilon[u^\delta(x)]$ . It is less regular than required in the definition but the results remain valid as shown in [16]. Thus it is possible to pass to the two-scale limit on both sides, yielding

$$\begin{aligned} & \int_D \int_{\mathcal{Y}} C(y) (\varepsilon_x[u^*(x)] + \varepsilon_y[\tilde{u}(x, y)]) : (\varepsilon_x[\vartheta^*(x)] + \varepsilon_y[\tilde{\vartheta}(x, y)]) \, dy \, dx \\ &= \int_D \int_{\mathcal{Y}} f(x) \cdot \vartheta^*(x) \, dy \, dx. \end{aligned} \tag{3.28}$$

This weak formulation is in fact amenable to the Lax-Milgram lemma when using appropriate spaces. To this end note first that (3.28) remains valid for any  $(\vartheta^*, \tilde{\vartheta})$  from the product space  $H_{\Gamma_D}^1(D; \mathbb{R}^2) \times L^2(D; H_{\text{per},0}^1(\mathcal{Y}; \mathbb{R}^2))$  by a density argument. Next this space is endowed with the norm  $\|\varepsilon[\vartheta^*] + \varepsilon_y[\tilde{\vartheta}]\|_{0,2,D \times \mathcal{Y}}$  and a bilinear form is defined by the left hand side of (3.28). It is bounded and coercive due to ellipticity of  $C$  and Korn's inequality, Theorem 3.7. The linear form on the right hand side was not substantially altered. On the whole the Lax-Milgram lemma guarantees a unique solution of the weak problem (3.28) and consequently the whole sequences  $u^\delta$  and  $\varepsilon[u^\delta]$  converge.

Integrating (3.28) by parts in  $x$  w.r.t.  $\varepsilon_x[\vartheta^*(x)]$  and in  $y$  w.r.t.  $\varepsilon_y[\tilde{\vartheta}(x, y)]$  produces equations (3.24) and (3.20). Using the same approach (3.22) for  $\tilde{u}$ , the homogenized equation (3.25) and the cell problems (3.23) are derived as before. Altogether the two-scale approach produces the homogenized equation and proves convergence of the functions involved in a single step.

Let us finally remark that the heuristic power series (3.18), in view of the findings from two-scale convergence, was indeed correct up to first order. More precisely, see [81, Chapter 1, Section 5.5] for details, the error to the solution with full microscopic dependence can be quantified.

**Theorem 3.17.** *Under the additional assumption that  $u^* \in W^{2,\infty}(D; \mathbb{R}^2)$ , and by using appropriate extensions, there holds*

$$\|u^\delta(x) - u^*(x) - \delta\tilde{u}(x, \frac{x}{\delta})\|_{1,2,D} \leq c\sqrt{\delta}.$$

**Further approaches.** The *oscillating test function method*, sometimes also called *energy method*, was devised by Murat and Tartar, see [302] for an English translation of the original work from 1977. It is not restricted to a periodic setting, but in this context it shows similarities to the previous expositions. Starting from the weak formulation (3.10) with  $\varepsilon[u^\delta]$  and  $C^\delta$  it

is not possible to directly pass to the limit as a product of two weakly converging sequences is involved. This difficulty can be obviated by using a specially devised sequence of test functions. The technique is therefore also known as a *compensated compactness* result. In the present situation one chooses

$$\vartheta^\delta\left(\frac{x}{\delta}\right) = \vartheta^*(x) + \delta \sum_{i,j=1}^2 (\varepsilon_x[\vartheta^*(x)])_{ij} \omega_{ij}\left(\frac{x}{\delta}\right)$$

with  $\vartheta^* \in C_c^\infty(D; \mathbb{R}^2)$  and cell solutions  $\omega_{ij} \in H_{\text{per},0}^1(\mathcal{Y}; \mathbb{R}^2)$  as defined before. After some calculation the equation can be rearranged to produce a product of  $u^\delta$  and a weakly converging sequence. By Rellich's theorem, cf. [31] as to the perforated setting, there exists a subsequence of  $u^\delta$  that strongly converges in  $L^2$  and this enables passing to the limit. Finally a problem, similar to the homogenized equation above in weak form, is achieved. As it allows for a unique solution the whole sequences converge and the homogenization result is proven.

Ultimately a fully distinct notion of convergence for homogenization problems as presented here was established under the name of *H-convergence*, see [302]. It is a generalization of *G-convergence*, devised by Spagnolo in [379], to possibly non symmetric operators. The definition is given implicitly through the postulated mutual convergence of the elasticity solution and the microstructured material properties.

**Definition 3.18** (H-convergence). *Let  $u^\delta \in H_{\Gamma_D}^1(\mathcal{O}^\delta; \mathbb{R}^2)$  be a sequence of solutions to the elasticity problem (3.10) involving the elasticity tensor  $C^\delta$ . The sequence  $C^\delta$  is said to H-converge to a limit  $C^*$  if  $u^\delta$  satisfies*

$$\begin{cases} u^\delta \rightharpoonup u^* & \text{weakly in } H_{\Gamma_D}^1(D; \mathbb{R}^2), \\ C^\delta \varepsilon[u^\delta] \rightharpoonup C^* \varepsilon[u^*] & \text{weakly in } L^2(D; \mathbb{R}_{\text{sym}}^{2 \times 2}), \end{cases}$$

where  $u^*$  is the solution of the homogenization equation (3.25) corresponding to the effective tensor  $C^*$ .

It can be shown that the definition of the H-limit  $C^*$  is independent of the domain, the right hand side  $f$  and the boundary conditions. Moreover important properties like compactness, locality of the limit, and convergence of the associated energy density  $C^* \varepsilon[u^*] : \varepsilon[u^*]$  can be shown, cf. [302]. Here the proofs often make use of the compensated compactness theory.

## 3.6. Numerical solution

In this thesis numerical experiments for the optimization of microstructured materials are conducted. Therefore it is necessary to transfer the appearing functions and governing equations of linearized elasticity into a discrete setting, involving only finitely many degrees of freedom. Two different methods will be used simultaneously, namely the finite element method on the macroscopic scale and the boundary element method on the microscopic scale.

### 3.6.1. Finite element method

For the presentation we focus on the problem setting relevant for this work, i. e. a discretization of the linearized elasticity problem in two space dimensions (3.10). A reference giving exhaustive

details is e. g. the textbook [128]. The finite element method is based on the weak formulation of the partial differential equations. Known as the *Galerkin method*, the key idea is to replace the trial and test space, here  $H_{\Gamma_D}^1(\mathcal{O}; \mathbb{R}^2)$ , by a finite dimensional subspace  $\mathcal{V}_h$ . The discretized problem is then immediately established.

**Definition 3.19** (Discrete elasticity problem). *Find  $u_h^0 \in \mathcal{V}_h$ , s. t.  $u_h = u_h^0 + u_h^\vartheta$  satisfies*

$$a(\mathcal{O}; u_h, \vartheta_h) = l(\mathcal{O}; \vartheta_h) \quad \forall \vartheta_h \in \mathcal{V}_h, \quad (3.29)$$

with the bilinear and linear form as defined in (3.9).

Discretized quantities will always be denoted by the subscript  $h$ , hinting at a mesh size function  $h: \mathcal{O} \rightarrow \mathbb{R}$  to be defined below. Because  $\mathcal{V}_h$  was chosen as a subspace, all reasoning from Section 3.3 remains valid. Especially existence and uniqueness of a discrete solution  $u_h$  to (3.10) is ensured. The task therefore is to construct appropriate spaces  $\mathcal{V}_h$ , referred to as *finite element spaces*. To begin with, a partition  $\mathcal{M}_h$  of the domain  $\mathcal{O} \subset \mathbb{R}^2$  under consideration, referred to as *computational grid*, into finitely many subsets  $E \in \mathcal{M}_h$ , called *finite elements*, is required. For the time being we assume that  $E$  are nondegenerate polygons, spanned by *vertices*  $v_i \in \mathcal{O}$  connected by *edges*. The mesh size function  $h_E = h(x)$  for  $x \in E$  is then defined as the longest edge of the element  $E$ . We furthermore require

- (1)  $\bar{\mathcal{O}} = \bigcup_{E \in \mathcal{M}_h} E$ , therefore  $\mathcal{O}$  is assumed to be polygonally bounded,
- (2) distinct  $E_1, E_2 \in \mathcal{M}_h$  do not overlap, i. e.  $\overset{\circ}{E}_1 \cap \overset{\circ}{E}_2 = \emptyset$ ,
- (3) any edge of any element  $E_1 \in \mathcal{M}_h$  is either part of the domain boundary  $\Gamma$  or an edge of another element  $E_2 \in \mathcal{M}_h$ , and
- (4) each element  $E \in \mathcal{M}_h$  is *regular*, i. e. there exists a constant  $c > 0$ , s. t.  $\frac{h_E}{b_E} \leq c$ , where  $b_E$  denotes the maximal diameter of a ball contained in  $E$ .

Next a discrete approximation of the continuous quantities is to be constructed on the grid elements. Here we resort to globally continuous and piecewise polynomial functions.

**Definition 3.20** (Finite element space). *Let  $\mathcal{P}_k(E)$  be the space of polynomials of degree up to  $k$  on the domain  $E$ . The vector-valued finite element space of globally continuous and piecewise polynomial functions in each component is defined as*

$$\mathcal{V}_h^{(k)}(\mathcal{M}_h) = \{ \vartheta_h \in C^0(\mathcal{M}_h; \mathbb{R}^2) : (\vartheta_h \cdot e_i)|_E \in \mathcal{P}_k(E) \quad \forall E \in \mathcal{M}_h, \quad i = 1, 2 \} .$$

From a computational point of view it is important that all finite element functions from  $\mathcal{V}_h^{(k)}(\mathcal{M}_h)$  are composable from a finite set of basis functions, which should ideally be locally supported and easy to evaluate. Therefore note that a polynomial from  $\mathcal{P}_k(E)$  on an element  $E$  is uniquely determined by a set of prescribed values on a finite number of distinct points  $\xi_k \in E$ , also referred to as *nodes*. When located on edges, these nodes are shared among adjacent elements, ensuring continuity of the global finite element function. Denoting by  $\mathcal{N}_h$  the union of all nodes  $\xi_k$  on all  $E \in \mathcal{M}_h$  and by  $N := |\mathcal{N}_h|$  its cardinality, this set represents the overall degrees of freedom for a discrete function. For the setting at hand *Lagrangian* basis functions are well suited. They are characterized by

$$\psi_j^i(\xi_k) = \delta_{jk} e_i \quad \forall \xi_k \in \mathcal{N}_h, \quad i = 1, 2,$$

i. e. each basis function attains value 1 for one of the components at a single node while it is 0 for all other nodes and in the other components. Functions from  $\mathcal{V}_h^{(k)}(\mathcal{M}_h)$  can thus be written as a linear combination of those basis functions. For this purpose an interpolation operator is defined.

**Definition 3.21** (Lagrangian interpolation). *Let  $\vartheta: \mathcal{O} \rightarrow \mathbb{R}^2$  be an arbitrary function, then its Lagrangian interpolating polynomial of degree  $k$  is defined as*

$$\mathcal{I}_h^{(k)}[\vartheta](x) = \sum_{i=1}^2 \sum_{j=1}^N \Theta_j^i \psi_j^i(x), \quad x \in \mathcal{O},$$

where the entries of the associated coefficient vector  $(\Theta_j^i)_{j=1, \dots, N}^{i=1, 2}$  are given by the nodal evaluations  $\Theta_j^i = \vartheta(\xi_j) \cdot e_i$  and  $\psi_j^i \in \mathcal{V}_h^{(k)}(\mathcal{M}_h)$ .

By construction the interpolation of any function  $\vartheta_h \in \mathcal{V}_h^{(k)}(\mathcal{M}_h)$  is exact. For functions of different kind suitable approximations in the chosen discrete spaces are obtained. In particular we define the discretized right hand side and boundary conditions by  $f_h := \mathcal{I}_h^{(k)}[f]$ ,  $g_h := \mathcal{I}_h^{(k)}[g]$ , and  $u_h^\partial := \mathcal{I}_h^{(k)}[u^\partial]$ . Using the basis functions the discrete problem (3.29) can be cast into a linear system of equations. To this end we define the *mass* and the *stiffness* matrix as

$$M := \begin{pmatrix} M^{(1,1)} & 0 \\ 0 & M^{(2,2)} \end{pmatrix} \quad \text{and} \quad L := \begin{pmatrix} L^{(1,1)} & L^{(1,2)} \\ L^{(2,1)} & L^{(2,2)} \end{pmatrix},$$

respectively, with the blocks given by

$$M_{ij}^{(k,l)} := \int_{\mathcal{O}} \psi_i^k(x) \cdot \psi_j^l(x) \, dx \quad \text{and} \quad L_{ij}^{(k,l)} := \int_{\mathcal{O}} C\varepsilon[\psi_i^k(x)] : \varepsilon[\psi_j^l(x)] \, dx. \quad (3.30)$$

Likewise a mass matrix for boundary integrals  $M^\partial$  is defined by integrating over  $\Gamma$  in (3.30). All those integrals are usually evaluated by using numerical quadrature. With these definitions the discretized elasticity problem (3.29) is equivalent to the linear system of equations  $LU = MF + M^\partial G$  where the coefficient vectors  $U$ ,  $F$ , and  $G$  of the corresponding finite element functions  $u_h$ ,  $f_h$ , and  $g_h$  contain entries for the two components of the vector-valued functions in a concatenated way.

**Remark 3.22.** From the definition of the matrices some properties of the linear system of equations can be read off immediately.

1. The diagonal blocks are symmetric, i. e.  $M^{(i,i)} = (M^{(i,i)})^\top$ ,  $L^{(i,i)} = (L^{(i,i)})^\top$ ,  $i = 1, 2$ .
2. For  $M$  the two diagonal blocks moreover coincide, i. e.  $M^{(1,1)} = M^{(2,2)}$ .
3. The off-diagonal blocks of  $M$  vanish because entries in different components never meet in (3.30).
4. The off-diagonal blocks of  $L$  appear transposed to each other, i. e.  $L^{(1,2)} = (L^{(2,1)})^\top$ .
5. Altogether  $M$  and  $L$  are symmetric matrices.

6. The structure of  $M$  and  $L$  is sparse because distant, locally supported basis functions do not attain nonzero values simultaneously.

So far we did not comment on the boundary conditions of the elasticity problem, which we now briefly make up for. Inhomogeneous Dirichlet boundary conditions are treated in the same way as in the continuous setting, i. e. we consider  $u_h = u_h^0 + u_h^\partial$ , rearrange the equation to yield  $LU^0 = MF - LU^\partial$ , and solve for  $U^0$  with homogeneous Dirichlet conditions. To take into account homogeneous Dirichlet conditions the corresponding degrees of freedom have to be eliminated from the linear system of equations because their values are fixed a priori. This can be achieved by setting all entries in the appropriate rows and columns of  $L$  for both components to 0 and the diagonal entries of  $L^{(1,1)}$ ,  $L^{(2,2)}$  corresponding to Dirichlet nodes to 1. Respective entries in  $U$  are set to 0 a priori. This approach avoids a reindexing of the remaining real degrees of freedom while it accepts an unnecessarily larger system matrix in return. Similarly periodic boundary conditions are handled. Here the degrees of freedom on opposing sides of the domain are identified with each other. One part has to be eliminated, but their contributions to the matrices have to be added to entries of their remaining counterparts. This is done by adding respective rows and columns to the rows and columns of the corresponding counterparts before they are set to 0, except for value 1 on the main diagonal of  $L$ , as described before.

The approximation of continuous functions by discrete finite element functions naturally comes along with a certain deviation. Quantifying this approximation error is of paramount importance in the theory of the finite element method. The following theorem lays the foundations for such results.

**Theorem 3.23** (Cea's lemma). *There exists a constant  $c > 0$ , independent of the chosen finite element space  $\mathcal{V}_h$ , s. t.*

$$\|u - u_h\|_{1,2,\mathcal{O}} \leq c \inf_{\vartheta_h \in \mathcal{V}_h} \|u - \vartheta_h\|_{1,2,\mathcal{O}}.$$

In essence Cea's lemma asserts that the error of the discretized solution is proportional to the least approximation discrepancy achievable within the chosen finite element space. Therefore interpolation error estimates play a crucial role for devising further results. Here we restate [128, Theorem 3.1.6], adapted to the setting at hand.

**Theorem 3.24** (Interpolation error estimate). *Let  $m, k \in \mathbb{N}$  and  $p \in \mathbb{N} \cup \{\infty\}$  be given numbers, for which  $(k + 1)p > d$  and  $k + 1 \geq m$  hold. Then there exists a constant  $c > 0$ , depending on the chosen finite element space  $\mathcal{V}_h$ , s. t. for all  $E \in \mathcal{M}_h$  and all  $\vartheta \in W^{k+1,p}(E; \mathbb{R}^d)$*

$$\|\vartheta - \mathcal{I}_h \vartheta\|_{m,p,E} \leq c h_E^{k+1-m} |\vartheta|_{k+1,p,E}.$$

The postulated inequalities are due to required Sobolev embeddings. In view of Cea's lemma an  $H^1$ -estimate, i. e.  $m = 1$  and  $p = 2$ , is required. Under the assumptions made so far, the approximation of the elasticity solution fulfills  $u \in H_{\Gamma_D}^1(\mathcal{O}; \mathbb{R}^2)$ , i. e.  $d = 2$  and  $k = 0$ . Hence Theorem 3.24 is not applicable, unless higher regularity is assumed. In case  $u \in H^2(\mathcal{O}; \mathbb{R}^2)$ , e. g., one can immediately deduce

$$\|u - u_h\|_{1,2,\mathcal{O}} \leq c h |u|_{2,2,\mathcal{O}}. \quad (3.31)$$

Here  $h = \max_{E \in \mathcal{M}_h} h_E$  is a global measure of the mesh size. Alternatively, for  $u \in H^1(\mathcal{O}; \mathbb{R}^2)$  only, it is shown in [128, Theorem 3.2.3] that  $\lim_{h \rightarrow 0} \|u - u_h\|_{1,2,\mathcal{O}} = 0$  holds, via a density

argument. In particular those results guarantee convergence of the finite element method, i. e. they confirm the intuitive idea that an approximation improves as the grid is refined.

### 3.6.2. Boundary element method

The boundary element method is an entirely different approach. Although in the end finite elements are employed as well, the discretization only occurs at the boundary. For this reason the method became popular during the twentieth century when computational resources were limited. A historical overview can be found in [116]. In order to transform the elasticity problem into a boundary integral equation a fundamental solution is required. This is a set of vector-valued functions  $\hat{u}_1, \hat{u}_2 : \mathbb{R}^2 \times \mathbb{R}^2 \rightarrow \mathbb{R}^2$ , s. t.

$$-\operatorname{div}_x C(x) \varepsilon_x [\hat{u}_i(\xi, x)] = \delta(x - \xi) e_i, \quad i = 1, 2 \quad (3.32)$$

holds in the sense of distributions. Here  $\delta$ , for once, denotes the Dirac function. For the present setting of linearized elasticity in two space dimensions such fundamental solutions have been devised. They differ w. r. t. the material properties given by the elasticity tensor. In the isotropic case they read

$$\hat{u}_{ki}(\xi, x) = \frac{\lambda + \mu}{4\pi(\mu(\lambda + 2\mu))} \left( -\delta_{ki} \frac{\lambda + 3\mu}{\lambda + \mu} \ln|x - \xi| + \frac{(x_k - \xi_k)(x_i - \xi_i)}{|x - \xi|^2} \right),$$

where  $i \in \{1, 2\}$  denotes the index of the fundamental solution and  $k \in \{1, 2\}$  its component, cf. [384, p. 98]. For the anisotropic case in two space dimensions a complex logarithm can be employed and they are given by

$$\hat{u}_{ki}(\xi, x) = \frac{1}{2\pi} \sum_{t=1}^2 \operatorname{Re} \left\{ \sum_{n=1}^2 A_{kn} N_{nt} \ln(z_n(x - \xi)) \right\} d_{ti},$$

where  $z_n(x) = x_1 + p_n x_2$  maps  $x \in \mathbb{R}^2$  to the complex plane using calculated constants  $p_n \in \mathbb{C}$  and  $A_{kn}$ ,  $N_{nt}$ , and  $d_{ti}$  are appropriately chosen coefficients. The construction originates from [134], see [259, 182] for details of the derivation. Remarkably the derivation fails for isotropic materials, even when considered as a limiting case. However, numerical experiments show convergence of pointwise evaluations of the anisotropic fundamental solutions to those obtained for the isotropic case when approaching an isotropic configuration in the elasticity coefficients. Furthermore they behave adequately stable in this regime [259], s. t. both variants could be used within this thesis.

To make use of the fundamental solutions, the weak formulation (3.11) is considered again and integrated by parts once more, leading to

$$\int_{\mathcal{O}} f \cdot \vartheta \, dx = - \int_{\mathcal{O}} \operatorname{div} C\varepsilon[\vartheta] \cdot u \, dx + \int_{\Gamma} C\varepsilon[\vartheta] n \cdot u \, da(x) - \int_{\Gamma} C\varepsilon[u] n \cdot \vartheta \, da(x).$$

Next, the fundamental solutions are used in lieu of the test function  $\vartheta$  and their defining property (3.32) is employed for the first term on the right hand side. Rearranging yields

$$u_i(\xi) = \int_{\Gamma} C\varepsilon[u] n \cdot \hat{u}_i \, da(x) - \int_{\Gamma} C\varepsilon[\hat{u}_i] n \cdot u \, da(x) + \int_{\mathcal{O}} f \cdot \hat{u}_i \, dx \quad (3.33)$$



for  $i = 1, 2$  and  $\xi \in \mathcal{O}$ . This amounts to an explicit formula for the elasticity solution in terms of its Dirichlet and Neumann boundary values, known as *Somigliana identity* [378]. For  $\xi \in \Gamma$ , equation (3.33) is initially not defined due to the appearing singularities. It is however possible to prove that the integrals exist also in this case, see e. g. [207] and [259, 182] for further details. If in addition  $f \equiv 0$ , which will be the case for the numerical experiments in this work, a pure boundary integral equation is obtained. If not, a suitable approximation technique is described in [207, Section 9.5]. The boundary integral equation (3.33) can be expressed compactly as

$$u = V[t] - W[u] \quad \text{on } \Gamma \tag{3.34}$$

with the short notation  $t = C\varepsilon[u]n$  for the normal stresses on the boundary. Here  $V$  denotes the *single layer operator*, acting on the normal stresses, and  $W$  the *double layer operator*, acting on the displacements. Equation (3.34) is therefore also called *Dirichlet-to-Neumann map*. It can be shown that the boundary integral operators define linear, bounded, and coercive mappings

$$\begin{aligned} V: H^{-\frac{1}{2}}(\Gamma; \mathbb{R}^d) &\rightarrow H^{\frac{1}{2}}(\Gamma; \mathbb{R}^d), \\ W: H^{\frac{1}{2}}(\Gamma; \mathbb{R}^d) &\rightarrow H^{\frac{1}{2}}(\Gamma; \mathbb{R}^d), \end{aligned}$$

see [384, Section 6.7].

For a numerical treatment only quantities on the boundary have to be taken into account. As we assumed  $\mathcal{O}$  to be polygonally bounded, its boundary  $\Gamma$  therefore consists of vertices  $v_j \in \Gamma$ , connected by straight line segments. In this setting the finite element space  $\mathcal{V}_h^{(1)}(\Gamma)$  of piecewise linear and globally continuous functions can be considered, defining discretized displacements  $u_h$  and normal stresses  $t_h$  via the Lagrange interpolation  $\mathcal{I}_h^{(1)}$ . They are uniquely determined by their values on nodes  $\xi_j = v_j$ , which are called *collocation points* and coincide with the vertices here. After discretization the applications of the single and the double layer operator to basis functions, i. e.  $V[\psi_j^i]$  and  $W[\psi_j^i]$  respectively, have to be computed. In the special situation here, with a one dimensional integration domain, this can even be done analytically. Only the case where a nodal basis function needs to be integrated over the singularity is critical, especially for the double layer operator. Fortunately a trick, based on applying the operator to a rigid body motion, which has to yield a vanishing displacement, can be used to implicitly gain the correct entries, see [259, Section 6.4]. Requiring (3.34) to hold pointwise for all  $\xi_j \in \mathcal{N}_h$ , a linear system of  $dN$  equations is obtained. From the setup of the elasticity problem (3.2) one can see that on each  $\xi_j \in \mathcal{N}_h$  either the displacement  $u(\xi_j)$  or the normal stress  $t(\xi_j)$  is prescribed by a boundary condition, while the other has to be determined. This results in  $dN$  unknowns overall. If a mixed boundary value problem is considered, equation (3.34) has to be rearranged according to given and unknown values. As to the periodic cell problem (3.13), displacements and tensions on opposing sides of the cell are identified, reducing the number of unknowns. As the normal jumps in the corners of the domain, the nodes for normal stresses are duplicated at those positions, resulting in two independent degrees of freedom at a single vertex. The system is made solvable by adding equations for the component wise vanishing mean displacements, cf. (3.17).

The boundary integral equation (3.33) can furthermore be cast into a variational formulation by multiplying with appropriate test functions and additional integration. This allows to carry over the established theory of the finite element method. In particular, error estimates for the approximated displacements and normal stresses on the boundary  $\Gamma$  can be obtained. Via (3.33) convergence to the continuous solution is ensured for the full domain  $\mathcal{O}$ .



OPTIMIZING the shape of an elastic body is the next building block, which will be tackled in this chapter. The distinctive feature of such problems is that the variable to be optimized is the domain itself. Therefore appropriate means for varying the shape of an elastic domain have to be taken into account and relevant results from shape calculus will be outlined. To enable a mathematical treatment of the optimization task suitable cost functionals measuring the performance of a design need to be considered. These will usually incorporate the elastic displacement, determined as a solution of the underlying governing equations. Altogether a PDE constrained optimization problem is obtained, which will be studied via a Lagrangian formulation. The concepts will be applied to the classical compliance cost functional representing a global measure of rigidity. As it turns out, the resulting shape optimization problem is in general ill-posed and one needs to restrict or relax the space of admissible designs. In the latter case the sequential lamination construction provides a model for provable optimal shapes and will be presented in two space dimensions.

## 4.1. PDE constrained optimization

In this section we will gather all ingredients needed to ultimately deduce the shape derivative of the compliance cost functional. For this it is crucial that both the explicit dependence of the cost functional on the domain and the implicit dependence through the elasticity solution on this very domain are taken into account.

### 4.1.1. Shape calculus

Derivatives w. r. t. the domain  $\mathcal{O}$  will be required in subsequent sections and are therefore introduced rigorously here. For this purpose, first of all a notion for varying the domain's shape has to be established. We follow the *velocity method* here and refer to the textbook [146] for details. To provide local variations of the domain, a vector field  $V: \mathbb{R}^+ \times \bar{D} \rightarrow \mathbb{R}^2$  is considered. Furthermore we demand for  $\tau > 0$

- (1)  $t \mapsto V(t, x) \in \mathcal{C}^0([0, \tau]; \mathbb{R}^2)$  for all  $x \in \bar{D}$ ,
- (2)  $x \mapsto V(t, x) \in \mathcal{C}^{0,1}(\bar{D}; \mathbb{R}^2)$ , i. e. Lipschitz continuous, for all  $t \in [0, \tau]$ ,
- (3)  $V(t, x) \in T_x \partial D$  for all  $t \in [0, \tau]$  and  $x \in \partial D$ , i. e. the velocity vector is in the tangent space,

and denote the set of all vector fields fulfilling these assumptions by  $\mathcal{F}(D)$ . A family of transformations  $\phi: \mathbb{R}^+ \times \bar{D} \rightarrow \mathbb{R}^2$  with  $\phi(t, x) = x(t)$  is chosen from  $V \in \mathcal{F}(D)$  in such a way that the trajectory of a point  $x_0 \in D$  satisfies the ordinary differential equation

$$\begin{cases} \frac{d}{dt} x(t) = V(t, x(t)) & t \geq 0, \\ x(0) = x_0, \end{cases}$$

which has a unique solution due to the requirements (1) and (2). Denoting the deformed domain at time  $t$  by  $\mathcal{O}_t = \{\phi(t, x) : x \in \mathcal{O}\}$ , the shape derivative can be defined.

**Definition 4.1** (Eulerian shape derivative). *A functional  $\mathbf{J}$  has an Eulerian semiderivative at  $\mathcal{O}$  in the direction  $V \in \mathcal{F}(D)$  given by*

$$d_{\mathcal{O}}^E \mathbf{J}[\mathcal{O}](V) := \lim_{t \searrow 0} \frac{\mathbf{J}[\mathcal{O}_t] - \mathbf{J}[\mathcal{O}]}{t}$$

if the limit exists.

*It has an Eulerian derivative at  $\mathcal{O}$  if the Eulerian semiderivative exists for all directions  $V \in \mathcal{F}$  and the mapping  $V \mapsto d_{\mathcal{O}}^E \mathbf{J}[\mathcal{O}](V)$  is linear and continuous.*

A point of concern with this definition is that it depends on values of the chosen field  $V$  for  $t > 0$ . Moreover it will not satisfy the chain rule. Thus a stronger notion is required.

**Definition 4.2** (Hadamard shape derivative). *Let  $\bar{V} \in \mathcal{C}^{0,1}(D; \mathbb{R}^2)$  be a fixed vector field, constant in time. A functional  $\mathbf{J}$  has a Hadamard semiderivative at  $\mathcal{O}$  in the direction  $\bar{V}$  if the limit*

$$d_{\mathcal{O}}^H \mathbf{J}[\mathcal{O}](\bar{V}) := \lim_{\substack{V \in \mathcal{F}(D) \\ V(0) = \bar{V} \\ t \searrow 0}} \frac{\mathbf{J}[\mathcal{O}_t] - \mathbf{J}[\mathcal{O}]}{t}$$

*exists, depends on  $\bar{V}$  only, and is independent of the choice of  $V$ .*

*The functional has a Hadamard derivative at  $\mathcal{O}$ , if the Hadamard semiderivative exists for all directions  $\bar{V} \in \mathcal{C}^{0,1}(D; \mathbb{R}^2)$  and the mapping  $\bar{V} \mapsto d_{\mathcal{O}}^H \mathbf{J}[\mathcal{O}](\bar{V})$  is linear and continuous.*

As mentioned before, the Hadamard type derivative allows for the chain rule for compositions of functions, in contrast to the Eulerian type. Both concepts can however be related to each other. If e. g. an Eulerian semiderivative exists for all appropriate vector fields and the resulting mapping is continuous, the existence of a Hadamard semiderivative can be established, cf. [146, Chapter 9, Theorem 3.1]. Subsequently we have the Hadamard type derivative in mind when speaking of a shape derivative and simply write  $d_{\mathcal{O}} \mathbf{J}[\mathcal{O}]$  for the ease of notation.

For basic types of functionals the shape derivative can be given explicitly, cf. [146, Chapter 9, Theorem 4.2, 4.3].

**Lemma 4.3** (Shape derivative for domain integrals). *Let  $V \in \mathcal{F}(\mathbb{R}^2)$  be given, which additionally satisfies  $x \mapsto V(t, x) \in \mathcal{C}_{\text{loc}}^1(\mathbb{R}^2; \mathbb{R}^2)$ . Furthermore let  $f \in W_{\text{loc}}^{1,1}(\mathbb{R}^2; \mathbb{R})$  and  $\mathcal{O}$  be a bounded, open domain with Lipschitz boundary. Then the semiderivative for domain integrals is given by*

$$d_{\mathcal{O}} \left( \int_{\mathcal{O}} j \, dx \right) (V) = \int_{\Gamma} (V(0) \cdot n) j \, da(x).$$

**Lemma 4.4** (Shape derivative for boundary integrals). *Let  $V \in \mathcal{F}(\mathbb{R}^2)$  be given, which additionally satisfies  $x \mapsto V(t, x) \in C_{\text{loc}}^1(\mathbb{R}^2; \mathbb{R}^2)$ . Furthermore let  $g \in W_{\text{loc}}^{2,2}(\mathbb{R}^2; \mathbb{R})$  and  $\mathcal{O}$  be a bounded, open domain with  $C^2$  boundary. Then the semiderivative for boundary integrals is given by*

$$d_{\mathcal{O}} \left( \int_{\Gamma} k \, da(x) \right) (V) = \int_{\Gamma} (V(0) \cdot n) (\partial_n k + h k) \, da(x),$$

where  $h$  here denotes the mean curvature of  $\Gamma$  and  $\partial_n$  is the normal derivative.

A mentionable fact is that the shape derivative in general is supported on the boundary of the varying domain only, cf. [146, Chapter 9, Theorem 3.6], and solely depends on the normal component of the velocity field.

### 4.1.2. Lagrangian calculus

To set up a shape optimization problem, first of all appropriate functionals need to be found that are amenable to a mathematical treatment and reflect desirable properties of specific designs  $\mathcal{O}$  of the elastic domain under given loadings. It is therefore reasonable to incorporate the displacement  $u[\mathcal{O}]$ , obtained as the unique solution of the elasticity problem. To this end we consider general *cost functionals* in integral form.

**Definition 4.5** (Cost functional). *A cost functional is a mapping  $\mathbf{J}: \mathcal{U}_{ad} \rightarrow \mathbb{R}$  given in general form by*

$$\mathbf{J}[\mathcal{O}] = \mathbf{J}[\mathcal{O}; u[\mathcal{O}]] = \int_{\mathcal{O}} j[u[\mathcal{O}]] \, dx + \int_{\Gamma} k[u[\mathcal{O}]] \, da(x), \quad (4.1)$$

where  $\mathcal{U}_{ad}$  denotes the set of admissible shapes, i. e. domains  $\mathcal{O}$  fulfilling the prerequisites of Section 3.1, and  $u[\mathcal{O}]$  is the solution of the weak elasticity problem (3.10).

Whenever the domain is altered, as e. g. in the course of optimization, not only the direct impact on the cost functional, but also the implicit dependence via the elastic solution has to be taken into account. This observation makes the problem a PDE constrained optimization problem, which are commonly approached via a Lagrangian formulation.

**Definition 4.6** (Lagrangian). *Given an arbitrary cost functional  $\mathbf{J}: \mathcal{U}_{ad} \rightarrow \mathbb{R}$  and bilinear and linear forms as defined in (3.9), the Lagrangian is defined as*

$$\mathcal{L}(\mathcal{O}, u, p) := \mathbf{J}[\mathcal{O}; u] + a(\mathcal{O}; u, p) - l(\mathcal{O}; p) \quad (4.2)$$

with arbitrary  $\mathcal{O} \in \mathcal{U}_{ad}$  and  $u, p \in \mathcal{V}$ , where  $\mathcal{V}$  is an appropriate function space for the specific elasticity problem.

Most important, and in contrast to the definition of the cost functional above,  $\mathcal{O}$  and  $u$  are initially decoupled in the Lagrangian formulation. Instead the newly introduced function  $p$  ties in the PDE constraint in weak form. A relation is however established via a saddle point problem, namely

$$\mathbf{J}[\mathcal{O}, u[\mathcal{O}]] = \inf_{u \in \mathcal{V}} \sup_{p \in \mathcal{V}} \mathcal{L}(\mathcal{O}, u, p). \quad (4.3)$$

To see this, let  $\bar{u}$  be the unique solution to the elasticity problem in weak form. Choosing  $u = \bar{u}$  for the outer minimization in (4.3) above reduces  $\mathcal{L}(\mathcal{O}, \bar{u}, p)$  to  $\mathbf{J}[\mathcal{O}; \bar{u}]$ , not involving  $p$

anymore, and making the inner maximization dispensable. On the contrary for  $u \neq \bar{u}$  there must be a  $p$  s. t.  $a(\mathcal{O}; u, p) - l(\mathcal{O}; p) \neq 0$  as there is no further solution to the weak problem. Since  $p$  enters linearly in the Lagrangian it can be scaled s. t.  $\mathcal{L}(\mathcal{O}, u, p)$  approaches  $\infty$  for the inner maximization, which clearly is worse for the outer minimization.

The saddle point property can be further analyzed if additional prerequisites are deployed. In detail, let

- (1)  $\mathcal{V}$  be convex, closed, and non-empty,
- (2)  $p \mapsto \mathcal{L}(\mathcal{O}, u, p)$  be concave and upper semicontinuous for all  $u$ ,
- (3)  $u \mapsto \mathcal{L}(\mathcal{O}, u, p)$  be convex and lower semicontinuous for all  $p$ ,
- (4)  $p \mapsto \mathcal{L}(\mathcal{O}, u, p)$  be Gâteaux differentiable for all  $u$ ,
- (5)  $u \mapsto \mathcal{L}(\mathcal{O}, u, p)$  be Gâteaux differentiable for all  $p$ ,
- (6) there be a  $u_0$  s. t.  $\lim_{\|p\|_{\mathcal{V}} \rightarrow \infty} \mathcal{L}(\mathcal{O}, u_0, p) = -\infty$ ,
- (7) there be a  $p_0$  s. t.  $\lim_{\|u\|_{\mathcal{V}} \rightarrow \infty} \mathcal{L}(\mathcal{O}, u, p_0) = +\infty$ .

In our framework  $\mathcal{V}$  is the respective solution space for the elasticity problem, i. e.  $H_{\Gamma_D}^1$  or  $H_{\text{per},0}^1$ , and thus (1) is always fulfilled. As mentioned before  $\mathcal{L}(\mathcal{O}, u, p)$  is linear in  $p$  and therefore (2), (4), and (6) directly hold. An analogous argument applies for  $u$  entering  $a(\mathcal{O}; u, p)$ , so (3), (5), and (7) become assumptions for the cost functional  $\mathbf{J}[\mathcal{O}; u]$ . Within this setup we restate two important results from [168, Chapter 6], namely Proposition 1.6 and Proposition 2.2.

**Theorem 4.7** (Characterization of saddle points). *Under the assumption that (2)–(5) hold,  $(\bar{u}, \bar{p})$  is a saddle point of  $\mathcal{L}(\mathcal{O}, u, p)$  if and only if*

$$\begin{aligned} \mathcal{L}_{,u}(\mathcal{O}, \bar{u}, \bar{p})(\vartheta) &= 0 \quad \forall \vartheta \in \mathcal{V}, \\ \mathcal{L}_{,p}(\mathcal{O}, \bar{u}, \bar{p})(\vartheta) &= 0 \quad \forall \vartheta \in \mathcal{V}. \end{aligned} \tag{4.4}$$

**Theorem 4.8** (Existence of saddle points). *Under the assumption that (1)–(7) hold,  $\mathcal{L}(\mathcal{O}, u, p)$  possesses at least one saddle point.*

The stationarity conditions (4.4) are worthy of special attention. Computing the Gâteaux derivatives explicitly yields

$$\mathbf{J}_{,u}[\mathcal{O}; \bar{u}](\vartheta) + a(\mathcal{O}; \vartheta, \bar{p}) = 0 \quad \forall \vartheta \in \mathcal{V}, \tag{4.5}$$

$$a(\mathcal{O}; \bar{u}, \vartheta) - l(\mathcal{O}; \vartheta) = 0 \quad \forall \vartheta \in \mathcal{V}. \tag{4.6}$$

Equation (4.6) is exactly the weak elasticity problem, which was set up here as a constraint. Equation (4.5) on the other hand defines a new problem, referred to as *dual* or *adjoint* problem. It is based on the same function space and shares the structure of the weak elasticity problem, but with a different linear form.

The shape was so far considered as a fixed parameter. For optimization it should of course be varied, but the derivation of analogous optimality criteria is not straightforward. In any case the stationarity of the Lagrangian w. r. t. the domain is at least a necessary condition for an optimal shape, i. e. for all  $V$

$$d_{\mathcal{O}} \mathcal{L}(\mathcal{O}, u, p)(V) = d_{\mathcal{O}} \mathbf{J}[\mathcal{O}; u](V) + d_{\mathcal{O}} a(\mathcal{O}; u, p)(V) - d_{\mathcal{O}} l(\mathcal{O}; p)(V) = 0. \tag{4.7}$$

### 4.1.3. Shape derivative of cost functionals

As mentioned before the derivative w. r. t. the domain is used in characterizing optimality of a shape. Moreover it is required if a gradient based scheme is employed for numerical optimization. In the following we presume sufficient differentiability and do a formal calculation. We differentiate the cost functional (4.1) and use the usual chain rule because of the implicit dependence via  $u[\mathcal{O}]$ , yielding

$$d_{\mathcal{O}} \mathbf{J}[\mathcal{O}; u[\mathcal{O}]](V) = d_{\mathcal{O}} \mathbf{J}[\mathcal{O}; u](V) + \mathbf{J}_{,u}[\mathcal{O}; u] (d_{\mathcal{O}} u[\mathcal{O}](V)) . \quad (4.8)$$

Here the last term is especially intricate as it represents sensitivities of the PDE solution  $u$  w. r. t. arbitrary shape variations. As a remedy the dual solution derived before can be employed. For this note first that by virtue of (4.5)

$$\mathbf{J}_{,u}[\mathcal{O}; u] (d_{\mathcal{O}} u[\mathcal{O}](V)) = -a_{,u}(\mathcal{O}; u, p) (d_{\mathcal{O}} u[\mathcal{O}](V)) , \quad (4.9)$$

when  $d_{\mathcal{O}} u[\mathcal{O}](V)$  is used in lieu of the test function  $\vartheta$ . On the other hand deriving the weak problem w. r. t. the domain gives

$$\begin{aligned} 0 &= d_{\mathcal{O}} (a(\mathcal{O}; u[\mathcal{O}], p) - l(\mathcal{O}; p)) (V) \\ &= d_{\mathcal{O}} a(\mathcal{O}; u, p)(V) + a_{,u}(\mathcal{O}; u, p) (d_{\mathcal{O}} u[\mathcal{O}](V)) - d_{\mathcal{O}} l(\mathcal{O}; p)(V) . \end{aligned}$$

Assuming the implicit function theorem can be applied, the last equation is rewritten as

$$d_{\mathcal{O}} u[\mathcal{O}](V) = (a_{,u}(\mathcal{O}; u, p))^{-1} (-d_{\mathcal{O}} a(\mathcal{O}; u, p)(V) + d_{\mathcal{O}} l(\mathcal{O}; p)(V)) .$$

Plugging into (4.9) yields

$$\mathbf{J}_{,u}[\mathcal{O}; u] (d_{\mathcal{O}} u[\mathcal{O}](V)) = d_{\mathcal{O}} a(\mathcal{O}; u, p)(V) - d_{\mathcal{O}} l(\mathcal{O}; p)(V) .$$

Altogether (4.8) can thereby be reformulated as

$$d_{\mathcal{O}} \mathbf{J}[\mathcal{O}; u[\mathcal{O}]](V) = d_{\mathcal{O}} \mathbf{J}[\mathcal{O}; u](V) + d_{\mathcal{O}} a(\mathcal{O}; u, p)(V) - d_{\mathcal{O}} l(\mathcal{O}; p)(V) . \quad (4.10)$$

In fact, the expression is the same as in the derived necessary condition (4.7) before. The demonstrated trick of eliminating the sensitivities of the PDE solution by introducing an adjoint problem is de facto standard for optimal control problems. For an early reference see [107].

### 4.1.4. Application to the compliance cost functional

We now apply the presented concepts to a specific cost functional that serves as a global measure of rigidity, namely the *compliance*.

**Definition 4.9** (Generalized compliance). *Let  $u[\mathcal{O}]$  be the elasticity solution of the weak elasticity problem (3.10). The generalized compliance cost functional is then defined as*

$$\mathbf{J}^c[\mathcal{O}; u[\mathcal{O}]] := \int_{\mathcal{O}} f \cdot u[\mathcal{O}] \, dx + \int_{\Gamma_N} g \cdot u[\mathcal{O}] \, da(x) - \int_{\Gamma_D} \sigma[\mathcal{O}]n \cdot u^{\partial} \, da(x) . \quad (4.11)$$

The formulation allows for an intuitive explanation of the cost functional. If the elastic displacement  $u[\mathcal{O}]$  is aligned with the body forces  $f$  within the domain and the surface forces  $g$  on the boundary, the scalar products in the first two terms of (4.11) become large when the absolute value of the displacement is large as well. In this case the deformation of the domain, so to speak, complies with the loadings. Consequently, when aiming for a rigid design, these contributions should be minimized. On the contrary in the third term the boundary displacement is fixed and the normal stresses required to produce those displacements should be as high as possible when aiming for a rigid design. Due to the negative sign, it is still appropriate to minimize this contribution and hence the overall functional should be minimized.

**Remark 4.10.** In most expositions the compliance is defined by the first two terms on the right hand side of (4.11) only. The additional term is however required if elasticity problems with inhomogeneous Dirichlet boundary conditions are considered. Obviously the common formulation is regained by setting  $u^\partial \equiv 0$ . For further discussion see [58] and the references therein.

**Remark 4.11.** The terms involved in the definition appeared earlier in (3.9) when setting up the weak formulation of the elasticity problem. In fact the functional can be written equivalently as

$$\begin{aligned} \mathbf{J}^c[\mathcal{O}; u[\mathcal{O}]] &= l(\mathcal{O}; u[\mathcal{O}]) - \int_{\Gamma_D} \sigma[\mathcal{O}]n \cdot u^\partial \, da(x) \\ &= a(\mathcal{O}; u[\mathcal{O}], u[\mathcal{O}]) - 2 \int_{\Gamma_D} \sigma[\mathcal{O}]n \cdot u^\partial \, da(x) \\ &= -2 \mathbf{J}^{\text{total}}[\mathcal{O}; u[\mathcal{O}]]. \end{aligned} \tag{4.12}$$

The first identity is exactly the definition. The second follows from using  $u^0[\mathcal{O}]$  of the elasticity solution in the weak formulation (3.10) as a test function and applying partial integration to the remaining term. And the third follows from the second, the definition of the total free energy (3.12), and again partial integration. In general each term has an innate physical meaning. The coincidence here is an exclusive feature of the linearized elasticity model and does not hold anymore for nonlinear models, see [325] as an example.

**Remark 4.12.** For non-mixed inhomogeneous boundary conditions there is a direct correspondence of the compliance cost functional and the *elastic energy*  $a(\mathcal{O}; u[\mathcal{O}], u[\mathcal{O}])$ . By virtue of (4.12) we get  $\mathbf{J}^c[\mathcal{O}; u[\mathcal{O}]] = a(\mathcal{O}; u[\mathcal{O}], u[\mathcal{O}])$  for a Neumann problem, possibly with additional homogeneous Dirichlet boundary conditions, whereas for a Dirichlet problem without volume forces, and possibly with additional homogeneous Neumann boundary conditions, the sign is inverted, i. e.  $\mathbf{J}^c[\mathcal{O}; u[\mathcal{O}]] = -a(\mathcal{O}; u[\mathcal{O}], u[\mathcal{O}])$ . All test cases investigated in this thesis fall under these categories and we will therefore often make use of these equivalent formulations.

Following the procedure of the previous section, the adjoint problem (4.5) in case of the compliance functional reads

$$a(\mathcal{O}; \vartheta, p) = -\mathbf{J}_{,u}^c[\mathcal{O}; u[\mathcal{O}]](\vartheta) = 2a(\mathcal{O}; u, \vartheta) - 2l(\mathcal{O}; \vartheta) = 0$$

for all  $\vartheta \in \mathcal{V}$ . Here we rewrote the compliance functional in terms of the total free energy as in (4.12), computed the Gâteaux derivative, and used the weak formulation of the elasticity



problem (3.10). The unique solution of the resulting elasticity problem is trivially given by  $p = 0$ . For the total derivative w. r. t. the domain (4.10) we obtain in virtue of Lemma 4.3 and 4.4

$$\begin{aligned}
 d_{\mathcal{O}} \mathbf{J}^c[\mathcal{O}; u[\mathcal{O}]](V) &= d_{\mathcal{O}} (-a(\mathcal{O}; u, u) + 2l(\mathcal{O}; u))(V) + d_{\mathcal{O}} a(\mathcal{O}; u, 0)(V) - d_{\mathcal{O}} l(\mathcal{O}; 0)(V) \\
 &= - \int_{\Gamma} (V(0) \cdot n) (C\varepsilon[u] : \varepsilon[u]) \, da(x) \\
 &\quad + 2 \int_{\Gamma} (V(0) \cdot n) (f \cdot u) \, da(x) \\
 &\quad + 2 \int_{\Gamma} (V(0) \cdot n) (\partial_n (g \cdot u) + h(g \cdot u)) \, da(x).
 \end{aligned} \tag{4.13}$$

**Remark 4.13.** If the procedure above is followed using a different formulation of the compliance functional, a different adjoint problem with a different solution may be obtained. Upon inserting into the expression for the total derivative however the same result as in (4.13) is recovered. Common to all variants is that the solution of the adjoint problem can be deduced directly without the need to solve another elasticity problem. This is again an exclusive property of the compliance functional, which is therefore sometimes termed *self-adjoint*.

## 4.2. Optimal shapes

Having laid the foundations for varying the shape of a domain in elasticity problems, we now turn to the task of actually finding an optimal layout for the compliance cost functional. First of all we remark that a trivial solution is obtained by filling the whole working domain with material, i. e.  $\mathcal{O} = D$ . It is also intuitively not desirable to have holes in the elastic domain as they weaken its rigidity. This fact can be inferred rigorously by looking at the *topological derivative* of the compliance functional. Measuring the sensitivity for the nucleation of infinitesimally small holes, positive values are taken throughout the domain, indicating an increase in compliance, cf. [376, 181]. Hence this exceptional case is usually ruled out by imposing a volume constraint, i. e.

$$\text{Vol}(\mathcal{O}) = \Theta \quad \text{with } 0 < c < \Theta < \text{Vol}(D) \tag{4.14}$$

is required to hold. This can be motivated from a practical point of view as well because keeping a low volume fraction corresponds to finding a design with low material weight or costs. Further aspects like manufacturing constraints and design requirements, which could imply a functional purpose of holes, like e. g. in bones, make up for an own field of research and are not taken into account here.

The introduced constraint on the available volume on the other hand renders the optimization problem ill-posed, in the sense that classical designs with solid and void regions never achieve a minimum. Such counter examples can e. g. be found in [298, 299] for the scalar setting, where coefficients in the state equation are subject to optimization, and e. g. in [256, Example 8.3] for elasticity problems. The popular direct method of the calculus of variations fails here because of lacking compactness. This deficiency becomes apparent in branched out structures, that achieve a lower energy while retaining the prescribed overall volume. Well-posedness can be recovered by introducing a larger class of admissible designs, referred to as *relaxation*.

In particular arbitrary fine mixtures of material and void regions are allowed, leading to intermediate local densities  $\theta: D \rightarrow [0, 1]$  in the limit. Physical meaningfulness comes from the theory of homogenization, which allows to derive effective material properties of a microscopic structure. Its concrete setup is of paramount importance for the optimality of the resulting shape and in fact for the compliance objective several optimal, yet diverse, constructions exist. In this regard we present the sequential lamination model in detail and touch on several other approaches afterwards. We mainly follow the exposition in [12], which nicely compiles all required ingredients from shape optimization, relaxation and homogenization theory and eventually derives a fully practical numerical optimization scheme. The individual results therein usually date back to earlier publications and we will refer to them later on.

### 4.2.1. Relaxation

In the following we consider the elasticity problem in an equivalent stress based formulation, i. e. instead of  $u$  and  $\varepsilon[u]$  the equations are expressed in terms of the unknown stress tensor field  $\sigma: \mathcal{O} \rightarrow \mathbb{R}_{\text{sym}}^{2 \times 2}$  as in (3.2). Moreover a Neumann problem without volume forces is assumed, i. e.  $f \equiv 0$  and  $u^\partial \equiv 0$ . Let  $\chi_{\mathcal{O}}: D \rightarrow \{0, 1\}$  denote the characteristic function of the elastic body  $\mathcal{O}$  and define the set of statically admissible stress fields by

$$\Sigma(\chi_{\mathcal{O}}) := \{ \sigma \in L^2(D; \mathbb{R}_{\text{sym}}^{2 \times 2}) : \sigma \text{ satisfies (3.2) for } \chi_{\mathcal{O}} = 1, \sigma = 0 \text{ else} \} .$$

An element  $\sigma$  of this set, or  $\varepsilon[u] = C^{-1}\sigma$  respectively, is a solution of the elasticity problem for the domain  $\mathcal{O}$  and extended by zero outside of the domain. This requirement reflects the fact that holes in the domain should be stress free. The characteristic function  $\chi_{\mathcal{O}}$  assigns material or void to each point  $x \in D$  and can therefore be regarded here as subject to optimization. In case arbitrary characteristic functions  $\chi \in L^\infty(D; \{0, 1\})$  are permitted,  $\Sigma(\chi)$  might be empty if the associated domain  $\mathcal{O}_\chi = \{x \in D : \chi(x) = 1\}$  fails to satisfy the geometric assumptions of Section 3.1. As per Remark 4.12 the compliance functional in this setting is given by

$$\mathbf{J}^c[\mathcal{O}_\chi; \sigma[\mathcal{O}_\chi]] = \int_D \chi_{\mathcal{O}} C^{-1} \sigma : \sigma \, dx .$$

The volume constraint can be tied in via a positive Lagrangian multiplier  $l \in [0, \infty)$  and thus the final minimization problem for the combined objective functional reads

$$\inf_{\chi \in L^\infty(D; \{0, 1\})} \mathbf{J}^c[\mathcal{O}_\chi; \sigma[\mathcal{O}_\chi]] + l \int_D \chi_{\mathcal{O}} \, dx . \quad (4.15)$$

In this framework the fundamental relaxation result can be established.

**Theorem 4.14** (Relaxed problem). *The shape optimization problem (4.15) admits the relaxed formulation*

$$\min_{\sigma \in \Sigma(D)} \int_D \min_{0 \leq \theta \leq 1} \min_{C^* \in G_\theta} C^{*-1} \sigma : \sigma + l \theta \, dx , \quad (4.16)$$

where  $\Sigma(D) := \{ \sigma \in L^2(D; \mathbb{R}_{\text{sym}}^{2 \times 2}) : \sigma \text{ satisfies (3.2) in } D \}$  denotes an unconstrained set of admissible stress fields for the whole working domain,  $\theta: D \rightarrow [0, 1]$  is the density function, and the set  $G_\theta$  comprises all effective homogenized elasticity tensors resulting from mixtures of material  $C$  with fraction  $\theta$  and void in the sense of  $H$ -convergence. In particular for fixed  $l \in [0, \infty)$

1. there exists at least one solution  $\sigma \in \Sigma(D)$  of (4.16), and (4.15) and (4.16) coincide,
2. up to a subsequence, any minimizing sequence  $\sigma_n$  for (4.15) converges weakly in  $L^2(D; \mathbb{R}_{\text{sym}}^{2 \times 2})$  to a minimizer  $\sigma$  of (4.16),
3. for any minimizer  $\sigma$  of (4.16) there exists a minimizing sequence  $\sigma_n$  for (4.15) which converges weakly in  $L^2(D; \mathbb{R}_{\text{sym}}^{2 \times 2})$  to  $\sigma$ ,
4. there exists at least one optimal relaxed shape, i. e. a density function  $\theta$ ,
5. up to a subsequence, any minimizing sequence of characteristic functions converges weakly-\* in  $L^\infty(D; \{0, 1\})$  to an optimal relaxed shape  $\theta$ .

This theorem depicts the central result for relaxing the shape optimization problem and calls for some further explanation. In particular existence of an optimal relaxed shape is guaranteed and (4.16) provides the formula for its computation. Reading from left to right, at first an admissible stress field is selected. Moving inside the integral makes the following considerations pointwise for  $x \in D$ . Here initially a local material density  $\theta(x)$  is fixed. Then, in the inner minimization, an elasticity tensor is to be chosen in order to minimize the local elastic energy. Afterwards minimizations in the preselected variables  $\theta$  and  $\sigma$  follow. As we will show later on, all those minimizations can actually be performed explicitly.

The relaxation result has first been derived in [15] in a two dimensional plane stress setting and was extended to arbitrary dimensions and multiple loads in [12]. Interestingly the relaxed formulation can be obtained equivalently by the use of homogenization or the method of *quasiconvexification*. The later concept was already explored in [254, 255, 256], where primarily scalar problems are considered, but several remarks as to the vectorial case in limited configurations are included as well. It is applicable in our setting, as done in [12], but valid in far more general situations as shown in [176].

Let us now comment on the crucial points in the derivation of the relaxed formulation when taking the perspective of homogenization. The first step is the actual relaxation, i. e. instead of the characteristic function, an effective elasticity tensor field  $C^*$  and a density function  $\theta$ , which can take any value in  $[0, 1]$ , is introduced. The shape optimization problem then becomes

$$\min_{0 \leq \theta \leq 1} \min_{C^* \in G_\theta} \mathbf{J}^c[D; \sigma[C^*]] + l \int_D \theta \, dx. \quad (4.17)$$

Classical designs are still included by setting  $\theta = 1$ ,  $C^* = C$  where  $\chi = 1$  and  $\theta = 0$ ,  $C^* = 0$  where  $\chi = 0$ . Furthermore any minimizing sequence of characteristic functions  $\chi_n$  converges weakly to a density  $\theta$  and the corresponding sequence of elasticity tensors  $C_n$  converges to an effective tensor  $C^*$  in the sense of H-convergence, cf. Definition 3.18. This is the main ingredient of the proof, see [15, pp. 849, 850].

To continue, the *principle of minimum complementary energy* is used to rewrite the compliance variationally as

$$\mathbf{J}^c[D; \sigma[C^*]] = \inf_{\sigma \in \Sigma(D)} \int_D C^{*-1} \sigma : \sigma \, dx.$$

It states that the minimal energy is attained by the actual solution of the elasticity problem, see e. g. [388], and allows to eliminate the explicit dependence on  $C^*$  here. Assuming that a

minimizing  $\sigma$  exists, the order of minimization over different variables can be interchanged, s. t. (4.17) becomes

$$\min_{\sigma \in \Sigma(D)} \min_{0 \leq \theta \leq 1} \min_{C^* \in G_\theta} \int_D C^{*-1} \sigma : \sigma + l \theta \, dx .$$

Next the minimization over  $\theta$  and  $C^*$  is moved inside the integral, i. e.

$$\min_{\sigma \in \Sigma(D)} \int_D \min_{0 \leq \theta \leq 1} \min_{C^* \in G_\theta} C^{*-1} \sigma : \sigma + l \theta \, dx ,$$

which is possible due to the local character of H-convergence, cf. [18, Theorem 2.1.2]. Hence (4.16) is obtained.

We have to remark that the outlined procedure, especially w. r. t. H-convergence, is initially not applicable to our shape optimization setting, which uses regions of material and voids. This issue is avoided by replacing perforations with inclusions of a very weak material. The theory then works and leads to (4.16) with the exception that elasticity tensors in  $G_\theta$  are made of a mixture of  $C$  and the weak substitute. At this point it is possible to pass to the degenerate limit, see [15, Section 3B], and to obtain the desired result.

#### 4.2.2. Bounds on the elastic energy

With the relaxed shape optimization problem (4.16) at hand, the next crucial step is to select the optimal effective elasticity tensor in the inner minimization from the set  $G_\theta$ . This set is called *G-closure* as it comprises all effective tensors obtained by limiting processes from classical designs via H-convergence, which is a generalization of G-convergence. The selection is especially difficult as there is no closed algebraic formula for the candidates in  $G_\theta$ , which is in contrast to the scalar conductivity setting, see e. g. [267, 268, 392, 297]. Instead candidates are identified as optimal if they realize lower bounds on the elastic energy. Thereby also a class of optimal materials is found. The exciting insight is that the employed geometric constructions are not unique and can in fact be fundamentally different. As it turns out, the sequential lamination model is most general. It was also often used in proofs. We will discuss it in the following section and mention some other constructions afterwards.

For the elastic energy as a cost functional the derivation of bounds for two-phase composites attracted much attention. Let  $\theta$  be the fixed proportion of the rigid material characterized by  $C$  and let  $B$  denote the elasticity tensor for the weak substitute. Unless otherwise noted the materials are assumed to be isotropic. The most fundamental lower and upper bounds are given by the harmonic and the arithmetic mean, respectively, i. e.

$$\left( \theta C^{-1} + (1 - \theta) B^{-1} \right)^{-1} \varepsilon[u] : \varepsilon[u] \leq C^* \varepsilon[u] : \varepsilon[u] \leq (\theta C + (1 - \theta) B) \varepsilon[u] : \varepsilon[u] .$$

In the conductivity setting they are attributed to Voigt [408], Wiener [418], and Reuss [343], whereas for elasticity they are first found in [227, 321]. Hashin and Shtrikman derive improved bounds on the bulk and shear modulus under the assumption that the composite material is isotropic as well in [212]. They require that the bulk and shear moduli of the constituents satisfy the same ordering relation, referred to as *well-ordered* materials. Walpole in [412] later obtains similar results without that restriction. Optimality of the bounds in [212], i. e. the fact that the bounds are actually realized by some candidate, is proven amongst others in the seminal work [178] by Francfort and Murat in 1986. Here the sequential lamination construction and

compensated compactness are employed in the proof. Independently Gibiansky and Cherkaev in 1984 derive and prove optimal bounds in the context of plate theory in [190] and in the full elasticity setting for two and three spatial dimensions in [193] via the *translation method*. English translations are available in [191, 192]. Using different techniques Kantor and Bergman in [246] obtain similar results that furthermore extend to a class of anisotropic composite materials. On the other hand the *Hashin-Shtrikman variational principle*, introduced in [210, 211], is adopted by a large community for the study of optimal bounds and the G-closure problem. In essence, by using techniques of convex analysis, the variational inequality

$$C^{*-1}\sigma : \sigma \geq C^{-1}\sigma : \sigma + \sup_{\eta} 2(1 - \theta) C^{*-1}\sigma : \eta - (1 - \theta)(B - C)^{-1}\eta : \eta + \inf_{\vartheta} \int_{D^{\mathcal{Y}}} C\varepsilon[\vartheta] : \varepsilon[\vartheta] + 2(1 - \chi_{\mathcal{Y}})\eta : \varepsilon[\vartheta] \, dx \quad (4.18)$$

is derived. The key for obtaining bounds then is the estimation of the second term in (4.18), often referred to as *nonlocal* term. Kohn and Milton derive results in conductivity [253]. Avellaneda derives optimal bounds on elastic energies for unrestricted composite materials made from isotropic constituents. Lipton considers the special case of incompressible elasticity in two space dimensions [261], and in [252] the generalization to higher dimensions can be found. Optimal and explicitly computable bounds are derived for unrestricted composites. Composites made from anisotropic constituents are addressed in [288, 36]. Allaire and Kohn derive bounds equivalent to those in [37] by Avellaneda, but give them explicitly using a simplified evaluation developed in [30]. Eventually, for our shape optimization problem with solid and void regions, we rely on the following formulation of an optimal lower bound, see [15, pp. 854, 857–858] for reference, which builds upon the optimal bounds derived in [30].

**Theorem 4.15** (Lower Hashin-Shtrikman bound). *In two spatial dimensions the local elastic energy term in (4.16) for given material density  $\theta$  and stress  $\sigma$  is bounded from below, in particular*

$$C^{*-1}\sigma : \sigma \geq C^{-1}\sigma : \sigma + \frac{(\kappa + \mu)\theta}{4\kappa\mu(1 - \theta)} (|\lambda^{(1)}| + |\lambda^{(2)}|)^2, \quad (4.19)$$

where  $\kappa$  and  $\mu$  are elasticity coefficients of the material given by  $C$ , cf. (3.8), and  $\lambda^{(1)}, \lambda^{(2)}$  are the eigenvalues of  $\sigma$ .

**Remark 4.16.** In correspondence to (4.19) there exists an upper bound for the energy  $C^{*-1}\sigma : \sigma$  and there are lower and upper bounds for the elastic energy expressed in terms of strains,  $C^*\varepsilon[u] : \varepsilon[u]$ , as well. All of those can be derived using the same technique and they are furthermore related in pairs by the Fenchel transform, see [30, Proposition 8.2].

### 4.2.3. Sequential lamination model

The bounds discussed in the preceding section are optimal in the sense that there exist composites whose associated elastic energy attains them. A construction based on successive layering and homogenization turns out to be most flexible and was hence employed in many proofs. From a physical perspective effective properties of laminated composite materials are well studied. One of the earliest references is [418] by Wiener from 1912, where bounds on dielectric coefficients are computed. Bruggeman gives an overview of the earliest achievements and presents explicit formulae for the dielectric coefficient in [94] and for elasticity coefficients

in [95] already in 1937. A rigorous treatment, including explicit formulae obtained via homogenization, starts with works by Murat and Tartar [392, 297]. See [301, 394] for English translations.

Let us now describe the construction, cf. Figure 4.1. Starting on a scale  $\epsilon_1$ , rigid and weak materials  $C$  and  $B$  are stacked in alternation with a certain proportion and along a certain direction. By means of homogenization, effective material properties are computed and this newly obtained material is used in the next iteration on a substantially larger scale  $\epsilon_2 \gg \epsilon_1$  in place of the weak material. The process is iterated and the number of laminations is defined as the *rank*. In each step the ratios are chosen in such a way that the resulting overall fraction of material matches the locally prescribed density  $\theta$ . At the very end the passage  $B \searrow 0$  is taken into account, in the sense that the weak material ultimately gives way to real perforations, cf. [15, Section 3B]. The optimality of the sequential lamination construction for the elastic

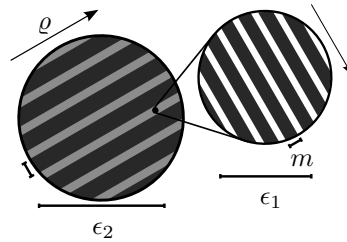


Figure 4.1.: Sketch of the rank-2 sequential lamination construction.

energy was proven in [37] in the two-phase context by showing that the Hashin-Shtrikman bounds can always be attained by a finite rank sequential laminate. For our two dimensional setting even stronger results were derived in [252, 30] or [190, 193] respectively. In particular it is shown that a rank-2 sequential laminate is already sufficient to attain the lower bound. See [15, Section 3B] for the passage to void. Moreover the parameters of the construction can be computed directly from the eigenvalues  $\lambda^{(1)}$ ,  $\lambda^{(2)}$  and the eigenvectors  $\tau^{(1)}$ ,  $\tau^{(2)}$  of the local stress tensor  $\sigma$ .

**Theorem 4.17** (Parameters of sequential lamination). *In two space dimensions and for the compliance cost functional the parameters of an optimal sequentially laminated microstructure are locally given by a mapping  $x \mapsto q[\sigma](x) = (\varrho[\sigma](x), m[\sigma](x), \theta[\sigma](x))^T$  with*

$$\begin{aligned} \varrho[\sigma](x) &= \arctan \left( \frac{\tau_y^{(1)}(\sigma)}{\tau_x^{(1)}(\sigma)} \right), \\ m[\sigma](x) &= \frac{|\lambda^{(2)}(\sigma)|}{|\lambda^{(1)}(\sigma)| + |\lambda^{(2)}(\sigma)|}, \\ \theta[\sigma](x) &= \min \left\{ 1, \sqrt{\frac{2\mu + \lambda}{4\mu(\mu + \lambda)l}} (|\lambda^{(1)}(\sigma)| + |\lambda^{(2)}(\sigma)|) \right\}, \end{aligned} \tag{4.20}$$

where  $\lambda$  and  $\mu$  are the Lamé parameters of  $C$  as seen in (3.8).

The result states that the lamination directions are aligned with the eigenvectors. Here  $\varrho$  specifies the inclination of the first direction, and the second direction is always perpendicular

due to orthogonality of the eigenvectors. The ratio relates to the ratio of the eigenvalues. Here  $m$  specifies the ratio used in the first iteration, and the second is given by  $1 - m$  due to normalization. The formulae for  $\varrho$  and  $m$  can be found in [15, Equation (4.23)]. Finally the local density is proportional to the combined magnitude of both eigenvalues, see [15, p. 856]. As can be seen there is a threshold behavior for the local density. From a certain magnitude of stress on it is preferable to resort to solid material, i. e.  $\theta = 1$ . Naturally this value also depends on the chosen Lagrangian multiplier. Given those parameters the effective homogenized elasticity tensor  $C^*[q](x)$  can likewise be computed explicitly.

**Theorem 4.18** (Effective tensor for sequential lamination). *Given the parameters  $q = (\varrho, m, \theta)^\top$  of a twofold sequentially laminated microstructure, the associated homogenized elasticity tensor is given by*

$$\begin{aligned}
 C_{ijkl}^*[q] &= R[\varrho] \bar{C}^*[m, \theta] := \sum_{a,b,c,d=1}^2 Q_{ia}[\varrho] Q_{jb}[\varrho] Q_{kc}[\varrho] Q_{ld}[\varrho] \bar{C}_{abcd}^*[m, \theta], \\
 \bar{C}_{1111}^*[m, \theta] &= \frac{4\kappa\mu(\kappa + \mu)\theta(1 - \theta(1 - m))(1 - m)}{4\kappa\mu m(1 - m)\theta^2 + (\kappa + \mu)^2(1 - \theta)}, \\
 \bar{C}_{2222}^*[m, \theta] &= \frac{4\kappa\mu(\kappa + \mu)\theta(1 - \theta)m}{4\kappa\mu m(1 - m)\theta^2 + (\kappa + \mu)^2(1 - \theta)}, \\
 \bar{C}_{1122}^*[m, \theta] &= \frac{4\kappa\mu\lambda\theta^2 m(1 - m)}{4\kappa\mu m(1 - m)\theta^2 + (\kappa + \mu)^2(1 - \theta)},
 \end{aligned} \tag{4.21}$$

for  $i, j, k, l \in \{1, 2\}$ . Here the effective tensor in reference configuration  $\bar{C}^*$  is rotated by the linear operator  $R$  to the appropriate coordinate frame specified by  $\varrho$  using usual rotation matrices  $Q \in SO(2)$ . The remaining entries of  $\bar{C}^*$ , which cannot be identified via the symmetry properties (3.4), are set to zero.

Explicit formulae for effective tensors of sequentially laminated composites were already given in [178]. Their evaluation however is tedious in general, but succinctly possible in our situation of rank-2 sequential orthogonal laminates comprising voids, cf. [15, Equation (4.21)].

Looking back at the relaxed minimization problem (4.16) the solution to the inner minimization problem is now known explicitly. It remains to fix the Lagrangian multiplier in order to fulfill the volume constraint (4.14). To this end, it can be shown that the overall volume is a decreasing function of  $l$ , see [12, Remark 3.5 and Lemma 3.6], which facilitates an adaptation by bisection in the course of an optimization algorithm.

**Remark 4.19** (Degeneracy of the elasticity tensor). The elasticity tensor in (4.21) is degenerate, in the sense that  $\bar{C}_{1212}^* = 0$ . Consequently the composite material cannot sustain a nonaligned shear stress. An optimal sequential laminate will however always be aligned.

In view of robustness, especially for numerical application, an optimal and nondegenerate rank-4 laminate can be constructed when  $\det \sigma > 0$ , see [11, Proposition 3]. For  $\det \sigma \leq 0$ , the degeneracy is a general result for optimal elasticity tensors, see [11, Theorem 2].

**Remark 4.20** (Higher space dimension). Avellaneda's result [37] that finite rank sequential laminates attain the optimal bounds is valid in higher dimensions as well. The fact that rank- $d$  laminates are sufficient in dimension  $d$  is shown in [30]. Explicit formulae for the lamination parameters and the effective elasticity tensor are given in [17] and independently in [193].

**Remark 4.21** (Effective isotropy). The optimal sequential lamination constructions discussed so far in general lead to orthotropic effective materials. For an optimal isotropic material, three lamination steps are required in two space dimensions, and six in three dimensions [179].

**Remark 4.22** (Multiple loads). In case multiple state equations (3.2) are considered for varying loads, finite sums of elastic energies appear in the objective functional. This situation is already covered in Avellaneda's work. In two space dimensions, three lamination steps are required to produce an optimal microstructure [36], in three space dimensions, six are necessary [179].

**Remark 4.23** (Uniaxial loading). For a uniaxial load in two space dimensions a rank-1 laminate is the only possible optimal microstructure, cf. Figure 1.3(a) in the introduction. This fact was already shown by Ball and James [49], in the context of phase transformations in metallurgy.

#### 4.2.4. Further results on optimal microstructures

The sequential lamination microstructure is not the only possible construction attaining optimal values on the elastic energy. Worth mentioning are the following important results.

**Concentric spheres.** Historically, the *concentric spheres* assemblage employed by Hashin in [213] is the first optimal microstructure. It is valid for the special case of  $C^*\mathbb{1} : \mathbb{1}$ , i. e. a hydrostatic strain is considered. Given a domain occupied by one of the constituents, spherical inclusions of the other constituent are successively introduced. Building upon Eshelby's result in [170], the change in stored elastic energy is computed. By theory, the occurring stresses can only be determined in case of an infinite body loaded at infinity, but for the derivation of bounds they can be chosen as energetically optimal. A circular boundary around each inclusion is chosen in such a way that the resulting coating and its core possess the correct volume ratio.

Bergman [82], Milton [284], and Tartar [392] use a generalized construction made from coated *confocal ellipsoids* in the conductivity setting to prove nonuniqueness of optimal designs and sharpness of bounds. Grabovsky and Kohn carry over this concept to the elasticity setting and achieve a generalization for anisotropic strains and stresses in [197], i. e. the optimal bound  $C^*\varepsilon[u] : \varepsilon[u]$  is attained for a certain nontrivial set of strains  $\varepsilon[u]$ . Their work is based on Cherepanov [118], where the shape of *equally strong* holes, i. e. those with constant tangential stress on their outlines, is derived. The two dimensional isotropic elasticity problem is transferred to the complex plane using Kolosov-Muskhelishvili potentials [303] and a conformal mapping of the annulus region is considered. Boundary conditions are chosen in such a way that the global strain field  $\varepsilon[u]$  remains uniform and unaltered. As it turns out, the construction is successful in a certain regime of strains where the hydrostatic part  $c\mathbb{1}$  is large compared to the *deviatoric* part  $\varepsilon[u] - c\mathbb{1}$ . In this case confocal ellipsoids are obtained, with concentric circles included as a special case. The eccentricity depends on the strain and the direction of the semimajor axis is aligned with the eigenvector of  $\varepsilon[u]$  with larger modulus, in case the core is made from the weaker material. As the scaling is arbitrary, the whole domain can finally be covered by scaled copies of the construction, see Figure 4.2(a) for a sketch. In contrast to the sequential lamination model, which requires possibly several H-limit passages, the construction is genuine from the start. Still a finite covering would result in only



a near optimal design. Furthermore there is a limiting regime. Upon approaching its defining constraint, the eccentricity increases and the ellipsoids resemble a layering. Also an explicit formula for the elasticity tensor is not available. The construction can be generalized to three spatial dimension, see [196], but not to anisotropic components.

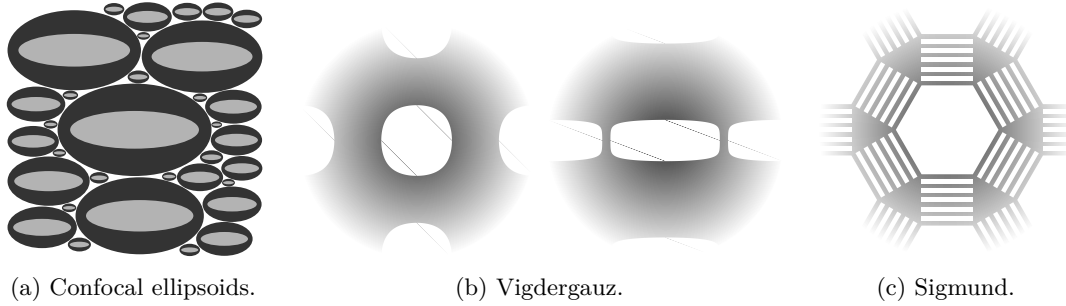


Figure 4.2.: Exemplary sketches of alternative optimal microstructure models.

**Vigdergauz microstructure.** A fundamentally different construction was given by Vigdergauz in [406] and further discussed by Grabovsky and Kohn [198]. In a series of papers starting with [404], Vigdergauz derived an integral equation for holes in plates minimizing the stress concentration and later extended this concept to periodic arrays and the full elasticity setting. He then computed the elastic energy and found that it achieved the optimal bounds. The derivation in [198] proceeds along the same lines as in [197], i. e. the problem is transferred to the complex plane, optimality criteria are derived, and a conformal mapping to the unit cell is set up. This time a periodic problem is considered and it is found that the cells should be aligned with the principal strain direction. Finally an explicit parametrization is obtained in terms of elliptic integrals. In Figure 4.2(b) resulting shapes for a hydrostatic and a near uniaxial strain are displayed. The construction has the same limiting regime as the confocal ellipsoids construction and in fact the defining constraint depicts the demarcation towards a regime where rank-2 sequential laminations are necessary to achieve the optimal bound. Upon approaching, the inclusions degenerate to bars, which are in fact rank-1 laminated microstructures. By changing the unit cell to a rectangle with arbitrary small aspect ratio, an additional scale can be generated and even rank-2 sequentially laminated microstructures obtained in the limit. If the volume of the inclusion tends to zero it is shown that an ellipsoidal shape is obtained. The authors also discuss implications of a stress based shape optimization setup with solid and void regions. Among other things  $\det \sigma > 0$  turns out to be the constraint for nondegenerate optimal shapes. An explicit evaluation of the elasticity tensor was claimed by Vigdergauz but questioned by Grabovsky. It is possible to extent the construction for certain choices of anisotropic constituents. According to [406] an extension to three space dimensions is conceivable, but would require fundamentally different techniques. A corresponding result in case of heat conduction is the subject of [405]. In [403], optimal two dimensional periodic inclusions yielding isotropic materials were identified on hexagonal and triangular lattices with the help of numerics.

**Sigmund microstructure.** Another microstructure was suggested by Sigmund [372], inspired by numerical topology optimization results for inverse homogenization. In its general form it comprises polygonal regions with pure phases and interconnecting sequential laminates of lower rank, see Figure 4.2(c) for an example. In two and three space dimensions the exact elasticity solutions for a hydrostatic loading are computed and optimality is proven. Furthermore, the construction on a hexagonal periodic lattice yields an isotropic effective material which has a lower shear modulus than previously known composites. This is interesting in the context of *coupled bounds*. The bounds described before in Section 4.2.2 are applied independently to derive optimal effective bulk and shear moduli. In contrast, Cherkaev and Gibiansky [120] consider both simultaneously and obtain a relation. It is however unknown whether these coupled bounds can actually be attained.

**Michell trusses.** The Michell truss construction was already mentioned in Chapter 2. At first glance, it seems unrelated because of the different material model comprising idealized joints and rods. However, it turns out that the rods have to be aligned with the principal stress directions and have to sustain a proportional corresponding load. When the framework is confined to a fixed region  $D$ , then  $\int_D |\lambda^{(1)}(\sigma)| + |\lambda^{(2)}(\sigma)| dx$  is an appropriate cost functional in this context, to be optimized among all admissible stress fields. Allaire and Kohn argue that the two dimensional compliance minimization problem under volume constraint (4.15) is formally equivalent in the low volume limit, i. e. for  $l \rightarrow \infty$ , when the overall volume should tend to zero. They moreover identify a dominant, common term in the relaxed formulation even when the volume is not small and thereby account for similarities of optimal relaxed shapes and Michell trusses. Grabovsky and Kohn [198] point out that the periodic array of Vigdergauz's inclusions also resembles Michell trusses with specifically designed joints in the low volume regime.

**Results on periodic microstructures.** In the context of optimal microstructures there is a striking fundamental results stating that the set of effective elasticity tensors obtained from periodic composites is dense in the set obtained from all composites. This allows to resort to periodic microstructures, enables the use of the rich theory of periodic homogenization, and justifies our two-scale approach based on assuming local periodicity. The result is attributed to unpublished work by Dal Maso and Kohn, and has been further generalized in [338, 38]. On the other hand, Allaire and Aubry [11] prove that for  $\det \sigma < 0$  an optimal periodic microstructure does not exist. In fact, the periodic constructions presented above have a limiting regime and cease to exist outside. Before the result was published, Cherkaev et al. [123] solved a related problem of finding an optimally shaped, simply connected cavity in an infinite elastic plate under shearing loads. They found a curved quadrilateral, but also remarked that the associated energy was significantly higher than that of an optimal rank-2 laminate. This was not surprising as it was shown before by Grabovsky [196] that an optimal microstructure in such a regime must have straight interfaces to allow for discontinuities in the strain field.

Periodic constructions however remain highly relevant due to their approximation properties and technical manageability. A further important aspect is material symmetry. The effective properties of homogenized elasticity tensors depend on the properties of the microscopic constituents and their arrangement. Classical results [204, 239] show how symmetries in the microscopic arrangement carry over to the macroscale. A more recent, generalized result is

show by Ptashnyk and Seguin [335]. They consider symmetries of periodic elastic structures generated by volume-preserving affine transformations

$$h(y) = y_0 + a + H(y - y_0),$$

where  $y_0$  is the origin of the transformation,  $a$  an arbitrary translation vector, and  $H$  a unimodular linear mapping. If such  $h$  generates a symmetry of the microscopic periodic construction, there holds

$$C^* X = H (C^*(H^\top X H)) H^\top, \quad \forall X \in \mathbb{R}_{\text{sym}}^{d \times d}.$$

This means that the gradient of the linear mapping yields a material symmetry of the macroscopic effective material. The converse is not true. There are effective materials with symmetries that do not appear in the periodic microscopic construction. As an example, a material with hexagonal symmetry is already isotropic [204], cf. the Sigmund microstructure above.

The models considered in this work will yield orthotropic materials. In this regard, there is an important result by Pedersen [323], stating that in order to be optimal, the symmetry axes have to be aligned with the principal stress directions. For the three dimensional case, optimality conditions were derived by Norris [308].



---

## CHAPTER 5

### A two-scale approach

---

THE two-scale model for shape optimization that is at the core of this thesis will be developed in this chapter. It builds upon locally periodic assemblages of geometrically simple perforations located on an underlying lattice of microscopic length scale. Their elastic behavior is probed at discrete macroscopic points by determining the elastic reaction to given linearized deformations. The approach turns out to be related to several established concepts for multiscale problems. For the numerical treatment we will combine a macroscopic coarse finite element discretization with a boundary element approach for the solution of microscopic cell problems. The latter requires a discretization of the one dimensional boundaries only and we therefore achieve a convenient and flexible testing ground for numerical experiments with different microstructure models.

#### 5.1. Derivation of the two-scale model

We will start by reviewing some decisive analytical and numerical aspects of shape optimization in the usual single-scale setting. Based upon those we will motivate our two-scale approach and discuss the basic modeling assumptions. We will then sketch our procedure in an intuitive manner and embed it into a rigorous framework afterwards.

##### 5.1.1. Motivation

Two aspects motivate the numerical investigation of microstructured materials. Firstly the classical shape optimization problem for the compliance objective is ill-posed as discussed in Section 4.2. An optimal shape will develop oscillations in the material distribution on a microscopic scale whereas numerical approaches will show similar structures on the grid scale and therefore produce mesh dependent, suboptimal results. The deficiency can be obviated by allowing generalized materials with intermediate density on the macroscopic scale stemming from microscopic geometries via homogenization. In fact several microstructure models with fundamentally different geometric designs exist that deliver an optimal solution. Secondly these models typically do not generate materials with a physical equivalent. They are of theoretical importance but cannot provide a guideline for manufacturing real materials.

Consequently our model shall combine two important features. Firstly it shall be able to capture microstructure formation by employing an additional microscopic scale. Effective material properties will then enter the macroscale via homogenization and oscillations on the macroscopic scale as observed for single-scale computations should be obviated. Secondly the microstructures shall be made up of geometrically simple perforations that could in principle be manufactured, except for the arbitrary small size.

Looking at the single-scale results shown in Figure 1.1 it becomes apparent that optimized shapes are characterized by both a global distribution of material, strongly depending on the considered loads, and tiny structures in regions with intermediate amount of material. Within small surroundings these structures show similar shapes and smooth transitions, unless they jump to a fundamentally different shape when passing a macroscopic interface. Hence we propose locally periodic perforations on an underlying microscopic lattice, i. e. for every point on the usual macroscopic domain  $x \in D$  there will be an underlying lattice of periodic cells  $\mathcal{Y}(x)$  with microscopic edge length  $\delta$  comprising perforations of geometrically simple shape, which can be described by a small finite set of parameters. Assuming periodicity will ease the mathematical analysis through available concepts from periodic homogenization and enable an efficient algorithmic treatment. The separation of scales is justified in the context of latest achievements in material science, where the characterizing length scale of structures in composites is extremely small compared to the size of the fabricated components.

It is unsettled how two of these periodic lattices will meet at a microscopic interface. Practically we think of a smoothly varying microstructure, so there should be some kind of transition layer or a compatibility condition. In our numerical computations however we will only consider periodic assemblages at macroscopic points with significant distance to each other. We thus ignore such imponderables and content ourselves with the assumption that any effects due to microscopic interfaces can be safely ignored because of the strongly separated scales. Furthermore we will not impose any constraints on the microscopic shapes, except that they should not overlap their representative cell. Neither will we take into account a macroscopic constraint on the variation of the underlying periodic microstructures. We are aware that such conditions are crucial for a real construction but we rather want to enable a most unrestricted evolution of microstructures. As to the incorporation of the mentioned types of constraints we refer to [360, 200, 145] as examples.

### 5.1.2. Intuitive idea

Let us start on the macroscopic scale, where we want to solve an elasticity problem for given loads, as described in Section 3.1 for the classical single-scale setting, and compute cost functionals like the compliance (4.12). Both tasks require evaluations of the bilinear and linear form defined in (3.9), either for certain test functions  $\vartheta$  or already known displacements  $u$ . As long as only macroscopic quantities are involved the integration is straightforward and can be done by numerical quadrature in an actual algorithmic realization. However the material properties represented by the elasticity tensor now depend on the underlying microscopic scale.

Evaluating the bilinear form  $a(\mathcal{O}; u, u) = \int_{\mathcal{O}} C\varepsilon[u] : \varepsilon[u] \, dx$  in a numerical computation amounts to assess the local energy density on several quadrature points. Hence for a fixed macroscopic point  $x \in D$  the locally stored energy due to acting strains and related stresses in the underlying microstructured material has to be evaluated. Here the shape of the locally periodic perforations is known. Furthermore the macroscopic displacement and its Jacobian are available. The latter constitutes a linear approximation to the local displacement in a neighborhood of  $x$  and will be used to probe the influence of the local microstructure. The crucial idea is to use the displacement gradient to set up a linear mapping  $\mathbb{1} + Du(x) \in \mathbb{R}^{2 \times 2}$ , deforming the microscopic lattice. Under the applied linear deformation a microscopic cell problem is considered. Due to the perforations, its solution will in general not be trivial, but lead to a decrease of the microscopic elastic energy, when compared to the purely linear

deformation. Upon proper scaling this corrected microscopic energy can be used as a scale independent approximation to the macroscopic energy density sought after. This intuitive procedure was already sketched exemplarily in Figure 1.2.

### 5.1.3. Formal description

We will now formalize the two-scale model for microstructured shape optimization. To this end let  $\delta$  denote the characteristic microscopic length scale. At each point  $x \in D$  a representative cell  $\mathcal{Y}(x) \subset D^\mathcal{Y} = [0, 1]^2$  with edge length 1 is considered. As before we allow for perforations but require them to keep a distance to the cell boundary. The afore mentioned lattice is obtained via periodic extension, i. e. the local underlying microscopic domain at  $x$  is obtained as  $\mathcal{O}^\delta(x) = \bigcup_{c_i \in \mathbb{Z}^2} \delta Q(c_i + \mathcal{Y}(x))$ , where  $Q$  possibly provides an additional rotation of the lattice. The overall elasticity tensor is correspondingly given by  $C^\delta(x) = C(x, y)$ . As in Section 3.5  $x$  denotes the slow variable varying with order 1 macroscopically and specifying pointwise the microscopic geometric setup via a parameter mapping  $q: D \rightarrow \mathbb{R}^l$ . The second argument  $y := \frac{x}{\delta}$  is the fast variable, rescaled to unit cells, and varies among the actual representative microscopic geometry. Due to the assumption of scale separation, the two spatial variables  $x, y$  can be considered independent. By the periodicity assumption the elasticity tensor  $C: D \times \mathbb{R}^2 \rightarrow \mathbb{R}^{2^4}$  is  $\mathcal{Y}$ -periodic in  $y$ , i. e. for  $c \in Q\mathbb{Z}^2$  there holds  $C(x, y + c) = C(x, y)$  and any considerations on the microscale can be restricted to the representative local cell  $\mathcal{Y}(x)$ .

When looking at the problem set up so far in terms of the dependent variables  $x$  and  $\frac{x}{\delta}$  we are still within the framework of classical elasticity problems of Section 3.1. Resolving the microscopic features by a numerical scheme is however prohibitive due to the required fineness of a computational grid. Indeed, in the present situation typical regularity estimates like  $|u|_{2,2,D} \leq c\delta^{-1}\|f\|_{0,2,D}$  hold. In view of the approximation error in (3.31) the convergence rate then degrades to  $h/\delta$ , cf. [233, Corollary 4.3.] and the preceding discussion therein. This requires to choose a mesh width of the same order of magnitude as the microscopic scale. It would moreover counteract the idea of an independent detached microstructure. We therefore use the approach sketched above to approximate the bilinear form  $a(\mathcal{O}^\delta; u^\delta, u^\delta)$ . Notably it is the only term with microscopic dependence, both the right hand side and any boundary forces are assumed to be defined on the macroscale. The crucial point is to resort to the decoupled perspective and assume a splitting of the displacement into a macroscopically varying part  $u^*$ , depending on  $x$ , and a microscopic part  $\tilde{u}(x, y)$ , being periodic in  $y$  for any fixed  $x$ , in analogy to the setup of the two-scale microstructured domain. Locally, at an arbitrary, fixed point  $x$ , the macroscopic part enters the elastic energy density in terms of its symmetrized gradient  $\varepsilon_x[u^*](x)$ . The microscopic part now is to be determined as the elasticity solution of a microscopic cell problem in presence of the macroscopic displacement linearization. Thus we define the corrector problem as

$$\begin{aligned} \int_{\mathcal{Y}(x)} C(x, y) \varepsilon_y[\tilde{u}](x, y) : \varepsilon_y[\vartheta](y) \, dy &= - \int_{\mathcal{Y}(x)} C(x, y) \varepsilon_x[u^*](x) : \varepsilon_y[\vartheta](y) \, dy \\ \iff: a(\mathcal{Y}(x); \mathcal{R}[u], \vartheta) &= 0 \quad \forall x \in D, \vartheta \in H_{\text{per},0}^1(\mathcal{Y}(x); \mathbb{R}^2). \end{aligned} \quad (5.1)$$

For the newly defined operator  $\mathcal{R}$  we especially have  $\varepsilon_y[\mathcal{R}[u]](x, y) = \varepsilon_x[u^*](x) + \varepsilon_y[\tilde{u}](x, y)$ . The arrangement in (5.1) reveals a linear form on the right hand side for the given macroscopic Jacobian, making the corrector problem a periodic cell problem in weak formulation as

considered in Section 3.4. Its corresponding strong formulation reads

$$\begin{cases} -\operatorname{div}_y C(x, y) \varepsilon_y[\tilde{u}](x, y) = \operatorname{div}_y C(x, y) \varepsilon_x[u^*](x) & \text{in } \mathcal{Y}(x), \\ \tilde{u} \in H_{\text{per},0}^1(\mathcal{Y}(x); \mathbb{R}^2) \end{cases} \quad (5.2)$$

for all  $x \in D$ . In this regard the problem admits for a unique periodic solution  $\tilde{u} \in H_{\text{per},0}^1(\mathcal{Y}(x); \mathbb{R}^2)$  because the right hand side vanishes when integrated against constant test functions, cf. (3.21). Finally the hereby determined two-scale solution is used to evaluate the microscale elastic energy, i. e. we employ the approximation

$$(C^\delta \varepsilon[u^\delta] : \varepsilon[u^\delta])(x) \approx \operatorname{Vol}(D^\mathcal{Y})^{-1} \int_{\mathcal{Y}(x)} C(x, y) \varepsilon_y[\mathcal{R}[u](x, y)] : \varepsilon_y[\mathcal{R}[u](x, y)] \, dy. \quad (5.3)$$

Some aspects of the two-scale model are worthy of a more detailed inspection at this point.

**Remark 5.1** (Inhomogeneous Dirichlet boundary conditions). The varying variable in (5.2) is  $y$  and hence  $\varepsilon_x[u^*](x)$  simply depicts a constant symmetric matrix. Due to linearity, the equation can be rearranged to read

$$-\operatorname{div}_y C(x, y) \varepsilon_y[\tilde{u}(x, y) + (\varepsilon_x[u^*](x))y] = 0,$$

where the matrix  $\varepsilon_x[u^*](x)$  is applied to the vector  $y$ . This superposition resembles the usual procedure for including inhomogeneous Dirichlet boundary conditions in (3.13) or (3.2), given here by  $u^\partial(y) := (\varepsilon_x[u^*](x))y$ . In fact this representation fits the intuitive sketch in Figure 1.2, insofar as an affine displacement is prescribed and the superimposed reaction of the periodic assemblage sought.

**Remark 5.2** (Scale invariance). The approximation of the elastic energy density as defined in (5.3) is invariant w. r. t. scaling of the cell problem. To see this let  $\tilde{\delta} > 0$  denote an arbitrary scaling factor and  $\mathcal{Y}^{\tilde{\delta}} \subseteq D^{\mathcal{Y}^{\tilde{\delta}}} = [0, \tilde{\delta}]^2$  the scaled representative cell with corresponding variable  $y^{\tilde{\delta}} = \tilde{\delta}y$ . Likewise let further quantities defined in the scaled setting be denoted by a superscript  $\tilde{\delta}$ . Then we have e. g.  $\vartheta^{\tilde{\delta}}(y^{\tilde{\delta}}) = \vartheta(y)$ . We now consider the scaled corrector problem and transform it to the reference setting, where  $\mathcal{Y} \subseteq D^\mathcal{Y} = [0, 1]^2$ . In particular for fixed  $x$

$$\begin{aligned} & \int_{\mathcal{Y}^{\tilde{\delta}}} C^{\tilde{\delta}}(y^{\tilde{\delta}}) \varepsilon_{y^{\tilde{\delta}}}[\tilde{u}^{\tilde{\delta}}](y^{\tilde{\delta}}) : \varepsilon_{y^{\tilde{\delta}}}[\vartheta^{\tilde{\delta}}](y^{\tilde{\delta}}) \, dy^{\tilde{\delta}} = - \int_{\mathcal{Y}^{\tilde{\delta}}} C^{\tilde{\delta}}(y^{\tilde{\delta}}) \varepsilon_x[u^*] : \varepsilon_{y^{\tilde{\delta}}}[\vartheta^{\tilde{\delta}}](y^{\tilde{\delta}}) \, dy^{\tilde{\delta}} \\ \iff & \int_{\mathcal{Y}} C(y) \tilde{\delta}^{-1} \varepsilon_y[\tilde{u}](y) : \tilde{\delta}^{-1} \varepsilon_y[\vartheta](y) \tilde{\delta}^2 \, dy = - \int_{\mathcal{Y}} C(y) \varepsilon_x[u^*] : \tilde{\delta}^{-1} \varepsilon_y[\vartheta](y) \tilde{\delta}^2 \, dy \end{aligned}$$

holds, where  $\tilde{\delta}^2$  is the volume element stemming from the transformation and  $\tilde{\delta}^{-1}$  emerges due to the derivatives. Comparing to (5.1) an additional factor  $\tilde{\delta}^{-1}$  is present on the left hand side, which cancels when choosing  $\tilde{u}^{\tilde{\delta}}(y^{\tilde{\delta}}) = \tilde{\delta}\tilde{u}(y)$ . This is supported by the intuitive viewpoint, insofar as a displacement given by a linear mapping is proportional to the extent of the domain and so should be the elastic reaction, at least in the linearized setting.

We now consider approximation (5.3), plug in the scaled periodic correction, and perform the same transformation as before, leading to

$$\begin{aligned} & \operatorname{Vol}(D^{\mathcal{Y}^{\tilde{\delta}}})^{-1} \int_{\mathcal{Y}^{\tilde{\delta}}} C^{\tilde{\delta}}(y^{\tilde{\delta}}) \left( \varepsilon_x[u^*] + \varepsilon_{y^{\tilde{\delta}}}[\tilde{u}^{\tilde{\delta}}](y^{\tilde{\delta}}) \right) : \left( \varepsilon_x[u^*] + \varepsilon_{y^{\tilde{\delta}}}[\tilde{u}^{\tilde{\delta}}](y^{\tilde{\delta}}) \right) \, dy^{\tilde{\delta}} \\ = & \operatorname{Vol}(D^{\mathcal{Y}^{\tilde{\delta}}})^{-1} \int_{\mathcal{Y}} C(y) \left( \varepsilon_x[u^*] + \tilde{\delta}^{-1} \varepsilon_y[\tilde{\delta}\tilde{u}](y) \right) : \left( \varepsilon_x[u^*] + \tilde{\delta}^{-1} \varepsilon_y[\tilde{\delta}\tilde{u}](y) \right) \tilde{\delta}^2 \, dy. \end{aligned}$$



Observing  $\text{Vol} \left( D^{\mathcal{Y}^\delta} \right)^{-1} \tilde{\delta}^2 = 1 = \text{Vol} \left( D^{\mathcal{Y}} \right)^{-1}$  completes our statement of scale invariance.

Due to the preceding remark, it is justified to restrict all considerations of the microscale to the reference frame of length scale 1, as assumed initially. If the full elasticity solution for a microstructured domain is wanted, the scaling is of course relevant and the approximation used in our two-scale model is ultimately given by  $u^\delta(x) \approx u^*(x) + \delta \tilde{u}(x, y)$ .

## 5.2. Application of the two-scale model

In the preceding section the microscale problem has been laid out based on the approximation of a local energy density in terms of  $a(\mathcal{O}^\delta; u^\delta, u^\delta)$  for given macroscopic displacements. We will now be concerned with finding an actual solution to the two-scale elasticity problem for given macroscopic boundary conditions. This can be accomplished in analogy to the single-scale case by searching for minimizers of the two-scale total free energy, cf. Corollary 3.11. Thereby techniques from the calculus of variations will be used. Furthermore the concepts from shape calculus presented in Section 4.1.1 will be transferred to the two-scale setting to infer the sensitivities of the cost w. r. t. the parameters of the underlying microscopic geometries.

### 5.2.1. Solving of the elasticity problem

We consider the two-scale total free energy  $\mathbf{J}^{\text{total}} [\mathcal{O}^\delta; u^\delta] = \frac{1}{2} a(\mathcal{O}^\delta; u^\delta, u^\delta) - l(\mathcal{O}; u^\delta)$  in analogy to Corollary 3.11. In order to determine minimizers we compute the first order necessary condition  $\frac{d}{dt} \mathbf{J}^{\text{total}} [\mathcal{O}^\delta; u^\delta + t\vartheta^\delta] \big|_{t=0} = 0$ . To this end

$$\begin{aligned} \frac{d}{dt} \mathbf{J}^{\text{total}} [\mathcal{O}^\delta; u^\delta + t\vartheta^\delta] &= \frac{1}{2} \int_{\mathcal{O}^\delta} \frac{d}{dt} C^\delta \varepsilon [u^\delta + t\vartheta^\delta] : \varepsilon [u^\delta + t\vartheta^\delta] \, dx \\ &\quad - \int_{\mathcal{O}^\delta} \frac{d}{dt} f \cdot (u^\delta + t\vartheta^\delta) \, dx - \int_{\Gamma_N} \frac{d}{dt} g \cdot (u^\delta + t\vartheta^\delta) \, da(x). \end{aligned}$$

Now we apply the two-scale approach and replace  $u^\delta, \vartheta^\delta$  by  $(u^*, \tilde{u}), (\vartheta^*, \tilde{\vartheta})$  from the space  $H_{\Gamma_D}^1(D; \mathbb{R}^2) \times H_{\text{per},0}^1(\mathcal{Y}; \mathbb{R}^2)$ , respectively. A macroscopic inhomogeneous Dirichlet part would be handled via splitting as before but is not explicitly written here for clarity reasons. According to (5.3) for fixed  $x \in D$  the quadratic term is locally approximated by

$$\int_{\mathcal{Y}(x)} C(x, y) \varepsilon_y [\mathcal{R}[u + t\vartheta](x, y)] : \varepsilon_y [\mathcal{R}[u + t\vartheta](x, y)] \, dy \quad (5.4)$$

and the cell problem reads

$$\begin{aligned} \int_{\mathcal{Y}(x)} C(x, y) \varepsilon_y [\tilde{u} + t\tilde{\vartheta}](x, y) : \varepsilon_y [\vartheta](y) \, dy &= - \int_{\mathcal{Y}(x)} C(x, y) \varepsilon_x [u^* + t\vartheta^*](x) : \varepsilon_y [\vartheta](y) \, dy \\ \forall \vartheta &\in H_{\text{per}}^1(\mathcal{Y}(x); \mathbb{R}^2) \end{aligned} \quad (5.5)$$

with the usual test functions  $\vartheta$ . For the time being let  $\tilde{u}$  and  $\tilde{\vartheta}$  be the unique solutions of the specific cell problems

$$\begin{aligned} \int_{\mathcal{Y}(x)} C(x, y) \varepsilon_y[\tilde{u}](x, y) : \varepsilon_y[\vartheta](y) \, dy &= - \int_{\mathcal{Y}(x)} C(x, y) \varepsilon_x[u^*](x) : \varepsilon_y[\vartheta](y) \, dy, \\ \int_{\mathcal{Y}(x)} C(x, y) \varepsilon_y[\tilde{\vartheta}](x, y) : \varepsilon_y[\vartheta](y) \, dy &= - \int_{\mathcal{Y}(x)} C(x, y) \varepsilon_x[\vartheta^*](x) : \varepsilon_y[\vartheta](y) \, dy, \end{aligned}$$

respectively. Due to the linearity of  $\varepsilon_y$  and  $\varepsilon_x$ , multiplying the second equation by  $t$  and adding both regains a cell problem in the shape of (5.5) with the same right hand side. Consequently  $\tilde{u} + t\tilde{\vartheta}$  is a solution of (5.5) and since the cell problem has a unique solution it already is this very solution. Thus we can insert the determined microscopic solution into the approximation of the quadratic term (5.4), yielding

$$\int_{\mathcal{Y}(x)} C(x, y) (\varepsilon_x[u^* + t\vartheta^*] + \varepsilon_y[\tilde{u} + t\tilde{\vartheta}]) : (\varepsilon_x[u^* + t\vartheta^*] + \varepsilon_y[\tilde{u} + t\tilde{\vartheta}]) \, dy.$$

Exploiting linearity once again we can now take the derivative w. r. t.  $t$  and evaluate at  $t = 0$ , resulting in

$$\int_D \int_{\mathcal{Y}(x)} C(x, y) (\varepsilon_x[u^*] + \varepsilon_y[\tilde{u}]) : (\varepsilon_x[\vartheta^*] + \varepsilon_y[\tilde{\vartheta}]) \, dy \, dx$$

for the quadratic term in the first variation. The linear form was assumed to only depend on functions defined on the macroscale. Indeed, when plugging in our approximation in expanded form and integrating over  $\mathcal{Y}(x)$  for every  $x$ , we obtain

$$\int_D \int_{\mathcal{Y}(x)} \frac{d}{dt} f(x) \cdot (u^*(x) + \delta \tilde{u}(x, y) + t\vartheta^*(x) + t\delta \tilde{\vartheta}(x, y)) \, dy \, dx$$

for the volume forces integral. Due to the enforced vanishing component wise integral mean, integrating the  $y$ -constant  $f$  against microscale functions over  $\mathcal{Y}(x)$  yields zero and only the macroscopic terms remain. The same reasoning holds for the surface integral. Taking the derivative w. r. t.  $t$  and evaluating at  $t = 0$  gives the remaining terms for the first variation. As it has to vanish for all valid  $\vartheta^\delta$  we altogether obtain

$$\begin{aligned} a^M(D; u^*, \vartheta^*) &= l(D; \vartheta^*) \quad \forall \vartheta^* \in H_{\Gamma_D}^1(D; \mathbb{R}^2) \quad \text{with} \\ a^M(D; u^*, \vartheta^*) &:= \int_D \int_{\mathcal{Y}(x)} C(x, y) (\varepsilon_x[u^*] + \varepsilon_y[\tilde{u}]) : (\varepsilon_x[\vartheta^*] + \varepsilon_y[\tilde{\vartheta}]) \, dy \, dx \end{aligned} \quad (5.6)$$

as the first order necessary condition. The linear form is identical to the one in the single-scale setting, cf. (3.9). The newly introduced bilinear form  $a^M$  for the approximating microstructure model depends formally on macroscopic quantities only. Sure enough the microscale is still involved in terms of the cell integral and the periodic correction but this correction is uniquely determined for a given macroscopic strain. Moreover the crucial insight is that both are coupled in virtue of a bounded linear operator. Due to the similarity to the single-scale setting, we find ourselves in a comfortable situation where we can carry over a lot of results.

Most significantly, the derived two-scale approach admits for a unique solution. To this end it is sufficient to check boundedness and coerciveness of the bilinear form  $a^M$  in analogy to

the proof of Theorem 3.8. Regarding boundedness we see

$$\begin{aligned} & \int_D \int_{\mathcal{Y}(x)} C(x, y) (\varepsilon_x[u^*] + \varepsilon_y[\tilde{u}]) : (\varepsilon_x[\vartheta^*] + \varepsilon_y[\tilde{\vartheta}]) \, dy \, dx \\ & \leq \| \| C \| \| \left| \int_D \mathbf{D}u^* : \mathbf{D}\vartheta^* + \int_{\mathcal{Y}(x)} \mathbf{D}\tilde{u} : \mathbf{D}\tilde{\vartheta} + \mathbf{D}u^* : \mathbf{D}\tilde{\vartheta} + \mathbf{D}\tilde{u} : \mathbf{D}\vartheta^* \, dy \, dx \right|. \end{aligned}$$

The first term reproduces the single-scale setting. The mixed terms can be rewritten and estimated like  $\max_{i,j} (\mathbf{D}u^*)_{ij} \operatorname{div}(\tilde{\vartheta}) \cdot \mathbf{1}$ . That way we get an integrated divergence of a  $\mathcal{Y}$ -periodic function, which vanishes by virtue of Lemma 3.13. For the last term we use the Cauchy-Schwartz inequality w. r. t. the cell integral. Altogether this yields

$$a^{\mathbf{M}}(D; u^*, \vartheta^*) \leq \| \| C \| \| \left( |u^*|_{1,2,D} |\vartheta^*|_{1,2,D} + \int_D |\tilde{u}|_{1,2,\mathcal{Y}(x)} |\tilde{\vartheta}|_{1,2,\mathcal{Y}(x)} \, dx \right).$$

Finally the  $H^1(\mathcal{Y}(x); \mathbb{R}^2)$ -norm can be estimated by the local macroscopic strains due to the bounded linear relation. Regarding coerciveness we get by the same computation

$$a^{\mathbf{M}}(D; \vartheta^*, \vartheta^*) \geq c \int_D \varepsilon_x[\vartheta^*] : \varepsilon_x[\vartheta^*] + \int_{\mathcal{Y}(x)} \varepsilon_y[\tilde{\vartheta}] : \varepsilon_y[\tilde{\vartheta}] \, dy \, dx.$$

At this point Korn's inequality, Theorem 3.7, is used both for the macroscopic part on  $D$  and the microscopic part on  $\mathcal{Y}$ . Finally the  $H^1(\mathcal{Y}(x); \mathbb{R}^2)$ -norm is once again estimated by the macroscopic strain as before.

### 5.2.2. Optimization of microscopic geometries

The key aspect of this thesis is the numerical optimization of microscopic geometries. We will therefore transfer the concepts from Section 4.1 to the deployed two-scale setting. As objective we will focus on a two-scale approximation of the total free energy that was already tackled above. Note that, due to the definition of the weak problem (5.6) and the identity (4.12), this equals the compliance cost functional. For optimization we allow the shape of microscopic perforations in the locally periodic cell problems to vary. To this end we assume a family of smooth functions  $\gamma[q(x)]: [0, 1] \mapsto \partial\mathcal{Y}(x) \setminus \partial D^{\mathcal{Y}}$  for every  $x \in D$ , which parametrize the connected components of each perforation's boundary within the unit cell. Here  $q \in \mathbb{R}^l$  denotes an, ideally short, vector of coefficients, constituting the actual degrees of freedom that influence the parametrization and shall be optimized. Furthermore we impose a constraint on the overall volume stemming from the local material fractions  $\theta(x)$  in each microscopic cell. Thus the optimization problem is finally given by

$$\begin{aligned} & \min_q -2 \mathbf{J}^{\mathbf{M}}[q; u^*] \quad \text{s. t.} \quad \int_D \theta \, dx = \Theta, \\ & \mathbf{J}^{\mathbf{M}}[q; u^*] := \frac{1}{2} a^{\mathbf{M}}(q; u^*, u^*) - l(u^*). \end{aligned} \tag{5.7}$$

Here we adapted the arguments of the bilinear and linear form to reflect the actual dependence on the parameters of the microscopic shapes.

For solving the optimization problem we are interested in gradient information and would therefore like to apply the results of Section 4.1.1. In view of the velocity method we can

generate a vector field that varies the perforations' boundaries in each microscopic cell  $\mathcal{Y}(x)$  for each direction  $\beta \in \mathbb{R}^l$  in the coefficient space via

$$V[x; \beta](t, y) := \left( \frac{d}{dq} \gamma[q(x)](s) \right) (\beta) \quad (5.8)$$

for every point  $y \in \partial\mathcal{Y}(x) \setminus \partial D^{\mathcal{Y}}$  with  $y = \gamma[q(x)](s)$  for some corresponding  $s$ . Note that the defined vector field is constant w. r. t. the artificial time  $t$ , which is in line with Definition 4.2 of the Hadamard shape derivative. Furthermore note that in order to satisfy the prerequisites of the definitions, technically a suitable extension to the whole domain  $\overline{D^{\mathcal{Y}}}$  would have to be constructed, which we will however not detail here. The total derivative of the total free energy is initially given by

$$\begin{aligned} \frac{d}{dq} \mathbf{J}^M[q; u^*](\beta) = \\ \int_D d_{\mathcal{Y}(x)} \left( \frac{1}{2} \int_{\mathcal{Y}(x)} C(x, y) (\varepsilon_x[u^*] + \varepsilon_y[\tilde{u}]) : (\varepsilon_x[u^*] + \varepsilon_y[\tilde{u}]) \, dy \right) (V[x; \beta]) \, dx. \end{aligned}$$

Note that purely macroscopic quantities vanish under the derivative as the macroscopic domain is independent of the chosen parameters  $q$ . Furthermore note that the defined velocity field (5.8) enters naturally here by virtue of the chain rule. To continue we need to observe the implicit dependence of the two-scale solution  $(u^*, \tilde{u})$  on the shape of the microscopic domain. Due to the common structure, setting up the Lagrangian, deriving the dual problem and computing the total derivative is a rephrasing of the procedure in the single-scale setting detailed in Section 4.1.4. The major difference is the two-scale product space  $H_{\Gamma_D}^1(D; \mathbb{R}^2) \times H_{\text{per},0}^1(\mathcal{Y}; \mathbb{R}^2)$  that is used in lieu of  $\mathcal{V}$ . A comprehensive derivation is included in Appendix B. In particular, the adjoint solution still is trivial, given by  $(p^*, \tilde{p}) = (0, 0)$ , and the total derivative finally reads

$$\begin{aligned} \frac{d}{dq} (-2 \mathbf{J}^M[q; u^*]) (\beta) &= \frac{d}{dq} (-a^M(q; u^*, u^*)) (\beta) \\ &= - \int_D \int_{\partial\mathcal{Y}(x)} (V[x; \beta] \cdot n(y)) C(x, y) (\varepsilon_x[u^*] + \varepsilon_y[\tilde{u}]) : (\varepsilon_x[u^*] + \varepsilon_y[\tilde{u}]) \, da(y) \, dx. \quad (5.9) \end{aligned}$$

### 5.2.3. Numerical treatment

In the preceding sections the two-scale approach has been described extensively. In order to gain an approximation of the, still unknown, macroscopic displacement  $u^*$  it is now straightforward to apply the finite element approach. As was detailed in Section 3.6.1 we consider a computational grid  $\mathcal{M}_h$  covering the macroscopic domain  $D$ , select a suitable finite element space  $\mathcal{V}_h^{(k)}$ , and write the unknown macroscopic displacement as a linear combination of basis functions via its Lagrangian interpolant  $\mathcal{I}_h^{(k)}[u^*]$ . Since the linear form in the two-scale weak formulation coincides with the one in the single scale setting we obtain the same right hand side in the discrete system as before. Concerning the bilinear form we need to compute  $a^M(q; (\psi^*)_i^k, (\psi^*)_j^l)$  for given pairs of macroscopic basis functions via numerical quadrature. To this end, periodic corrections have to be computed for macroscopic strains  $(\psi^*)_i^k(x_m)$  at each quadrature point  $x_m \in D$ , which act as given affine displacements, cf. Remark 5.1. For

the solution of the corresponding cell problems (5.1) in  $\mathcal{Y}(x_m)$  the boundary element method is employed, as described in Section 3.6.2. It provides numerical approximations  $(\tilde{\psi}_h)_i^k$  of the displacement correction and its normal stresses on the boundary. The volume integral in the two-scale approximation of the elastic energy (5.3) is conveniently rewritten as a boundary integral, cf. (3.11), s. t. the stiffness matrix can be setup with entries

$$(L^M)_{ij}^{(k,l)} := \int_D \int_{\partial\mathcal{Y}(x)} C(x, y) (\varepsilon_x [(\psi^*)_i^k] + \varepsilon_y [(\tilde{\psi}_h)_i^k]) n \cdot ((\psi^*)_j^l + (\tilde{\psi}_h)_j^l) da(y) dx.$$

The overall discretized two-scale approximation can then be determined as the solution of a sparse linear system of equations, just as in the single-scale setting. In particular all properties from Remark 3.22 still hold. To this end note that a vanishing macroscopic strain results in zero displacement for the cell problem.

**Remark 5.3** (Symmetrization). It turns out to be numerically favorable to replace the integrand in  $(L^M)_{i,j}^{(k,l)}$  with

$$\begin{aligned} & \frac{1}{2} \left( C(x, y) (\varepsilon_x [(\psi^*)_i^k] + \varepsilon_y [(\tilde{\psi}_h)_i^k]) n \cdot ((\psi^*)_j^l + (\tilde{\psi}_h)_j^l) \right. \\ & \left. + C(x, y) (\varepsilon_x [(\psi^*)_j^l] + \varepsilon_y [(\tilde{\psi}_h)_j^l]) n \cdot ((\psi^*)_i^k + (\tilde{\psi}_h)_i^k) \right) \end{aligned}$$

by duplicating the expression and applying partial integration in reverse w. r. t. alternating functions. Although being equivalent, this representation ensures symmetry of the resulting matrix, even in presence of any numerical inaccuracy.

With the full two-scale solution at hand the compliance objective can be evaluated in analogy to the entries of the stiffness matrix. Its shape derivative can be computed using (5.9). Here it is fortunate that the shape derivative is given by a boundary integral as well. However the integrand involves full Jacobians whereas we only have numerical approximations of the normal stress at our disposal. As a remedy finite differences of the periodic displacements on the boundary provide an approximation of the stress in tangential direction, which can then be used to reconstruct the required terms, cf. [182, Section 5.5.1].

## 5.3. Relation to other approaches

Our two-scale model is linked to other approaches for the treatment of multiscale problems, which we will now briefly discuss. In view of Section 3.5 a relation to periodic homogenization is immanent. For us this enables a direct computation of locally effective material properties on the macroscopic scale. Furthermore our model falls under the general paradigm of the *heterogeneous multiscale method (HMM)*. This allows to adopt discretization error estimates for homogenization type problems found in the literature. Finally it can be linked to the works by Barbarosie and Toader [59, 61], whose approach to elastic two-scale optimization turns out to be equivalent to ours.

### 5.3.1. Periodic homogenization

The periodic cell problems considered at each macroscopic point and the assumed expansion  $u^\delta(x) \approx u^*(x) + \delta \tilde{u}(x, y)$  of the two-scale model coincide with the setting treated in Section 3.5.

We can therefore carry over the results to our local problems. In particular our defined corrector problem (5.2) has the same structure as the cell problems in homogenization (3.23). The only difference is that we prescribe an arbitrary macroscopic strain matrix  $\varepsilon_x[u^*]$  whereas special base matrices were used in the homogenization context. From the correctors obtained for those matrices the homogenized effective elasticity tensor could be derived entry wise, cf. (3.27). The same type of expression is found in our approximation of the elastic energy (5.3). Thus we can directly obtain entries of the effective elasticity tensors  $C^*(x)$  at each macroscopic point  $x \in D$  by applying our two-scale approach to the synthetic strains  $\varepsilon_{ij}$ ,  $i, j = 1, 2$ . Conversely, when macroscopic strains  $\varepsilon_x[u^*]$  are expressed as linear combinations of  $\varepsilon_{ij}$ , the corresponding linear combination of (3.27) shows that  $C^* \varepsilon_x[u^*] : \varepsilon_x[u^*]$  equals (5.3). Consequently the bilinear form  $a^M(D; u^*, \vartheta^*)$  defined in (5.6) can equivalently be written in a purely macroscopic fashion as

$$a^M(D; u^*, \vartheta^*) = \int_D C^*(x) \varepsilon[u^*] : \varepsilon[\vartheta^*] \, dx. \quad (5.10)$$

A further aspect is that our local problems are amenable to the theory of two-scale convergence. Thus the error estimate of Theorem 3.17 holds and shows that our two-scale approach indeed approximates the fully resolved solution.

### 5.3.2. Heterogeneous multiscale method

The *heterogeneous multiscale method (HMM)* as introduced in [163, 161] initially depicts an abstract methodology for treating multiple scales or multiple levels of physics. It is termed heterogeneous as the modeling and the employed methods may be entirely different. The building blocks are a macroscopic and a microscopic scheme, which solve the respective problems numerically in an autonomous fashion, and compression and reconstruction operators, which pass information between the involved scales. The key advantage is that no adaptation of the macroscopic scheme to the microscopic problem is required. Instead whenever information is missing on the macroscopic scale a microscopic cell problem is considered. That way the computational complexity does not increase when  $\delta$  is decreased and it is overall restricted as these microscopic probes are only considered on a small set of points, e. g. in the course of numerical quadrature. In our proposed two-scale model the macroscopic scheme is a conventional finite element approach whereas on the microscale we employ the boundary element method for the solution of periodic cell problems. The reconstruction operator assigns a microscopic periodic correction  $\tilde{u}$  to a given macroscopic displacement  $u^*$  and is precisely given by  $\mathcal{R}[u]$  in (5.1). Conversely the compression operator  $\mathcal{Q}$  eliminates microscopic information, s. t.  $\mathcal{Q}[u^* + \delta\tilde{u}](x) = u^*(x)$ . In our situation it is realized by integration on the local cell  $\mathcal{Y}(x)$  and utilizing that the integral mean of the periodic correction vanishes.

Homogenization problems similar to ours, but in the scalar context, are addressed in [162]. Analytical results are elaborated in [164], based on canonical properties of the underlying elliptic equations, and in [2], where the analysis is extended to the fully discrete setting. Among others, the following important error estimates are obtained.

**Theorem 5.4.** *Under appropriate regularity assumptions there holds*

$$\|u^* - u_h^*\|_{1,2,D} \leq c(h + h_\delta^2)\|f\|_{0,2,D}, \quad (5.11)$$

$$\|u^* - u_h^*\|_{0,2,D} \leq c(h^2 + h_\delta^2)\|f\|_{0,2,D}, \quad (5.12)$$

$$\sum_{E \in \mathcal{M}_h} \|\nabla(u^\delta - u_h^* - \delta \tilde{u}_h)\|_{0,2,E} \leq c(\sqrt{\delta} + h + h_\delta)\|f\|_{0,2,D}. \quad (5.13)$$

In particular, (5.11) [2, (3.18)] and (5.12) [2, (3.19)] measure the approximation error of the homogenized solution w. r. t. the macroscopic and microscopic discretization  $h$  and  $h_\delta$ , respectively. They correspond to [164, (1.11) and (1.12)], but were improved to not depend on  $\delta$  [5, Appendix A], and take into account the microscopic error. The approximation of the fully resolved multiscale solution by the reconstructed numerical solution is measured in (5.13) [2, (3.26)] and corresponds to [164, (1.16)], cf. also Theorem 3.17. The results are extended to the setting of linearized elasticity in [3]. To this end, the approximation errors w. r. t. the displacement  $u$ , the strain tensor  $\varepsilon[u]$ , the stress tensor  $\sigma$ , and the homogenized coefficients  $C_{ijkl}^*$  are estimated. In [313] the discretization of the heterogeneous multiscale method is considered as well, but based on a direct finite element discretization of the two-scale homogenized equation, which is essentially (5.6) in our context. Results include an a-priori estimate, in line with (5.13), and an a posteriori estimate, which allows to steer an adaptive algorithm. We retrace its derivation in the context of our problem in Appendix B.2.

### 5.3.3. Works by Barbarosie and Toader

In a series of papers Barbarosie and Toader developed a methodology for multiscale shape optimization that turned out to be equivalent to our approach. At first, in [59, 60], only periodic homogenization problems like our cell problems are considered. As described in the preceding section it is straightforward to derive a macroscopic effective elasticity tensor from the microscopic geometries. Some entries of this tensor are directly related to certain characteristic elastic quantities, e. g.  $C^* \mathbb{1} : \mathbb{1}$  yields the bulk modulus, cf. (3.8). The key idea thus is to prescribe a strain  $A \in \mathbb{R}_{\text{sym}}^{2 \times 2}$  and solve a cell problem for the *linear plus periodic* function  $u = Ax + \tilde{u}$  with  $\tilde{u} \in H_{\text{per}}^1(\mathcal{Y}(x); \mathbb{R}^2)$ . Upon insertion into the formula for the homogenized tensor, cf. (3.26), the desired quantity is evaluated. At this point the analogy to our approach is most evident. The linear part  $A$  corresponds to our macroscopic strain tensor that enters the corrector problem (5.1). As mentioned in Remark 5.1 it can be regarded as an inhomogeneous Dirichlet boundary condition, just as depicted in Figure 1.2. As to the implementation, the authors set up a volume constrained optimization problem for the shape of perforations on the unit torus, resembling the unit cell with periodic boundary conditions. The microscopic geometry is described by a level set function that is evolved in the course of optimization. Furthermore the topological derivative is employed to possibly nucleate additional holes from time to time. The approach has been continuously advanced. A recent publication [57] deals with multi-objective optimization for obtaining auxetic materials, i. e. those with negative Poisson ratio.

In [61] the authors transfer their concept to a two-scale setting. They consider a macroscopic domain with underlying microscopic periodic cells like we do. Correspondingly linear plus periodic functions are assumed at each macroscopic point. By using basis strains as described above effective elasticity tensors are obtained and used to solve the macroscopic elasticity problem and evaluate the compliance objective. Optimization is done in analogy to the earlier

periodic setting. The approach was further extended in [62], where not only the shape of the perforations but also the spanning vectors for the local cells are subject to optimization. In conclusion both methodologies for multiscale shape optimization coincide. The approach by Barbarosie and Toader was developed in a bottom-up manner, starting from the periodic cell problems, whereas ours was initiated from macroscopic observations and derived top-down.

## 5.4. Investigated microstructure models

In this section we present the investigated models which comprise microscopic shapes within our two-scale framework as well as single-scale models with effective material properties used for comparison. Due to the boundary element method, employed for solving the microscopic cell problems, only the one dimensional boundary of the perforation needs to be discretized. This allows for a convenient and flexible investigation of different microstructure types. Our focus is on simple constructions with few design parameters. Still it should be possible to find layouts that are capable of bearing typical loadings encountered in shape optimization problems adequately. Figure 5.1 shows an overview of the constructions considered.

### 5.4.1. Ellipsoidal shaped perforations

As the starting point we choose an ellipsoidal perforation as a very simple shape with smooth parametrization, see Figure 5.1(a). Unequal scaling of the semiaxes allows for a prevailing direction in which loads are supported. An additional rotation enables the thereby generated anisotropic effective material to align with the main loading direction. For the ease of notion we assume the unit cell to be centered at the origin, i. e.  $D^{\mathcal{Y}} = [-\frac{1}{2}, \frac{1}{2}]^2$ . The boundary of the perforation is then given by

$$\gamma[q](s) = Q(q_3) \begin{pmatrix} q_1 \frac{1}{2} \cos(s) \\ q_2 \frac{1}{2} \sin(s) \end{pmatrix}, \quad s \in [0, 2\pi],$$

where  $Q$  denotes the usual matrix for a rotation by  $q_3$ . To prevent the perforation from collapsing and ensure numerical stability in the nearby parameter regime we require the scaling parameters to be bounded from below by a small constant. In our numerical implementation we choose  $c = 10^{-6}$ . Likewise we require a bound from above to prevent the perforation from outreaching the cell boundary. This means that the inequality constraints

$$0 < c \leq q_i \leq 1 - c, \quad i \in \{1, 2\}, \quad (5.14)$$

have to hold throughout the optimization process. On the contrary the rotation parameter need not be bounded. The volume of the remaining area in the unit cell is given by

$$\theta = 1 - \frac{1}{4} q_1 q_2 \pi, \quad (5.15)$$

which enters the macroscopic overall volume equality constraint, cf. (5.7). Following Section 5.2.2 it is straightforward to compute the shape derivatives of the cost functional w. r. t. the design parameters.

Due to the underlying assumption of periodic microstructures, the current description does not allow for alternating shapes of the perforations, as could be observed in the single-scale setting, cf. Figure 1.1. However our modeling can easily be extended by dividing each unit cell



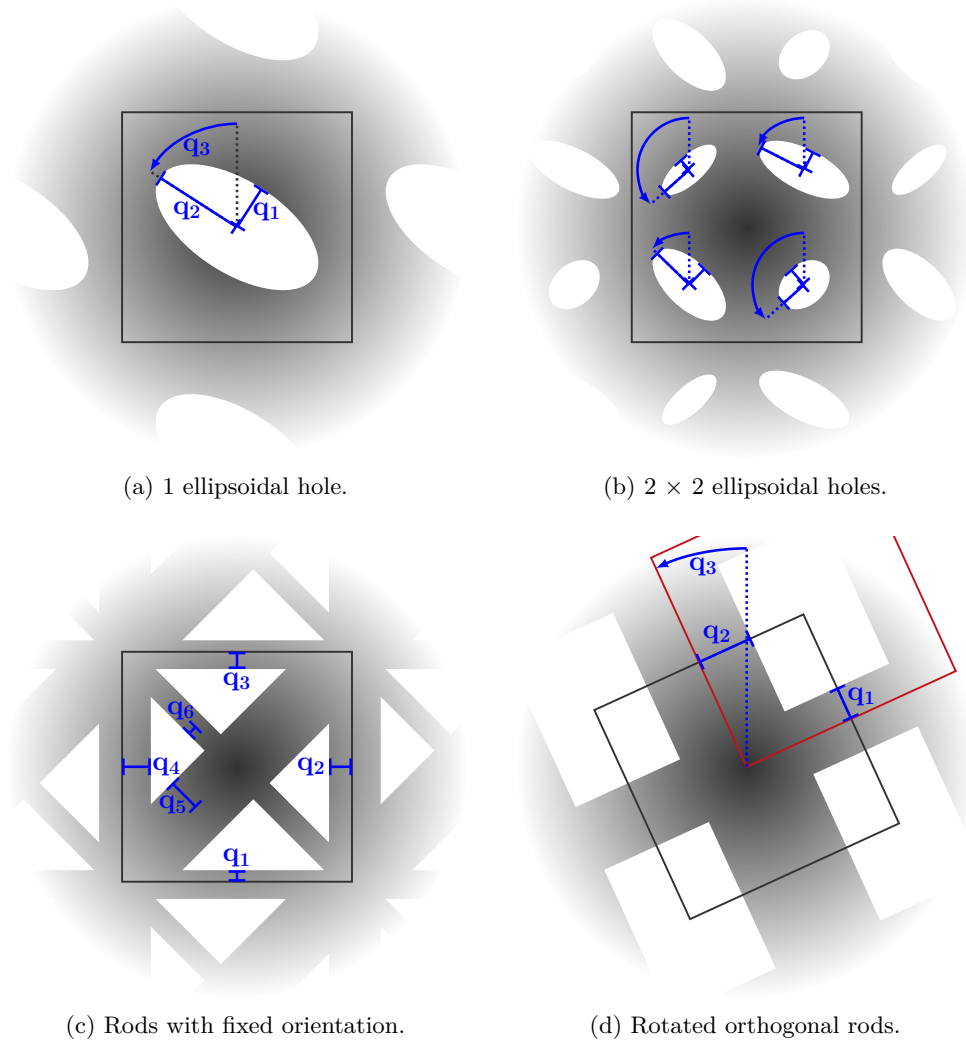


Figure 5.1.: Sketches of periodic microscopic geometries with indicated design parameters.

uniformly into subcells with individually parametrized perforations. See Figure 5.1(b) for a sketch with four individual ellipsoidal holes. Every aspect discussed so far remains applicable, only the reduced size of the individual sub cells has to be observed.

**Remark 5.5.** The presented geometric description implies several ambiguities. The rotation parameter is only determined up to additional multiples of  $\pi$ . It is furthermore meaningless if the scaling parameters coincide and a circle is represented. If the scaling parameters are swapped and the rotation is adapted adequately by  $\frac{\pi}{2}$  again the same shape is obtained.

**Remark 5.6.** The largest perforation possible is a circle whose radius attains the upper bounds of (5.15). The resulting body is obviously not stiff due to the tiny fillets that remain

between neighboring holes. However the volume of the remaining material still is about  $1 - \frac{\pi}{4} \approx 21\%$ , which is lost for the other cells.

### 5.4.2. Rods with fixed orientation

Another kind of construction, which might reflect an intuitive approach for building a supporting shape, makes use of rods with different orientations and thicknesses. In this first model we fix the orientation and consider six rods that are aligned horizontally, vertically and along both diagonal directions, see Figure 5.1(c). This results in four perforations that are isosceles right triangles and are determined by the position of the vertices at the base. Within  $D^{\mathcal{Y}} = [0, 1]^2$  they are given by

$$\begin{aligned} a^{\text{bottom}} &= \begin{pmatrix} q_5\sqrt{2} + q_1 \\ q_1 \end{pmatrix}, & b^{\text{bottom}} &= \begin{pmatrix} 1 - (q_6\sqrt{2} + q_1) \\ q_1 \end{pmatrix}, \\ a^{\text{right}} &= \begin{pmatrix} 1 - q_2 \\ q_6\sqrt{2} + q_2 \end{pmatrix}, & b^{\text{right}} &= \begin{pmatrix} 1 - q_2 \\ 1 - (q_5\sqrt{2} + q_2) \end{pmatrix}, \\ a^{\text{top}} &= \begin{pmatrix} 1 - (q_5\sqrt{2} + q_3) \\ 1 - q_3 \end{pmatrix}, & b^{\text{top}} &= \begin{pmatrix} q_6\sqrt{2} + q_3 \\ 1 - q_3 \end{pmatrix}, \\ a^{\text{left}} &= \begin{pmatrix} q_4 \\ 1 - (q_6\sqrt{2} + q_4) \end{pmatrix}, & b^{\text{left}} &= \begin{pmatrix} q_4 \\ q_5\sqrt{2} + q_4 \end{pmatrix}. \end{aligned}$$

A piecewise parametrization for each triangle is obtained by considering convex combinations of the vertices and from those it is straightforward to deduce the velocity fields entering the shape derivative. The thickness parameters must be bounded from below in order to maintain a small distance of the perforations to each other, i. e.

$$0 < c \leq q_i, \quad i \in \{1, \dots, 6\}.$$

Individual upper bounds could be considered as well, but it is even more restrictive to ensure that the triangular perforations do not collapse. To this end it is sufficient to require that the length of the bases does not go to zero, which for the bottom triangle reads as

$$0 < c \leq b^{\text{bottom}} - a^{\text{bottom}}$$

and likewise for the others. Finally some combinations of the thickness parameters lead to perforations that do not have a triangular shape anymore. In the practical implementation this would require to insert another vertex and another segment into the polygonal arc. With suitable constants for numerical stability, like  $c$  above, this transition cannot be realized in a smooth manner and might introduce numerical inaccuracies that could impede an optimization algorithm. We therefore introduce another set of constraints that preserves the triangular shape. For the bottom triangle it is given by

$$0 < c \leq a^{\text{bottom}} - q_4, \quad 0 < c \leq q_2 - b^{\text{bottom}} \tag{5.16}$$

and likewise for the others. The local volume is computed by the volumes of the triangles subtracted from 1.

**Remark 5.7.** In contrast to the ellipsoidal holes above the boundary of the perforations here is not smooth anymore. While this is noncritical for the existence of a solution and also does not hinder the boundary element method from producing a sound numerical approximation, the velocity field for the variation of the boundary is non-smooth either and therefore violates the prerequisites of lemmata 4.3 and 4.4. As a fully accurate remedy one could replace the kinks at the vertices of the triangles by rounded corners with a very small diameter. For this smoothed boundary the theory is valid and the shape derivative could be computed. The original triangle would be recoverable by passing to the limit. It then seems obligatory to resolve the rounded corners by several discretization points on the boundary in a numerical scheme, especially since it is known that the first derivatives might exhibit a singularity at reentrant corners. On the other hand such a singularity can never be fully resolved numerically and tiny segments near the corner would balance its contribution to the boundary integral of the shape derivative (5.9). Practically our implementation does not allow to distribute the discretization points in the indicated non uniform way. Moreover we are necessitated to keep the number of degrees of freedom low in order to save computation time. Therefore we will actually not work with the smoothed boundary and presume that its influence is in the range of the immanent discretization error.

**Remark 5.8.** Ambiguities are introduced by the individual thickness parameters at the top and bottom and at the left and right hand side, respectively. It would alternatively be possible to choose  $q'_1 = \frac{1}{2}(q_1 + q_3)$ ,  $q'_2 = \frac{1}{2}(q_2 + q_4)$ ,  $q'_3 = q_5$ , and  $q'_4 = q_6$  as the only design parameters.

**Remark 5.9.** While it is possible to choose the maximal thickness for a diagonal rod and leave the others at minimal thickness, this is not possible for the vertical or horizontal rods due to the triangular shape constraint.

### 5.4.3. Rotating orthogonal rods

In this second model we only consider two rods in orthogonal directions with varying thickness and let the whole periodic lattice rotate freely to keep the rods connected over the cell boundary, see Figure 5.1(d). Due to periodicity, it is equivalent to describe a cell with a rectangular shaped hole, see the red marking in Figure 5.1(d). Here the inner boundary has less segments and therefore eases the practical implementation. For  $D^{\mathcal{Y}} = [-\frac{1}{2}, \frac{1}{2}]^2$  the corners of the unrotated rectangular hole are given by

$$a = \begin{pmatrix} -\frac{1}{2} + q_2 \\ -\frac{1}{2} + q_1 \end{pmatrix}, \quad b = \begin{pmatrix} \frac{1}{2} - q_2 \\ -\frac{1}{2} + q_1 \end{pmatrix}, \quad c = \begin{pmatrix} -\frac{1}{2} - q_2 \\ \frac{1}{2} - q_1 \end{pmatrix}, \quad d = \begin{pmatrix} \frac{1}{2} + q_2 \\ \frac{1}{2} - q_1 \end{pmatrix}.$$

The rotation is realized by rotating the mandated affine displacement profile in the opposite direction, i. e. by  $-q_3$ . This changes the frame of references but our quantities of interest, as e. g. the elastic energy, are invariant w. r. t. these changes. Again a piecewise parametrization is obtained by considering convex combinations of the respective vertices and the velocity fields are deduced. The explanations of Remark 5.7 apply again. Ambiguities in the design parameters occur comparable to the ellipsoidal perforations, described in Remark 5.5. The inequality constraints

$$0 < c \leq q_i \leq \frac{1}{2} - c, \quad i \in \{1, 2\},$$

prevent the perforations from collapsing and leaving the unit cell and the volume is given by the volume of the rectangle subtracted from 1.

**Remark 5.10.** In contrast to the others, this model allows for a nearly void unit cell.

## 5.5. Aspects of practical realization

In this section we describe all the technical details required to finally obtain a fully practical algorithmic scheme of the developed two-scale shape optimization model.

### 5.5.1. Discrete spaces

In Section 5.2.3 the discrete realization of the two-scale model was described, including the solving of the microscopic and macroscopic elasticity problems and the evaluations of the two-scale cost functional and its derivative w. r. t. design parameters. It remains to fix the concrete setup of the employed numerical approaches. Besides the two-scale displacement, also the parameter function  $q$ , which is to be optimized, needs to be considered. So far  $q$ , and thus the effective macroscopic elasticity tensor  $C^*(x)$ , was assumed to be smoothly varying and hence it would take different values at any points occurring in the course of numerical quadrature. Such a situation is known from physical problems involving highly heterogeneous media. Building upon *Strang's first lemma* one can show that the error caused by sampling the continuously varying coefficient only at discrete quadrature points can be controlled by the anyway existing error caused by the approximation of the continuous solution, see [128, Theorem 4.1.6, Exercise 4.18]. The upshot is that a quadrature scheme that would evaluate the bilinear form exactly for constant coefficients is sufficient. However we are not only interested in evaluating the effective elasticity tensor but also in its optimization. To this end it seems counterintuitive that the number of degrees of freedom available for optimization is dictated by a numerical parameter. Consequently the coefficient function  $q$  needs discretization as well, and the most easy choice is to put up a piecewise constant approximation, i. e.  $q_h \in \mathcal{V}_h^{(0)}(\mathcal{M}_h)$ . In fact we implemented both versions but focused on the piecewise constant setting for multiple reasons. Firstly it seemed more natural to us to discretize the parameter function as well, secondly we observed checkerboard-like instabilities if we allowed varying coefficients, and thirdly it enabled a comparison to the well-established literature. While we did not find references for optimization in the smoothly varying setting, the piecewise constant choice is classical, see e. g. [79], a textbook on the topic of material distribution problems. Likewise it is a known fact that numerical schemes dealing with piecewise constant densities are also prone to checkerboard instabilities, cf. Section 5.5.4. Common suggested remedies are perimeter penalization, filtering, or the use of higher order elements. The first option is ineligible for our work as we are aiming for a relaxed, unconstrained setting. Filtering, e. g. averaging of neighboring coefficients, would ruin the spatial resolution of parameters determined by our, possibly costly, optimization scheme. So we finally resorted to higher order finite elements on the macroscale. The classical, most simple choice for second order partial differential equations in weak formulation (3.29) is  $\mathcal{V}_h^{(1)}$ , the finite element space of piecewise linear functions. Consequently we are using  $\mathcal{V}_h^{(2)}$ , the space of quadratic functions. On a triangle, a quadratic polynomial is uniquely determined by six values, on each vertex and on each edge midpoint, and spanned by Lagrangian basis functions written in terms of barycentric coordinates. On a rectangle, nine values, on each vertex, on each edge midpoint, and in the center, are required and basis functions can be set up as tensor products of one dimensional quadratic functions, defined along each spanning direction of the rectangle and referred to as *biquadratic*, cf. [128, Section 2.2].

### 5.5.2. Implementation of the two-scale elasticity problem

Our algorithm builds upon the `QuocMesh` library<sup>1</sup>, developed by the research group of Prof. Dr. Martin Rumpf at the Institute for Numerical Simulation of the University of Bonn, and available under an open source license. Its main focus is on finite element based numerical analysis of various problems motivated from physics and imaging in computer science. A complete framework for the boundary element method applied to elasticity problems is included as well. The library is written in the `C++` programming language, follows the object oriented paradigm, and makes extensive use of template programming to provide high performance while retaining flexibility.

The central part of our code is an `Evaluator` class that provides an interface to every aspect of the two-scale shape optimization scheme. It holds the macroscopic finite element matrix and a `Coupling` class designated to communicate with the microscopic models. This class hooks into the `QuocMesh` finite element operators and triggers the solution and evaluation of microscopic cell problems needed during assembly of the macroscopic matrix. An overview of the software design is given in Appendix C. As a special case the call of a microscale problem can be superseded by the evaluation of a single-scale elastic energy, as e. g. in the context of sequential lamination where the effective tensor is known. The energy and the gradient needed for optimization are evaluated by computing (5.7) and (5.9) using numerical quadrature.

For the macroscale problem we use a uniform mesh with quadratic elements dividing the unit cell. Each element is of size  $2^{-l} \times 2^{-l}$  for  $l \in \mathbb{N}$ , referred to as *level*. Due to the uniformity, an individual element need not be stored as an object with vertices, edges, and a transformation to a reference element. Instead values at given quadrature points for the chosen type of basis functions are always identical and are therefore cached upon the first instantiation of the used finite element operator class. Indexing is done implicitly by assuming a lexicographic ordering, which leads to sparse matrices with banded structure. For grid adaptive computations the `QuocMesh` library supports refinement of individual cells by uniform subdivision into four *child* elements. Additionally a maximal difference of one level between neighboring elements is enforced. Organization of the actual elements is realized in a hierarchical *quadtrees* structure. Thereby indexing can be done via a fast hashing strategy, where the level and the position of an element in the tree is used to obtain a unique identifier, see Figure 5.2 for an illustration. If

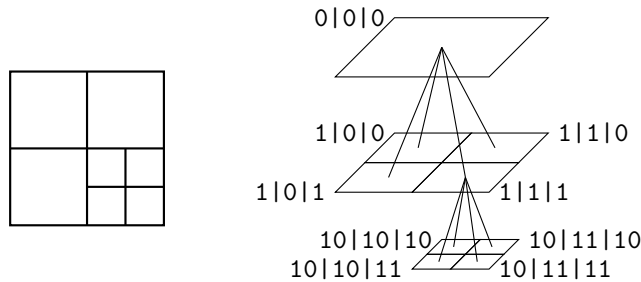


Figure 5.2.: Adaptive grid and illustration of the quadtree structure with binary identifiers of the elements.

neighboring elements differ in their level, condition (3) of the finite element method described

<sup>1</sup><https://archive.ins.uni-bonn.de/numod.ins.uni-bonn.de/software/quocmesh/index.html>

in Section 3.6.1 is violated due to a generated *hanging node*. This is handled subsequently by constraining its value to the value obtained on the opposing, non-refined element. Concerning quadrature we use a tensor product Gaussian quadrature rule of order 5.

The microscopic models are realized in separate classes derived from a common interface class and are easily exchangeable due to the template programming. They set up the polygonal boundary based on passed design parameters, define periodic boundary conditions, and prescribe the supplied affine displacement part. Evaluation of boundary element operators as described in Section 3.6.2, assembly of the system matrix, and its solution are undertaken by the `QuocMesh` boundary element module, see [259, Section 6.1, 6.2] for technical details. Furthermore the constraints on the design parameters and the volume fraction are provided. The number of discretization points on the boundary is chosen individually for each type of microstructure. Details will be discussed in Section 6.1.3.

### 5.5.3. Implementation of the optimization algorithm

For optimization we rely on the open source software `Ipopt`<sup>2</sup> [409, 410] for constrained finite dimensional optimization, which has been successfully applied to PDE constrained optimization problems previously, e. g. in [380]. For a summary of the involved theory and methods see [182, Chapter 6]. A class implementing the abstract C++ interface of `Ipopt` was created. It holds an `Evaluator` object and is therefore able to access every information required by `Ipopt` while the concrete realization stays separated. `Ipopt` internally maintains a C-type array of the design parameters  $q$  that are passed through the interface to the microscopic models where the corresponding set is accessed using the number of the macroscopic cell. Constraints on those parameters are implemented as inequality constraints. The global volume condition leads to an additional equality constraint. A termination threshold of  $10^{-4}$  and user-scaling with an objective scaling factor typically about 100 was selected.

### 5.5.4. Implementation of the sequential lamination algorithm

The sequential lamination model is adduced in this work as an optimal microstructure for comparison. As its optimal parameters and the resulting homogenized elasticity tensor can be computed explicitly, it is unnecessary to apply a gradient based optimization algorithm. Instead we reimplemented the alternating scheme proposed in [12]. Starting with some initialization for the piecewise constant elasticity tensor field, the elasticity problem is solved using the single-scale specialization of the finite element framework described above. From the obtained strains stresses are computed using the current elasticity tensors. Optimal lamination parameters are deduced using (4.20) and the effective tensors are updated using (4.21). In order to exactly fulfill the volume constraint, the Lagrangian multiplier is adapted using bisection, cf. Section 4.2.3. As initialization we use a constant, axis aligned, i. e.  $\varrho = 0$ , rank-2 sequential lamination microstructure with equal ratios, i. e.  $m = 0.5$ , everywhere. The density parameter is chosen in agreement with the volume constraint. Convergence is detected if the absolute difference of the cost functional in two subsequent iterations is less than  $10^{-7}$ . The alternating scheme is guaranteed to converge as the elastic energy is decreased in every iteration, see [12, p. 56]. However there are some difficulties that need to be heeded. The piecewise constant approximation of the sequential lamination microstructure is also prone

---

<sup>2</sup><https://github.com/coin-or/Ipopt>

to checkerboard instabilities. This special setting was further investigated in [243]. In our implementation the instabilities are eliminated by using higher order elements as discussed before. The homogenized elasticity tensor, cf. (4.21), is degenerate, in the sense that a strain with just off-diagonal entries would be mapped to zero. Additionally to (4.21) we therefore set  $\bar{C}_{1212}^*$  to a positive regularization constant of magnitude  $10^{-2}$  in accordance with [12]. Furthermore we bound the density  $\theta$  from below by  $10^{-3}$  to prevent the elasticity tensor from vanishing and bound the ratio parameter  $m$  from below by  $10^{-3}$  and from above by  $1 - 10^{-3}$  to rule out rank-1 sequential lamination, which results in a degenerate tensor as well.

## 5.6. Computational speedup

As a matter of course it is important to consider the computational time of the final optimization scheme. Here the bottle neck can be easily identified. As the set of degrees of freedom for optimization is small, the optimization scheme itself does not require much computational time. In particular `Ipopt` was designed with large optimization problems in mind and our small instances do not pose a challenge. It is however costly to evaluate the cost functional, which entails the solution of the two-scale problem. In this regard `Ipopt` tries to behave as economical as possible. To support this effort a general recommendation is that gradient information should be as precise as possible. Apart from this the termination tolerances can be tuned to decrease the number of iterations of the optimization algorithm. Hence each solution of the two-scale problem should be available as fast as possible. Here the macroscopic part is in fact a small, well behaved finite element problem, which can be solved without problems due to the sparsity, even by explicit methods. However during assembly of the finite element stiffness matrix lots of microscale problems have to be tackled. Owing to the boundary element method, which only requires a discretization on the boundary of our simple geometries, those are of small size as well. However the resulting matrices are densely populated and this makes up for almost the entire overall computational time. We therefore focus on this issue in the following.

### 5.6.1. Exploitation of matrix structure

To reduce the number of microscale problems it is essential to observe the special structure of the stiffness matrix. As pointed out in Remark 3.22 there are inherent symmetries and those still hold for the two-scale setting. Therefore only about half of the entries need to be effectively computed. The rest can be copied or a specialized matrix implementation be used that looks up symmetric entries at the same location. The sparsity structure makes iterative solvers seem attractive as an application of the matrix only requires few operations and the complexity grows linearly with the problem size. However the instances appearing in this work are still processible by explicit solvers as well. We use the `CHOLMOD` solver [115] of the `SuiteSparse`<sup>3</sup> sparse matrix algorithm library, implementing a Cholesky decomposition exploiting sparsity and designed to reduce fill-in by permutation. To further support this solver a special `TripletMatrix` class is used where entries are stored in triplets comprising the row and column index, and the corresponding value. Using this format the data in memory can directly be accessed by `CHOLMOD` without any copying.

<sup>3</sup><https://people.engr.tamu.edu/davis/suitesparse.html>

### 5.6.2. Exploitation of linearity

Up to now it seems that the microscopic elasticity problem (5.2) has to be solved for every occurring macroscopic strain and at each quadrature point when a two-scale functional like (5.3) is to be computed. However the macroscopic strain at a quadrature points enters the microscale problem as right hand side, cf. (5.2). For linearized elasticity the solution depends linearly on the data, i. e. for a weighted sum of right hand sides, an equally weighted sum of their corresponding solutions can be considered. Due to linearity, this sum is a solution, and since the solution is always unique, it is also the right one. This observation opens up the possibility for a radical algorithmic shortcut. It is sufficient to compute periodic correction profiles for a basis of macroscopic strains only, e. g.

$$\varepsilon_{11} = \begin{pmatrix} 1 & 0 \\ 0 & 0 \end{pmatrix}, \quad \varepsilon_{22} = \begin{pmatrix} 0 & 0 \\ 0 & 1 \end{pmatrix}, \quad \varepsilon_{12} = \begin{pmatrix} 0 & \frac{1}{2} \\ \frac{1}{2} & 0 \end{pmatrix}.$$

Thus for each specific realization of a microstructure a basis of correction profiles  $\{\tilde{u}_{11}, \tilde{u}_{22}, \tilde{u}_{12}\}$  can be computed which can then be linearly combined. This drastically reduces computational time especially when numerous evaluations are needed for a fixed set of design parameters, which is the case here as we need a high order quadrature scheme for the macroscopic biquadratic basis functions and furthermore need to subsequently evaluate the energy and the gradient. This observation is strongly related to the periodic homogenization context. As remarked in Section 5.3.1, exactly those basis functions are considered for computation of the entries of the effective homogenized tensor. This implies that we can directly compute an effective tensor for our microscale models if we combine our base correction profiles in the two-scale elastic energy (5.3). For the two-scale elasticity problem it would be sufficient to compute and store the local effective tensors, and this was in fact done by Barbarosie and Toader, cf. Section 5.3.3. Since we need the displacement for evaluating the gradient as well we however decided to store the three periodic solutions for each cell within the `Coupling` class. Due to the boundary element method, these vectors are however short.

### 5.6.3. Parallelization

In view of nowadays developments in computing hardware, where more and more individual processing cores are integrated instead of trying to accelerate a single unit, a huge speedup can be achieved by implementing parallel execution of the most time consuming routines. Ideally one aims for a decrease in computational time which scales with the number of processors used. In practice such an ideal scaling cannot be expected due to overhead for setting up and synchronizing the individual processes. A general recommendation for most effective parallelization is to split the data equally and let instances of the same algorithm work on each chunk in parallel. In this regard we are in an ideal situation. The most costly part of our scheme is the solution procedure for the microscopic problems. Many of those need to be handled for a single two-scale problem, but they are completely independent of each other. We can therefore proceed as follows. Upon any request by the optimization algorithm its parameters are compared to the currently saved parameters and every cell where a difference above numerical tolerance occurs is marked for recomputation of the basis elasticity solutions. Typically almost all cells are selected after a completed optimization iteration. Those recomputations are then processed in parallel. The maximal reasonable number of processes is thus given by the number of marked cells. Within this range we can expect a



significant speedup. Concerning the implementation we use shared memory parallelization following the OpenMP<sup>4</sup> specification.

#### 5.6.4. Microstructure look-up table

A totally different idea was motivated by the observation that in the final results several cells comprised identical microstructures. In this situation it would be more efficient to compute the microscopic base solutions only once and let all cells with the same microstructure reference them. Certainly it is not possible to provide such data for all possible configurations. Therefore the parameter space needs to be discretized. To be precise, assume without loss of generality that normalized parameters  $q_i \in [0, 1]$ ,  $i = 1, \dots, l$  are used. The range of each parameter is now divided into  $L$  intervals of equal width. That way, for any given value  $q_i$  a containing interval with lower and upper end points  $\underline{q}_i$  and  $\bar{q}_i$ , respectively, can be found. If from each interval one fixed parameter value, e. g. the midpoint, would be taken for the computation of the corresponding elasticity problem, its solution and the cost functional would effectively become step functions of the continuously varying parameters. In particular they would not be smooth anymore and a gradient based optimization scheme would be crippled. Instead we have to resort to an interpolation of several elasticity solutions. Therefore we consider the unique convex combination  $q_i = \lambda_i \underline{q}_i + (1 - \lambda_i) \bar{q}_i$  with  $\lambda_i = (\bar{q}_i - q_i) / (\bar{q}_i - \underline{q}_i)$ . Likewise an elasticity solution can be interpolated from elasticity solutions for the interval endpoints using the same weights. This idea can be generalized to higher dimensions via a tensor product approach. An arbitrary function  $f: \mathbb{R}^l \rightarrow \mathbb{R}^d$  whose values at the corners of the  $l$ -dimensional cube are known can then be evaluated for any parameter vector  $q$  by  $f(q) = \sum_{\tilde{q}} \lambda^{\tilde{q}} f(\tilde{q})$ , where  $\tilde{q}$  is a coefficient vector with  $\tilde{q}_i \in \{\underline{q}_i, \bar{q}_i\}$ ,  $\lambda^{\tilde{q}}$  is meant as a product over  $i$  with factors  $\lambda_i \underline{q}_i$ , or  $(1 - \lambda_i) \bar{q}_i$ , respectively, and the sum is taken over all possible assignments of  $\tilde{q}$ . Elasticity solutions for arbitrary parameters can then be computed from elasticity solutions for parameter sets at the corners of the  $l$ -dimensional cube. Due to the linear combination, gradients can likewise be computed as weighted sums of gradients for parameter sets at the corners. In contrast to all other speedup measures this approach effectively alters the numerical scheme and a new source of errors due to discretization of the parameter space needs to be observed. Certainly the concrete choice of the number of intervals  $L$  plays a crucial role both for the overall accuracy and the speedup gained.

#### 5.6.5. Notes on the microscopic problem

The solving process of the microscale problem itself could not be accelerated significantly. Shared memory parallelization was employed for the explicit computation of boundary integrals of basis functions on segments of the polygonal arc in the course of matrix assembly, cf. Section 3.6.2. In contrast the used QR decomposition based on Householder reflections is not amenable to parallel execution and no satisfactory scaling w. r. t. the number of processors could be achieved. A promising approach for speeding up the treatment of boundary element based discretized problems are *hierarchical matrices*, where matrices are split into blocks based on clustering algorithms and low-rank approximations of the boundary integrals are computed for each block. In particular the *AHMED* library [64] was successfully employed in [183] for a single-scale shape optimization problem. This application showed that the overall

<sup>4</sup><https://www.openmp.org>

computational time could be improved for a large system and an iterative solver. The full potential however is only unleashed if preconditioning based on a low-rank LU decomposition is used, as demonstrated in [259] for a problem in material science. To this end the involved matrices need to have full rank and this is not the case in our situation due to the periodic identification of some of the boundary nodes.

---

## Numerical experiments for the two-scale model

---

RESULTS of numerical shape optimization employing the two-scale model as developed before are presented in this section. In this regard we will first consider synthetic examples that allow to specify the elastic state and, in view of the sequential lamination model, an optimal microstructure a priori. This will enable us to analyze capabilities of the implemented microscopic geometries, but also reveal challenges of the applied optimization scheme. A classical shape optimization problem from the literature will then be examined to get an impression of the two-scale optimization and to compare the different microstructure models among each other. It will also be used to assess numerical aspects of the macroscopic and the microscopic discretization and for an analysis of the asymptotic behavior for increasingly finely resolved shapes. Finally the effects of the applied speed-up measures will be investigated.

### 6.1. Results for prescribed constant strains

For the assessment of the two-scale material model it is desirable to consider scenarios where an optimal shape and the associated displacement field are known a priori and can be consulted for comparison. Setting up such a synthetic benchmark is however not trivial. Firstly the solution to an elasticity problem for fixed domain and boundary conditions can be given explicitly only in very few special cases. Secondly the domain here is not fixed but subject to optimization, which in turn influences the elasticity solution. Therefore both have to be given and need to be in correspondence.

#### 6.1.1. Setting of the problem

The simplest strategy is to aim for a uniform microstructure within the whole domain, resulting in homogeneous effective elastic properties on the macroscale. In view of the sequential lamination construction the stress field should therefore be homogeneous as well. Both together imply a homogeneous strain field, which can be obtained from an affine displacement  $Ax + b$  for  $A \in \mathbb{R}^{2 \times 2}$  and  $b \in \mathbb{R}^2$ . Such a solution arises from an elasticity problem with affine-periodic boundary conditions. To be precise, we choose  $A \in \mathbb{R}_{\text{sym}}^{2 \times 2}$ , as only the symmetric part will appear as the strain tensor, and set  $u(x) = Ax + \tilde{u}(x)$  with  $\tilde{u} \in H_{\text{per},0}^1$ . Rearranging equation (3.14) yields

$$a(\mathcal{Y}; \tilde{u}, \vartheta) = -a(\mathcal{Y}; A, \vartheta) \quad \forall \vartheta \in H_{\text{per}}^1(\mathcal{Y}; \mathbb{R}^2),$$

where  $A$  is to be understood as a linear mapping,  $\mathcal{Y}$  is the unit cell, now used as the macroscopic domain, and no body forces are prescribed, i. e.  $f \equiv 0$ . Thereby we arrive at an elasticity

problem with usual periodic boundary conditions for  $\tilde{u}$  and a modified right hand side. Existence and uniqueness is ensured by Theorem 3.12 as discussed before in Section 3.4 and Section 5.1.3. We act on the assumption that  $\tilde{u} \equiv 0$  will be the periodic solution, and thus  $\varepsilon[u] = A$  and  $\sigma = C^*A$ . We however do not fix this solution a priori as the optimization scheme should in principle be able to choose nonhomogeneous macroscopic material properties, resulting in nontrivial periodic parts.

We remark that this problem is practically identical to the cell problems we consider on the microscale for the two-scale approach. However we face perforated domains there, leading to nontrivial periodic parts, which ultimately let the homogenized material differ from its constituents. Furthermore we only solve the cell problems for basis displacement gradients and use the boundary element method. Here on the macroscale we are using a finite element approach. Hence we need to restrict the matrices according to the periodically identified degrees of freedom as described in Section 3.6.1. The system is then solved using a conjugate gradient method with projection to prevent a drifting of the solution away from zero integral mean. To be precise we calculate the deviations  $M^{(i,i)}\mathbf{1} \cdot u_i$  for  $i \in \{1, 2\}$  in every tenth iteration and apply a projection  $Pu_i = u_i - (M^{(i,i)}\mathbf{1} \cdot u_i)\mathbf{1}$  if the deviation exceeds a certain threshold. The compliance cost functional is used for optimization as detailed in Section 5.2.2 and in accordance to Remark 4.12 its value will be negative here.

### 6.1.2. Numerical results

We now turn to the experiments. In reference frame, i. e. aligned with the coordinate axes, we consider five strain tensors to be prescribed, ranging from hydrostatic over uniaxial to biaxial, opposing loads, given by

$$\begin{aligned} A^{(1)} &= \begin{pmatrix} 0.5 & 0 \\ 0 & 0.5 \end{pmatrix}, & A^{(2)} &= \begin{pmatrix} 0.6 & 0 \\ 0 & 0.4 \end{pmatrix}, \\ A^{(3)} &= \begin{pmatrix} 1 & 0 \\ 0 & 0 \end{pmatrix}, & A^{(4)} &= \begin{pmatrix} 0.6 & 0 \\ 0 & -0.4 \end{pmatrix}, \\ A^{(5)} &= \begin{pmatrix} 0.5 & 0 \\ 0 & -0.5 \end{pmatrix}. \end{aligned}$$

The entries are chosen s. t.  $|\lambda^{(1)}(A)| + |\lambda^{(2)}(A)| = 1$ , where  $\lambda^{(1)}$  and  $\lambda^{(2)}$  are the eigenvalues of  $A$ , sorted according to their absolute value. Each strain tensor is furthermore rotated to two additional frames by  $\frac{\pi}{8}$  and  $\frac{\pi}{4}$ , producing strains

$$A^{(i,j)} = Q(j \frac{\pi}{8})A^{(i)}Q^\top(j \frac{\pi}{8}), \quad i \in \{1, 2, 3, 4, 5\}, \quad j \in \{0, 1, 2\}.$$

Note that  $A^{(1,0)} = A^{(1,1)} = A^{(1,2)}$  as the identity mapping does not change for any change of basis. The lamination parameter functions (4.20) applied to the strain tensors consequentially take the values

$$m[A^{(i,j)}] \in \{0, 0.4, 0.5\}, \quad \varrho[A^{(i,j)}] \in \{0, \frac{\pi}{8}, \frac{\pi}{4}\}.$$

These will be compared to the corresponding parameters of the ultimately obtained macroscopic stress tensors  $\sigma$  after optimization to analyze the alignment of principle strains and stresses. Specifically we will consider the discrepancies

$$\Delta_m := |m[\varepsilon[u]] - m[\sigma]|, \quad \Delta_\varrho := |\varrho[\varepsilon[u]] - \varrho[\sigma]|,$$

where  $\varepsilon[u]$  is the finally obtained strain. It should be identical to  $A$ , and we checked this to ensure there was no drift. As the rotation parameter is ambiguous we will always compute the difference to the closest equivalent value.

The numerical experiments to be described in the following are performed on a macroscopic grid of level 0, i. e. with just one element. In case of homogeneous effective properties there should not be any difference when using a grid with more elements, and we will consider an example in this regard later on. The global volume constraint is set to 50%. Unless otherwise noted all computations indeed arrive at the predicted affine solution with vanishing periodic part. The effective macroscopic elasticity tensor field is then homogeneous and the local density matches the globally prescribed volume fraction.

**Sequential lamination.** We start with the sequential lamination model, which will also serve as a benchmark due to its established optimality. In Table 6.1 we show for each prescribed strain the ratio parameter  $m$  and inclination  $\varrho$  of the finally obtained stress field and their discrepancies to the corresponding parameters of the strain. Furthermore we list the value of the cost functional. The results agree with the findings of Pedersen [323] that an orthotropic

	$m[\sigma]$	$\Delta_m$	$\varrho[\sigma]/\pi$	$\Delta_\varrho/\pi$	$\mathbf{J}^M$
$A^{(1,0)}$	0.49997	0.00003	-0.51166	0.48834	-0.50000
$A^{(2,0)}$	0.29991	0.10009	-0.99897	0.00103	-0.54000
$A^{(2,1)}$	0.30000	0.10000	-0.87577	0.00077	-0.54000
$A^{(2,2)}$	0.30000	0.10000	-0.74977	0.00023	-0.54000
$A^{(3,0)}$	<0.00001	<0.00001	-0.99981	0.00019	-1.33333
$A^{(3,1)}$	<0.00001	<0.00001	-0.87515	0.00015	-1.33333
$A^{(3,2)}$	<0.00001	<0.00001	-0.75008	0.00008	-1.33333
$A^{(4,0)}$	0.00322	0.39678	-1.00000	<0.00001	-0.48000
$A^{(4,1)}$	0.00191	0.39809	-0.87513	0.00013	-0.48000
$A^{(4,2)}$	0.00334	0.39666	-0.75009	0.00009	-0.48000
$A^{(5,0)}$	0.50010	0.00010	-0.99979	0.00021	-0.40000
$A^{(5,1)}$	0.50000	<0.00001	-0.87515	0.00015	-0.40000
$A^{(5,2)}$	0.50002	0.00002	-0.75020	0.01002	-0.40000

Table 6.1.: Results of the sequential lamination model for prescribed strains: ratio and inclination parameters of the finally obtained stress, discrepancies to corresponding parameters of the strain, and compliance costs.

material with a certain condition on its material parameters, which is fulfilled here, must be aligned with the principal strains in order to be optimal. Furthermore principal strains and stresses coincide. The discrepancy for  $A^{(1,0)}$  is due to the afore mentioned arbitrary choice of a basis. As per the results of Section 4.2.3 the sequential lamination construction generates an effective elasticity tensor that represents an orthotropic material in the respectively rotated coordinate frame. Hence the cost functional is actually independent of the additional rotation, which can also be seen from the numerical results. The comparison of the ratio parameter shows that unequally strong principal strains lead to unequal principal stresses with an

amplified disparity, in particular when the eigenvalues have opposite signs.

**Remark 6.1** (Explicit example). For these simple problems formulae (4.21) allow an explicit computation of the elasticity tensor, the resultant stress tensor, and the cost functional. Let us consider the hydrostatic setting as an example. Assume that the stress tensor corresponding to  $\varepsilon[u] = A^{(1)}$  is likewise given by  $\sigma = A^{(1)}$ . Then optimal parameters for a sequential lamination construction are  $\varrho[\sigma] = 0$ ,  $m[\sigma] = 0.5$ , and, owing to the volume constraint,  $\theta = 0.5$ . With  $\lambda = \mu = 1$  the corresponding elasticity tensor has entries  $C_{1111}^* = C_{2222}^* = 0.9$  and  $C_{1122}^* = 0.1$  and so  $C^*\varepsilon[u] = \sigma$  indeed holds. Finally the negative elastic energy  $-\varepsilon[u] : \sigma = -0.5$  equals the numerical results.

The elasticity tensor for the rigid constituent has entries  $C_{1111} = C_{2222} = 3$ ,  $C_{1122} = 1$ , and  $C_{1212} = 1$ , see Section 3.2. In order to achieve the same stress tensor as above the strain has to be chosen as  $\varepsilon[u] = \frac{1}{8}\mathbb{1}$ , and the elastic energy then evaluates to  $\frac{1}{8}$ . This allows to compute the Hashin-Shtrikman bound (4.16) and it turns out to be 0.5. As mentioned in Remark 4.16 there is a relation to the bounds on the elastic energy for strain based problems and in fact for this example  $-\frac{1}{2} \leq -\sigma : \varepsilon[u]$  is obtained. Altogether this verifies the optimal result obtained with the sequential lamination model for hydrostatic strains.

**Ellipsoidal perforations.** Next we consider ellipsoidal perforations as the microstructure in the first genuine two-scale model. As before we show the ratio of the eigenvalues and orientation of the eigenvectors for the obtained stresses along with their discrepancies to the corresponding values of the prescribed strains, and the value of the cost functional in Table 6.2. Additionally we state the ratio of the scaling parameters of the ellipsoidal perforation, i. e.

$$m[q_1, q_2] := \frac{q_2}{q_1 + q_2}$$

and its rotation parameter  $q_3$ , which could be different from the orientation of the eigenvectors. The finally obtained shapes are shown in Figure 6.1. For  $A^{(1,0)}$  we see nearly identical scaling parameters after optimization, hence the shape created is close to a circle. The hydrostatic strain is transformed to a corresponding stress and there is nearly no rotation. As before a numerical artifact stemming from the calculation of the under-determined system of eigenvectors is responsible for the discrepancy between  $\varrho[\sigma]$  and  $q_3$  here. For the other outcomes of the optimization it is important to realize that only the perforation is able to rotate, but not the full unit cell. Therefore, in the periodic assemblage, the inclusions are only aligned whenever  $q_3$  is a multiple of  $\frac{\pi}{2}$ . For  $q_3 = \frac{\pi}{4}$  an alignment along the diagonal can be achieved, but it has a larger spacing and every other row of perforations appears shifted. It is therefore no surprise that the observed elastic energies for a fixed strain and varying rotation do not coincide. In fact the ellipsoidal shapes align with horizontal or vertical, or diagonal principal strains, but for  $q_3 = \frac{\pi}{8}$  they neither coincide with the strain eigenvectors nor with the stress eigenvectors. For  $A^{(2,0)}$  the perforation is a nontrivial ellipse, but it is not fully elongated as for all other strains with a dominant eigenvalue. The energies corresponding to the different rotations are close to each other for  $A^{(2)}$ , but become worse for larger rotations both for  $A^{(3)}$  and  $A^{(4)}$ . Finally for  $A^{(5)}$  a circle is obtained for all rotations. Here it is striking how much worse the energy gets when the principal strains rotate out of the cells spanning axes. Comparing to the results of the sequential lamination microstructure we see that the ellipsoidal perforations are competitive for  $A^{(1)}$  and  $A^{(2)}$  where the elastic energy differs only by a magnitude of  $10^{-2}$ . It is worse for the other strains where only the axes aligned

	$m[\sigma]$	$\Delta_m$	$\varrho[\sigma]/\pi$	$\Delta_\varrho/\pi$	$m[q_1, q_2]$	$q_3/\pi$	$\mathbf{J}^M$
$A^{(1,0)}$	0.50000	<0.00001	-0.50182	0.00182	0.50000	-0.00324	-0.48441
$A^{(2,0)}$	0.32381	0.07619	<0.00001	<0.00001	0.44522	<0.00001	-0.51892
$A^{(2,1)}$	0.32084	0.07916	-0.86129	0.01371	0.38899	0.19087	-0.52602
$A^{(2,2)}$	0.34270	0.05730	-0.75000	<0.00001	0.38899	-0.25000	-0.52768
$A^{(3,0)}$	0.02810	0.02810	<0.00001	<0.00001	0.38898	<0.00001	-1.16868
$A^{(3,1)}$	0.19612	0.19612	-0.93077	0.05577	0.38898	0.13972	-0.95251
$A^{(3,2)}$	0.27390	0.27390	-0.75000	<0.00001	0.38898	0.25000	-0.86913
$A^{(4,0)}$	0.06909	0.33091	-1.00000	<0.00001	0.38900	<0.00001	-0.42792
$A^{(4,1)}$	0.01054	0.38946	-0.92550	0.05050	0.38899	0.18594	-0.27068
$A^{(4,2)}$	0.11990	0.51990	-0.75000	<0.00001	0.38898	-0.25000	-0.21293
$A^{(5,0)}$	0.50000	<0.00001	<0.00001	<0.00001	0.50000	-0.00323	-0.34795
$A^{(5,1)}$	0.50000	<0.00001	-0.95616	0.08116	0.50000	-0.00336	-0.22315
$A^{(5,2)}$	0.50000	<0.00001	-0.75000	<0.00001	0.50000	-0.00324	-0.09834

Table 6.2.: Results of the two-scale model with one ellipsoidal perforation for prescribed strains: ratio of eigenvalues and inclination of eigenvector of the finally obtained stress with discrepancies to corresponding parameters of the strain, ratio of scaling parameters, rotation parameter, and cost functional.

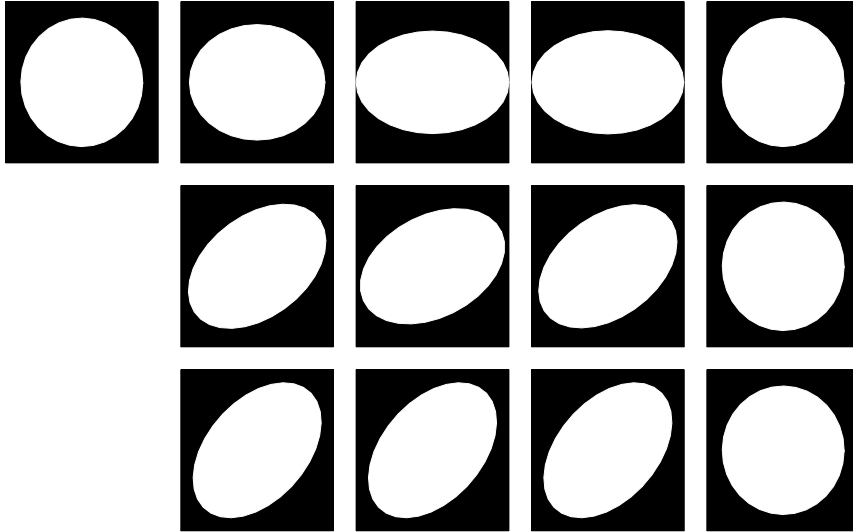


Figure 6.1.: Results for prescribed strains with one ellipsoidal perforation per cell: strains  $A^{(i)}$  from left to right, rotations from top to bottom.

settings yield close results, up to differences of magnitude  $10^{-1}$ . These observations seem plausible as the ellipsoidal shape can be viewed as an approximation of an optimal Vigdergauz microstructure, cf. Section 4.2.4. This construction is however not possible for  $A^{(3)}$ ,  $A^{(4)}$ , and

$A^{(5)}$ .

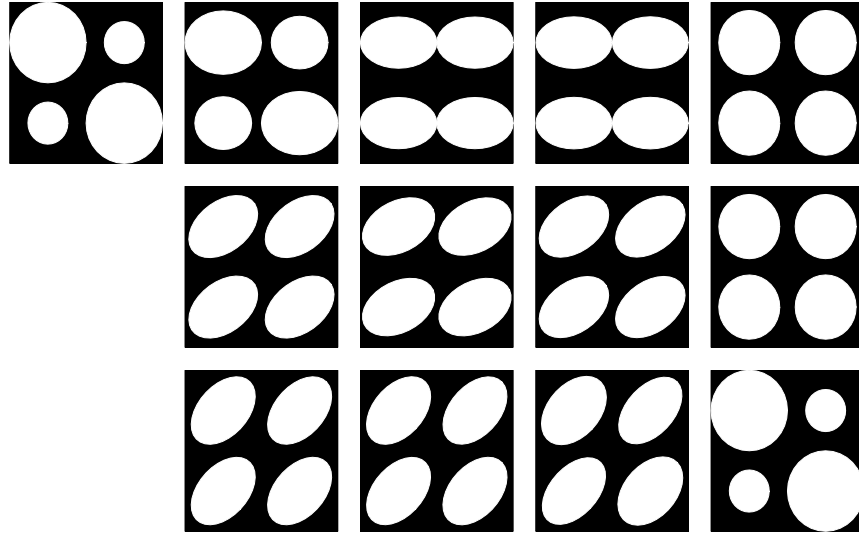


Figure 6.2.: Results for prescribed strains with  $2 \times 2$  ellipsoidal perforations per cell: strains  $A^{(i)}$  from left to right, rotations from top to bottom.

An obvious enrichment of the microstructure model is achieved by allowing for more than one perforation in each cell. We therefore display the outcomes for  $2 \times 2$  ellipsoidal perforations in Figure 6.2. In the trivial case all four perforations can take identical shapes and thereby reproduce the same microstructure as with a single perforation due to the periodic setup. As it turns out this situation occurs for every strain except for the hydrostatic, for  $A^{(5,2)}$ , which is a shearing, cf. Figure 1.3(b), and, to lesser extend,  $A^{(2,0)}$ . Only the former two achieve a significant improvement in the cost functional, cf. Table 6.4. For  $A^{(2,0)}$  the difference is small, but the attained cost is indeed better than for a uniform design. The difference for all other scenarios is smaller by orders of magnitude and has to be attributed to the numerical approximation. The nontrivial results however exhibit a remarkable microstructure. Here the geometric flexibility of the ellipsoidal holes to create anisotropic elongations and align themselves, is not used. Instead merely volume is distributed at the microscopic scale by growing and shrinking circles in an alternating fashion. Through periodic extension this leads to an approximation of an infinitesimal criss-crossing pattern, which seems to be well suited to withstand stresses that do not possess a dominant direction.

**Rods with fixed orientation.** We turn to microstructures built from rods next. In Figure 6.3 we display the results with optimized thicknesses of six rods at fixed positions. For a hydrostatic strain two orthogonal rods of maximal possible thickness each are formed. It can be seen, cf. Table 6.4, that the thereby obtained square holes perform worse than circular perforations obtained before. The microstructure is also unsuitable for alignments of  $\frac{\pi}{8}$  as no rods in this direction are provided. Accordingly the cost functional values are worse for  $A^{(2,1)}$  and  $A^{(3,1)}$ , and about the same for  $A^{(4,1)}$  and  $A^{(5,1)}$ , where the determinant is negative. Unfortunately a horizontal alignment for scenarios  $A^{(2,0)}$ ,  $A^{(3,0)}$ , and  $A^{(4,0)}$ , which exhibit a dominant direction,



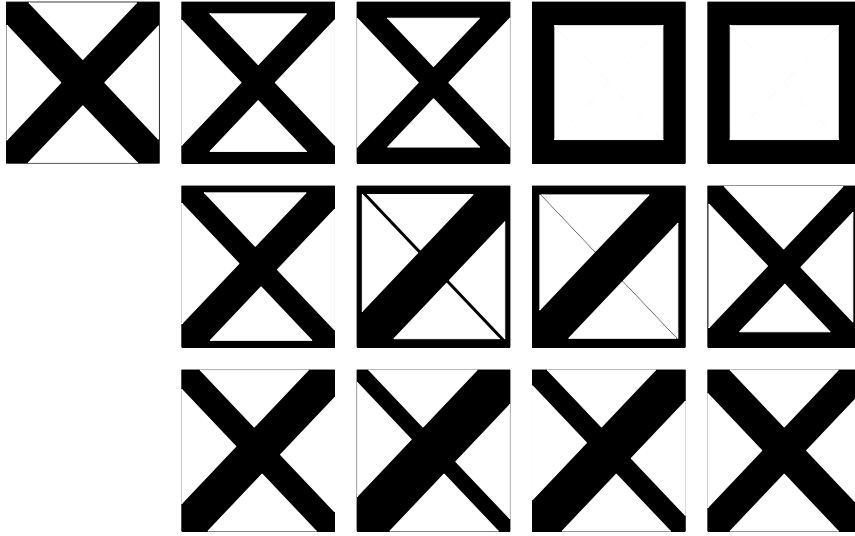


Figure 6.3.: Results for prescribed strains with rods of fixed orientation: strains  $A^{(i)}$  from left to right, rotations from top to bottom.

is hindered by the geometric constraint that triangular shaped holes have to be maintained, cf. (5.16). Interestingly enough additional diagonal rods are selected as long as the determinant is non negative, and vertical rods as soon as it becomes negative. The situation improves drastically for strains aligned with the diagonal rods. For scenarios with a dominant direction the expected rods receive more material, but at the same time a certain ratio to the other diagonal rods, corresponding to the ratio of the eigenvalues, is maintained. In those cases the ellipsoidal perforations are outperformed, especially when the determinant is negative. For the axes aligned  $A^{(5,0)}$  a good result is obtained, too. Indeed it corresponds to the rotated shape for  $A^{(5,2)}$  and the cost functional values are identical within the approximation error.

**Rotating orthogonal rods.** Finally we consider a pair of orthogonal rods that are allowed to rotate freely. In contrast to the ellipsoidal perforations this is realized by rotating the whole unit cell, cf. Section 5.4.3. In Figure 6.4 we show the obtained results. Here a representative of the local microstructure is drawn inside a macroscopic, unrotated cell as before, but it is important to keep in mind that the microscopic lattice is actually rotated along. In Table 6.3 we list important quantities of the optimized shapes as we did for the ellipsoidal perforations before. The most noticeable difference is that, up to some tolerance, cost functional values are close to each other for all rotations of each prescribed strain. This is clearly due to the rotating lattice, and comparable to the sequential lamination model. For the hydrostatic strain, the axes aligned  $A^{(5,0)}$ , and the diagonally aligned  $A^{(5,2)}$ , square holes are obtained as with the fixed rods before, and indeed the costs are comparable, cf. Table 6.4. All other scenarios lead to holes with varying aspect ratios, corresponding to the changing ratios of the eigenvalues. These are moreover rotated along with the prescribed strain. The fixed rods cannot compete for a horizontally aligned stress due to the mentioned geometric constraint. They can neither compete for diagonally aligned stresses with unequal eigenvalues because in

	$m[\sigma]$	$\Delta_m$	$\varrho[\sigma]/\pi$	$\Delta_\varrho/\pi$	$m[q_1, q_2]$	$q_3/\pi$	$\mathbf{J}^M$
$A^{(1,0)}$	0.50000	<0.00001	-0.50016	0.00016	0.50000	0.24781	-0.47499
$A^{(2,0)}$	0.21632	0.18368	1.00000	<0.00001	0.38981	<0.00001	-0.52284
$A^{(2,1)}$	0.21632	0.18368	-0.87500	<0.00001	0.38981	0.12500	-0.52284
$A^{(2,2)}$	0.21632	0.18368	-0.75000	<0.00001	0.38981	0.25000	-0.52284
$A^{(3,0)}$	0.00147	0.00147	<0.00001	<0.00001	0.33360	<0.00001	-1.33138
$A^{(3,1)}$	0.00147	0.00147	-0.87500	<0.00001	0.33360	0.12500	-1.33138
$A^{(3,2)}$	0.00147	0.00147	-0.75000	<0.00001	0.33360	0.25000	-1.33138
$A^{(4,0)}$	-0.00500	0.39500	<0.00001	<0.00001	0.33433	<0.00001	-0.47921
$A^{(4,1)}$	-0.00500	0.39500	-0.87500	<0.00001	0.33433	0.12500	-0.47921
$A^{(4,2)}$	-0.00500	0.39500	-0.75000	<0.00001	0.33433	0.25000	-0.47921
$A^{(5,0)}$	-0.50000	<0.00001	-1.00000	<0.00001	0.50000	-0.50000	-0.36615
$A^{(5,1)}$	-0.50000	<0.00001	-0.87500	<0.00001	0.50000	-0.37500	-0.36615
$A^{(5,2)}$	-0.50000	<0.00001	-0.75000	<0.00001	0.50000	0.25000	-0.36615

Table 6.3.: Results of the two-scale model with rotating orthogonal rods for prescribed strains: ratio of eigenvalues and inclination of eigenvector of the finally obtained stress with discrepancies to corresponding parameters of the strain, ratio of scaling parameters, rotation parameter, and cost functional.

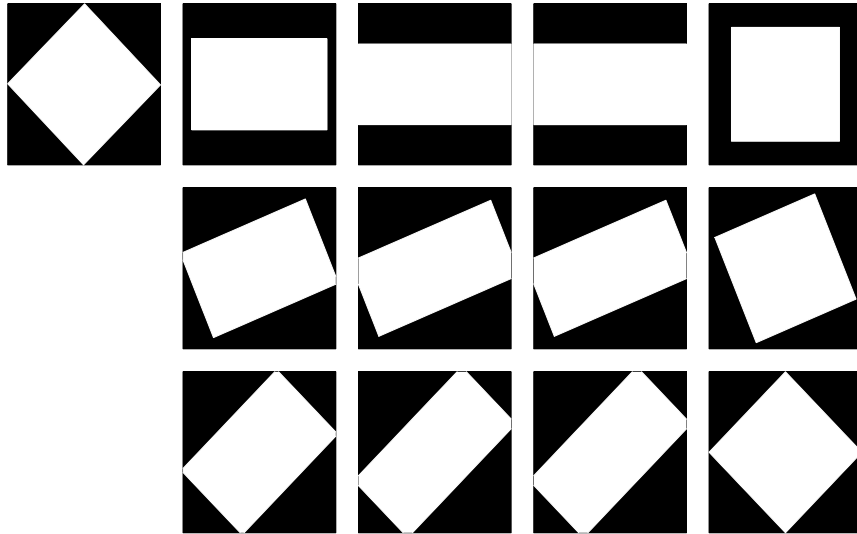


Figure 6.4.: Results for prescribed strains with rotating orthogonal rods: strains  $A^{(i)}$  from left to right, rotations from top to bottom.

this case the periodic extension would result in diagonal rods with notches. Thereby all other two-scale models are outperformed by the rotating orthogonal rods microstructure. Moreover we observe that the costs are remarkably close to optimal values given by the sequential

lamination model. The discrepancies are largest for  $A^{(1)}$  and  $A^{(5)}$ , which are characterized by rank-2 sequential lamination with equal ratios, i.e.  $m = 0.5$ , as an optimal microstructure. It seems that the gain of the additional scales employed in the derivation of the sequential lamination microstructure is most prominent for these scenarios.

	sequential lamination	ellipsoidal $1 \times 1$	ellipsoidal $2 \times 2$	rods fixed	rods rotating
$A^{(1,0)}$	-0.50000	-0.48441	-0.49946	-0.47315	-0.47499
$A^{(2,0)}$	-0.54000	-0.51892	-0.52237	-0.49555	-0.52284
$A^{(2,1)}$	-0.54000	-0.52602	-0.52649	-0.49216	-0.52284
$A^{(2,2)}$	-0.54000	-0.52768	-0.52815	-0.49531	-0.52233
$A^{(3,0)}$	-1.33333	-1.16868	-1.16882	-0.84567	-1.33138
$A^{(3,1)}$	-1.33333	-0.95251	-0.95544	-0.85535	-1.33138
$A^{(3,2)}$	-1.33333	-0.86913	-0.87232	-0.97533	-1.33138
$A^{(4,0)}$	-0.48000	-0.42792	-0.42840	-0.38452	-0.47921
$A^{(4,1)}$	-0.48000	-0.27068	-0.27318	-0.27838	-0.47921
$A^{(4,2)}$	-0.48000	-0.21293	-0.21568	-0.40230	-0.47921
$A^{(5,0)}$	-0.40000	-0.34795	-0.34764	-0.36549	-0.36615
$A^{(5,1)}$	-0.40000	-0.22315	-0.22455	-0.22095	-0.36615
$A^{(5,2)}$	-0.40000	-0.09834	-0.16052	-0.36511	-0.36615

Table 6.4.: Comparison of cost functional values for all investigated models.

**Comparison to Barbarosie and Toader.** As an amendment to the investigations in the context of prescribed strains we revisit the work by Barbarosie and Toader [60] as it includes numerical examples that can be compared to our results. Firstly they consider the maximization of the bulk modules, which is equivalent to maximizing the elastic energy for a prescribed strain  $A = -1$ , cf. [60, Section 6.2]. Up to scaling it is the same problem that we considered with  $A^{(1)}$  above. The target volume is set to 30% and different elasticity coefficients, namely  $\lambda = 3$  and  $\mu = 1$ , are used. Both influence the concrete values of the cost functional. Secondly they investigate the rigidity for shear response, cf. [60, Section 6.5], which corresponds to our  $A^{(5,2)}$  scenario up to scaling. Here a final volume of 57.29% was achieved, which we prescribe as the volume constraint. In Table 6.5 we list the finally obtained cost functional values of our optimization runs. We can see that our microstructures made from rods basically agree with the values obtained by Barbarosie and Toader. Neither of them is able to bridge the gap towards the results of the sequential lamination model.

### 6.1.3. Numerical issues

The considered synthetic shape optimization scenarios follow a most simplistic setup but are already rich enough to hint at emerging numerical challenges. Most prominent here are local minima. In fact the considered compliance cost functional is convex in its arguments and their originating spaces are convex as well. However, due to constraints that couple multiple design



is especially severe as a shape with a smooth curved boundary is approximated by a polygonal arc. The volume of the shape is however computed based on the formula for an exact ellipse, and this enters the equality constraint. Thereby also an error in the size of the void region, which should be 0.5 here, is introduced and the outcome of optimization is naturally falsified, cf. Table 6.6(a). We next use 32 points on the boundary of the perforation and vary the number of points on the outer boundary. The influence is much less severe, and the effective difference is lower by more than one order of magnitude, cf. Table 6.6(b). Finally we consider the rotating rods microstructure model and vary the number of discretization points on edges, which influences both the outer and inner boundary. Again a significant influence can be observed, although smaller than for the ellipsoidal holes, cf. Table 6.6(c). Here it is important that the shape is reproduced exactly by the polygonal arc. On the other hand the non-smooth boundary induces further difficulties as discussed in Remark 5.7. In [182, sections 8.1, 8.2] a further analysis of errors in the elasticity solution and depending quantities can be found. To consider meaningful examples in our numerical studies we will accept the depicted deficiencies and aim for a good compromise between accuracy and computational complexity.

Issues with the macroscopic resolution were ruled out in the previous investigations by only considering one macroscopic cell. As noted we expect homogeneous strain, stress, and elasticity tensor fields also for higher resolutions. In this regard we show an example in Figure 6.5, where a macroscopic grid of level 3, i. e.  $8 \times 8$  cells and ellipsoidal perforations as the microstructure model were used for the prescribed strain  $A^{(1)}$ . A completely random initialization was used but the optimization algorithm nevertheless finds the homogeneous solution and its associated cost functional value is within machine precision of the value obtained before for macroscopic level 0. Of course this is just one example, and there are indeed instances where the homogeneous solution is not recovered. This especially occurs when the microstructure in some cells has adopted an extremely anisotropic shape or very low volume. From this observation we draw the conclusion that shapes in the initialization should be as neutral as possible.

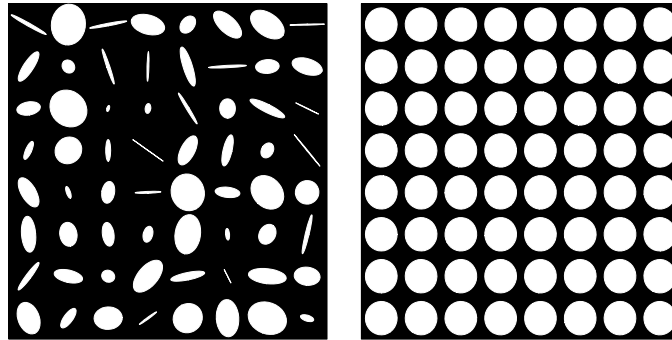


Figure 6.5.: Random initialization and optimized result for prescribed hydrostatic strains and ellipsoidal perforations as the microstructure model on a macroscopic grid of level 3.

## 6.2. Results for a classical shape optimization problem

So far we focused on the behavior of the different microstructure models under optimization for a prescribed synthetic macroscopic homogeneous strain field. In this section we turn our attention to a classical, less trivial shape optimization scenario. We again investigate the different microscopic models and compare them to each other. Since the macroscopic resolution determines the number of degrees of freedom for optimization we compute series for increasing macroscopic grid levels to investigate the asymptotic behavior of the optimized shapes and compliance functional values. As to the microscopic discretization, which was already studied in the preceding section, we check its influence in this more complex situation. Finally we assess the effectiveness of the employed speed-up measures.

As described in Section 5.5.2 we are restricted to the unit cell as the computational domain. Therefore we consider the following example, which we call a *carrier plate*. As the working domain the unit cell is used, i. e.  $D = [0, 1]^2$ . The lower boundary  $\Gamma_D = [0, 1] \times \{0\}$  is assumed to be fixated, i. e. homogeneous Dirichlet boundary conditions are prescribed. On the upper boundary  $\Gamma_N = [0, 1] \times \{1\}$  shearing forces are applied in terms of inhomogeneous Neumann boundary conditions, i. e.  $g \equiv (1, 0)$  on  $\Gamma_N$ . The left and right boundaries are allowed to evolve freely in terms of homogeneous Neumann boundary conditions. The overall volume fraction is constrained to 67%. No volume forces are considered, i. e.  $f \equiv 0$ .

### 6.2.1. Numerical results

In figures 6.6–6.9 we display the results of optimization for the two-scale shape optimization model using different microscopic models on grids of increasing macroscopic resolution. As before we visualize each two-scale result in a single image by drawing the macroscopic domain subdivided into its square cells and a representative of the underlying microstructure in each individual cell. One has to keep in mind that the actual microstructure is obtained by repeating the representative shape on a periodic lattice, which was assumed to reside on a much smaller length scale. On the macroscale it only becomes apparent by means of a volume density and an effective elasticity tensor. The volume distribution is visualized in addition below each two-scale image using a grayscale plot.

We start with the microstructure made from a single ellipsoidal perforation, see Figure 6.6. Here we expect analogies to the single-scale case shown in Figure 1.1. In fact the two-scale model has been motivated by the single-scale results, which show a problem specific volume distribution and in addition a local adaptation of the considered perforations. Hence it is expected to be able to capture both phenomena on distinct scales. Although the macroscopic resolution of  $45 \times 45$  ellipsoidal perforations for the single-scale setting is not exactly reflected in the two-scale setting, strong similarities can indeed be observed in the overall distribution of available volume. The hereby identifiable macroscopic shapes are not superimposable because the effective elastic properties of the arbitrary fine periodic lattices have a different influence locally than the macroscopic perforations. As already discussed in Remark 5.6 a fundamental cell can never be void using this microstructure. Therefore no white regions are present in the volume plots, but only light gray ones. With respect to the microstructure we can clearly identify an alignment of anisotropically shaped perforations with the main stress directions within the two macroscopic trusses rising from the lower corners. This has also been observed for the single-scale setting and is now successfully captured in the two-scale model as well.

**Remark 6.2** (Symmetry of optimal shapes). The obtained shapes, in terms of the optimized

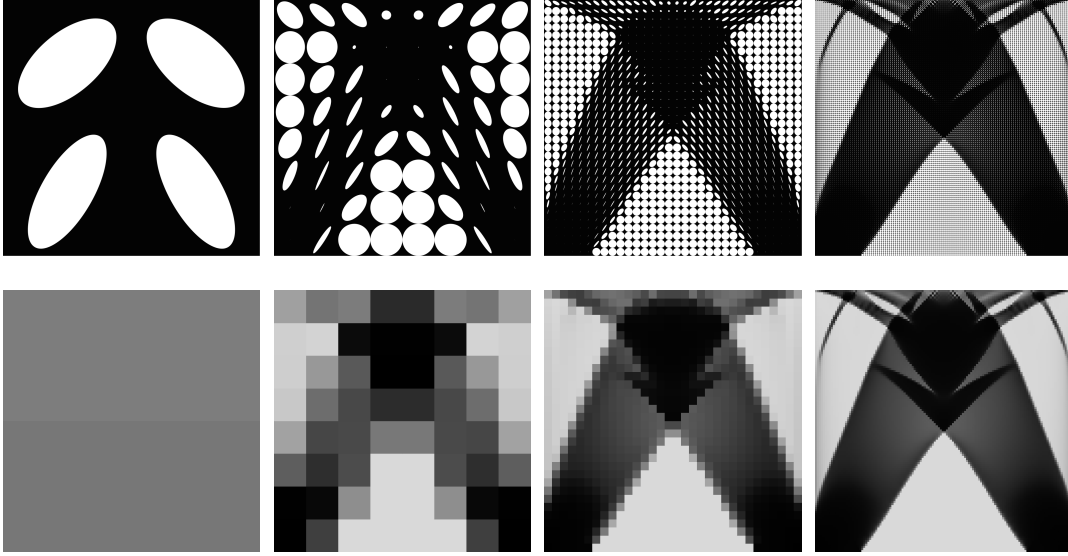


Figure 6.6.: Two-scale results for the carrier plate scenario and one ellipsoidal perforation as the microstructure model on macroscopic grids of level 1, 3, 5, and 7. In the upper row a representative of the microstructure is drawn in each macroscopic cell. In the lower row the effective macroscopic volume distribution is shown, with white corresponding to void and black corresponding to solid matter.

parameters  $q_h^{\text{opt}}$ , are symmetric about the central vertical axis. In the context of linearized elasticity and for a scenario like the one considered, this is indeed expected, with the following reasoning. Assume that the parameter field, and hereby the elasticity tensor field  $C^*[q_h^{\text{opt}}]$ , is not symmetric and consider a reflection of the entire problem about the central vertical axis. Thereby the horizontal orientation is reversed, which amounts to a change of the frame of reference. In particular, the cost functional value does not change. Let  $\check{D}$  denote the mirrored working domain and  $\check{g}$  the corresponding boundary value. Now consider another elasticity problem in the mirrored configuration with an inverted loading, i. e.  $-\check{g}$ . Due to linearity of the PDE,  $-\check{u}_h$  is the unique solution. It enters the bilinear form  $a^M(\check{q}_h^{\text{opt}}; -\check{u}_h, -\check{u}_h)$  quadratically and thereby the cost functional value again does not change, cf. the equivalent expressions in (4.12). Furthermore, for the scenario considered, there holds  $\check{D} = D$  and  $-\check{g} = g$ . Thus the newly obtained solution in the mirrored configuration solves the original problem as well. Now divide the working domain into halves along the central vertical axes, i. e.  $D = D^{\text{left}} \cup D^{\text{right}}$  and consider the cost functional for each of them separately. There holds  $\mathbf{J}^M[q_h^{\text{opt}}, u_h]|_{D^{\text{left}}} = \mathbf{J}^M[\check{q}_h^{\text{opt}}, -\check{u}_h]|_{D^{\text{right}}}$  and  $\mathbf{J}^M[q_h^{\text{opt}}, u_h]|_{D^{\text{right}}} = \mathbf{J}^M[\check{q}_h^{\text{opt}}, -\check{u}_h]|_{D^{\text{left}}}$ . Choose the half with the lower value in the original setting and combine it with the corresponding half in the mirrored setting. Thereby a symmetric tensor field and corresponding displacements are obtained, which satisfy the elasticity PDE and yield a cost functional value which is less or equal to the initial value. Hence we expect a symmetric result, especially when the initialization is already symmetric.

A deficiency that can be observed is that the oscillating pattern seen in the upper middle

region for the single-scale case has not been reproduced. Seemingly a criss-crossing pattern is to be realized here, but such a construction is ruled out in the two-scale setting with just a single perforation. We therefore consider the microstructure made from  $2 \times 2$  ellipsoidal perforations, see Figure 6.7. This model led to an oscillating pattern in the preceding section,

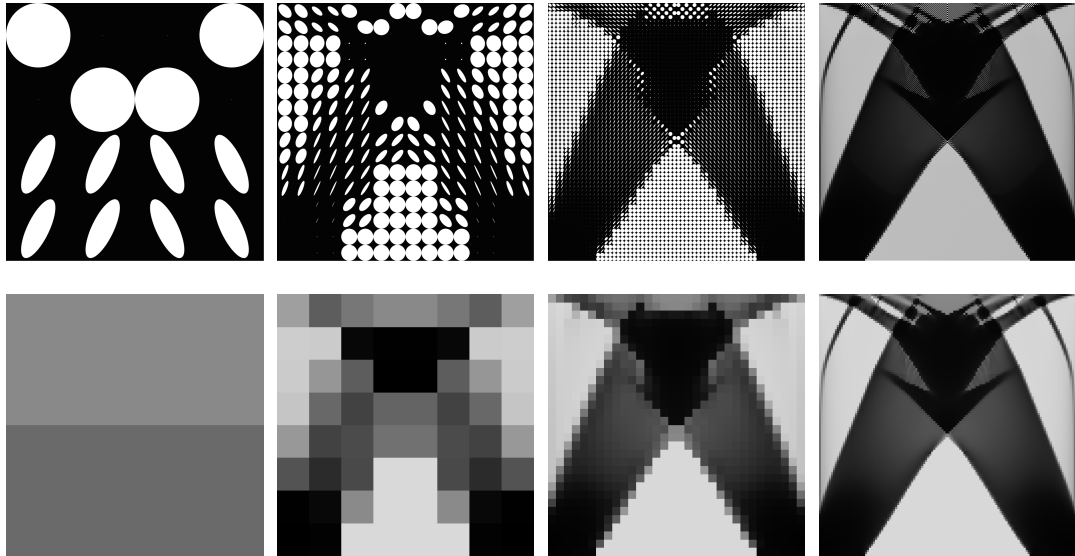


Figure 6.7.: Two-scale results for the carrier plate scenario and  $2 \times 2$  ellipsoidal perforations as the microstructure model on macroscopic grids of level 1, 3, 5, and 7. In the upper row a representative of the microstructure is drawn in each macroscopic cell. In the lower row the effective macroscopic volume distribution is shown, with white corresponding to void and black corresponding to solid matter.

cf. Figure 6.2, and indeed this pattern is also developed here for the carrier plate scenario as expected. In the other regions the same microstructure as before is reproduced by copying the shape of the former single perforation. The volume distributions are nearly identical to the previous ones.

We now turn to microstructures made from rods. In Figure 6.8 the results for six rods at fixed positions are shown. The model is perfectly suited for the criss-crossing pattern observed previously and indeed it is captured in the upper middle region. Furthermore it is present in the lower middle region where the amount of material increases from bottom to top. Diagonal rods with a single dominating direction can be found in the upper left and right region, at least for the coarse and medium fine macroscopic grids. The thick trusses rising from the lower corners are made from solid material here and do not show any specific microstructure. This is because the main trusses are not inclined in such a way that any of the offered rods would be beneficial. Consequently the macroscopic shapes differ from the ones obtained for the ellipsoidal perforations. The main trusses are thinner and the upper supporting structure seems flatter. For the fine macroscopic grids the auxiliary trusses on the left and right hand side are however thicker than in the results before.

Finally we consider rotating orthogonal rods as the microstructure model, which allow both for a criss-crossing pattern and for alignment with arbitrary directions. The results are



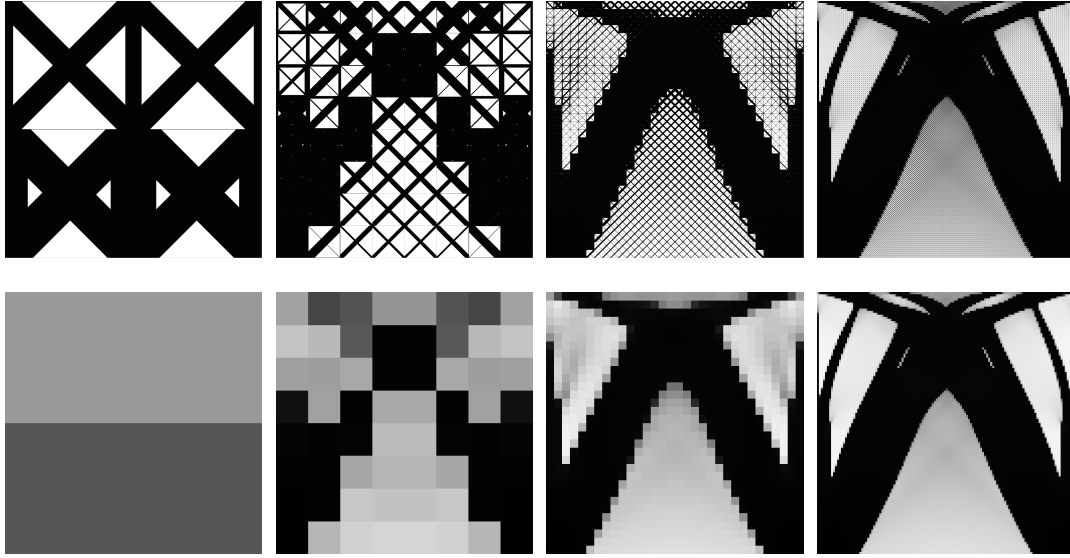


Figure 6.8.: Two-scale results for the carrier plate scenario and rods with fixed orientation as the microstructure model on macroscopic grids of level 1, 3, 5, and 7. In the upper row a representative of the microstructure is drawn in each macroscopic cell. In the lower row the effective macroscopic volume distribution is shown, with white corresponding to void and black corresponding to solid matter.

shown in Figure 6.9. As expected the criss-crossing pattern is captured and a microstructure with an aligned dominating axis is produced within the thick trusses. Solid material is only found in the lower corners and the center region where the trusses meet. Beyond that the microstructure seems to vary smoothly within the upper region below the loaded boundary and in the vicinity of the lower thick trusses. Sharp interfaces are only formed on the lower left and right edge of the upper supporting structure, which besides are much more curved than in the previous results. For the finest grid a break in symmetry can be observed in the upper middle region and tiny trusses are built instead of the criss-crossing pattern. This might be a hint of non-optimal local minima that are attained due to inaccuracies in the approximated gradient. The influence of single parameters on the cost functional decreases for increasingly fine cells and as a consequence non-optimal optimization steps might get accepted.

A comparison of the optimized shapes for the different microstructure models suggests itself. We will see in the next section that the performance effectively increases in the order of the presentation of the results here. As pointed out before we cannot aim for optimal shapes because of our geometrically simple constructions, but it is meaningful to investigate the gap towards optimality. Therefore we also compute optimized results for the carrier plate scenario with the sequential lamination model, see Figure 6.10. Here only the macroscopic volume distribution is shown, which corresponds to the parameter  $\theta$ . The other parameters are known from their relation to the stresses, cf. (4.20). As can be seen the volume distribution shares some characteristic features with the distribution seen previously for the rotating orthogonal rods microstructure model. The upper supporting structure with its lower curved boundary is nearly identical. The lower trusses with intermediate density in the middle section are

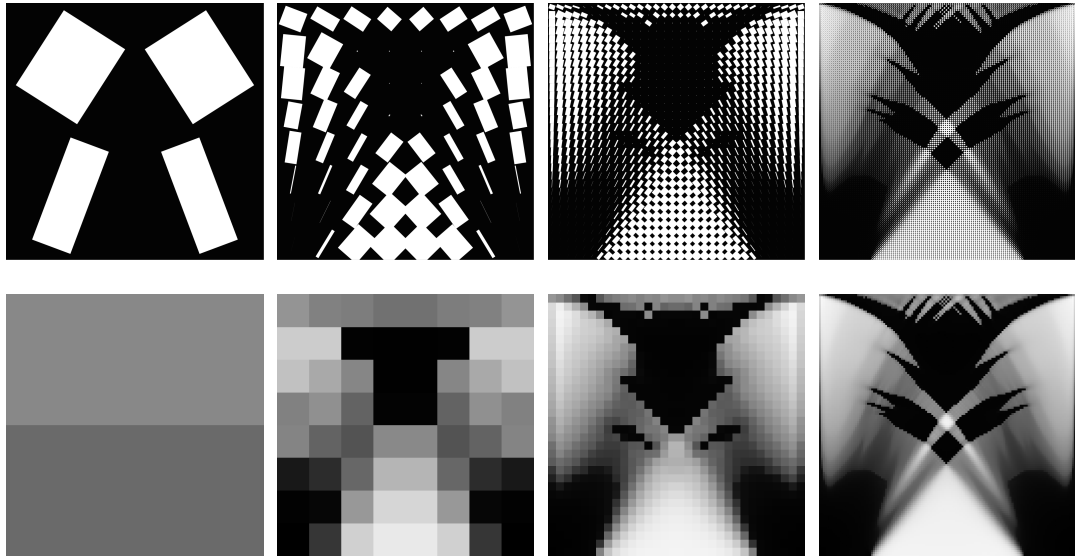


Figure 6.9.: Two-scale results for the carrier plate scenario and rotating orthogonal rods as the microstructure model on macroscopic grids of level 1, 3, 5, and 7. In the upper row a representative of the microstructure is drawn in each macroscopic cell. In the lower row the effective macroscopic volume distribution is shown, with white corresponding to void and black corresponding to solid matter.

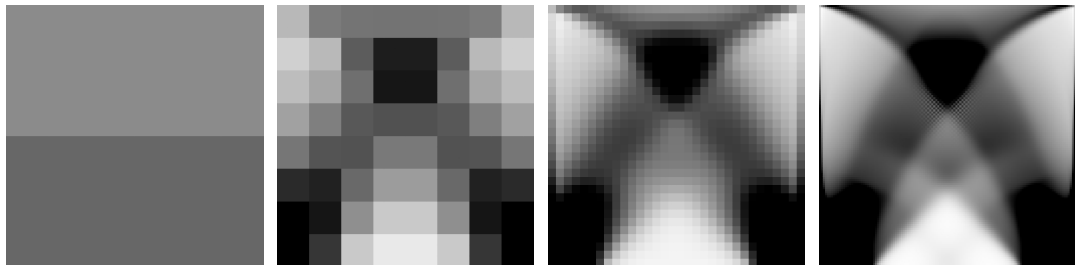


Figure 6.10.: Results for the carrier plate scenario and the sequential lamination model on macroscopic grids of level 1, 3, 5, and 7. The effective macroscopic volume distribution  $\theta$  is shown, with white corresponding to void and black corresponding to solid matter.

also present for both models. There are however distinctive interfaces of the lower trusses' boundaries for the sequential lamination model, which, in contrast, were smeared out for the rotating rods model. Furthermore we observed, in spite of the applied stabilization by higher order finite elements, a light checkerboard pattern in a small region around the center. Such oscillations were not found in the results for the two-scale model.

### 6.2.2. Asymptotic analysis of macroscopic discretization

In this section we do a quantitative comparison of the shape optimization results obtained for the carrier plate scenario and different microstructure models on macroscopic grids of different resolutions. The two-scale optimizations can be run on macroscopic grids of level 7 with acceptable computational time. For the sequential lamination model, which does not require the solution of microscopic cell problems, we use grids up to level 10. In Table 6.7 we list the finally obtained compliance values. As can be seen, from grid level 2 the different

level	ellipsoidal $1 \times 1$	ellipsoidal $2 \times 2$	rods fixed	rods rotating	sequential lamination
1	4.18550	3.61328	4.16885	3.76358	2.78695
2	2.92714	2.76865	2.70341	2.51117	2.25219
3	2.48219	2.44227	2.41991	2.16348	2.04026
4	2.27240	2.25742	2.15789	1.99244	1.93584
5	2.17419	2.16656	2.08473	1.91864	1.88600
6	2.12508	2.12468	1.99909	1.88294	1.86230
7	2.09675	2.09445	1.96623	1.86587	1.85091
8					1.84537
9					1.84264
10					1.84130

Table 6.7.: Comparison of cost functional values for the carrier plate scenario and all investigated models on macroscopic grids of different resolution.

microstructure models rank in the order they were presented in the preceding section. For coarse and medium fine macroscopic grids the gain by advancing to the next level is typically larger than the improvement realized by changing the model. For fine grids the improvement due to discretization gradually decreases, but an innate gap between the different models remains. To support this claim we analyze the asymptotic behavior of the computed cost functional values. To this end we assume that the compliance values  $\mathbf{J}^M[q_h^{\text{opt}}, u_h]$  of optimized shapes will converge to an asymptotic value  $\mathbf{J}_0^M$  if the macroscopic mesh is successively refined, i. e.  $h \rightarrow 0$ . We also assume a decay behavior, expressed as

$$\mathbf{J}^M - \mathbf{J}_0^M = c h^p. \quad (6.1)$$

The constants  $\mathbf{J}_0^M$ ,  $c$ , and  $p$  are unknown, but can be determined numerically using least squares fitting to our recorded results. In Table 6.8 the obtained parameters are listed. In Figure 6.11 the decay  $c h^p$  is plotted along with the discrepancy  $\mathbf{J}^M - \mathbf{J}_0^M$  for the different microstructure models and varying macroscopic resolution. As shown the fitting of the assumed decay behavior to the recorded results is very good. For most models a linear decay, i. e.  $p \approx 1$ , was found, which meets with our expectations due to the applied numerical approach. The most interesting results however are the obtained asymptotic cost functional values  $\mathbf{J}_0^M$ , which can be regarded as approximations of the true, grid converged compliance values. They show that the ranking of the microstructure models and the gaps demarcating the different models remain. On the other hand it is noteworthy that the rotating rods microstructure has a relative discrepancy towards the optimal sequential lamination construction of just about 0.56% and as such is a close approximation.

model	$\mathbf{J}_0^M$	$c$	$p$	error
ellipsoidal $1 \times 1$	2.07901	3.71	1.07	0.00001
ellipsoidal $2 \times 2$	2.06611	2.53	0.92	0.00004
rods fixed	1.89318	2.23	0.72	0.00122
rods rotating	1.85024	3.00	1.09	0.00001
sequential lamination	1.83992	1.76	1.05	<0.00001

Table 6.8.: Results of least squares fitting of the results obtained from computed series using the different microstructure models: obtained parameters for (6.1) and least squares error.

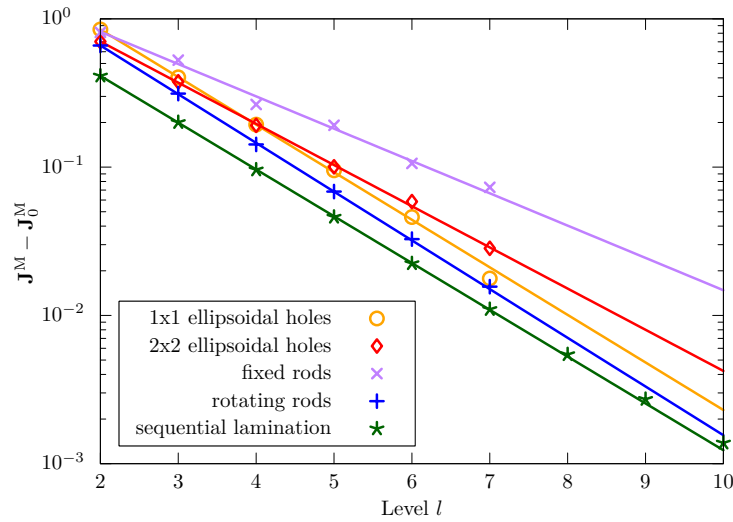


Figure 6.11.: Plot of the error in the left hand side of (6.1), using points, and the right hand side of (6.1), using lines, for the different microstructure models and varying macroscopic resolution using the parameters from Table 6.8.

**Remark 6.3** (Objective scaling). The results presented here differ from previously published results in [137]. We now use an objective scaling for the optimizer `Ipopt`, that had not yet been implemented at that time. As a guideline the `Ipopt` manual suggests to scale the optimization problem so that all nonzero first partial derivatives are of magnitude  $10^{-1} - 10$ . Indeed we observed for our two-scale optimization problems that a large scaling caused the optimization algorithm to not converge anymore for problems on coarse grids. On the other hand a small scaling led to premature termination with apparently non-converged results on fine grids. This is due to the scaling by the macroscopic cell size when evaluating the cost functional (5.7) or the gradient (5.9) respectively. For the objective functional the values on the macroscopic cells add up to a cost functional value that is of the same order of magnitude for different macroscopic grid levels as expected. For the gradient however, a separate set of parameters is given on each macroscopic cell and the total number of degrees of freedom increases with macroscopic refinement. Consequently the sensitivity w. r. t. a single parameter decreases. It is

divided by 4 for each macroscopic refinement to be precise. Therefore increasing the objective scaling by a factor of 4 for each macroscopic refinement has proven useful.

### 6.2.3. Influence of microscopic discretization

To investigate the influence of the number of discretization points used in the microscopic cell problems we focus on microstructures made from single ellipsoidal perforations and rotating orthogonal rods, as we did before in the context of prescribed strains. We take the carrier plate scenario on a macroscopic grid of level 3 as an example and consider several variants of discretizations. First of all we have to remark that by an optical inspection almost no differences in the outcomes of optimization can be identified. We therefore do not display the individual results but focus on a quantitative analysis. The cost functional values as well as the number of iterations the optimization algorithm needed for convergence are summarized in Table 6.9. As before we notice the effect of the discretization on the cost functional to be more

points edges	points perforation	iterations	$\mathbf{J}^M$	points edges	iterations	$\mathbf{J}^M$
3	12	30	2.33570	4	47	2.13301
4	16	33	2.42458	8	37	2.15811
8	16	39	2.47202	12	90	2.16304
16	16	40	2.48719	16	118	2.16701
8	32	39	2.54873	32	134	2.16569
16	64	47	2.59463	64	198	2.17078

(a)
(b)

Table 6.9.: Comparison of cost functional values and numbers of iterations needed for optimization for the carrier plate scenario and (a) ellipsoidal perforation as microstructure with varying number of discretization points on the outer edges and the inner perforation, and (b) rotating rods as microstructure with varying number of discretization points on the outer and inner edges.

drastic for the ellipsoidal perforations. In particular the discretization of the perforation has a strong influence. Again, this can be attributed to the polygonal discretization of a smooth curve. Common to both models is that the objective functional increases for increased numbers of discretization points. The number of iterations increases as well, but here the differences are larger for the rotating rods microstructure. From these observations we draw the following conclusions. Meaningful results are already achievable for low numbers of discretization points. This is indeed plausible as the cost functional and gradient are computed on the same grid. Moreover the convergence of the optimizer is faster then, especially for the rotating rods microstructure. Both conclusions justify the use of a rather coarse discretization to save computational time. The cost functional however is underrated then, which must be kept in mind when comparing different models.

### 6.3. Inspection of speed-up measures

Finally we take a look at the employed speed-up measures. Regarding the different approaches explained in Section 5.6 the benefits of exploiting the linear dependence on the microscopic cell problem solutions and the a priori known macroscopic system matrix structure are indisputable. They represent equivalent formulations of the original scheme and obviously require less computational time. The effects of parallelization, on the contrary, are hard to estimate beforehand. Finally the introduction of a look-up table for microscopic solutions adds another layer of approximation to the overall scheme and hence needs to be evaluated.

#### 6.3.1. Parallelization

Measuring the parallel performance of an algorithm receives much attention in the field of *high performance computing (HPC)*, see e. g. [199]. For a computer program relying primarily on computing cycles of the *central processing unit (CPU)* it is common to consider a representative problem of fixed, typical size. The workload is distributed among several processes, each of which is assigned to an individual and independent central processing unit. Finally the time until termination is measured for a varying number of such processes. Modern computing hardware makes use of various sophisticated methods to speed up the execution, like individual overloading within the thermal and electric budget, out of order execution, and shared access to distributed cache memory. All of these might interfere with an unbiased comparison of the runtimes for varying number of processes and we therefore try to disable such technology where possible. Our experiments are done on a computing server with 40 individual processing units. We choose the optimization run for the carrier plate scenario with rotating rods as the microstructure model on a macroscopic grid of level 4, i. e. 256 cells on which microscopic solutions need to be computed. For each number of processes we perform three individual runs, check the difference in execution time to be within reasonable limits, and take the mean runtime. As absolute values highly depend on the used hardware, we list normalized values in Table 6.10, where the mean runtime of the program with one process corresponds to a normalized time of 100. To assess the parallel performance we consider two benchmark values. First the *speedup* when doubling the number of processes, i. e.

$$S_{\text{speedup}} := \frac{t_n}{t_{2n}},$$

where  $t_n$  is the runtime when using  $n$  processes. In an idealized setting its best value would be 2, when doubling the number of processes would reduce the runtime by half. The second benchmark is more common in HPC, namely the *strong scaling efficiency*

$$S_{\text{scaling}} := \frac{t_1}{n t_n} 100\%.$$

Here an ideal value of 100% would correspond to a perfect parallel executing without any communication or synchronization overhead and no serial parts in the algorithm. As can be seen, the speedup is near 2 only when moving from 1 process to 2 processes. But it does not decrease much until 16 processes are used. The continued decrease of the strong scaling benchmark also confirms a non-ideal parallelization, which however is a usual observation for a realistic algorithm. Strong scaling values for up to and including 16 processes are in fact quite good, especially when keeping in mind that only the most computationally intensive

processes	normalized runtime	$S_{\text{speedup}}$	$S_{\text{scaling}}$
1	100.00		
2	50.54	1.98	98.93
4	27.21	1.86	91.87
8	14.62	1.86	85.47
16	8.40	1.74	74.38
32	5.36	1.57	58.31

Table 6.10.: Normalized runtime, speedup and strong scaling benchmark values for the optimization of the carrier plate scenario with the rotating rods microstructure model on a macroscopic grid of level 4 for different numbers of processes used in parallel.

part was parallelized, using rather simple techniques. The bottom line is that it is reasonable to run the algorithm with the investigated number of processes.

### 6.3.2. Microstructure look-up table

As described in Section 5.6.4 a look-up table can be employed to reuse previously computed microscopic solutions corresponding to certain parameter sets. In order to evaluate the objective functional and its gradient for arbitrary choices of the parameters a multi-linear interpolation has to be used, which adds another type of approximation to the overall scheme. It is in particular controlled by the number of intervals  $L$  each parameter range is divided into. We investigate one example to get an idea of the effects of this approach. The optimization of the carrier plate scenario on a macroscopic grid of level 3 with one ellipsoidal perforation or rotating rods as the microstructure model is considered again. It is run using the ordinary algorithm without a look-up table, using a look-up table built up during the optimization from scratch, and using a previously saved look-up table. Here we choose  $L = 100$ . For each setup we perform three individual runs, check the difference in execution time to be within reasonable limits, take the mean runtime, and normalize it to the mean runtime of the setup without a look-up table. In Table 6.11 we list the results. Most importantly the obtained cost

	ellipsoidal perforation				rotating rods			
	time	iter.	comp.	$\mathbf{J}^M$	time	iter.	comp.	$\mathbf{J}^M$
no table	100.00	23	1536	2.48460	100.00	58	8796	2.16348
new table	537.31	30	8311	2.48559	131.93	58	12362	2.16412
loaded table	13.22	30	0	2.48559	2.45	58	0	2.16346

Table 6.11.: Comparison of the normalized runtimes, the number of iterations until termination, the number of computations of microscopic cell solutions, and the final objective functional value for the carrier plate scenario on a macroscopic grid of level 3 and one ellipsoidal perforation or rotating rods as the microstructure model, without a look-up table, with a look-up table built up from scratch, and with a loaded precomputed look-up table.

functional values are close to each other for all the setups and both microstructure models, respectively. The qualitative outcomes do not show any obvious differences to the results displayed before and are therefore not shown here. The course of the optimization scheme however changes and thereby influences the runtime.

For the ellipsoidal perforations the convergence without a look-up table is fast, only 23 iterations are needed and `Ipopt` reports just 24 evaluations of the objective functional. For every evaluation every cell problem is solved, leading to a total number of  $24 \times 2^3 = 1536$  computations as reported. When using a look-up table that is empty at the beginning of the algorithm the number of considered cell problems increases drastically. This is plausible as for every interpolation  $2^3$  neighboring parameter sets and their corresponding cell solutions are taken into account. Furthermore `Ipopt` needs significantly more iterations and objective function evaluations, leading to an increased number of different required parameter sets in the course of the algorithm. Consequently the runtime increases, in fact proportional to the number of cell problems solved by more than a factor of 5. We remark that the number of considered cell problems is still far away from the theoretical maximum of  $101^3$  possible combinations in the discretized parameter space. The full potential of the look-up table approach becomes apparent when a previously saved table is loaded at the beginning of the optimization scheme. Not a single solution of a cell problem needs to be recomputed and the overall runtime drops to about 13% of the runtime without a look-up table. It seems strange that the final objective values are not exactly identical for the two runs with an initially empty and a loaded look-up table. This has to be attributed to technical specifics of the compiled software code. There might be a difference in computer arithmetic precision if a calculation is done with a cell solution that has just been recomputed in comparison to a solution that had been written to a file in a specified binary format. These tiny differences give rise to a divergent behavior of the optimization algorithm, starting at some point, e. g. in the course of line search, and leading to a slight difference in the ultimate results.

For the rotating rods microstructure the situation is different. The optimization algorithm without a look-up table requires more than twice the number of iterations than for the ellipsoidal perforation microstructure and `Ipopt` reports about six times more evaluations of the objective functional. Thereby also the number of computed cell problems is increased. Since the computational time for the two microstructure models is not comparable in any case we normalize the runtimes individually. When using the look-up table approach the number of cell problems increases only mildly. Seemingly several parameter sets and their solutions can already be reused during the same run. By chance the number of iterations remains the same, but the actually required number of evaluations changes. When the saved look-up table is loaded in advance, again no cell solution needs to be recomputed. Here the runtime drops to about 2% and the gain is even more significant due to the slower convergence and higher number of evaluations for the run without a look-up table.

We conclude that the employed look-up table approach with linear interpolation provides an outstanding speed-up for the two-scale shape optimization scheme. Although the course of optimization changes and typically more iterations are required the overall runtime is decreased by one or even two orders of magnitude in the investigated examples. The saved tables of these optimization runs require only 33 and 78 megabytes of disk space, respectively. For macroscopic domains with higher refinement levels the look-up tables will certainly grow up to a certain extend as further, different microscopic cell geometries will emerge. The important point however is that their sizes, and thereby the computational times, are actually not coupled to the number of cells. We therefore expect an even higher gain for larger



problem sizes and cases where several optimization runs need to be performed for the same microstructure model. On the other hand the size of a look-up table depends on the number of parameters required for the microstructure model and the approach therefore suffers from the curse of dimensionality. For the fixed rods model, e. g.,  $2^6 = 64$  neighboring parameter sets would have to be considered for each evaluation, whereas only 8 were required in the examples above. It is thus foreseeable that the overall scheme will become computationally infeasible for more complex microscopic geometries.

## 6.4. Conclusion

First of all, the two-scale shape optimization method devised and realized in this work performed very well and produced the anticipated results. Optimizations for varying prescribed macroscopic strains displayed the distinctive capabilities of the different investigated microstructure models. Here the ability for an arbitrary rotation of the complete microscopic cell turned out to be crucial. The reason is that a shape with symmetry axes and a dominant elongation leads to an orthotropic effective elasticity tensor, whose frame of reference should be aligned with the principal strain and stress directions in order to be optimal. Furthermore the ability to create a criss-crossing pattern was favorable, especially for strains with eigenvalues of equal magnitude. Exactly those scenarios also revealed the most significant discrepancies to optimal shapes, represented by the sequential lamination model. As expected the geometrically simple constructions did not lead to optimal results, but the approximation by the rotating rods microstructure was remarkable in cases where the ratio parameter of the sequential lamination model was not too close to 0.5. The carrier plate scenario was investigated as a macroscopically more complex scenario and in analogy to the single-scale results that motivated this work. Indeed the two-scale results showed a characteristic distribution of material on the macroscale and microstructures within regions of intermediate density. The macroscopic shapes varied with the employed microscopic model due to the different effective material properties. Mostly, sharp interfaces, separating regions with significant difference in the effective density, but also smooth transitions were observed. Within certain regions patterns known from the single-scale setting were indeed captured in the microscopic part of the two-scale approach, provided they could be realized by the actual microstructure model.

The impact of discretization of the microscopic model was investigated and turned out to be significant for the synthetic scenarios with prescribed macroscopic strain. While the qualitative outcomes were comparable, the cost functional values clearly differed. This was in particular observed for the smooth perforations due to the non-exact geometric discretization. For the carrier plate scenario the impact was in general less critical. Regarding the macroscopic discretization a series of computations was done for all microscopic models and increasingly refined macroscopic grids. By an extrapolation, ideal, grid converged functional values were obtained, which still showed distinct gaps between the different models and towards optimal shapes. In this connection a predominant linear error decay rate in the cost functional was confirmed. Local minima were an issue for the employed optimization scheme. However they could often be attributed to an ambiguous choice of design parameters and did not deteriorate the final results. More critical instances were observed as well. For their avoidance an unbiased initialization turned out as best practice.

Several speed-up measures were directly incorporated in the implementation. The effect of parallelization on the contrary had to be evaluated. It turned out that for numbers of

processes typically used on modern workstations the parallel efficiency was acceptable. An optimal scaling behavior is never realistic and in particular for our algorithm only the most time consuming part was parallelized. Finally look-up tables proved to be a powerful tool to overcome the computational complexity caused by the microscopic cell problems. They were applicable as long as the dimension of the design parameter space was low, and became otherwise infeasible due to the curse of dimensionality. The number of intervals in the range of the individual parameters could be chosen in a way that results remained comparable to those obtained without the look-up table approximation.

---

## CHAPTER 7

### Stochastic Shape Optimization

---

UNCERTAINTY is a prevailing issue in the simulation of natural scientific phenomena. In this chapter we broaden our perspective by allowing for stochastically varying loadings in the context of the two-scale shape optimization model. This takes into account that for shape optimization problems met in reality a deterministic loading is usually not a realistic assumption. Instead, when e. g. thinking about atmospheric exposure, surface loadings may change abruptly and typically vary continually over time. These variations can be modeled by probability distributions or practically given by frequency distributions resulting from measurements and quantization. In terms of shape optimization this implies that for a fixed shape each realization of the stochastic load determines a particular elasticity solution and a corresponding value of the cost functional. Effectively this turns the objective into a random variable and shape optimization then amounts to finding the best candidate from a set of random variables for admissible shapes. Borrowing concepts from finite dimensional two-stage stochastic programming we will establish suitable ranking functions for those random variables reflecting both a risk neutral and a risk averse perspective. While in the former different realizations of the cost will get weighted by their probability, in the later special statistical parameters will give precedence to realizations regarded as risky for the structural setup. Finally we will introduce the concept of stochastic dominance, which provides means for ordering shapes according to their performance and allows for an optimization based on comparison to a reference design.

The presented ideas and concepts for treating shape optimization problems in the stochastic context as well as the considered numerical examples trace back to the work by Conti et al. in [136, 139]. For this thesis it is worth to study the performance of the two-scale model in matters of the considered nonlinear, more complex objective functionals.

#### 7.1. Preliminaries

Let  $(\Omega, \Sigma, \mathbb{P})$  be a probability space with finitely many events  $\omega_i \in \Omega$ ,  $i = 1, \dots, S$ , and a discrete probability distribution function with  $\mathbb{P}(\omega_i) = \pi_i$ . For shape optimization a surface loading  $g$  turns into a random variable, indicated by writing  $g(\omega)$ , where  $\omega$  can be any of the  $\omega_i$  above. Leaving volume forces aside as before, the realizations of the random variable  $g(\omega_i)$  will be referred to as loading scenarios, which define different vector-valued normal stresses prescribed on  $\Gamma_N$ . Consequently the elastic displacement becomes a random variable as well. Its realizations  $u[\omega_i]$  are given by the unique solutions of the elasticity problem (3.10) for the corresponding realizations of the load  $g(\omega_i)$ . Finally also the cost functional takes the role of a random variable, with realizations  $\mathbf{J}[\omega_i, \mathcal{O}; u]$  obtained by evaluating the objective for given

$u[\omega_i]$ . Within this setting the ultimate goal is to find a shape  $\mathcal{O}^{\text{opt}}$  that is admissible, denoted by  $\mathcal{O}^{\text{opt}} \in \mathcal{U}_{\text{ad}}$ , and performs best when taking into account all possible loadings  $g(\omega_i)$ .

The concepts introduced here originate from *two-stage stochastic programming*, see [221] for an in-depth discussion. To illustrate the connection we will sketch a generic problem formulation in this context and relate the problem of shape optimization to it afterwards. Therefore consider the stochastic optimization problem

$$\min \{c^\top x + q^\top y : Tx + Wy = z(\omega), x \in X, y \in Y\}, \quad (7.1)$$

for fixed *cost vectors*  $c$  and  $q$ , linear operators  $T$  and  $W$ , a vector-valued random variable  $z$ , and polyhedra  $X$  and  $Y$  in Euclidean spaces. Furthermore take into account the *information constraint*

$$\text{decide } x \mapsto \text{observe } z(\omega) \mapsto \text{decide } y = y(x, z(\omega)).$$

This constraint constitutes a two-stage scheme of alternating decision and observation. Here the first-stage decision  $x$  must not anticipate future outcomes of the random variable  $z(\omega)$ . The second-stage decision  $y = y(x, z(\omega))$ , often referred to as a *recourse action*, is given by the optimal solution to the second-stage problem, a minimization problem remaining after  $x$  and  $z(\omega)$  have been fixed. This is clarified by rewriting (7.1) into

$$\min_x \left\{ c^\top x + \min_y \{ q^\top y : Wy = z(\omega) - Tx, y \in Y \} : x \in X \right\},$$

where the second-stage decision corresponds to the inner minimization problem. Due to the dependence on the random outcome  $z(\omega)$ , finding an optimal  $x$  from the set  $X$  amounts to a minimization problem over a family of random variables.

Coming back to shape optimization,  $\mathcal{O}$  now takes the role of  $x$  and the elastic displacement replaces  $y$ . The surface load  $g(\omega)$  represents the random data  $z$  and the cost functional  $\mathbf{J}[\omega, \mathcal{O}; u]$  is the cost to be minimized, i. e.  $c^\top x$  in the example above. First, and independently of  $g(\omega)$ , a shape  $\mathcal{O}$  has to be found. Then, after commencing of  $g(\omega_i)$ , the elasticity solution is determined by virtue of (3.10), which corresponds to the second-stage problem, and finally  $\mathbf{J}[\omega_i, \mathcal{O}; u]$  is evaluated. The second-stage problem here can in fact be expressed as a minimization problem as well, because the displacement  $u$  can equivalently be characterized as a minimizer of the elastic energy, cf. Corollary 3.11. Altogether we obtain the minimization problem

$$\min \left\{ \mathbf{J}[\omega, \mathcal{O}; u] : u[\omega, \mathcal{O}] = \arg \min_{u \in H_{\Gamma_D}^1(\mathcal{O}; \mathbb{R}^2)} \mathbf{J}^{\text{total}}[\omega, \mathcal{O}; u], \mathcal{O} \in \mathcal{U}_{\text{ad}} \right\}.$$

The solution of the inner minimization is however uniquely determined, s. t. there is actually no decision to make. Still the analogy to the two-stage problem is noteworthy.

## 7.2. Stochastic optimization

As seen in the preceding section a shape optimization problem involving stochastic loads amounts to a minimization over a family of random variables. This can be enabled by applying suitable ranking functions. Here different functionals lead to different perceptions of the occurring loads. In the following we will introduce the considered optimization problems.

### 7.2.1. Definition of stochastic cost functionals

The general procedure is to compute the expected value of the costs, possibly transformed beforehand by a monotonically increasing function  $r: \mathbb{R} \rightarrow \mathbb{R}$ , which could also be nonlinear. Then the corresponding minimization problem reads

$$\min \left\{ \mathbf{Q}(\mathcal{O}) := \mathbb{E} [r(\mathbf{J}[\omega, \mathcal{O}; u])] = \sum_{i=1}^S \pi_i r(\mathbf{J}[\omega_i, \mathcal{O}; u]) : \mathcal{O} \in \mathcal{U}_{\text{ad}} \right\}. \quad (7.2)$$

Note that by this approach the stochastic problem is actually converted to a deterministic problem, which however involves several objectives and solutions for the different realizations of the loading.

**Remark 7.1** (Expected value of the loads). For the sake of completeness let us mention that it is of course also possible to reduce the stochastic shape optimization problem to a deterministic one by considering the expectation of the loads  $\bar{g} = \sum_i \pi_i g(\omega_i)$ . This however can lead to full cancelation of certain realizations of the load, excluding them from the optimization. A striking example is given in [136, Figure 4.2] but the phenomenon can also be seen in the numerical results later on.

The trivial choice of  $r$  being the identity, i.e.  $r(t) = t$ , reduces (7.2) to a minimization problem of the expected value of the costs.

**Definition 7.2** (Expected value of the costs). *The expected value of the costs functional is given by*

$$\mathbf{Q}_{EV}(\mathcal{O}) := \mathbb{E} [\mathbf{J}[\omega, \mathcal{O}; u]]. \quad (7.3)$$

Apparently the formulation is entirely different from the deterministic objective w. r. t. the expected value of the loads. In particular all possible loads are taken into account via their induced elastic displacements and cost functional values. This influence is moreover weighted by the corresponding probability of the realization. A deficiency is that any variability of the random variable is ignored. Referred to as *risk neutral*, the ranking might not adequately account for a scenario with low probability but fatal outcome for the elastic structure, in terms of high objective values. As a consequence *risk aversion* can be added by introducing a statistical parameter, supposed to realize a specific perception of risk.

**Definition 7.3** (Expected excess). *Let  $\eta$  be a preselected threshold value for the cost functional and consider  $r(t) = \max\{t - \eta, 0\}$ . The expected excess functional is then given by*

$$\mathbf{Q}_{EE_\eta}(\mathcal{O}) := \mathbb{E} [\max\{\mathbf{J}[\omega, \mathcal{O}; u] - \eta, 0\}].$$

For minimization thereby only values above the threshold are taken into account unaltered. Values below the threshold are mapped to 0 and practically ignored. This gives room, in terms of available volume, to further improve the situation for the exceeding scenarios. Their influence is controlled by both the amount of excess and their probability. Another alternative is the *excess probability* functional.

**Definition 7.4** (Excess probability). *Let  $\eta$  be a preselected threshold value for the cost functional and consider the Heaviside function as  $r$ , i. e.*

$$r(t) = H(t - \eta) \quad \text{with } H(t) = \begin{cases} 1 & t > 0 \\ 0 & t \leq 0 \end{cases}.$$

The excess probability functional is then given by

$$\mathbf{Q}_{EP_\eta}(\mathcal{O}) := \mathbb{E}[H(\mathbf{J}[\omega, \mathcal{O}; u] - \eta)] = \mathbb{P}[\mathbf{J}[\omega, \mathcal{O}; u] > \eta] .$$

Here the second identity justifies the naming. Just as for the expected excess functional only values exceeding the threshold are taken into account. In contrast, the amount of excess is not relevant anymore, but rather a binary decision is made whether the threshold is exceeded or not.

### 7.2.2. Practical aspects

Having set up suitable stochastic cost functionals we can now approach their optimization. Besides fundamental algebraic expressions the newly obtained functionals only contain terms that are known from the previous chapters in the deterministic setup. We will now discuss remaining aspects for a numerical realization.

**Non-differentiability.** The introduction of the nontrivial transfer functions  $r(t)$  above comes along with non-differentiability of the resulting cost functionals at the threshold value  $\eta$ . As discussed before, we are employing a gradient based optimization scheme and therefore need to restore the differentiability via smooth approximations of the transfer functions. For the max function we use

$$\max\{t, 0\} = \frac{1}{2} (|t| + t) = \frac{1}{2} (\sqrt{t^2} + t) \approx \frac{1}{2} (\sqrt{t^2 + \epsilon} + t)$$

for a small regularization parameter  $\epsilon > 0$ , which smoothes the kink at  $t = 0$ . For the Heaviside function we use

$$H(t) \approx \frac{1}{2} + \frac{1}{2} \tanh\left(\frac{t}{\epsilon}\right) = \frac{1}{2} + \frac{1}{2} \frac{\sinh\left(\frac{t}{\epsilon}\right)}{\cosh\left(\frac{t}{\epsilon}\right)} = \frac{1}{2} + \frac{1}{2} \frac{e^{\frac{t}{\epsilon}} - e^{-\frac{t}{\epsilon}}}{e^{\frac{t}{\epsilon}} + e^{-\frac{t}{\epsilon}}} = \frac{1}{2} + \frac{1}{2} \frac{e^{2\frac{t}{\epsilon}} - 1}{e^{2\frac{t}{\epsilon}} + 1} = \frac{1}{1 + e^{-\frac{2t}{\epsilon}}} .$$

Thereby the jump from 0 to 1 at  $t = 0$  is replaced by a smooth transition. Its width is determined by the regularization parameter  $\epsilon$ . Note that the values 0 and 1 can only be attained here asymptotically. In summary we approximate the max and the Heaviside function in the definition of the stochastic cost functionals by

$$M_\eta^\epsilon(t) := \frac{1}{2} \left( \sqrt{(t - \eta)^2 + \epsilon} + (t - \eta) \right) , \quad (7.4)$$

$$H_\eta^\epsilon(t) := \left( 1 + e^{-\frac{2(t-\eta)}{\epsilon}} \right)^{-1} . \quad (7.5)$$

See also Figure 7.1 for an illustration. Obviously the newly introduced regularization parameter  $\epsilon$  has immediate influence on the functionals in the optimization. In fact it is of minor importance for the expected excess functional and can be chosen rather small. Objective values below threshold then get mapped to nearly 0 and the gradient indicates a plateau. Hence corresponding scenarios are not taken into account anymore. Above threshold the smoothed transfer functional behaves like the identity leading to unvaried consideration of those scenarios. Only when crossing the threshold, smoothing comes into play, ensuring valid conditions for the optimization algorithm. On the contrary the regularization parameter is highly significant for the excess probability functional. If it is chosen too small, the energy

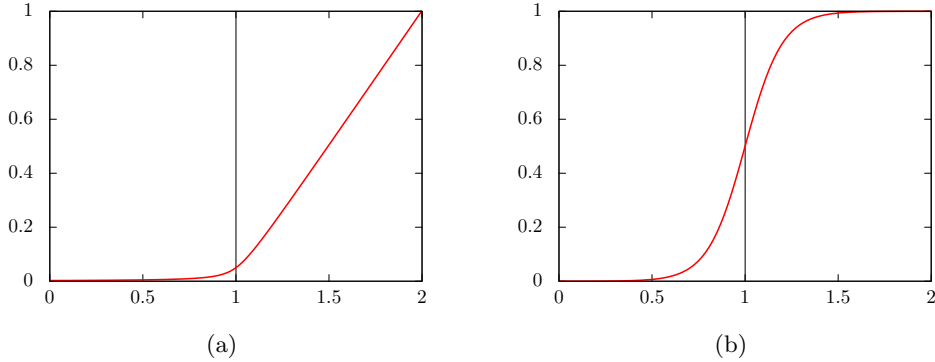


Figure 7.1.: Smooth approximations of the (a) max and (b) Heaviside function with regularization parameter  $\epsilon = 10^{-2}$  and  $\epsilon = 0.2$  respectively, and threshold  $\eta = 1$ .

landscape constitutes a plateau almost everywhere except for values very close to the threshold. As a result there will not be any optimization at all. On the other hand, if  $\epsilon$  is chosen too high, costs for many scenarios might fall into the transition zone of the Heaviside function, cf. Figure 7.1(b). In the vicinity of the threshold it approximately behaves like a linear profile, possibly leading to results comparable to those for the expected value of the costs. Effectively the distinguishing risk aversion is lost then. In the end  $\epsilon$  has to be carefully and individually selected for each investigated shape optimization problem to ensure the desired effect of the excess probability functional. For the expected excess functional no further attention is required. The resulting minimization problems finally read

$$\min \left\{ \mathbf{Q}_{\text{EE}_\eta}^\epsilon(\mathcal{O}) := \mathbb{E} [M_\eta^\epsilon(\mathbf{J}[\omega, \mathcal{O}; u])] : \mathcal{O} \in \mathcal{U}_{\text{ad}} \right\}, \quad (7.6)$$

$$\min \left\{ \mathbf{Q}_{\text{EP}_\eta}^\epsilon(\mathcal{O}) := \mathbb{E} [H_\eta^\epsilon(\mathbf{J}[\omega, \mathcal{O}; u])] : \mathcal{O} \in \mathcal{U}_{\text{ad}} \right\}. \quad (7.7)$$

**Algorithmic shortcut.** Up until now we have required that the elasticity problem (3.10) has to be solved for every realization of the load  $g(\omega_i)$ . As pointed out earlier, in a realistic setup one is interested in the approximation of continuous probability distributions leading to a huge number of equations to be solved. By exploiting the linearity of the considered linearized elasticity system, a significant speedup is possible if the occurring loads can be expressed as linear combinations of basis functions. To this end let  $g_1, \dots, g_K$  be a set of base surface loadings, s. t. each realization  $g(\omega_i)$  can be written as a linear combination

$$g(\omega_i) = \sum_{j=1}^K c_j(\omega_i) g_j. \quad (7.8)$$

Now  $g_j$  are deterministic loads and  $c_j : \Omega \rightarrow \mathbb{R}$  are random variables, whose realizations for an event  $\omega_i$  precisely give the corresponding fractions of the base forces. For each deterministic load  $g_j$  an elasticity solution  $u^j$  can be computed as before by virtue of (3.10). The crucial

observation is that by linearity the linear combination

$$u[\omega, \mathcal{O}] := \sum_{j=1}^K c_j(\omega) u^j \quad (7.9)$$

is an elasticity solution for the linear combination on the right hand side of (7.8). Since this solution is unique we can always directly construct the wanted solution from the set of base solutions. This trick has appeared before when we devised speedup measures for the two-scale approach, cf. Section 5.6.2. Here it is used on the macroscale. In case of  $S \gg K$  a lot of computations can be spared.

**Shape derivative.** For the employed optimization algorithm gradient information w. r. t. the presented stochastic cost functionals is needed. We will now reduce the corresponding expressions to the shape derivative known from the deterministic setting. First of all, for the derivative not only the primal solution  $u$ , but also the dual solution  $p$  is required. If we assume that the considered deterministic cost functional  $\mathbf{J}$  is at most quadratic in  $u$ , then its derivative in the adjoint equation (4.5) is at most linear in  $u$  and we can again apply the algorithmic shortcut as before. Given an elasticity base solution  $u^j$  and the derivative  $\mathbf{J}_{,u}[\omega, \mathcal{O}; u^j](\varphi)$ , a dual solution  $p^j$  can be obtained. By linearity and uniqueness the linear combination

$$p[\omega, \mathcal{O}] := \sum_{j=1}^K c_j(\omega) p^j \quad (7.10)$$

then is the wanted solution for the right hand side  $\sum_j \mathbf{J}_{,u}[\omega, \mathcal{O}; u^j](\varphi) = \mathbf{J}_{,u}[\omega, \mathcal{O}; u[\omega, \mathcal{O}]](\varphi)$ . With the primal solution (7.9) and the dual solution (7.10) at hand we can compute the derivatives of the stochastic cost functionals. Due to the additional transformation  $r$ , the chain rule has to be applied. Specifically we get

$$\begin{aligned} d_{\mathcal{O}} \mathbf{Q}_{\text{EV}}(\mathcal{O})(V) &= \sum_{i=1}^S \pi_i d_{\mathcal{O}} \mathbf{J}[\omega_i, \mathcal{O}; u](V), \\ d_{\mathcal{O}} \mathbf{Q}_{\text{EE}_{\eta}}^{\epsilon}(\mathcal{O})(V) &= \sum_{i=1}^S \frac{\pi_i}{2} d_{\mathcal{O}} \mathbf{J}[\omega_i, \mathcal{O}; u](V) \left( \frac{\mathbf{J}[\omega_i, \mathcal{O}; u] - \eta}{\sqrt{(\mathbf{J}[\omega_i, \mathcal{O}; u] - \eta)^2 + \epsilon}} + 1 \right), \\ d_{\mathcal{O}} \mathbf{Q}_{\text{EP}_{\eta}}^{\epsilon}(\mathcal{O})(V) &= \sum_{i=1}^S \frac{2\pi_i}{\epsilon} d_{\mathcal{O}} \mathbf{J}[\omega_i, \mathcal{O}; u](V) e^{-\frac{2}{\epsilon}(\mathbf{J}[\omega_i, \mathcal{O}; u] - \eta)} \left( 1 + e^{-\frac{2}{\epsilon}(\mathbf{J}[\omega_i, \mathcal{O}; u] - \eta)} \right)^{-2}, \end{aligned}$$

where the shape derivative  $d_{\mathcal{O}} \mathbf{J}[\omega_i, \mathcal{O}; u](V)$  of the deterministic cost functional is given by (4.10) as before.

**Application of the two-scale model.** So far shape optimization in the stochastic setup was presented in a generic fashion with a shape  $\mathcal{O}$  as the object to be optimized. Our two-scale shape optimization model is however directly applicable. Therefore it is most convenient to take the macroscopic perspective. A shape then is an effective elasticity tensor field  $C^* \in L^{\infty}(D, \mathbb{R}^{2^4})$  that is locally obtained via homogenization from an underlying microstructure. It is considered admissible, i. e. from the set  $\mathcal{U}_{\text{ad}}$ , if the parameters comply with the constructive constraints,



as e.g. (5.14) for the ellipsoidal perforations, and if the effective densities globally fulfill the volume constraint, cf. (5.7). As done for optimization in the deterministic context, we use the two-scale compliance type functional (5.7) as objective. Here we already know that the dual problem is trivial and that the shape derivative w.r.t. the microscopic parameters is given by (5.9). Therefore all information needed by the optimization scheme in the stochastic context is explicitly available.

### 7.2.3. Numerical results for optimization of stochastic cost functionals

We are now ready to present and discuss the outcomes of our numerical optimization scheme for the presented stochastic cost functionals. Here we focus on two types of microstructures for the two-scale model, namely ellipsoidal perforations and rotating orthogonal rods. The former model has proven to be robust and has yielded fast convergence of the optimization algorithm, while the latter model has demonstrated the best performance in the deterministic setting. As a showcase scenario we again consider the unit square with homogeneous Dirichlet boundary conditions on the bottom. This time we prescribe loads on either the upper left or the upper right edge with different probabilities. To be more precise, the surface loading  $g$  either attacks at  $[0, \frac{1}{6}] \times \{1\}$  with a constant direction and constant magnitude of 0.1, or at  $[\frac{5}{6}, 1] \times \{1\}$  with a constant direction and a constant magnitude of 0.05. On each side five individual scenarios are realized by an inclination of the force by  $0, \frac{\pi}{4}, \frac{\pi}{2}, \frac{3\pi}{4},$  and  $\pi$  in radians, cf. Figure 7.2. All forces can be linearly combined using four basis loads, which

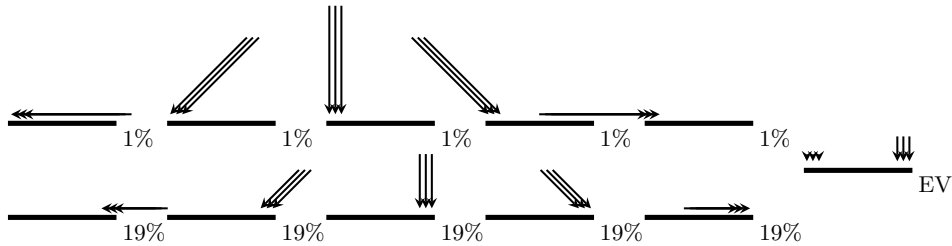


Figure 7.2.: Illustration of the loads acting on the top boundary of the carrier plate domain along with their probabilities and their expected value, in the context of stochastic optimization.

consist of the two unit vectors on each supporting edge. As remarked above this reduces the number of macroscopic elasticity problems to be solved from ten, the number of scenarios, to four, the number of basis loads. Scenarios on the right hand side appear with probability 19% each, whereas the stronger loads on the left hand side occur with probability 1% only. The overall volume fraction is constrained to 67% and a grid of refinement level 6 is used on the macroscale. The qualitative features of the results and especially the mode of action of the applied risk averse ranking functions have been discussed extensively in the original paper [139], in [138] for the two-scale model, and in [184, 183] for the single-scale setting with parametrized geometries. We summarize the essential observations in the following and display the two-scale results.

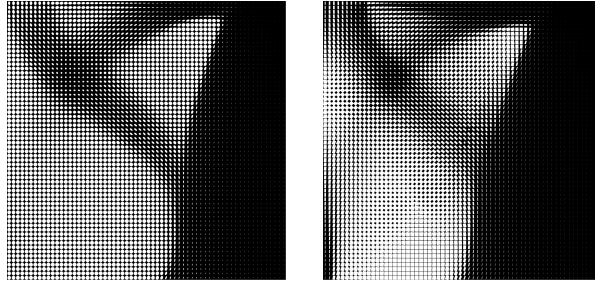


Figure 7.3.: Optimized two-scale designs using ellipsoidal perforations and rotating orthogonal rods, respectively, for optimization w. r. t. expectation of the loads.

**Expected value cost functional.** We start with the expected value of the costs functional (7.3) and present the results of optimization in Figure 7.4(a). The outcomes for the ellipsoidal holes and the rotating rods model are shown in the left and middle column, respectively. For comparison we also show the results in case a deterministic optimization problem for the expected value of the loads is considered instead, see Figure 7.3. As already mentioned, and apparent in Figure 7.2, the horizontal components of the forces cancel each other in the expectation of the loads. Consequently, for both microstructure models, a structure is laid out that is capable of withstanding vertical compression. Due to the different intensities, most of the available material is used on the right hand side to build a massive pillar consisting of solid material. Loads on the left hand side are sustained using trusses, which run along the upper boundary and through the center of the domain, and connect to the large pillar. They comprise material of intermediate density and, as seen in the deterministic setting before, microstructures have developed that are aligned with the truss direction, with the exception of a junction in the upper left region. For the rotating rods model a small pillar can also be found on the left hand side that connects to the afore mentioned junction. This is in contrast to the ellipsoidal perforations model, where however a lattice with tiny bonds is always present due to the design constraints (5.14). The shapes obtained w. r. t. the expectation of the costs look entirely different, cf. Figure 7.4(a). There is still a vertical pillar on the right hand side consisting of nearly solid material but it is much thinner. Instead most of the material is used to build a diagonal truss running from the lower left to the upper right hand side, which has an intermediate density and once again aligned microstructures, except for a junction as seen before. Its purpose is to support the high probability load with corresponding diagonal orientation. This can also be seen from the bar charts in the right column of Figure 7.4(a). Here we plot the finally attained compliance values for each individual scenario with red and blue bars, corresponding to the ellipsoidal holes and the rotating rods microstructure, respectively, and bar thicknesses indicating the different probabilities of the loadings. Clearly the vertical and the diagonal load in the direction of the built truss are best supported. Another truss in the other diagonal direction passes through the former at the junction. It is much thinner and has a lower effective density. Furthermore trusses can be observed on the upper and left hand side boundary. They are rather thick in case of the rotating rods microstructure model and lead to a frame-like structure. For the ellipsoidal perforations they exist as well but are harder to detect as the vertical alignment fades out towards the center of the domain. An overall comparison shows that the shapes using the rotating rods microstructure perform better

than the counterparts using the ellipsoidal perforations model for every individual scenario. Furthermore the stronger loadings on the left hand side in general receive little consideration in the optimization due to their low probabilities. This leads to excessively higher individual cost functional values and illustrates the drawback of the risk neutral approach as discussed before.

**Expected excess cost functional.** We now turn to the risk averse cost functionals, beginning with the expected excess. First of all it is important to note that the choice  $\eta = 0$  again leads to the expected value of the cost functional, despite the involved regularization. When increasing the threshold parameter, a continuous evolution of the shape can be observed, where more and more material is shifted to the left hand side, cf. figures 7.4 and 7.5. For  $\eta = 0.0002$  the individual costs for the loadings on the right hand side have fallen below the threshold for the first time, indicated by the horizontal line in the corresponding bar chart. Consequently from then on the optimization can focus on the left hand side scenarios. A configuration reflecting a balanced state between left and right hand side loadings is expected for a threshold value between 0.0002 and 0.0003. From  $\eta = 0.0003$  on the thickness of the diagonal truss supporting the right hand side is reduced while it is increased for the other diagonal truss. The outer frame does not undergo significant transformation for the ellipsoidal holes microstructure while for the rotating rods microstructure the pillar on the right hand side receives less and less effective density. From the bar charts we can see that for increasing threshold the cost functional values for the right hand side scenarios increase again as they are far below the threshold and practically ignored in the optimization. For  $\eta = 0.0006$  the diagonal rod that was dominating for  $\eta = 0$  is nearly removed. Ultimately for  $\eta = 0.0009$  the compliance for every scenario can easily be kept below the threshold. An indistinct shape is obtained that is rather close to the initialization.

**Excess probability cost functional.** Finally we consider the excess probability cost functional and display the results in figures 7.6 and 7.7. By trend similar effects in correspondence to the threshold can be observed. The concrete designs however seem more radical. In fact for both microstructure models the strong loads with low probability on the left hand side are completely ignored for low  $\eta$  and no structure in this direction is built at all. This is due to the Heaviside function, which transfers the initially high cost functional values to a plateau with value 1. The scenarios thus exceed the threshold in such a way that they are practically lost for the optimizer, which can also be seen from the bar charts. In fact their costs increase during optimization. Instead massive pillars made from nearly solid material are placed along the right boundary and the diagonal support of the upper right edge. For  $\eta = 0.0003$  all compliance values for the right hand side loadings are clearly below the threshold and moreover lower than for the expected excess cost functional. Some more material is used below the pillars. For the ellipsoidal holes model another diagonal truss is built whereas for the rotating rods model a rather smoothly varying microstructure can be observed, especially for  $\eta = 0.0003$ . A shift of volume to the left hand side can first be observed for  $\eta = 0.0004$  and thereby later as for the expected excess model. From  $\eta = 0.0005$  on the focus is clearly on the left hand side loadings. A thick diagonal truss supports these and an outer framework as seen similarly in the results for the expected excess functional can be identified. For increasing threshold the structures supporting the upper right edge are gradually cut back until they are ultimately removed and almost mirrored versions of the results for low  $\eta$  are obtained. In

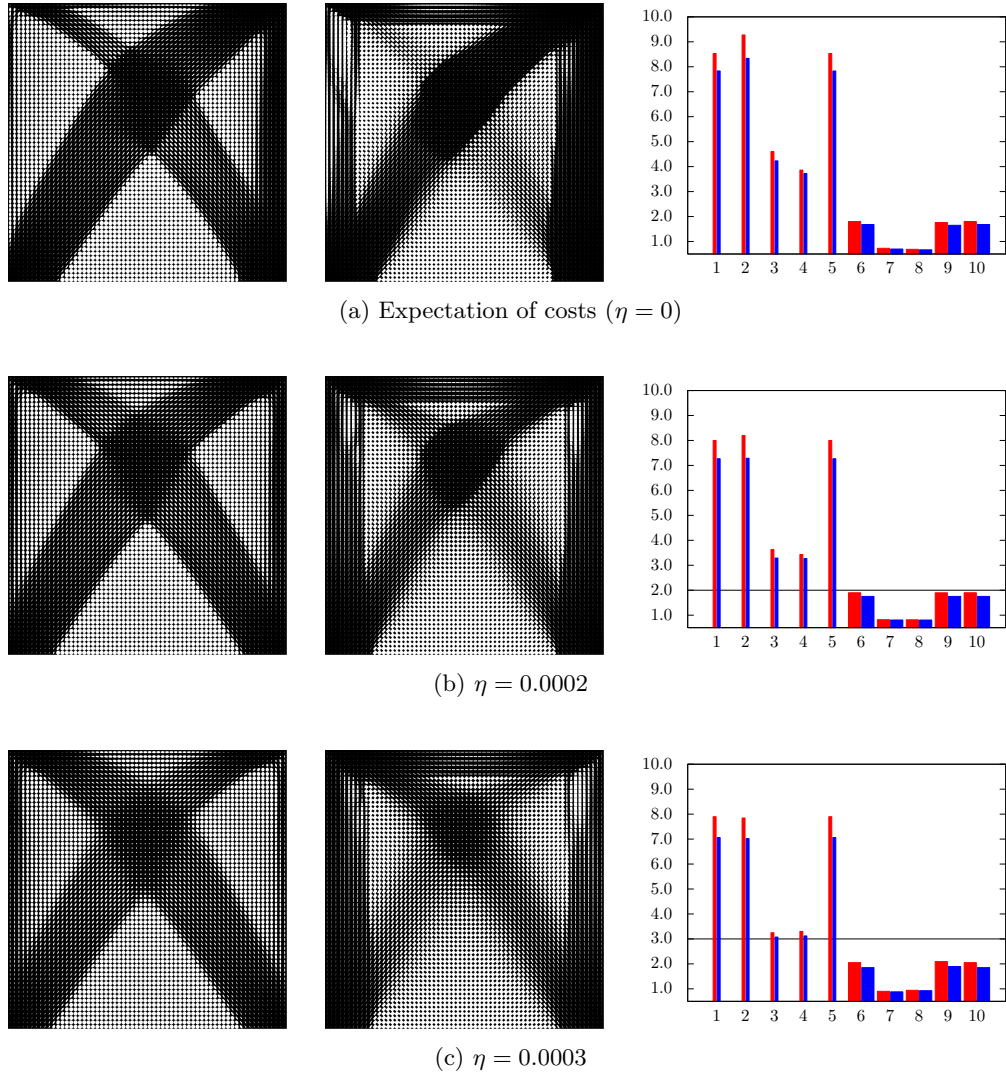


Figure 7.4.: Optimized two-scale designs for the expected excess cost functional and varying threshold parameter  $\eta$  using ellipsoidal perforations (left column) and rotating orthogonal rods (middle column), respectively, and bar charts (right column) showing the final objective function values, scaled by  $10^4$ , for each individual scenario.

this situation with  $\eta$  about 0.0009 all scenarios are below the threshold. The ones on the left hand side are still taken into account because of the relatively large regularization parameter, cf. Section 7.2.2. The ones on the right are further away and ignored, which leads to increasing costs as can be seen from the bar charts.

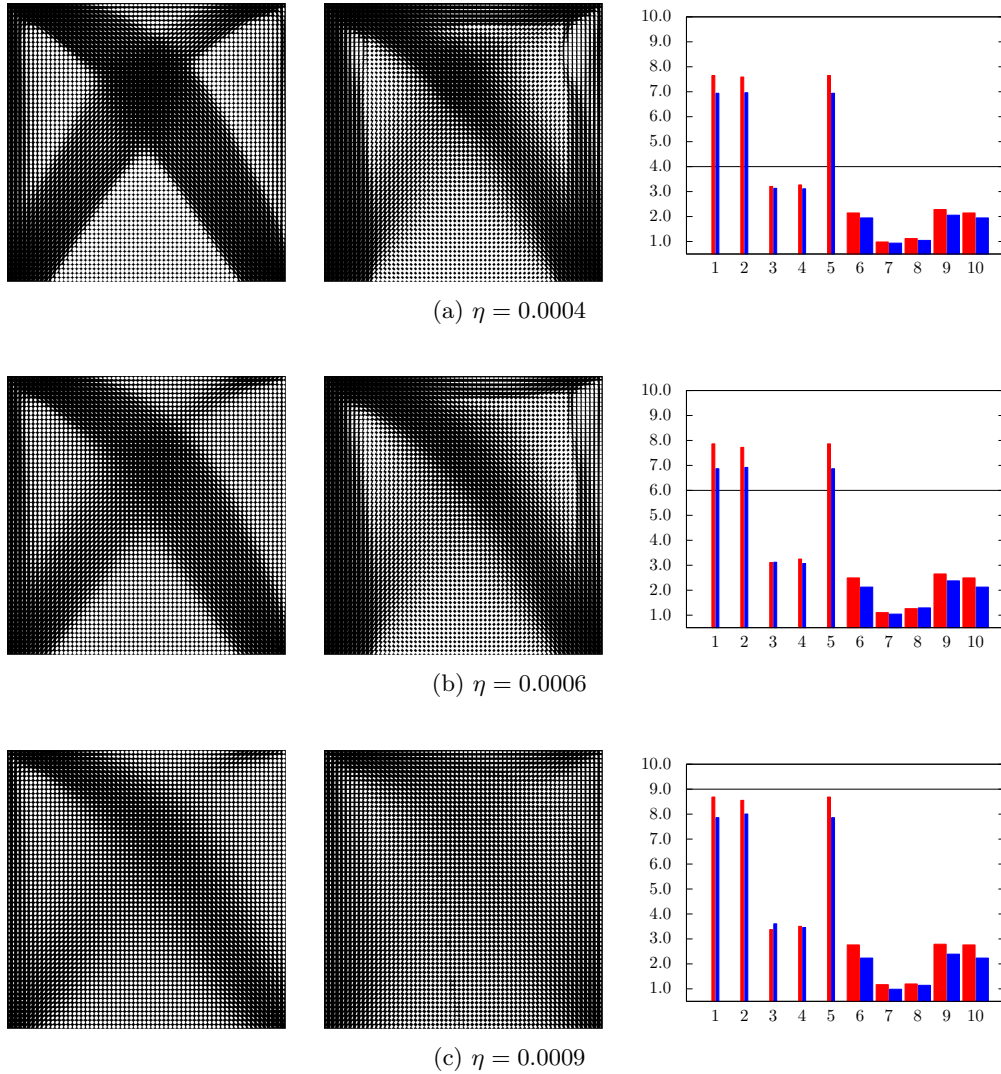


Figure 7.5.: Continuation of Figure 7.4: Optimized two-scale designs for the expected excess cost functional and varying threshold parameter  $\eta$  using ellipsoidal perforations (left column) and rotating orthogonal rods (middle column), respectively, and bar charts (right column) showing the final objective function values, scaled by  $10^4$ , for each individual scenario.

**Cross-check.** We complete this section on numerical results for stochastic optimization by presenting a cross-check of the obtained results as was also done in [139]. To this end the optimized shapes for the risk neutral and the two risk averse cost functionals, with  $\eta = 0.0003$  as an example, are considered and every functional is evaluated for each of them. Clearly the candidate stemming from optimization w. r. t. a functional should always rank best when

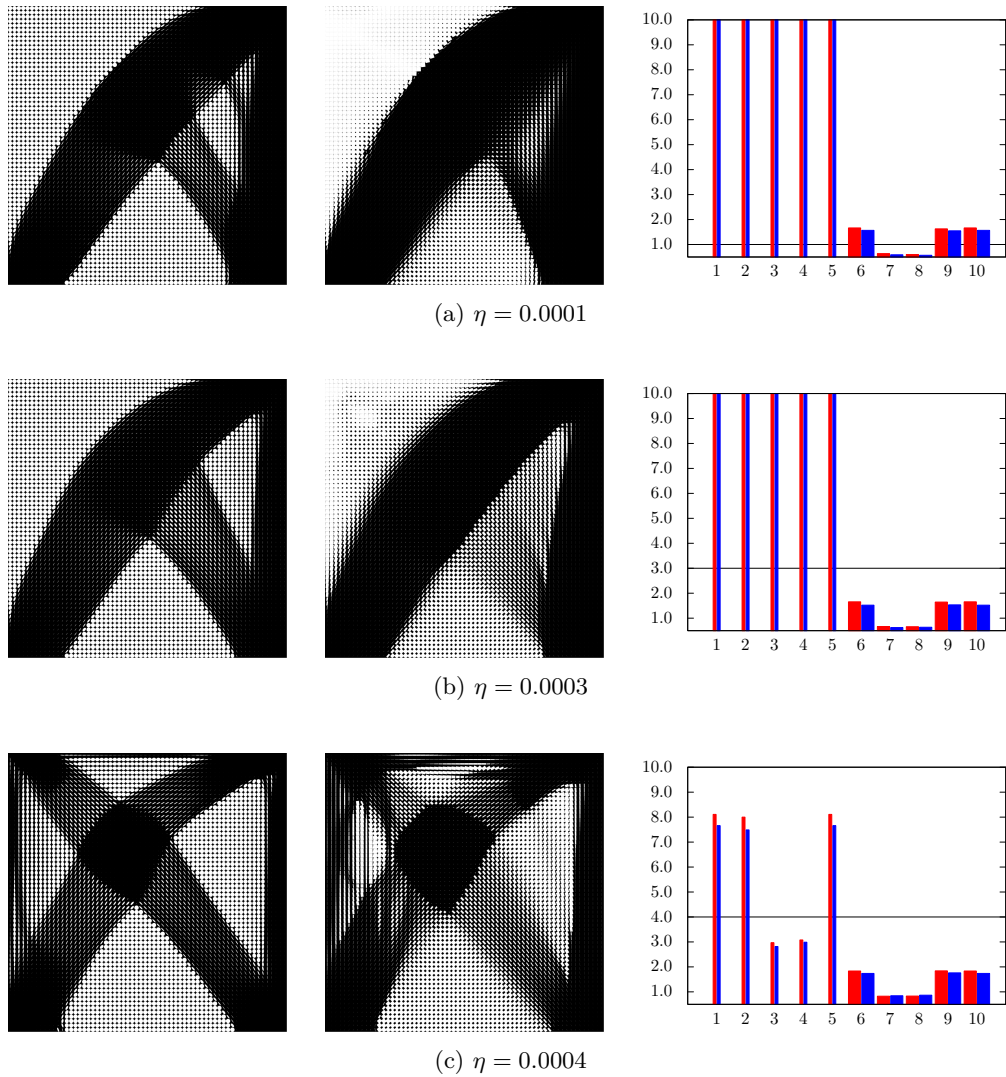


Figure 7.6.: Optimized two-scale designs for the excess probability cost functional and varying threshold parameter  $\eta$  using ellipsoidal perforations (left column) and rotating orthogonal rods (middle column), respectively, and bar charts (right column) showing the final objective function values, scaled by  $10^4$ , for each individual scenario.

comparing this functional's values among all candidates. As can be seen from Table 7.1 this is indeed the case in the example considered here.

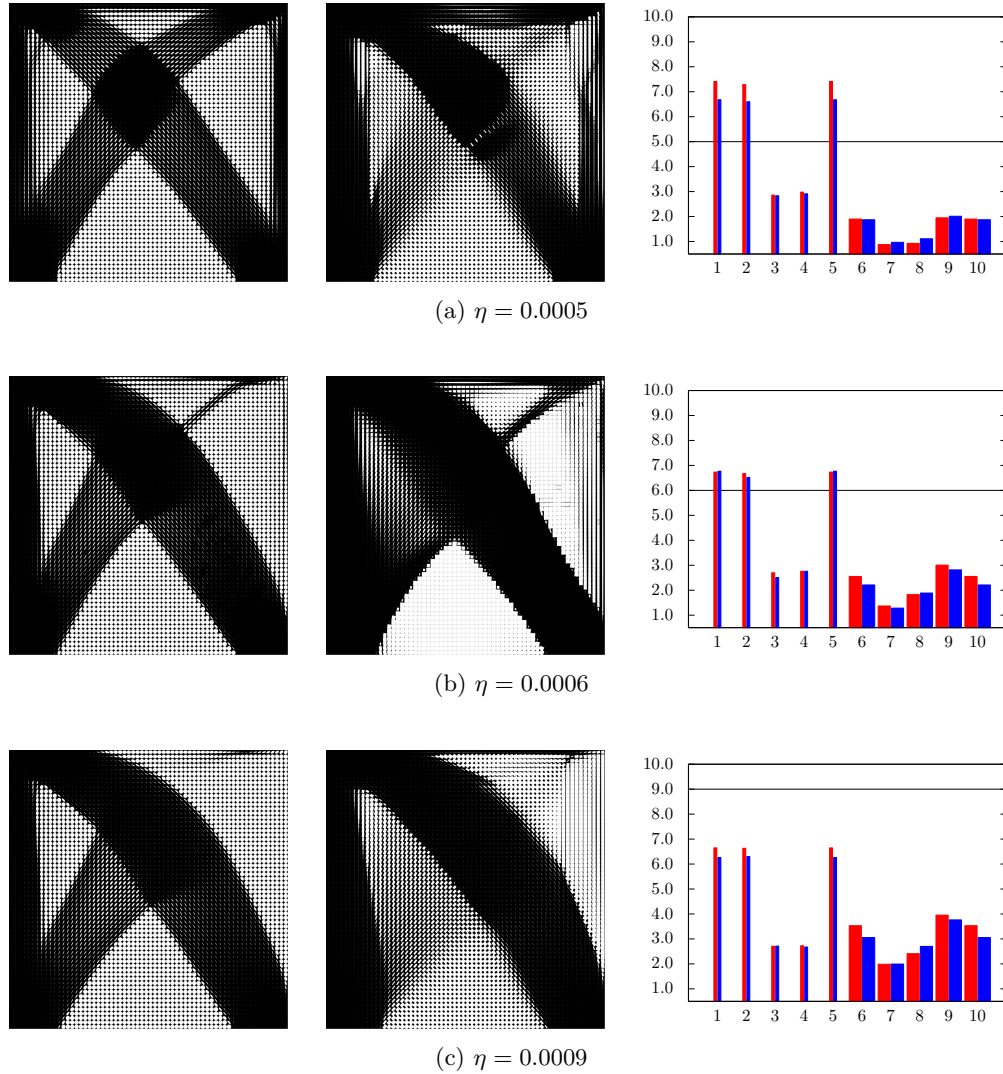


Figure 7.7.: Continuation of Figure 7.6: Optimized two-scale designs for the excess probability cost functional and varying threshold parameter  $\eta$  using ellipsoidal perforations (left column) and rotating orthogonal rods (middle column), respectively, and bar charts (right column) showing the final objective function values, scaled by  $10^4$ , for each individual scenario.

### 7.3. Stochastic dominance

The introduced stochastic cost functionals enable us to thoroughly handle shape optimization problems involving stochastic loadings. By the additional threshold parameter  $\eta$  it is moreover possible to make allowance for variability of the random variable  $\mathbf{J}[\omega, \mathcal{O}; u]$ . Tuning of this parameter however requires a priori knowledge of the range and spread of the individual

	$\mathcal{O}_{\text{EV}}^{\text{opt}}$	$\mathcal{O}_{\text{EE}_\eta}^{\text{opt}}$	$\mathcal{O}_{\text{EP}_\eta}^{\text{opt}}$		$\mathcal{O}_{\text{EV}}^{\text{opt}}$	$\mathcal{O}_{\text{EE}_\eta}^{\text{opt}}$	$\mathcal{O}_{\text{EP}_\eta}^{\text{opt}}$
$\mathbf{Q}_{\text{EV}} \cdot 10^4$	1.63	1.83	2.14	$\mathbf{Q}_{\text{EV}} \cdot 10^4$	1.53	1.68	26.20
$\mathbf{Q}_{\text{EE}_\eta}^\epsilon \cdot 10^4$	0.34	0.33	0.93	$\mathbf{Q}_{\text{EE}_\eta}^\epsilon \cdot 10^4$	0.31	0.28	25.07
$\mathbf{Q}_{\text{EP}_\eta}^\epsilon$	0.10	0.12	0.09	$\mathbf{Q}_{\text{EP}_\eta}^\epsilon$	0.09	0.10	0.08

(a) (b)

Table 7.1.: Cross-check of expected value of costs, expected excess and excess probability cost functionals with  $\eta = 0.0003$  for the optimized shapes using (a) ellipsoidal perforations and (b) rotating orthogonal rods as the microstructure model.

objectives. It is not obvious at all how and based upon which criterion a best value of  $\eta$  could be determined. In this section we therefore change our viewpoint and consider optimization under comparison constraints. Suppose we already have a reference design  $\mathcal{O}^{\text{ref}}$  that is known to perform well for a given loading scheme. This body might be the result of a previous optimization or an intuitive layout, an assumption that seems realistic for real world applications. We would now like to compare other candidates  $\mathcal{O}$  to the reference, or *benchmark*, shape and select those that perform at least as well as  $\mathcal{O}^{\text{ref}}$ . Thereby risk aversion is realized not just via a single scalar value  $\eta$ . Instead the benchmark allows to include distributional information as well. The concept of *stochastic dominance* facilitates this comparison by virtue of a mathematical partial order on the space of admissible shapes, or among random variables respectively. From the set of acceptable designs, i. e. those candidates that compare favorably, the best one can be chosen based on other quantities of interest, as for instance the total amount of material.

### 7.3.1. Definition of stochastic dominance

We will follow the exposition in [318] and summarize the main ideas. Further details can be found in [318] and the referenced textbook [296] therein. The definition will be based on the cumulative distribution function of a random variable  $X$ , given by  $F_X(x) = \mathbb{P}[X \leq x]$ .

**Definition 7.5** (First order stochastic dominance). *Let  $X$  and  $Y$  be real valued random variables.  $X$  is said to dominate  $Y$  to first order, denoted by  $X \preceq_1 Y$ , if*

$$F_X(\eta) \geq F_Y(\eta) \quad \forall \eta \in \mathbb{R}. \quad (7.11)$$

As to the interpretation, inequality (7.11) means  $\mathbb{P}[X \leq \eta] \geq \mathbb{P}[Y \leq \eta]$ , i. e. the probability that  $X$  takes values less than  $\eta$  is greater than for  $Y$ . As we have the objective functional for shape optimization in mind, smaller values are better, and therefore  $X$  is said to dominate  $Y$ . An equivalent characterization is

$$X \preceq_1 Y \iff \mathbb{E}[r(X)] \leq \mathbb{E}[r(Y)] \quad \forall r: \mathbb{R} \rightarrow \mathbb{R} \text{ nondecreasing}. \quad (7.12)$$

In fact “ $\Rightarrow$ ” follows from  $r$  being nondecreasing and  $X(\omega) < Y(\omega)$ , which in turn can be shown if (7.11) holds. Furthermore “ $\Leftarrow$ ” is obtained by choosing  $r(t) = H(t - \eta)$  as in Definition 7.4 of the excess probability. The alternative characterization establishes a link to decision making under risk, where  $r$  would be regarded as a disutility function. Higher costs mean worse



performance in shape optimization, so the disutility function should be nondecreasing as above.

Coming back to perceptions of risk, it seems meaningful to regard a single high outcome of the random variable  $X$  as more risky than a high averaged value  $\mathbb{E}[X]$ , which would be properly taken care of even in a risk neutral setting. This motivates to choose a disutility function s. t.  $r(\mathbb{E}[X]) \leq \mathbb{E}[r(X)]$ , which is just a convexity condition.

**Definition 7.6** (Second order stochastic dominance). *Let  $X$  and  $Y$  be real valued random variables.  $X$  is said to be stochastically smaller than  $Y$  in increasing convex order, or to dominate  $Y$  to second order, denoted by  $X \preceq_2 Y$ , if*

$$\mathbb{E}[r(X)] \leq \mathbb{E}[r(Y)] \quad \forall r: \mathbb{R} \rightarrow \mathbb{R} \text{ nondecreasing and convex.} \quad (7.13)$$

**Remark 7.7.** As the set of functions in (7.13) is contained in the set in (7.12), it is clear that first order dominance is a stricter condition and thus implies second order dominance.

Again there is an alternative characterization available, which makes second order dominance easier manageable, namely

$$X \preceq_2 Y \iff \mathbb{E}[\max\{X - \eta, 0\}] \leq \mathbb{E}[\max\{Y - \eta, 0\}] \quad \forall \eta \in \mathbb{R}. \quad (7.14)$$

In fact “ $\Rightarrow$ ” follows by choosing  $r(t) = \max\{t - \eta, 0\}$ . The other implication involves an approximation of an arbitrary convex function by a piecewise linear one and is more involved. As to the interpretation, inequality (7.14) states that on average  $X$  exceeds threshold values  $\eta$  less than  $Y$  does. By (7.11) and (7.14) we have now defined stochastic dominance via the already familiar excess probability and expected excess functionals. Still each relation poses an infinite number of constraints, hindering a practical application. Fortunately the next theorem states that for discrete probability distributions only a discrete number of constraints needs to be taken into account.

**Theorem 7.8.** *Assume the random variables  $X$  and  $Y$  have discrete distributions, i. e.  $X(\omega_i) = x_i$  and  $Y(\omega_i) = y_i$  for  $i = 1, \dots, S$ . Then there holds*

$$\begin{aligned} X \preceq_1 Y &\iff \mathbb{P}[X \leq y_i] \geq \mathbb{P}[Y \leq y_i] && \forall y_i, i = 1, \dots, S, \\ X \preceq_2 Y &\iff \mathbb{E}[\max\{X - y_i, 0\}] \leq \mathbb{E}[\max\{Y - y_i, 0\}] && \forall y_i, i = 1, \dots, S. \end{aligned}$$

The proof makes use of the monotonicity property and for the second statement again uses a piecewise linear approximation together with the convexity property.

We are finally ready to transfer the presented concepts to the shape optimization setting. Given the reference shape  $\mathcal{O}^{\text{ref}}$ , the associated costs

$$b_i := \mathbf{J}[\omega_i, \mathcal{O}^{\text{ref}}; u], \quad i = 1, \dots, S,$$

represent a random variable that is to be dominated and thus defines our benchmark. Another shape  $\mathcal{O}$  compares favorably to the benchmark if the stochastic dominance constraint of chosen order holds, i. e. if for all  $b_i, i = 1, \dots, S$ ,

$$\begin{aligned} \mathbf{J}[\omega, \mathcal{O}; u] \preceq_1 \mathbf{J}[\omega, \mathcal{O}^{\text{ref}}; u] &\iff \mathbb{P}[\mathbf{J}[\omega, \mathcal{O}; u] \leq b_i] \geq \mathbb{P}[\mathbf{J}[\omega, \mathcal{O}^{\text{ref}}; u] \leq b_i], \text{ or} && (7.15) \\ \mathbf{J}[\omega, \mathcal{O}; u] \preceq_2 \mathbf{J}[\omega, \mathcal{O}^{\text{ref}}; u] &\iff \mathbb{E}[\max\{\mathbf{J}[\omega, \mathcal{O}; u] - b_i, 0\}] \leq \mathbb{E}[\max\{\mathbf{J}[\omega, \mathcal{O}^{\text{ref}}; u] - b_i, 0\}], \end{aligned}$$

respectively. Thereby a set of acceptable designs is obtained, from which we can choose the best candidate based on another quantity of interest. For simplicity we will here aim for a reduction of the total effective volume. Altogether our shape optimization problem under the stochastic dominance of order  $k$  reads

$$\min \left\{ \text{Vol}(\mathcal{O}) : \mathbf{J}[\omega, \mathcal{O}; u] \preceq_k \mathbf{J}[\omega, \mathcal{O}^{\text{ref}}; u], \mathcal{O} \in \mathcal{U}_{\text{ad}} \right\}.$$

For obvious reasons we here do not require a shape to fulfill the volume constraint for being admissible.

### 7.3.2. Practical aspects

As before we need to replace the Heaviside function, used for first order dominance, and the max function, used for second order dominance, by smooth approximations to regain differentiability. To this end we can again employ (7.5) and (7.4), respectively. For the given benchmark  $\mathcal{O}^{\text{ref}}$  the associated stochastic cost functionals can be computed a priori leading to the bounds

$$c_i^{(1)} := \mathbb{E} [H_{b_i}^\epsilon(\mathbf{J}[\omega, \mathcal{O}^{\text{ref}}; u])] = \sum_{j=1}^S \pi_j H_{b_i}^\epsilon(b_j),$$

$$c_i^{(2)} := \mathbb{E} [M_{b_i}^\epsilon(\mathbf{J}[\omega, \mathcal{O}^{\text{ref}}; u])] = \sum_{j=1}^S \pi_j M_{b_i}^\epsilon(b_j)$$

with  $i = 1, \dots, S$  for the inequality constraints during optimization. Based on this derivation, practical shape optimization problems under dominance constraints read

$$\min \left\{ \text{Vol}(\mathcal{O}) : \mathbb{E} [H_{b_i}^\epsilon(\mathbf{J}[\omega, \mathcal{O}; u])] \geq c_i^{(1)} \forall i = 1, \dots, S, \mathcal{O} \in \mathcal{U}_{\text{ad}} \right\},$$

$$\min \left\{ \text{Vol}(\mathcal{O}) : \mathbb{E} [M_{b_i}^\epsilon(\mathbf{J}[\omega, \mathcal{O}; u])] \leq c_i^{(2)} \forall i = 1, \dots, S, \mathcal{O} \in \mathcal{U}_{\text{ad}} \right\}$$

for first and second order dominance, respectively. As before we can reduce the computation of derivatives of the constraints w.r.t. the shape, or its parameters, respectively, to the deterministic case. We like to point out the strong similarity of the above problem to the risk averse stochastic shape optimization problems (7.6) and (7.7). In fact we there have a preselected but arbitrary statistical parameter  $\eta$  entering the ranking functions to construct risk averse objectives. The same functionals reappear here, posing a number of constraints, which possibly have a risk averse impact via the benchmark shape  $\mathcal{O}^{\text{ref}}$ . Furthermore we had the total effective volume as constraint in (5.7) before, which now takes the role of the objective function. For the practical implementation this basically means that objectives and constraints and their derivatives have to switch roles when passed to the optimization algorithm.

### 7.3.3. Numerical example

In this section one example will be presented to demonstrate the concept of stochastic dominance. The loading scheme will be more complex than before, hinting at a more realistic scenario. We still consider the carrier plate scenario but this time the upper boundary is split

into the three segments  $[0, 0.25] \times \{1\}$ ,  $[0.25, 0.75] \times \{1\}$ , and  $[0.75, 1] \times \{1\}$ . We allow for constant shear and pull forces on the left and the right hand side, which require two base loads each, and for linear profiles in between, which require four base loads to enable a blending of the vertical and horizontal forces. Using these bases a stochastic loading scheme as depicted in Figure 7.8 is built up. For each scenario varying loads are applied on the complete upper boundary. The first scenario comprises an exceptionally strong shearing force on the left hand side. As before the horizontal components cancel in the expectation of the loads.

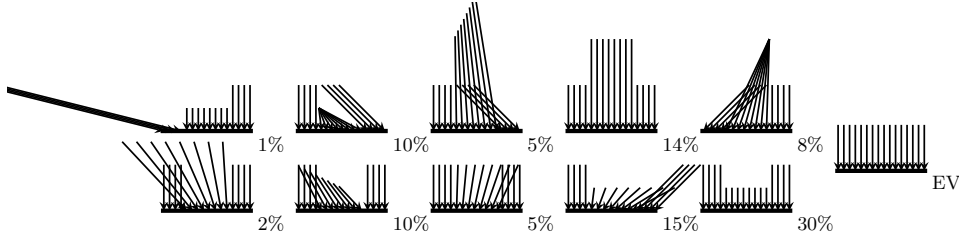


Figure 7.8.: Illustration of the loads acting on the top boundary of the carrier plate domain along with their probabilities and their expected value, in the context of stochastic dominance.

**Obtaining a suitable benchmark.** The investigation of shape optimization under stochastic dominance constraints was motivated by the assumption that in real life an eligible reference design  $\mathcal{O}^{\text{ref}}$  would be available, which a new shape has to compete with. For a numerical experiment such a benchmark needs to be generated. On the one hand the shape has to be well adapted to the posed loadings in order to make the dominance constraint not trivially satisfiable. On the other hand some room for improvement is needed to be able to study the effect of the employed functionals based on qualitative and quantitative numerical results. We propose to use a single-scale design optimized for the expectation of the costs. This way a nontrivial shape that is suitable for the stochastic loading is obtained. On the other hand we expect to find superior results using our developed two-scale approach. Regarding the benchmark we employ the *SIMP* model, with the abbreviation standing for *solid isotropic material with penalization*. In this approach a parameter  $\theta : D \rightarrow [0, 1]$  is introduced to scale the elasticity tensor  $C$  of a rigid material. The effective tensor is then given by  $C^* = \theta^n C$ , where  $n$  is an additional fixed constant. The idea is that, after optimization, regions with  $\theta \approx 0$  correspond to void whereas  $\theta \approx 1$  indicates solid material. The scaling of the elasticity tensor ensures that the effective material becomes weaker in a smooth fashion when  $\theta$  is decreased. However for any intermediate value of  $\theta$  there is no sound physical interpretation of the resulting effective material. Unlike in case of the sequential lamination model the parameter cannot be interpreted as an effective material density. The elastic energy, used as the cost functional as before, is evaluated in its macroscopic form, cf. equation (5.7) and (5.10), and its derivative w. r. t.  $\theta$  is trivially obtained. To practically avoid regions of intermediate density, it has turned out to be beneficial to choose values  $n > 1$  for the additional constant. The approach can readily be integrated into our algorithmic two-scale framework by evaluating only effective macroscopic functionals as described in Section 5.5.2. To maintain coercivity of the effective material tensor,  $\theta$  is bounded from below by a small threshold value of  $10^{-2}$ .



Figure 7.9.: Optimized results for the expected value of the costs functional for the carrier plate scenario and the SIMP model with  $n = 1$  and  $n = 3$ ,  $n = 5$  in continued optimization runs.

As no perimeter penalization is taken into account, microstructures could start to form, constrained only by the discretization. This implies that the benchmark shape will depend on the mesh we use for our computations. Since we will however use the same macroscopic mesh for the two-scale model afterwards, the comparison remains fair.

We performed an optimization for the loading scheme depicted above and the expectation of the costs functional using the SIMP model with a volume constraint of 50%. Initially  $n = 1$  was used which resulted in large regions of intermediate density, see Figure 7.9. This shape was then used as initialization for another run using  $n = 3$ , and this result was reused again for the third run using  $n = 5$ . The final shape did not contain significant regions with intermediate values anymore. Starting directly with  $n = 5$ , on the other hand, led to spurious results with tiny bars of cell width.

**Numerical results.** We performed an optimization under stochastic dominance constraints of first and second order, respectively, for the loading scheme depicted above and the SIMP benchmark. An unbiased initialization with 50% volume as for the benchmark was used. Upon termination the void volume was increased to 0.5446 and 0.5683, respectively, which corresponds to savings of 8.9% and 13.7%, respectively. Given the fact that the benchmark itself was stemming from optimization, this is a remarkable gain. In Figure 7.10 we show the corresponding two-scale visualizations. Obviously they differ a lot from the shapes seen before. In particular many tiny trusses have developed on the macroscale, some of which only span a single cell. We observed this tendency before for the SIMP benchmark and suspect it could be attributed to the different kind of loads. In the preceding sections the loading was uniform or concentrated on just small parts of the boundary. Now it is varying and applied along the full upper boundary.

More important however is the fulfillment of the dominance constraints. We therefore display the cumulative distribution functions of the random variables  $\mathbf{J}[\omega, \mathcal{O}; u]$  for the benchmark and the two obtained results in Figure 7.11. Due to the condition (7.15), it is clear that for first order dominance the graph always has to stay above the graph of the benchmark. As we only have a finite number of realizations and the ranking of those w. r. t. the costs has not changed compared to the benchmark, it means that the jumps in the distribution function are allowed to occur at lower cost functional values, but not at higher ones. This is

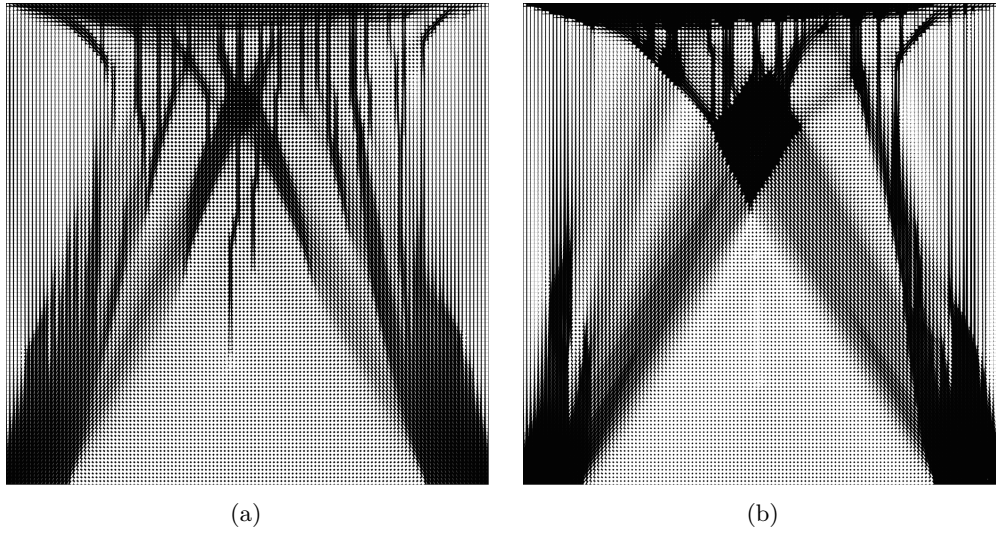


Figure 7.10.: Optimized shapes for stochastic dominance of (a) first and (b) second order.

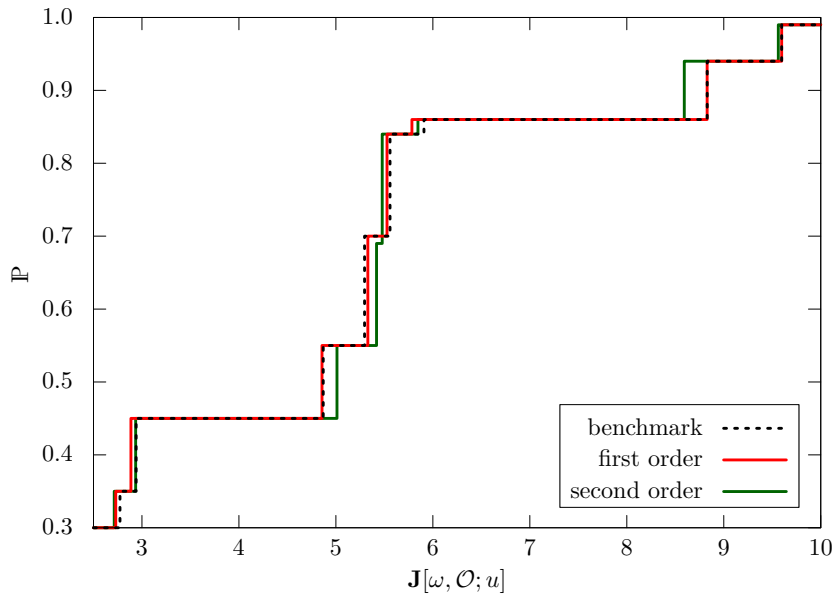


Figure 7.11.: Distribution functions w.r.t. the loading scenarios for the benchmark shape (black) and the optimized results for first (red) and second (green) order stochastic dominance.

the case here with a single exception at about  $\mathbf{J}[\omega, \mathcal{O}; u] \approx 5.3$ . In fact the optimizer reports zero constraint violation and this overshoot must be attributed to the applied regularization. It had to be chosen rather large and thus some balancing with the constraints at smaller

costs is enabled. Choosing second order dominance adds more flexibility as the conditions only need to be satisfied on average. We can nicely see how this is used in the results. For the scenarios with higher costs some buffer is gained which is expended for the scenarios with lower costs. Thereby also the ranking of the scenarios is changed at some place, which can be seen in the distribution function around  $\mathbf{J}[\omega, \mathcal{O}; u] \approx 5.5$  where the jumps occur in a different sequence compared to the benchmark. Looking back at Figure 7.10 it seems that the additional flexibility was exploited to build a more sophisticated shape with fewer tiny rods and an underlying structure that is familiar from the deterministic carrier plate results.

## 7.4. Conclusion

In this chapter the developed two-scale model was applied to shape optimization problems in the context of stochastic loadings. Apart from the more realistic nature of those the crucial difference was the introduction of nonlinear transfer functions into the cost functionals. Furthermore stochastic dominance brought in an entirely different concept for optimization based on ordering relations and led to a role reversal of objective and constraints. Regarding the two-scale materials similar observations as before could be made. Macroscopic structures were built with large regions of intermediate densities and microstructures therein, which aligned with the main stress directions. The most important insight however was that the two-scale scheme and the employed optimizer performed really robust. For the presented cross-check, e. g., the authors of [139] report that several restarts of the algorithm with adapted initializations were necessary to pass the test. For our computations, which were however done for a simpler loading scheme, no further action was required. All computations were started from unbiased initializations and found reasonable optima. We believe that the relatively small and simple parameter space of our microstructures, compared to the level set approach in [139], is the main reason for this.

**Adaptive schemes for optimal microstructures**

---

ARRANGEMENTS of microstructured regions have been observed in the optimized shapes throughout the preceding sections. While in areas with almost solid material or hardly any material an underlying microstructure model seems dispensable, there are indeed large regions with intermediate material density where complex geometric patterns emerge on the microscale. Their spatial evolution within the identified regions seems rather smooth, whereas sharp interfaces separate regions of diverse characteristics. The devised two-scale approach bears on the assumption of a smoothly varying microstructure. Hence it should benefit from sharply resolved interfaces across which jumps in the describing parameters may occur. With respect to computational costs, regions in which parameters do not show significant variation should be discretized on a coarse grid. Overall an adaptive meshing strategy is desirable, which ideally leads to better approximations of optimal shapes with reduced computational costs. To this end we pick up the *dual weighted residual* approach (DWR). In this chapter we will detail its derivation and application in the context of our two-scale shape optimization model.

### 8.1. Derivation of weighted error estimates

In this section we will derive weighted error estimates for two-scale shape optimization problems based on the dual weighted residual approach. The technique is based on a rigorous analytical foundation and has, among diversified applications, already been employed for optimal control problems, e. g. in [65]. It is *goal-oriented*, i. e. it controls the error in the costs  $|\mathbf{J}[\mathcal{O}^{\text{opt}}; u[\mathcal{O}^{\text{opt}}]] - \mathbf{J}[\mathcal{O}_h; u_h]|$ , for an optimal shape  $\mathcal{O}^{\text{opt}}$ , the associated elasticity solution  $u[\mathcal{O}^{\text{opt}}]$ , and approximations  $\mathcal{O}_h, u_h$ . For our application this is an essential feature as we want to lessen the gap toward an optimal shape. A classical a posteriori estimate on the other hand, measuring the discrepancy in the discrete PDE solution  $\|u - u_h\|$ , will not necessarily lead to refinement of regions that cause large errors in the costs.

We will use generic variables in the following to fit all models that have been discussed previously. In subsequent sections we will then apply the estimates to the analytical sequential lamination model and the numerical two-scale model and elaborate on further specific details. Let  $q: D \rightarrow \mathbb{R}^l$  be a vector-valued parameter function that characterizes a material pointwise by its effective elasticity tensor  $C^*[q(x)]$ . The concrete terms here depend on the microstructure model and could e. g. be given numerically or by analytical homogenization formulae. Concerning the solution of the elasticity PDE we take the macroscopic perspective, i. e. the bilinear form (5.10) is considered, which only contains macroscopic quantities explicitly. Let  $u^*$  be the associated solution for the given tensor field  $C^*[q]$ . In optimal control theory the parameter function  $q$  is referred to as *control* and the elastic displacement  $u^*$  as *state*. Let

$q_h$  be the discretized parameter function that could either be constant on each element of the macroscopic computational grid  $\mathcal{M}_h$  or be defined on the finite set of quadrature points on  $\mathcal{M}_h$ . And let  $u_h^*$  be the associated discrete solution. As objective we will use the same compliance type functional as before. In the following the parameters  $q$  and their discretized counterparts are assumed optimal, in the sense that they minimize the cost functional.

We start by considering the Lagrangian  $\mathcal{L}(q; u^*, p^*) := \mathbf{J}^M[q; u^*] + a^M(q; u^*, p^*) - l(p^*)$  as in Definition 4.6, such that the primal solution  $u^*$  is decoupled from the elasticity tensor parameters  $q$ . We already know that the dual solution is trivially given by 0, cf. Section 5.2.2, and therefore drop the dependence of the Lagrangian on  $p^*$  in the following. In the general case,  $u^*$  and  $u_h^*$  are solutions of the continuous and discrete weak elasticity problem, respectively. Either way there holds

$$e_{\mathcal{L}} := \mathcal{L}(q; u^*) - \mathcal{L}(q_h; u_h^*) = \mathbf{J}^M[q; u^*] - \mathbf{J}^M[q_h; u_h^*].$$

Error estimation can therefore be realized by inspecting the difference in the Lagrangian. Next a first order expansion of the Lagrangian is computed. As a shortcut notation we write  $e_{u^*} = u^* - u_h^*$  and  $e_q = q - q_h$  for the differences in the continuous and discrete elasticity solutions and controls, respectively. The error in the Lagrangian is now rewritten as a one dimensional integral

$$e_{\mathcal{L}} = \int_0^1 \frac{d}{ds} \mathcal{L}(q_h + se_q; u_h^* + se_{u^*}) ds,$$

where we interpolate linearly between continuous and discrete quantities. Let  $f(s)$  define the above integrand, i. e.  $f(s) := \frac{d}{ds} \mathcal{L}(q_h + se_q; u_h^* + se_{u^*})$ . We now apply the trapezoidal rule  $\int_0^1 f(s) ds = \frac{1}{2}(f(0) + f(1)) + \frac{1}{2} \int_0^1 f''(s)s(s-1) ds$ . As the Lagrangian is a polynomial in its arguments all derivatives indeed exist. For  $f(1)$  we use that  $q$  was assumed optimal and that  $u^*$  is the corresponding displacement. As such  $(q, u^*)$  is a stationary point of the Lagrangian and we get

$$f(1) = \nabla \mathcal{L}(q; u^*) \cdot (e_q, e_{u^*})^T = 0$$

because  $(e_q, e_{u^*})$  is a valid test function in the weak problem. For  $f(0)$  we introduce arbitrary discrete functions  $\vartheta_{q_h}$  and  $\vartheta_{u_h^*}$ , such that

$$\begin{aligned} f(0) &= \nabla \mathcal{L}(q_h; u_h^*) \cdot (e_q, e_{u^*})^T \\ &= \nabla \mathcal{L}(q_h; u_h^*) \cdot (q - \vartheta_{q_h}, u^* - \vartheta_{u_h^*})^T + \nabla \mathcal{L}(q_h; u_h^*) \cdot (\vartheta_{q_h} - q_h, \vartheta_{u_h^*} - u_h^*)^T. \end{aligned}$$

Here the second term vanishes because  $(q_h, u_h^*)$  was assumed to be a stationary point and  $(\vartheta_{q_h} - q_h, \vartheta_{u_h^*} - u_h^*)$  is a valid discrete test function. The remainder term is defined as  $\mathcal{R} := \frac{1}{2} \int_0^1 f''(s)s(s-1) ds$ . Altogether

$$e_{\mathcal{L}} = \frac{1}{2} \mathcal{L}_{,u_h^*}(q_h; u_h^*)(u^* - \vartheta_{u_h^*}) + \frac{1}{2} \mathcal{L}_{,q_h}(q_h; u_h^*)(q - \vartheta_{q_h}) + \mathcal{R} \quad (8.1)$$

is obtained. Next we compute the remaining terms explicitly by taking the compliance type cost functional (5.7) in its macroscopic form (5.10) into account. Moreover we split up the resulting integral according to the elements  $E$  of the computational grid  $\mathcal{M}_h$  and use Green's



first identity, resulting in

$$\begin{aligned}
 & \frac{1}{2} \mathcal{L}_{,u_h^*}(q_h; u_h^*)(u^* - \vartheta_{u_h^*}) \\
 &= \frac{1}{2} \left( - \int_D C^*[q_h] \varepsilon[u_h^*] : \varepsilon[u_h^*] \, dx + 2 \int_{\Gamma_N} g \cdot u_h^* \, da(x) \right)_{,u_h^*} (u^* - \vartheta_{u_h^*}) \\
 &= \int_D -C^*[q_h] \varepsilon[u_h^*] : \varepsilon[u^* - \vartheta_{u_h^*}] \, dx + \int_{\Gamma_N} g \cdot (u^* - \vartheta_{u_h^*}) \, da(x) \\
 &= \sum_E \left( \int_E \operatorname{div} \{C^*[q_h] \varepsilon[u_h^*]\} \cdot (u^* - \vartheta_{u_h^*}) \, dx \right. \\
 & \quad \left. - \int_{\partial E} C^*[q_h] \varepsilon[u_h^*] n \cdot (u^* - \vartheta_{u_h^*}) \, da(x) + \int_{\partial E \cap \Gamma_N} g \cdot (u^* - \vartheta_{u_h^*}) \, da(x) \right).
 \end{aligned}$$

We can now define the first contributions toward an error estimate.

**Definition 8.1** (Primal volume and edge residuals). *For an element  $E \in \mathcal{M}_h$  the full primal volume residual and the full primal edge residual are defined as*

$$\begin{aligned}
 \eta_E^u &:= \left| \int_E \operatorname{div} \{C^*[q_h] \varepsilon[u_h^*]\} \cdot (u^* - \vartheta_{u_h^*}) \, dx \right|, \\
 \eta_{\partial E}^u &:= \left| \int_{\partial E} j(C^*[q_h] \varepsilon[u_h^*]) \cdot (u^* - \vartheta_{u_h^*}) \, da(x) \right|,
 \end{aligned} \tag{8.2}$$

with  $j(\sigma)$  being the jump of the normal stress across an edge of  $E$  given by

$$j(\sigma)(x) = \begin{cases} \frac{1}{2} [\sigma(x) \cdot n(x)] & x \notin \partial D \\ \sigma(x) \cdot n(x) - g(x) & x \in \Gamma_N \cup \Gamma_F \\ 0 & x \in \Gamma_D \end{cases}$$

and  $[\sigma(x) \cdot n(x)] = |(\sigma(x)|_E - \sigma(x)|_{E'}) \cdot n(x)|$  for  $x \in E \cap E'$  with the outer normal  $n$  on  $\partial E$  and  $E'$  being a neighbor of  $E$ . Here  $\vartheta_{u_h^*}$  may be chosen arbitrarily from its discrete space.

The primal volume residual, primal volume weight, primal edge residual, and primal edge weight are defined as

$$\begin{aligned}
 \rho_E^u &:= \|\operatorname{div} \{C^*[q_h] \varepsilon[u_h^*]\}\|_{0,2,E}, & \omega_E^u &:= \|u^* - \vartheta_{u_h^*}\|_{0,2,E}, \\
 \rho_{\partial E}^u &:= \|j(C^*[q_h] \varepsilon[u_h^*])\|_{0,2,\partial E}, & \omega_{\partial E}^u &:= \|u^* - \vartheta_{u_h^*}\|_{0,2,\partial E}.
 \end{aligned} \tag{8.3}$$

With these definitions and the Cauchy-Schwarz inequality we get

$$\frac{1}{2} \mathcal{L}_{,u_h^*}(q_h; u_h^*)(u_h^* - \vartheta_{u_h^*}) \leq \sum_E (\eta_E^u + \eta_{\partial E}^u) \leq \sum_E (\rho_E^u \omega_E^u + \rho_{\partial E}^u \omega_{\partial E}^u).$$

We now turn to the second term of the derived expansion (8.1) and obtain

$$\begin{aligned}
 & \frac{1}{2} \mathcal{L}_{,q_h}(q_h; u_h^*)(q - \vartheta_{q_h}) \\
 &= \frac{1}{2} \left( - \int_D C^*[q_h] \varepsilon[u_h^*] : \varepsilon[u_h^*] \, dx + 2 \int_{\Gamma_N} g \cdot u_h^* \, da(x) \right)_{,q_h} (q - \vartheta_{q_h}) \\
 &= \sum_E \frac{1}{2} \left( - \int_E C^*[q_h] \varepsilon[u_h^*] : \varepsilon[u_h^*] \, dx \right)_{,q_h} (q - \vartheta_{q_h}).
 \end{aligned}$$

Hence we can define the next contributions.

**Definition 8.2** (Control residuals). *For an element  $E \in \mathcal{M}_h$  the full control residual is defined as*

$$\eta_E^q := \left| \left( \int_E C^*[q_h] \varepsilon[u_h^*] : \varepsilon[u_h^*] \, dx \right)_{,q_h} (q - \vartheta_{q_h}) \right|. \quad (8.4)$$

Here  $\vartheta_{q_h}$  may be chosen arbitrarily from its discrete space. The control residual and control weight are defined as

$$\rho_E^q := \left\| (C^*[q_h] \varepsilon[u_h^*] : \varepsilon[u_h^*])_{,q_h} \right\|_{0,1,E}, \quad \omega_E^q := \|q - \vartheta_{q_h}\|_{0,\infty,E}. \quad (8.5)$$

Concerning the splitting in equation (8.5) we have to assume that for admissible controls, which do not lead to degenerate microstructures and are therefore always bounded, the derived entries of the effective elasticity tensor will again be bounded. Then the whole integrand of  $\eta_E^q$  will be bounded in  $L_1$  and we obtain using Hölder's inequality with exponents 1 and  $\infty$

$$\frac{1}{2} \mathcal{L}_{,q_h}(q_h; u_h^*)(q - \vartheta_{q_h}) \leq \sum_E \frac{1}{2} \eta_E^q \leq \sum_E \frac{1}{2} \rho_E^q \omega_E^q.$$

Finally we have a look at the remainder term. As the linear form does not explicitly depend on the parameters  $q$  and is linear in  $u^*$  it vanishes under the derivative and

$$\mathcal{R} = -\frac{1}{2} \int_0^1 \frac{d^3}{ds^3} a(q_h + se_q; u_h^* + se_{u^*}, u_h^* + se_{u^*}) s(s-1) \, ds \quad (8.6)$$

is obtained. We summarize the derived goal-oriented error estimate in the following theorem.

**Theorem 8.3** (Weighted error estimate). *For given optimal, continuous and discrete parameters  $q$ ,  $q_h$ , and corresponding continuous and discrete elasticity solutions  $u^*$ ,  $u_h^*$  the following error estimate holds for the compliance objective.*

$$|\mathbf{J}^M[q; u^*] - \mathbf{J}^M[q_h; u_h^*]| \leq \sum_E \eta_E(q_h; u_h^*) + \mathcal{R}.$$

Here  $\mathcal{R}$  is a remainder term of higher order in the differences  $e_{u^*} = u^* - u_h^*$  and  $e_q = q - q_h$  and the local error indicators  $\eta_E$  of first order are given by

$$\begin{aligned} \eta_E(q_h; u_h^*) &= \eta_E^u + \eta_{\partial E}^u + \frac{1}{2} \eta_E^q \\ &\leq \rho_E^{u^*} \omega_E^{u^*} + \rho_{\partial E}^{u^*} \omega_{\partial E}^{u^*} + \frac{1}{2} \rho_E^q \omega_E^q \end{aligned}$$

with the individual residual and weighting terms as in Definition 8.1 and 8.2.

**Remark 8.4.** The primal volume and edge residuals reflect the error in the elasticity solution due to discretization and are known from classical PDE a posteriori error estimates, cf. the very first example in [8]. Additionally the control residual comes into play here, measuring locally the sensitivity of the elastic energy density and constituting the relation to the compliance energy to be minimized.

**Remark 8.5.** The residual terms only involve discrete quantities and can therefore be computed a posteriori, once the discrete PDE constrained optimization problem has been solved. In the weighting terms, however, still the unknown continuous state and controls enter in differences to their discrete counterparts. These terms can often be tackled analytically by a priori interpolation estimates and for this purpose the additional splitting into residual and weighting terms (8.3), (8.5) is beneficial. In a numerical scheme we will instead evaluate the full terms (8.2), (8.4), and need to devise a suitable approximation of the differences.

### 8.1.1. Practical aspects

Based on the previously presented work our numerical algorithm can be extended. An adaptive numerical scheme typically comprises a recurring sequence of steps, namely

$$\boxed{\text{solve}} \mapsto \boxed{\text{estimate}} \mapsto \boxed{\text{mark}} \mapsto \boxed{\text{refine}}.$$

In the *solve*-step the optimization problem is solved on a given mesh  $\mathcal{M}_h$  as done previously in Section 6.2. With the elasticity solution and the optimal parameters at hand, error estimators are computed for each element  $E \in \mathcal{M}_h$  in the *estimate*-step, as detailed in the following sections. Based on the locally estimated errors it has to be decided which elements should be *marked* for refinement. In this regard several strategies exist to choose a subset  $\mathcal{K} \subset \mathcal{M}_h$ . We follow Dörfler's approach [156] which amounts to determine  $\mathcal{K}$  such that

$$\sum_{E \in \mathcal{K}} \eta_E \geq r \sum_{E \in \mathcal{M}_h} \eta_E,$$

i. e. the accumulated error in the marked elements should make up for a fixed fraction  $r$  of the total estimated error. The set should be optimal in terms of cardinality, entailing as few additional finite elements as possible. We therefore sort the estimated values in decreasing order and add corresponding elements sequentially to the set  $\mathcal{K}$  until the prescribed fraction is attained. For sorting we use `std::sort` of the *C++ Standard Library*, which has linear-logarithmic runtime. One usually aims for linear complexity, cf. [328], but in our situation the computational cost of the optimization rises far above every other part of the algorithm anyway. Finally all grid elements in  $\mathcal{K}$  are *refined* using the quadtree structure as described in Section 5.5.2. Furthermore the discrete quantities are interpolated onto the new mesh. In our implementation we add an outer loop around the code interfacing with `Ipopt`, that is run until a prescribed number of refinement sequences has been performed. When passing to a new grid as much information of the optimizer as possible is transferred. This allows to use `Ipopt`'s *warm starting* capabilities, which generally lead to faster convergence. The software design is sketched in Appendix C.

## 8.2. Application to the sequential lamination model

The error estimates derived before can directly be applied to shape optimization problems with any parametrized microstructure model that allows to set up a macroscopic effective tensor and associated sensitivities w. r. t. the describing parameters. At first we will consider the sequential lamination model where the rotation, ratio and density parameters  $q^L := (\varrho, m, \theta)$ , cf. Section 4.2.3, take the roles of the controls  $q$  above. Here the effective homogenized material parameters  $C^L[q^L]$  are given explicitly by (4.21). Discretized controls are denoted by  $q_h^L := (\varrho_h, m_h, \theta_h)$  and the associated continuous and discrete solutions by  $u^L$  and  $u_h^L$ , respectively. To distinguish the models later on, the cost functional is denoted by  $\mathbf{J}^L$  here. Before dwelling on numerical aspects we will exploit the fundamental difference between the sequential lamination model and the two-scale model, namely the existence of explicit analytical formulae providing optimal parameters  $q^L$  from local stresses via (4.20). This relation will enable us to derive rigorous a priori error estimates. On the contrary parameters in the context of the two-scale model stem from numerical optimization schemes and effective tensors depend on numerical approximations of cell problem solutions. We will therefore not be able to establish similar results in that case.

### 8.2.1. A priori estimation of weights

In view of the weighting terms' definitions (8.3), (8.5), classical interpolation error estimates are available for the difference between sufficiently regular continuous and discrete primal solutions  $u^L$ ,  $u_h^L$ . For the lamination parameters  $q^L$ , however, we can merely assume boundedness. Therefore we aim for exploiting the explicit relations of the controls and the state, given by (4.20). First of all the parameters depend on the stress, which is coupled linearly to the strain tensor. Of the stress tensor eigenvalues and eigenvectors, or rather their rotation, have to be considered. This is the crucial point as indeed eigenvalues depend continuously on their matrices, whereas eigenvectors do not. This is illustrated by the following simple counterexample.

**Example 8.6.** Consider the following two stress tensors  $\sigma_\epsilon^{(1)}$ ,  $\sigma_\epsilon^{(2)}$  and observe the limiting process

$$\sigma_\epsilon^{(1)} := \begin{pmatrix} 1+\epsilon & 0 \\ 0 & 1-\epsilon \end{pmatrix} \xrightarrow{\epsilon \rightarrow 0} \begin{pmatrix} 1 & 0 \\ 0 & 1 \end{pmatrix} \xleftarrow{\epsilon \rightarrow 0} \begin{pmatrix} 1 & \epsilon \\ \epsilon & 1 \end{pmatrix} =: \sigma_\epsilon^{(2)} = Q \begin{pmatrix} 1+\epsilon & 0 \\ 0 & 1-\epsilon \end{pmatrix} Q^T.$$

Clearly both of them have eigenvalues  $(1+\epsilon, 1-\epsilon)$  tending to  $(1, 1)$  for  $\epsilon \rightarrow 0$ . However  $\sigma_\epsilon^{(1)}$  has the unit vectors as eigenvectors whereas  $\sigma_\epsilon^{(2)}$  has them rotated by  $45^\circ$  via  $Q$ . Both eigenvector pairs are independent of  $\epsilon$  and the orientation therefore jumps when  $\epsilon$  passes 0.

**Remark 8.7.** The given counterexample has an interesting interpretation in the context of the sequential lamination construction. For  $\sigma$  proportional to  $\mathbb{1}$ , also referred to as *hydrostatic stress*, the optimal microstructure is not unique. In fact any orthonormal basis of  $\mathbb{R}^2$  is a set of optimal lamination directions, cf. [12, Remark 4.3].

On grounds of these preliminary considerations, we cannot continue with estimating the weighting terms unless the contribution from the rotation parameter  $\varrho$  is removed from the control residual (8.4). But this is indeed possible by observing that the elastic energy density in case of optimal sequential lamination is invariant w. r. t. rotation. Intuitively it follows from the fact that the local lamination direction is always aligned with the local main stress direction, yielding orthotropic material properties within the likewise rotated coordinate frame. We formalize this observation in the following lemma.

**Lemma 8.8** (Invariance of optimal elastic energy w. r. t. rotation). *For any fixed  $x \in D$  let  $C^L[q^L](x)$  be the local effective elasticity tensor stemming from an optimal rank-2 sequential lamination microstructure. Let  $u^L[q^L]$  be the corresponding solution to the weak elasticity problem which in turn depends on the local elasticity tensors and therefore on  $q^L$ . The local elastic energy density in  $x$  is then invariant w. r. t. the rotation parameter  $\varrho$ , in particular*

$$\frac{d}{d\varrho} (C^L[q^L] \varepsilon[u^L[q^L]] : \varepsilon[u^L[q^L]])(x) = 0.$$

*Proof.* In the following all terms are considered pointwise for  $x$  arbitrary but fixed. Independence can be seen directly from the Hashin-Shtrikman bounds, which are given in terms of stresses. Let therefore  $\sigma^L[q^L](x) := C^L[q^L] \varepsilon[u^L]$  and rewrite the elastic energy density as

$$C^L[q^L] \varepsilon[u^L] : \varepsilon[u^L] = (C^L[q^L])^{-1} \sigma^L[q^L] : \sigma^L[q^L].$$

By assumption  $C^L[q^L]$  is an optimal effective elasticity tensor and the local elastic energy density thereby attains the lower Hashin-Shtrikman bound, cf. Theorem 4.15, i. e.

$$(C^L[q^L])^{-1} \sigma^L[q^L] : \sigma^L[q^L] = C^{-1} \sigma^L[q^L] : \sigma^L[q^L] + \frac{(\kappa + \mu)\theta}{4\kappa\mu(1-\theta)} (|\lambda^{(1)}| + |\lambda^{(2)}|)^2.$$

The eigenvalues  $\lambda^{(1)}, \lambda^{(2)}$  of  $\sigma^L$  do not depend on the rotation parameter, which is deduced from the orientation of the eigenvectors. Hence  $\varrho$  only enters the first term of the right hand side via  $\sigma^L$ . This term represents an elastic energy density as well, but this time involving the isotropic constituent  $C$ . Isotropy just means that the material's response to strains does not depend on their principal directions. Altering the alignment of  $\sigma^L$ , e. g. by rotating to reference configuration, therefore does not change the term. Altogether we see that the right hand side is not influenced by the rotation parameters  $\varrho$ , so the derivative of the left hand side w. r. t.  $\varrho$  has to vanish.  $\square$

Some aspects are important for the application of the above result in context of our error estimates. First of all we have to restrict ourselves to boundary value problems that allow to write the compliance cost equivalently in terms of the elastic energy, cf. Remark 4.12. Secondly the state  $u^L$  and the controls  $q^L$  have to be in correspondence at every point, i. e. the lamination parameters have to be optimal for  $\sigma^L$  in the sense of formula (4.20) and  $u^L$  has to be the elasticity solution for the continuous, spatially varying tensor field  $C^L[q^L]$ . Lastly this dependence of  $u^L$  on  $q^L$  has to be taken into account in the derivation of the error estimates and the total derivative has to be considered in order to track the mutual alignment of the material and the principal direction of the stress tensor. We can therefore not directly apply the invariance result to the control residual (8.4), where only partial derivatives appear. Instead we have to modify the calculations leading to Theorem 8.3 to explicitly generate the total derivative w. r. t.  $\varrho$ . To this end we formally introduce an artificial dependence  $u^L[\varrho]$  of the elasticity solution on the rotation parameter  $\varrho$ , which were technically decoupled by means of the Lagrangian formulation before. The error in the state then becomes  $e_{u^L}(s) = u^L[\varrho] - u_h^L[\varrho_h + s(\varrho - \varrho_h)]$ , yielding  $u_h^L[\varrho_h + s(\varrho - \varrho_h)] + se_{u^L}(s)|_{s=1} = u^L[\varrho]$  and  $u_h^L[\varrho_h + s(\varrho - \varrho_h)] + se_{u^L}(s)|_{s=0} = u_h^L[\varrho_h]$  as before. In the following we assume sufficient differentiability and that  $u_h^L$  is a discrete weak solution for continuous, spatially varying parameters as postulated above. With  $\frac{d}{ds} (u_h^L[\varrho_h + s(\varrho - \varrho_h)] + se_{u^L}(s))|_{s=0} = u_{h,\varrho}^L[\varrho_h](\varrho - \varrho_h) + e_{u^L}(0)$  the error in the Lagrangian (8.1) changes to

$$\begin{aligned} e_{\mathcal{L}} &= \frac{1}{2}f(0) + \mathcal{R} = \frac{1}{2}\mathcal{L}_{,u_h^L}(q_h^L, u_h^L[\varrho_h])(u_{h,\varrho}^L[\varrho_h](\varrho - \varrho_h)) + \frac{1}{2}\mathcal{L}_{,q_h^L}(q_h^L, u_h^L[\varrho_h])(u^L[\varrho] - u_h^L[\varrho_h]) \\ &\quad + \frac{1}{2}\mathcal{L}_{,\varrho_h}(q_h^L, u_h^L[\varrho_h])(\varrho - \varrho_h) + \frac{1}{2}\mathcal{L}_{,(m_h,\theta_h)}(q_h^L, u_h^L[\varrho_h]) \begin{pmatrix} m - m_h \\ \theta - \theta_h \end{pmatrix} + \mathcal{R} \\ &= \frac{1}{2}\mathcal{L}_{,u_h^L}(q_h^L, u_h^L[\varrho_h])(u^L[\varrho] - u_h^L[\varrho_h]) + \frac{1}{2}\mathcal{L}_{,(m_h,\theta_h)}(q_h^L, u_h^L[\varrho_h]) \begin{pmatrix} m - m_h \\ \theta - \theta_h \end{pmatrix} \\ &\quad + \frac{d}{d\varrho_h} \frac{1}{2}\mathcal{L}(q_h^L, u_h^L[\varrho_h])(\varrho - \varrho_h) + \mathcal{R}. \end{aligned}$$

In the last step we combined terms to obtain the total derivative w. r. t.  $\varrho$ . Under the assumptions already made we see

$$\frac{d}{d\varrho_h} \frac{1}{2}\mathcal{L}(q_h^L, u_h^L[\varrho_h]) = \frac{1}{2} \int_{\mathcal{O}} \frac{d}{d\varrho_h} C^L[q_h^L] \varepsilon[u_h^L[\varrho_h]] : \varepsilon[u_h^L[\varrho_h]] \, dx$$

and thus the corresponding term of  $e_{\mathcal{L}}$  vanishes by virtue of Lemma 8.8. Plugging in arbitrary discrete functions  $\vartheta_{u_h^*}$ ,  $\vartheta_{m_h}$ , and  $\vartheta_{\theta_h}$  we exactly regain the primal residual terms of Definition 8.1 and the control residual terms of Definition 8.2 except for the one w. r. t. the rotation parameter. Altogether, in consideration of (4.21), we now have

$$\begin{aligned} \rho_E^{u^L} &= \|\operatorname{div} \{ (R[\varrho_h] \bar{C}^L [m_h, \theta_h]) \varepsilon [u_h^L] \}\|_{0,2,E}, & \omega_E^{u^L} &= \|u^L - \vartheta_{u_h^*}\|_{0,2,E}, \\ \rho_{\partial E}^{u^L} &= \|j((R[\varrho_h] \bar{C}^L [m_h, \theta_h]) \varepsilon [u_h^L])\|_{0,2,\partial E}, & \omega_{\partial E}^{u^L} &= \|u^L - \vartheta_{u_h^*}\|_{0,2,\partial E}, \\ \rho_E^m &= \|(R[\varrho_h] \bar{C}_{,m}^L [m_h, \theta_h]) \varepsilon [u_h^L] : \varepsilon [u_h^L]\|_{0,1,E}, & \omega_E^m &= \|m - \vartheta_{m_h}\|_{0,\infty,E}, \\ \rho_E^\theta &= \|(R[\varrho_h] \bar{C}_{,\theta}^L [m_h, \theta_h]) \varepsilon [u_h^L] : \varepsilon [u_h^L]\|_{0,1,E}, & \omega_E^\theta &= \|\theta - \vartheta_{\theta_h}\|_{0,\infty,E}. \end{aligned} \quad (8.7)$$

Let us remark that for bounded parameters  $m_h$ ,  $\theta_h$  the differentiated entries of  $\bar{C}^L [m_h, \theta_h]$  will again be bounded, s. t. the control residual terms for  $m$  and  $\theta$  are indeed bounded in  $L^1$ . We are now ready to present the rigorous estimation of the weighting terms.

**Theorem 8.9** (Rigorous estimates of weighting terms). *Under the additional assumption that  $u^L \in W^{2,\infty}(D; \mathbb{R}^2)$  the following estimates for the weighting terms hold.*

$$\begin{aligned} \omega_E^{u^L} &\lesssim h_E^2 |u^L|_{2,2,E}, \\ \omega_{\partial E}^{u^L} &\lesssim h_{\partial E} \|u^L\|_{2,2,E}, \\ \omega_E^m &\lesssim h_E |u^L|_{2,\infty,E}, \\ \omega_E^\theta &\lesssim h_E |u^L|_{2,\infty,E}, \end{aligned}$$

where “ $\lesssim$ ” stands for “ $\leq$ ” up to multiplication on either side by a fixed constant.

*Proof.* Starting from equation (8.7) we choose  $\vartheta_{u_h^*} = \mathcal{I}_h u^L$ , i. e. the Lagrangian interpolant of the continuous solution in the employed finite element space, for the so far arbitrary discrete function in the primal weighting term. Interpolation estimates of Theorem 3.24 for  $m = 0$ ,  $p = 2$  and  $k = 1$ ,  $d = 2$  or  $k = 0$ ,  $d = 1$ , respectively, then give

$$\begin{aligned} \|u^L - \mathcal{I}_h u^L\|_{0,2,E} &\lesssim h_E^2 |u^L|_{2,2,E}, \\ \|u^L - \mathcal{I}_h u^L\|_{0,2,\partial E} &\lesssim h_{\partial E} |u^L|_{1,2,\partial E}. \end{aligned}$$

The final result for the boundary term follows by virtue of the trace theorem. Next we estimate the control weight for the ratio parameter  $m$ . The argument for the density parameter  $\theta$  is completely analogous. Let  $\sigma = C^L \varepsilon [u^L]$  be the stress tensor for the continuous elasticity solution and  $\sigma_h = C^L \varepsilon [\mathcal{I}_h u^L]$  likewise for the discrete interpolated solution. We then choose  $\vartheta_{m_h} = m[\sigma_h]$ , i. e. the discrete function  $\vartheta_{m_h}$  is obtained by pointwise evaluation of the interpolated solution  $\mathcal{I}_h u^L$ , computing the corresponding stress  $\sigma_h$ , deriving its eigenvalues and inserting them into formula 4.20. Thereby we obtain

$$\|m - \vartheta_{m_h}\|_{0,\infty,E} = \|m[\sigma] - m[\sigma_h]\|_{0,\infty,E} = \sup_{x \in E} |m[\sigma(x)] - m[\sigma_h(x)]|.$$

Since  $E$  is bounded a maximum is attained at some  $\bar{x} \in E$  with stresses  $\bar{\sigma} = \sigma(\bar{x})$  and  $\bar{\sigma}_h = \sigma_h(\bar{x})$ . The function  $m[\sigma]$  is Lipschitz continuous in the eigenvalues  $\lambda^{(1)}(\sigma)$ ,  $\lambda^{(2)}(\sigma)$  of  $\sigma$  as long as  $\sigma$  is bounded away from the zero matrix. We then obtain

$$|m[\bar{\sigma}] - m[\bar{\sigma}_h]| \lesssim \left( |\lambda^{(1)}(\bar{\sigma}) - \lambda^{(1)}(\bar{\sigma}_h)|^2 + |\lambda^{(2)}(\bar{\sigma}) - \lambda^{(2)}(\bar{\sigma}_h)|^2 \right)^{\frac{1}{2}}.$$

The eigenvalues are Lipschitz continuous functions of their matrices. In particular the Wielandt-Hoffmann inequality, [231] for  $n = 2$ , yields

$$\left( |\lambda^{(1)}(\bar{\sigma}) - \lambda^{(1)}(\bar{\sigma}_h)|^2 + |\lambda^{(2)}(\bar{\sigma}) - \lambda^{(2)}(\bar{\sigma}_h)|^2 \right)^{\frac{1}{2}} \leq \|\bar{\sigma} - \bar{\sigma}_h\|_F$$

where  $\|\cdot\|_F$  denotes the Frobenius norm. We then have

$$\|\bar{\sigma} - \bar{\sigma}_h\|_F \leq \sup_{x \in E} \|\sigma(x) - \sigma_h(x)\|_F = \|\sigma - \sigma_h\|_{0,\infty,E}.$$

Due to linearity of the mapping from strain to stress tensors by  $C^L$ , there holds

$$\|\sigma - \sigma_h\|_{0,\infty,E} = \|C^L(\varepsilon[u^L] - \varepsilon[\mathcal{I}_h u^L])\|_{0,\infty,E} \leq \| \|C^L\| \| \varepsilon[u^L] - \varepsilon[\mathcal{I}_h u^L] \|_{0,\infty,E},$$

where  $\| \|C^L\| \|$  is an appropriate operator norm for the elasticity tensor. Finally we pass from the symmetrized strain tensor to the full Jacobian, yielding

$$\|\varepsilon[u^L] - \varepsilon[\mathcal{I}_h u^L]\|_{0,\infty,E} \lesssim |u^L - \mathcal{I}_h u^L|_{1,\infty,E} \leq \|u^L - \mathcal{I}_h u^L\|_{1,\infty,E}.$$

Now the interpolation estimates of Theorem 3.24 for  $m = 1$ ,  $p = \infty$  and  $k = 1$  give

$$\|u^L - \mathcal{I}_h u^L\|_{1,\infty,E} \lesssim h_E |u^L|_{2,\infty,E}$$

concluding the proof.  $\square$

**Remark 8.10.** While the error estimates of Theorem 8.3 merely provide an upper bound for the error in the cost functional, the additional result of Theorem 8.9 guarantees that this upper bound will itself remain bounded and thus not become insignificant for the error control.

### 8.2.2. Numerical approximation of weights

For a practical numerical scheme the weighting terms in (8.7), involving the unknown continuous quantities  $u^L$ ,  $m$ , and  $\theta$ , need to be approximated using the numerical solution  $u_h^L$  and the derived parameters  $m_h$ ,  $\theta_h$ . A common approach is to exploit potential higher regularity of the continuous solution via a further discrete solution obtained by a higher order scheme. This however is computationally demanding and counteracts the typical requirement for an error estimator to be efficiently evaluable with negligible cost compared to the optimization. Instead [66] suggests to merely interpolate the discrete quantities to higher order polynomials. For our type of adaptive meshes, described in Section 5.5, this is instantly applicable. Due to the quadtree structure, each element  $E \in \mathcal{M}_h$  is always part of a super patch  $\mathcal{S} \subset \mathcal{M}_h$  consisting of the four children of its parent element. On this patch a higher order polynomial can be constructed taking into account the combined degrees of freedom from all sub-elements. For triangulated domains this approach is not easily applicable. See Appendix A for comments and results in this context.

For the primal solution  $u_h^L$  we use biquadratic finite element functions as explained in Section 5.5.1. They are determined by  $3 \times 3$  degrees of freedom per element. On a super patch  $\mathcal{S}$  we therefore have  $5 \times 5$  nodal values at our disposal, giving rise to a biquartic polynomial,

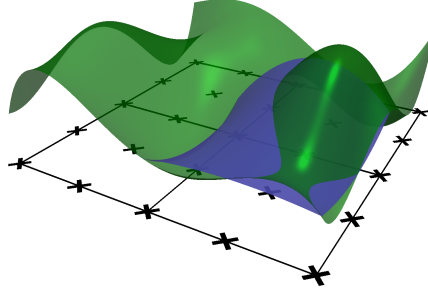


Figure 8.1.: Illustration of a super patch in an adaptive grid with a biquartic function on the patch (green) and the a usual biquadratic finite element function on one sub-element (blue).

denoted by  $\mathcal{I}_h^{(4)} u_h^L \Big|_{\mathcal{S}}$ . See Figure 8.1 for an exemplary illustration. The norm of its difference to the discrete solution is then evaluated using numerical quadrature.

Concerning the controls we first of all have to observe that the parameters  $q_h^L$  were assumed to vary continuously in space in the preceding section, especially in view of the application of Lemma 8.8. Obviously this is not practicable in a numerical algorithm. However, as remarked before in Section 5.5.1, the error due to discrete sampling is controlled as long as the chosen quadrature scheme is exact in the context of constant coefficients, which we will guarantee in our computations. The parameters  $\varrho$ ,  $m$ ,  $\theta$  therefore exist as degrees of freedom on all quadrature points. For the density parameter  $\theta$  this could again lead to checkerboard instabilities and it is therefore replaced by a piecewise constant average of the values on the element's quadrature points. The final approximation of the weights is hence different in each case. For the ratio parameter  $m$  the interpolated elasticity solution  $\mathcal{I}_h^{(4)} u_h^L$  and the existing elasticity tensor field  $C^L$  can be taken into account at each quadrature point. However lamination parameters corresponding to the interpolated solution, i. e.  $m[\mathcal{I}_h^{(4)} u_h^L]$ , cannot be directly computed from the stress  $C^L \varepsilon[\mathcal{I}_h^{(4)} u_h^L]$  as they would enter the effective elasticity tensor themselves. To overcome this chicken-and-egg situation we consider the rephrased linear strain-stress relation

$$\bar{C}^L \left[ m[\lambda^{(i)}], \theta \right] \varepsilon \left[ \mathcal{I}_h^{(4)} u_h^L \right] - Q[\varrho] \begin{pmatrix} \lambda^{(1)} & \\ & \lambda^{(2)} \end{pmatrix} Q[\varrho]^T = 0,$$

which consists of three independent equations due to symmetry. We use Newton's method to solve for the rotation parameter  $\varrho$  and the eigenvalues  $\lambda^{(i)}$ , from which  $m$  can be computed, while the density  $\theta$  is held fixed. The difference to the existing discrete ratio parameter can then be evaluated. This procedure is applicable for the rotation parameter  $\varrho$  as well, which however was eliminated from the error estimate. For the density parameter  $\theta$  the piecewise constant approximations on a super patch of four neighboring elements can be used to construct a bilinear profile. We summarize the approximation strategy in the following remark.

**Remark 8.11** (Approximation of local weights). To approximate the weighting terms for the primal and the control error indicator on every element  $E$  we consider a patch  $\mathcal{S}$  of four neighboring elements including  $E$  and proceed as follows.



- For the primal error indicator  $5 \times 5$  degrees of freedom stemming from all elements of the patch are used to construct a biquartic polynomial on the patch. This interpolation  $\mathcal{I}_h^{(4)} u_h^L$  is then compared to the original approximation.

$$\omega_E^{u^L} \approx \left\| \mathcal{I}_h^{(4)} u_h^L - u_h^L \right\|_{0,2,E}, \quad \omega_{\partial E}^{u^L} \approx \left\| \mathcal{I}_h^{(4)} u_h^L - u_h^L \right\|_{0,2,\partial E}$$

- For the ratio error indicator lamination parameters are computed iteratively from the interpolated elasticity solution and compared to the original parameters. For the density error indicator four piecewise constant values are used to construct a bilinear profile on the patch which is then compared to the original value.

$$\omega_E^m \approx \left\| m[\mathcal{I}_h^{(4)} u_h^L] - m[u_h^L] \right\|_{0,\infty,E}, \quad \omega_E^\theta \approx \left\| \mathcal{I}_h^{(1)} \theta_h - \theta_h \right\|_{0,\infty,E}$$

### 8.2.3. Numerical results

In this Section we present results obtained by the derived adaptive scheme using the sequential lamination model for several classical shape optimization problems. The parameter for the Dörfler marking was always set to  $r = 0.3$ .

**Carrier plate.** Our first example is the carrier plate under shearing that was already considered in Section 6.2. In Figure 8.2 generated meshes at selected intermediate refinement steps are shown. Figure 8.3 displays the optimal density distribution obtained by the fully converged sequential lamination algorithm on the respective meshes. Obviously interfaces within the domain are captured by the adaptive scheme and become increasingly resolved during the course of the algorithm. The results are reminiscent of Figure 6.10 where uniform refinement

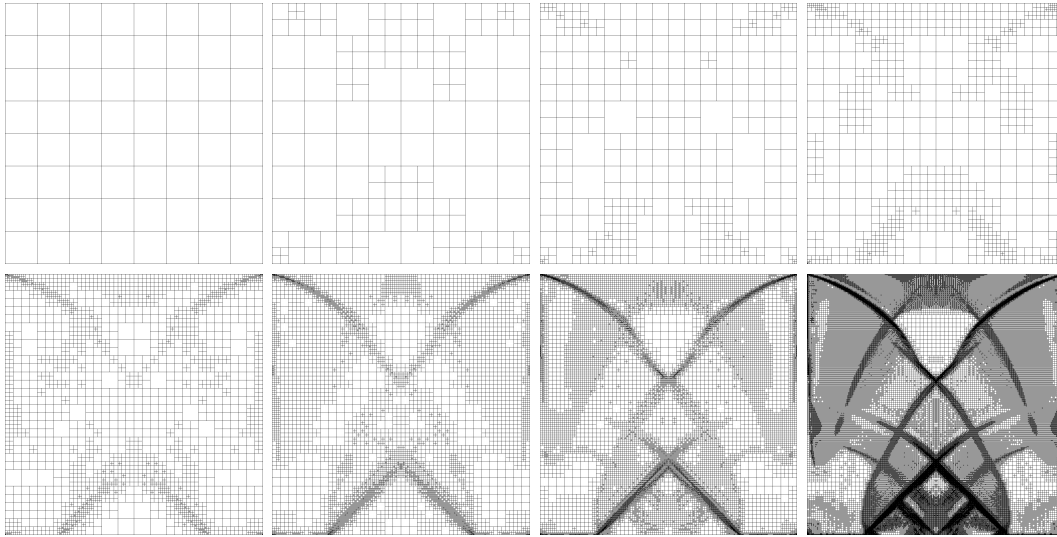


Figure 8.2.: Generated meshes after 0, 3, 6, 9, 13, 17, 21, and 29 refinement steps for the carrier plate scenario and the sequential lamination model.

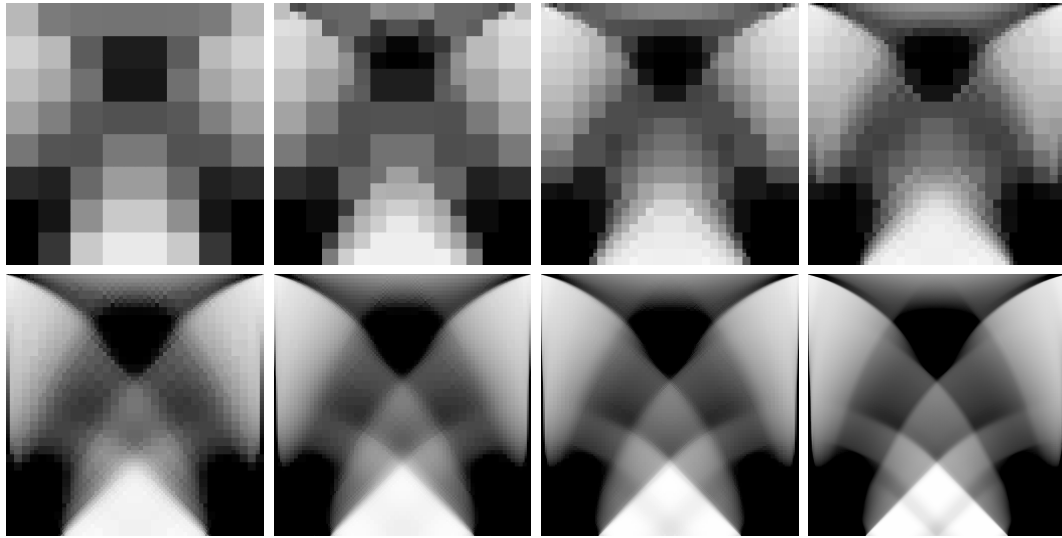


Figure 8.3.: Optimal density obtained after 0, 3, 6, 9, 13, 17, 21, and 29 refinement steps for the carrier plate scenario and the sequential lamination model.

was used. The crucial point is that comparable results are obtained here much more efficiently using the adaptive scheme. This is underlined by Figure 8.4, where the error in the costs is plotted against the number of elements in the computational grid. The error is computed

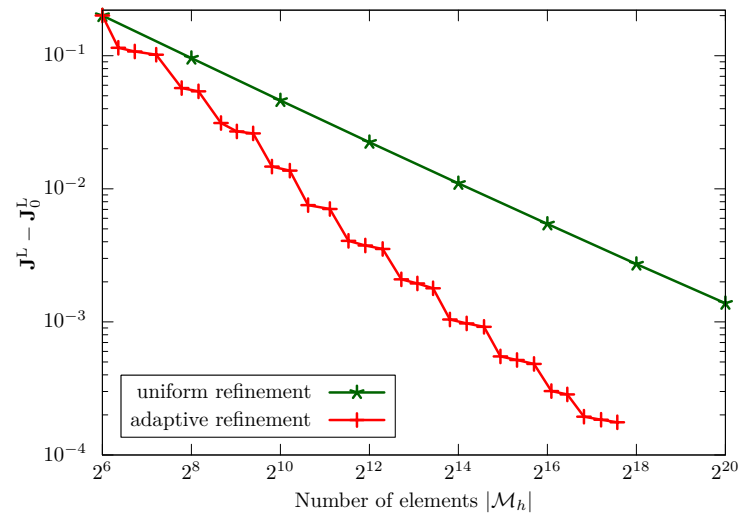


Figure 8.4.: Difference to the optimal cost value from Table 6.8 plotted against the number of elements in the computational grid for the carrier plate scenario and the sequential lamination model.

as  $\mathbf{J}^L - \mathbf{J}_0^L$  using the asymptotic value from Table 6.8 as the optimal cost  $\mathbf{J}_0^L$ . After 19 refinement steps in the adaptive scheme the cost functional has dropped below the value obtained after 10 uniform refinements. At this point there are 14 356 elements in the adaptive mesh. Compared to  $1024^2$  elements in the uniform grid this implies a reduction by almost two orders of magnitude.

A further striking observation in Figure 8.4 is the staircasing in the error of the adaptive scheme. It can be explained by examining the different contributions to the overall estimated error. This is done for four subsequent refinement steps in Figure 8.5.

In general the full primal volume residual  $\eta_E^{u,L}$  and the full control residual w.r.t. the density parameter  $\eta_E^\theta$  dominate the estimated error, but in different areas. The first column in Figure 8.5 depicts the situation after 8 refinement steps, where a set of elements is selected for refinement that will lead to a significant drop in the difference to the optimal objective, cf. Figure 8.4. The volume indicator shows high values in the vicinity of the lower corners. Due to the change from homogeneous Dirichlet to homogeneous Neumann boundary conditions, stress concentrations are found here. The density control indicator has several cells with even higher estimated values and these cells are located near the already established interfaces. This leads to further refinement of the interfaces as can be seen when comparing the grids in the first and second column. In the next step the volume indicator shows some cells as before. Those elements were ultimately not within the refinement set and are now candidates once again. Moreover cells appear in the central solid block. The density control indicator is now focused on other regions. Selected cells are still near interfaces, which appear clearer afterwards in the third column. However the difference in the density across the newly refined interfaces is less than before and thus the drop in the objective is less significant. More of the cells selected by the volume indicator are refined, but this seems to have less effect. In the next step the density control indicator induces a new refinement level for the interfaces toward the lower near void region. This again leads to a significant reduction in the costs. A similar behavior was observed in [4]. According to the authors, it was caused by calculating the global error as a sum of absolute values for each of the cells, which prevents error cancelation across elements.

Table 8.1 summarizes all important figures of the adaptive algorithm for the carrier plate. A new important quantity is the ratio between the total estimated error and the difference to the optimal objective in the last column. In view of Theorem 8.3 it is bounded from below by 1 if the estimator, and especially the weights, are evaluated exactly using the optimal continuous state and controls. In the numerical examples the condition is violated due to the approximation of the weighing terms. An important insight however is that the factor does not degenerate during the course of the algorithm. In fact it is always within the interval  $(0.096, 0.178)$ . This implies that the error in the cost functional and its estimate show the same behavior in decrease. The numerical quantity does not over- or underestimate the true error and thus neither leads to irrelevant refinements nor misses relevant ones. Underestimation of errors in the dual weighted residual approach is also discussed in [307].

After 21 refinement steps the lower corner cells have reached the maximal refinement level. This is a technical limitation due to the binary representation of elements' hash keys, which could be lifted easily. However in this example the subsequently missing refinement does not impede the overall scheme.

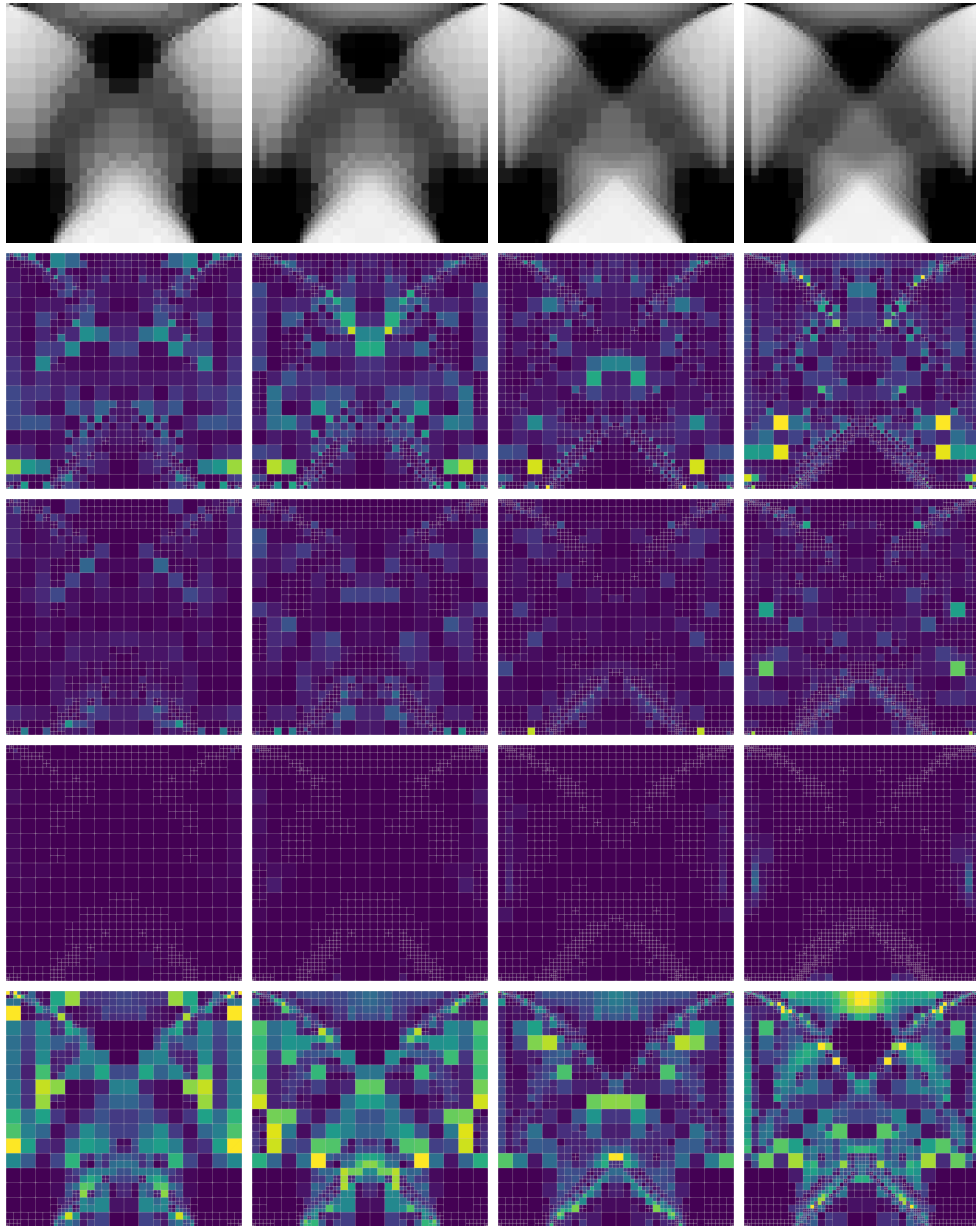



Figure 8.5.: Different terms in the estimated error after 8, 9, 10, and 11 refinement steps (left to right) for the carrier plate scenario and the sequential lamination model: optimized density as in Figure 8.3,  $\eta_E^{u^L}$ ,  $\eta_{\partial E}^{u^L}$ ,  $\frac{1}{2}\eta_E^m$ , and  $\frac{1}{2}\eta_E^\theta$  (top to bottom), visualized using color map  with consistent ranges of mapped values for each refinement step.

	$ \mathcal{M}_h $	$\sum_E \eta_E^L$	$\sum_E \eta_{\partial E}^L$	$\sum_E \frac{1}{2} \eta_E^m$	$\sum_E \frac{1}{2} \eta_E^\theta$	$\mathbf{J}^L$	$\frac{\sum_E \eta_E}{\mathbf{J}^L - \mathbf{J}_0^L}$
0	64	0.00801	0.00346	0.00005	0.00979	2.04031	0.10637
1	82	0.00723	0.00224	0.00012	0.00849	1.95462	0.15758
2	106	0.00424	0.00141	0.00008	0.00760	1.94747	0.12385
3	148	0.00326	0.00139	0.00007	0.00589	1.94171	0.10428
4	220	0.00237	0.00070	0.00004	0.00407	1.89705	0.12567
5	286	0.00167	0.00072	0.00005	0.00315	1.89389	0.10370
6	406	0.00116	0.00048	0.00003	0.00251	1.87112	0.13375
7	520	0.00089	0.00037	0.00002	0.00191	1.86690	0.11835
8	670	0.00073	0.00030	0.00002	0.00146	1.86600	0.09614
9	898	0.00060	0.00022	0.00001	0.00113	1.85461	0.13313
10	1186	0.00044	0.00019	0.00002	0.00089	1.85361	0.11295
11	1576	0.00032	0.00014	0.00002	0.00069	1.84746	0.15422
12	2212	0.00026	0.00011	0.00002	0.00053	1.84697	0.12935
13	2956	0.00021	0.00008	0.00002	0.00041	1.84398	0.17742
14	3844	0.00015	0.00007	0.00002	0.00032	1.84367	0.14852
15	5038	0.00011	0.00005	0.00001	0.00025	1.84345	0.12028
16	6736	0.00008	0.00004	0.00001	0.00020	1.84201	0.15759
17	8650	0.00007	0.00003	0.00001	0.00016	1.84186	0.14105
18	11044	0.00006	0.00003	0.00001	0.00013	1.84171	0.12677
19	14356	0.00005	0.00002	0.00001	0.00010	1.84096	0.17480
20	18640	0.00003	0.00002	0.00001	0.00008	1.84089	0.14670
21	24430	0.00003	0.00002	0.00001	0.00007	1.84084	0.12984
22	31522	0.00002	0.00001	0.00001	0.00005	1.84047	0.16997
23	40840	0.00002	0.00001	0.00001	0.00004	1.84044	0.14155
24	53224	0.00001	0.00001	<0.00001	0.00003	1.84040	0.11976
25	69748	0.00001	0.00001	0.00001	0.00003	1.84022	0.15588
26	89353	0.00001	0.00001	<0.00001	0.00002	1.84021	0.13038
27	115849	0.00001	<0.00001	<0.00001	0.00002	1.84011	0.15005
28	151183	0.00001	<0.00001	<0.00001	0.00001	1.84010	0.12874
29	194737	<0.00001	<0.00001	<0.00001	0.00001	1.84010	0.11046

Table 8.1.: Listing of important quantities obtained by the adaptive scheme for the carrier plate scenario and the sequential lamination model.

**Cantilever.** When dealing with classical shape optimization problems in Section 6.2, the underlying geometry was restricted to the unit square. In this regard the adaptive meshes allow for more flexibility. Given the quadtree structure, cf. Section 5.5.2, it is possible to leave out subtrees by supplying appropriate masks. Their roots are thereby identified via corresponding elements in the tree. The first instance is a cantilever with a rectangular working domain  $D = [0, 1] \times [0, \frac{1}{2}]$ . The left boundary  $\Gamma_D = \{0\} \times [0, \frac{1}{2}]$  is assumed to be fixated. In the middle of the right boundary,  $\Gamma_N = \{1\} \times [\frac{3}{16}, \frac{5}{16}]$ , a downwards pointing load  $g \equiv (0, -1)$  is applied. The remaining part of the boundary is allowed to evolve freely in terms of homogeneous Neumann boundary conditions. The overall volume fraction is constrained to 50% and no volume forces are considered, i. e.  $f \equiv 0$ . In Figure 8.6 generated meshes at

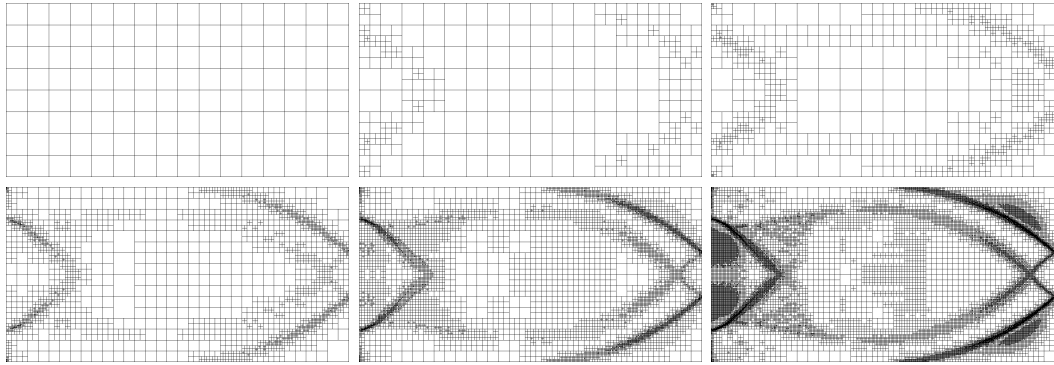


Figure 8.6.: Generated meshes after 0, 4, 8, 12, 16, and 20 refinement steps for the cantilever scenario and the sequential lamination model.

selected intermediate refinement steps are shown. Figure 8.7 displays the optimal density distribution obtained by the fully converged sequential lamination algorithm on the respective meshes. First of all a symmetric shape is obtained. This is expected for the same reasons

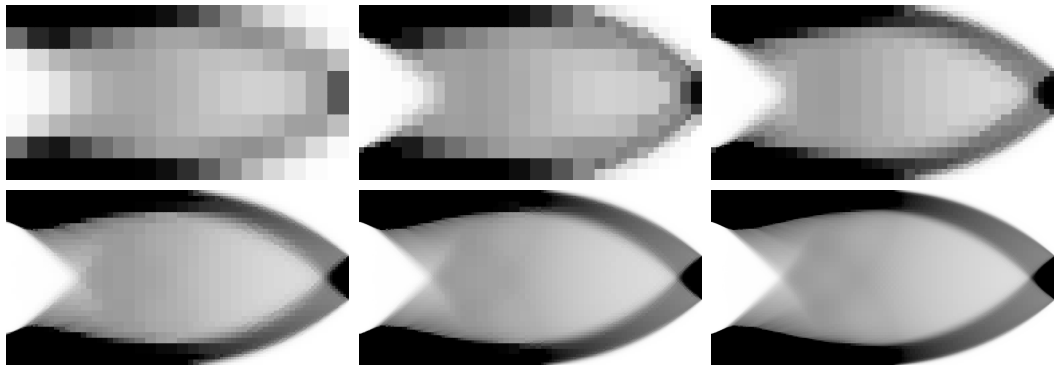


Figure 8.7.: Optimal density obtained after 0, 4, 8, 12, 16, and 20 refinement steps for the cantilever scenario and the sequential lamination model.

as discussed previously for the carrier plate scenario. The optimized configuration has two thick beams starting at the Dirichlet boundary with near solid material. Along their paths they become thinner and the effective density decreases as well. They finally overlap at the right hand side, where the loading is applied, within a triangular shaped area, filled with bulk material. On the left hand side a near void right-angled triangular area can be seen, which is similar to the lower central region in the carrier plate scenario. Moving toward the right hand side two pairs of small curved trusses can be recognized between the outer beams. In the right half of the enclosed area the density is overall homogeneous. Refinement occurs mainly for the boundaries of the thick beams and the left hand side void region. As observed previously it is stronger where the jump in density is higher. Additionally cells in the upper and lower left corners are refined. As for the carrier plate scenario, this is where the Dirichlet and Neumann boundaries meet. Table 8.2 summarizes all important figures of

the adaptive algorithm. Similar to before the full primal volume residual  $\eta_E^{u^L}$  and the full

	$ \mathcal{M}_h $	$\sum_E \eta_E^{u^L}$	$\sum_E \eta_{\partial E}^{u^L}$	$\sum_E \frac{1}{2} \eta_E^m$	$\sum_E \frac{1}{2} \eta_E^\theta$	$\mathbf{J}^L$	$\frac{\sum_E \eta_E}{\mathbf{J}^L - \mathbf{J}_0^L}$
0	128	0.00131	0.00070	0.00004	0.00151	0.23375	0.05397
1	152	0.00074	0.00040	0.00005	0.00129	0.20078	0.07538
2	182	0.00071	0.00037	0.00004	0.00108	0.19971	0.06914
3	260	0.00045	0.00025	0.00003	0.00082	0.19930	0.04942
4	344	0.00035	0.00020	0.00003	0.00064	0.19881	0.03941
5	428	0.00026	0.00016	0.00003	0.00050	0.18356	0.06027
6	566	0.00021	0.00013	0.00003	0.00038	0.18325	0.04834
7	764	0.00016	0.00008	0.00002	0.00029	0.17572	0.06990
8	998	0.00012	0.00007	0.00002	0.00023	0.17555	0.05571
9	1352	0.00009	0.00005	0.00002	0.00017	0.17526	0.04346
10	1754	0.00006	0.00004	0.00002	0.00013	0.17160	0.06476
11	2372	0.00005	0.00003	0.00002	0.00010	0.17152	0.05121
12	3146	0.00003	0.00002	0.00001	0.00008	0.17145	0.03929
13	4124	0.00002	0.00001	0.00001	0.00006	0.16962	0.05971
14	5420	0.00002	0.00001	0.00001	0.00004	0.16959	0.04713
15	7400	0.00001	0.00001	0.00001	0.00003	0.16869	0.07485
16	9902	0.00001	0.00001	0.00001	0.00002	0.16866	0.06010
17	12758	0.00001	0.00001	0.00001	0.00002	0.16865	0.05134
18	17120	0.00001	<0.00001	0.00001	0.00001	0.16820	0.09066
19	23534	0.00001	<0.00001	0.00001	0.00001	0.16819	0.08146
20	31787	<0.00001	<0.00001	0.00001	0.00001	0.16818	0.06897
21	42845	<0.00001	<0.00001	0.00001	0.00001	0.16796	0.15323
22	57938	<0.00001	<0.00001	0.00001	0.00001	0.16795	0.15000
23	78464	<0.00001	<0.00001	0.00001	<0.00001	0.16795	0.14530
24	110294	<0.00001	<0.00001	0.00001	<0.00001	0.16784	2.99946

Table 8.2.: Listing of important quantities obtained by the adaptive scheme for the cantilever scenario and the sequential lamination model.

control residual w. r. t. the density parameter  $\eta_E^\theta$  dominate the estimated error. This can be seen based on selected steps in Figure 8.8 as well. Especially in the later stages the density indicator concentrates on interfaces, whereas the volume indicator is active within regions of bulk material, as e. g. in the left hand side corners. All indicators decrease during the course of the adaptive scheme, along with the difference to the optimal objective  $\mathbf{J}_0^L$ , which was again obtained by running a series of computations and the asymptotic analysis as described in Section 6.2.2. The factor between both terms is kept within bounds until after refinement step 21. Here a significant jump occurs as the control residual  $\eta_E^m$  stagnates. Consequences can be seen in the last image of Figure 8.6. Additional refinement occurs in the void regions where it is obviously unnecessary. The root cause is the determination of the ratio parameter from the local stresses, which becomes an ill-posed problem when the effective density approaches zero. Apparently it is also not meaningful to compute the ratio of material in the two lamination directions when there is hardly any material. At the beginning spurious values of this indicator in the discussed regions are dominated by the other terms but at some point they become

noticeable. This can be observed clearly in Figure 8.6. Although not justified by the derivation

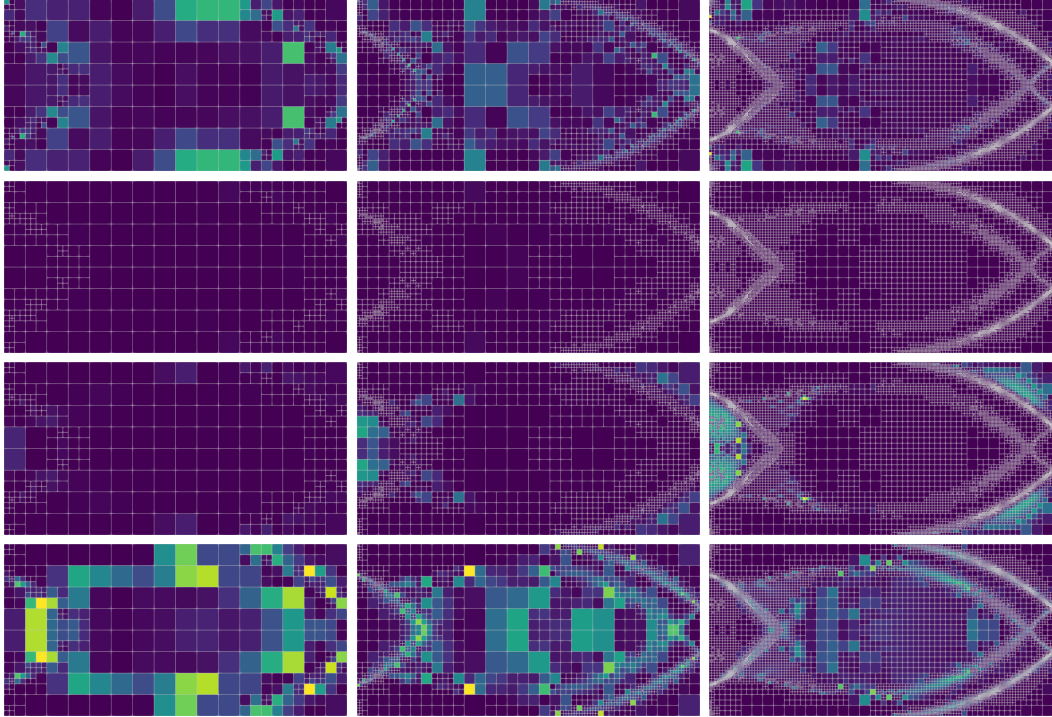



Figure 8.8.: Different terms in the estimated error after 4, 10, and 16 refinement steps (left to right) for the cantilever scenario and the sequential lamination model:  $\eta_E^u$ ,  $\eta_{\partial E}^u$ ,  $\frac{1}{2}\eta_E^m$ , and  $\frac{1}{2}\eta_E^\theta$  (top to bottom), visualized using color map  with consistent ranges of mapped values for each refinement step.

of the error estimate, the situation for this scenario can be improved by ignoring the control residual w. r. t. the ratio parameter. For demonstration we run the adaptive scheme again with this setup and show some steps of the refinement process in Figure 8.9. As can be seen, no more unnecessary refinement occurs in the near void region, cf. Figure 8.6.

**Bridge.** The next scenario resembles a bridge. Again the rectangular working domain  $D = [0, 1] \times [0, \frac{1}{2}]$  is used. On the lower boundary, supports are set on  $\Gamma_D = ([0, \frac{1}{16}] \cup [\frac{15}{16}, 1]) \times \{0\}$ . Here the  $y$ -component of the displacement is forced to zero whereas the  $x$ -component is unconstrained. This is sometimes referred to as *roller* boundary condition as it allows movements in the horizontal direction. To maintain a unique solution the  $x$ -component is additionally set to zero for a single node in the center of the lower boundary. In between the supports,  $\Gamma_N = (\frac{1}{16}, \frac{15}{16}) \times \{0\}$ , a downwards pointing load  $g \equiv (0, -1)$  is applied. The remaining part of the boundary is allowed to evolve freely in terms of homogeneous Neumann boundary conditions. The overall volume fraction is constrained to 33% and no volume forces are considered, i. e.  $f \equiv 0$ .

In Figure 8.10 generated meshes at selected intermediate refinement steps are shown.



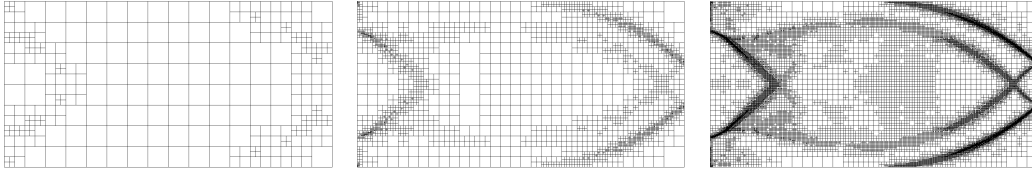


Figure 8.9.: Generated meshes after 4, 12, and 20 refinement steps for the cantilever scenario and the sequential lamination model with excluded control residual w. r. t. the ratio parameter in the error estimation.

Figure 8.11 displays the optimal density distribution obtained by the fully converged sequential

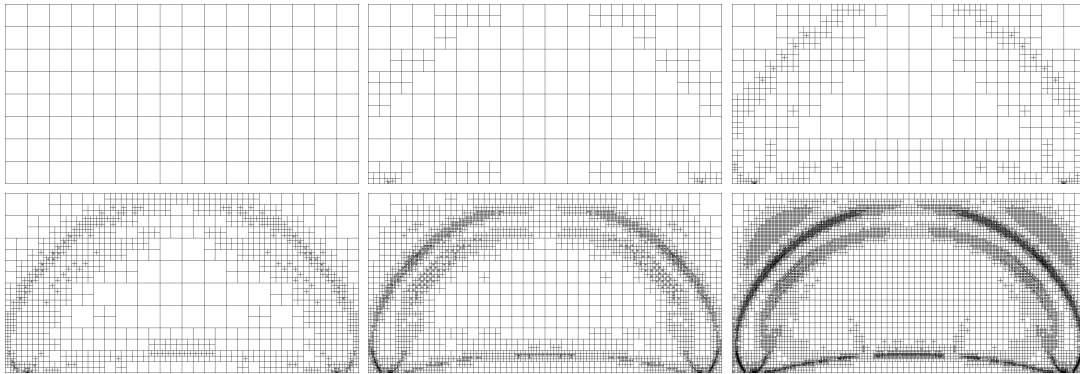


Figure 8.10.: Generated meshes after 0, 4, 8, 12, 16, and 20 refinement steps for the bridge scenario and the sequential lamination model.

lamination algorithm on the respective meshes. As before an overall symmetric picture is obtained. Along the lower boundary a horizontal bar from bulk material is established, which becomes thicker toward the center. Above an arc-shaped solid beam spans from one side to the other, utilizing the working domain to full extend. In between material with a homogeneous intermediate density is placed. Near void regions are left in the upper corners. No additional structures can be recognized in Figure 8.11 and the refinement process is fully focused on the boundaries of the beams and the supporting regions. The behavior of the adaptive scheme is comparable to the cantilever scenario before. Also here unnecessary refinement occurs in the near void regions due to spurious estimates of the control residual w. r. t. the ratio parameter. Table 8.3 summarizes all important figures and again shows the stagnation of the control residual estimator w. r. t. the ratio parameter.

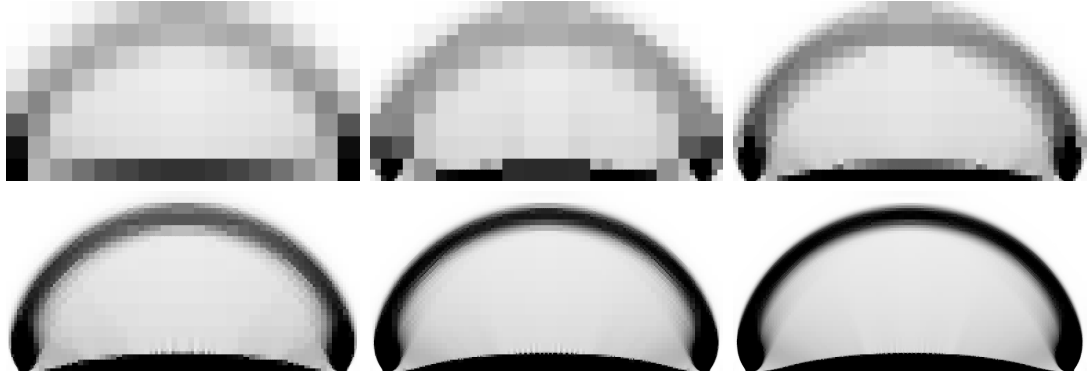


Figure 8.11.: Optimal density obtained after 0, 4, 8, 12, 16, and 20 refinement steps for the cantilever scenario and the sequential lamination model.

	$ \mathcal{M}_h $	$\sum_E \eta_E^{u^L}$	$\sum_E \eta_{\partial E}^{u^L}$	$\sum_E \frac{1}{2} \eta_E^m$	$\sum_E \frac{1}{2} \eta_E^\theta$	$\mathbf{J}^L$	$\frac{\sum_E \eta_E}{\mathbf{J}^L - \mathbf{J}_0^L}$
0	128	0.02008	0.01027	0.00024	0.01264	0.84652	0.24094
1	134	0.00926	0.00589	0.00017	0.01133	0.77227	0.25330
2	158	0.00598	0.00502	0.00017	0.00995	0.73678	0.30313
3	194	0.00464	0.00338	0.00017	0.00863	0.71706	0.33665
4	248	0.00405	0.00273	0.00017	0.00647	0.69809	0.43291
5	326	0.00344	0.00191	0.00017	0.00552	0.68744	0.54282
6	470	0.00222	0.00124	0.00014	0.00434	0.68410	0.46659
7	590	0.00204	0.00120	0.00015	0.00345	0.68150	0.47496
8	764	0.00149	0.00082	0.00012	0.00283	0.67814	0.47623
9	986	0.00127	0.00071	0.00014	0.00227	0.67479	0.57004
10	1268	0.00104	0.00058	0.00013	0.00174	0.67270	0.62141
11	1664	0.00073	0.00038	0.00012	0.00146	0.67140	0.62439
12	2150	0.00058	0.00034	0.00010	0.00118	0.67021	0.70456
13	2846	0.00049	0.00031	0.00009	0.00090	0.66938	0.78782
14	3848	0.00037	0.00023	0.00009	0.00070	0.66882	0.80640
15	4946	0.00027	0.00019	0.00008	0.00055	0.66839	0.83618
16	6509	0.00022	0.00013	0.00008	0.00043	0.66807	0.88104
17	8570	0.00016	0.00011	0.00008	0.00033	0.66785	0.89601
18	11261	0.00011	0.00008	0.00007	0.00024	0.66766	0.90927
19	14879	0.00008	0.00006	0.00007	0.00019	0.66753	0.92561
20	19316	0.00007	0.00005	0.00007	0.00015	0.66742	1.02171
21	26381	0.00006	0.00004	0.00007	0.00011	0.66732	1.25007
22	34358	0.00004	0.00003	0.00007	0.00009	0.66727	1.38833
23	45857	0.00003	0.00003	0.00007	0.00007	0.66722	1.70958

Table 8.3.: Listing of important quantities obtained by the adaptive scheme for the bridge scenario and the sequential lamination model.

**L-shaped domain.** In the last example an L-shaped domain is considered, which is obtained by excluding the upper right quadrant of the unit square, i. e.  $D = [0, 1]^2 \setminus (\frac{1}{2}, 1]^2$ . The upper boundary,  $\Gamma_D = [0, \frac{1}{2}] \times \{1\}$ , is fixated. In the middle of the right boundary,  $\Gamma_N = \{1\} \times [\frac{3}{16}, \frac{5}{16}]$ , a downwards pointing load  $g \equiv (0, -1)$  is applied. The remaining part of the boundary is allowed to evolve freely in terms of homogeneous Neumann boundary conditions. The overall volume fraction is constrained to 50% and no volume forces are considered, i. e.  $f \equiv 0$ . In Figure 8.12 generated meshes at selected intermediate refinement steps are shown. Figure 8.13

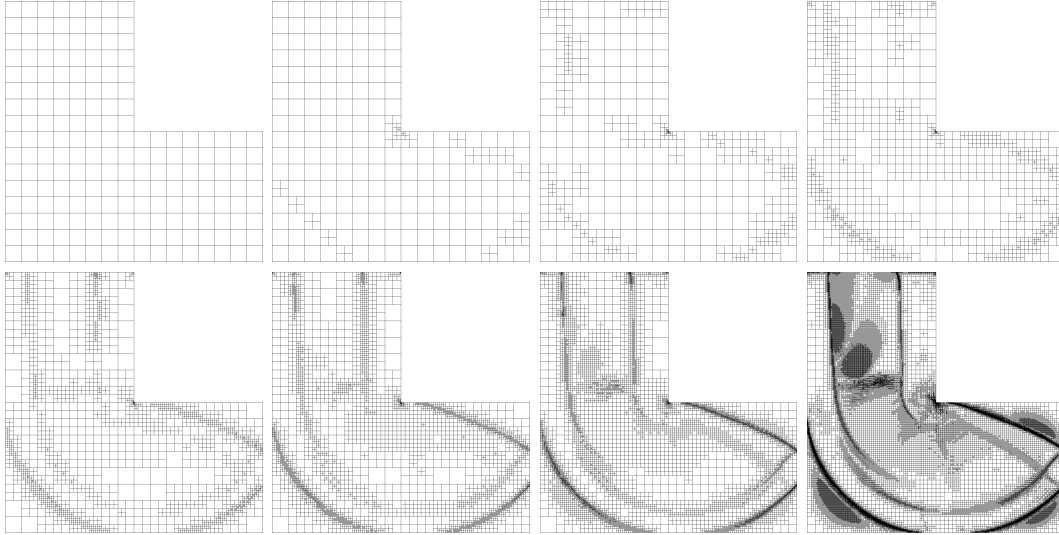


Figure 8.12.: Generated meshes after 0, 3, 6, 9, 12, 15, 18, and 24 refinement steps for the L-shaped domain and the sequential lamination model.

displays the optimal density distribution obtained by the fully converged sequential lamination algorithm on the respective meshes. The overall outcome of the optimization is reminiscent of a hook and shows different structures in each of the three quadrants. Solid beams are formed on the sides of the upper part, connecting the Dirichlet boundary to the rest of the domain. The region in between is near void. In the lower left quadrant the beams bend toward the right and continue similar to the cantilever. The region in between the beams shows an intermediate density. For coarser meshes it is homogeneous as in the bridge scenario, but in later refinements steps an additional arc and cross braces can be seen. As before refinement occurs for interfaces and is especially strong when the jump in density is high. Another focus is on the reentrant corner, where a singularity in the elasticity solution is expected. In fact Figure 8.14 shows that in this scenario the primal volume residual indicator attains higher values than the control residual w. r. t. the density parameter. In the upper corners, where Dirichlet and Neumann boundaries meet, refinement occurs as well, but at a later stage and with less intensity. The second column of Figure 8.14 clearly shows that the density indicator is active along the interfaces whereas the volume indicator also attains high values within the beams. As in the examples before unnecessary refinement occurs in the near void regions in later stages of the algorithm. The increasing influence of the control residual w. r. t. the ratio parameter can be seen in the third row of Figure 8.14. Table 8.4 lists details of the adaptive

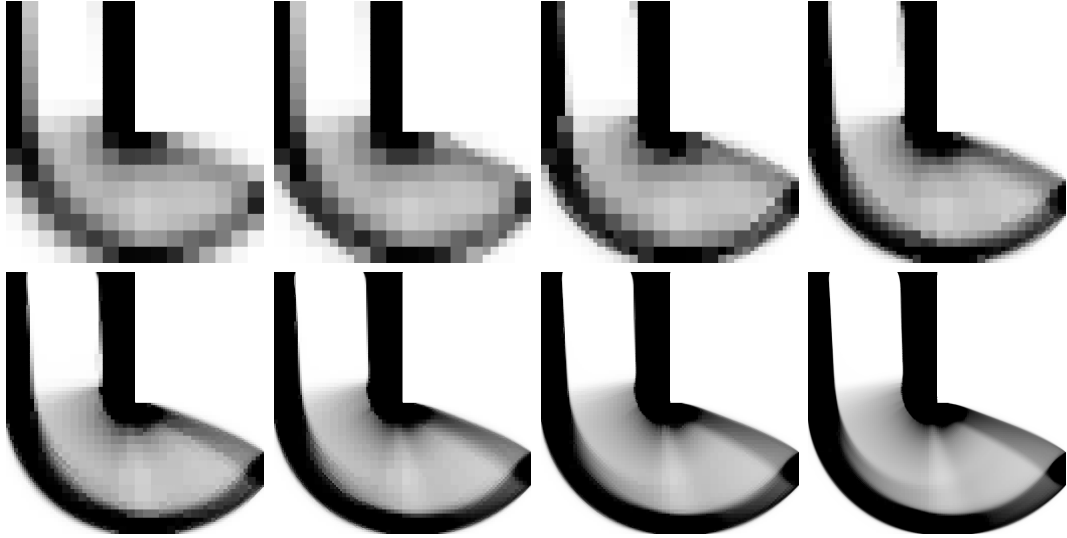


Figure 8.13.: Optimal density obtained after 0, 3, 6, 9, 12, 15, 18, and 24 refinement steps for the L-shaped domain and the sequential lamination model.

scheme.

Summarizing the presented results, the derived goal-oriented error estimator works well for the sequential lamination model. Sharply resolved interfaces, separating regions with almost no material from regions with bulk material or intermediate density, are generated. The main driver is the control residual w. r. t. the density parameter. This is in accordance with the general observation that the rigidity of a shape is mostly improved by an optimal distribution of the available material.

### 8.3. Application to the two-scale microstructure model

In this section we will apply the derived error estimates in the context of the two-scale shape optimization model that was presented in Chapter 5. Here the controls  $q$  are the parameters describing the perforations of the local, periodic microstructure for each investigated model, cf. Section 5.4. By solving cell problems, effective elasticity tensors  $C_h^M := C_h^*[q_h]$  are obtained via numerical homogenization as described in Section 5.3.1. Taking this macroscopic perspective, the error estimator can be computed directly. To be precise, the primal residual terms (8.2) can be evaluated as soon as the two-scale problem has been solved for a given configuration. For the control terms (8.4) entry-wise sensitivities of the effective elasticity tensor, and thereby of the associated two-scale elastic energy densities, are required. Those were already derived in the course of the shape derivative, cf. (5.9).

In the following we present results obtained by the adaptive scheme using ellipsoidal shaped perforations and rotating orthogonal rods as microscopic models, cf. Section 5.4. We will focus on the carrier plate scenario that was already considered in Section 6.2 and in the preceding section in context of the sequential lamination model. The microstructures are discretized by 12 points for each side of the outer boundary, each side of the inner boundary for rotating rods,

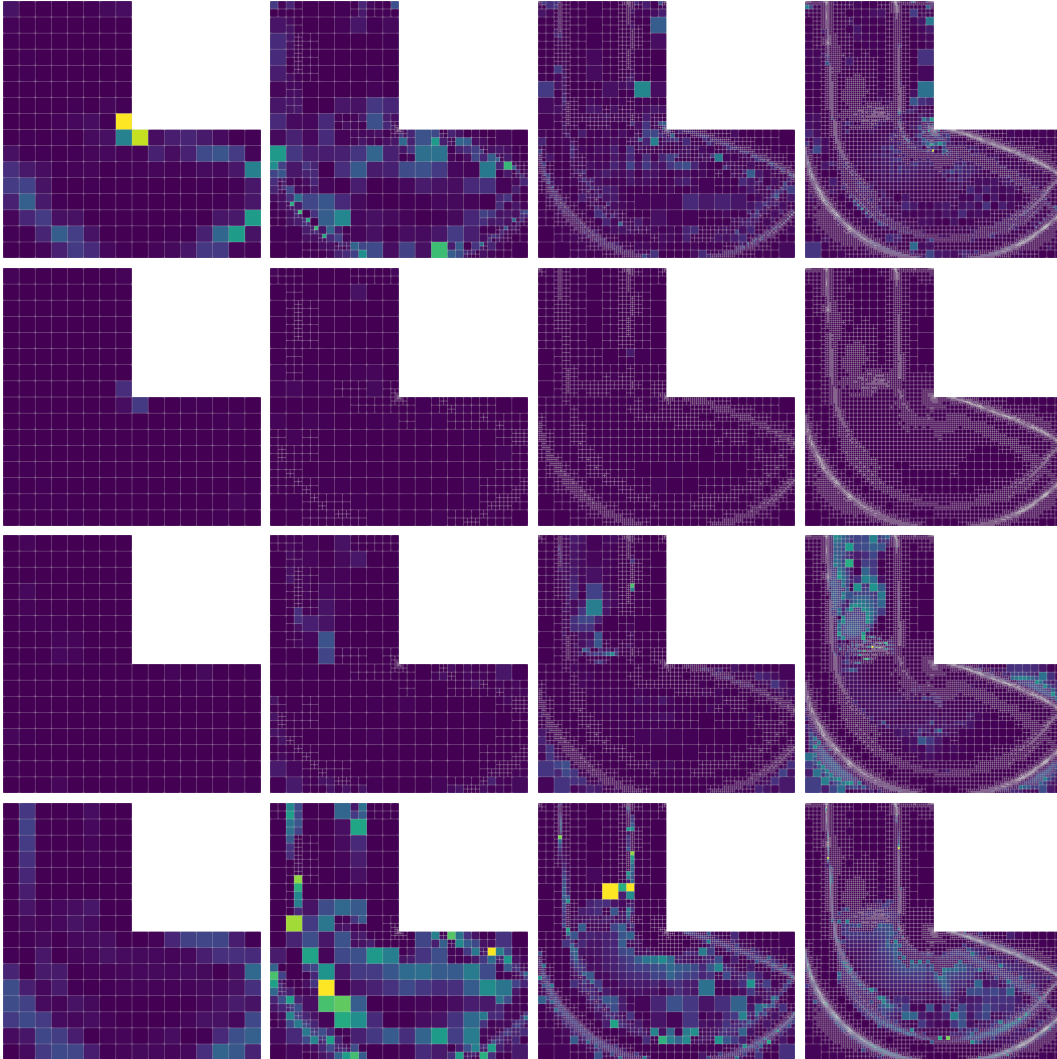



Figure 8.14.: Different terms in the estimated error after 0, 6, 12, and 18 refinement steps (left to right) for the L-shaped domain and the sequential lamination model:  $\eta_E^L$ ,  $\eta_{\partial E}^L$ ,  $\frac{1}{2}\eta_E^m$ , and  $\frac{1}{2}\eta_E^\theta$  (top to bottom), visualized using color map  with consistent ranges of mapped values for each refinement step.

and the ellipsoidal perforation, respectively. As was discussed in Section 6.2.3 this provides a good tradeoff between accuracy and computational effort. The adaptive scheme was started from a uniform grid of level 3 and the Dörfler marking parameter was set to  $r = 0.4$ . As done in Section 6.2 we display two-scale results by drawing the macroscopic domain subdivided into its square cells with a representative of the underlying microstructure in each cell. One has to keep in mind that the actual microstructure is obtained by repeating the representative shape on a microscopic periodic lattice.

	$ \mathcal{M}_h $	$\sum_E \eta_E^{\mathbf{u}^L}$	$\sum_E \eta_{\partial E}^{\mathbf{u}^L}$	$\sum_E \frac{1}{2} \eta_E^m$	$\sum_E \frac{1}{2} \eta_E^\theta$	$\mathbf{J}^L$	$\frac{\sum_E \eta_E}{\mathbf{J}^L - \mathbf{J}_0^L}$
0	192	0.00174	0.00151	0.00006	0.00163	0.27651	0.06421
1	204	0.00149	0.00094	0.00005	0.00163	0.27732	0.05293
2	225	0.00098	0.00059	0.00004	0.00134	0.23909	0.07454
3	258	0.00070	0.00046	0.00005	0.00124	0.23880	0.06240
4	312	0.00060	0.00036	0.00004	0.00095	0.23831	0.05023
5	399	0.00048	0.00026	0.00004	0.00081	0.22827	0.05553
6	525	0.00038	0.00022	0.00004	0.00061	0.21871	0.06494
7	669	0.00029	0.00017	0.00003	0.00051	0.21827	0.05371
8	858	0.00023	0.00013	0.00003	0.00043	0.21793	0.04486
9	1110	0.00017	0.00010	0.00004	0.00032	0.20906	0.06579
10	1407	0.00014	0.00008	0.00003	0.00027	0.20875	0.05714
11	1797	0.00011	0.00006	0.00003	0.00021	0.20857	0.04618
12	2334	0.00008	0.00005	0.00003	0.00017	0.20632	0.04797
13	3024	0.00006	0.00003	0.00002	0.00013	0.20406	0.05594
14	3912	0.00005	0.00003	0.00002	0.00010	0.20290	0.05990
15	4959	0.00004	0.00002	0.00002	0.00008	0.20283	0.04802
16	6339	0.00003	0.00002	0.00002	0.00006	0.20173	0.05659
17	8295	0.00002	0.00001	0.00002	0.00004	0.20117	0.06253
18	10953	0.00002	0.00001	0.00002	0.00003	0.20114	0.05110
19	14439	0.00001	0.00001	0.00002	0.00003	0.20059	0.06236
20	19119	0.00001	0.00001	0.00002	0.00002	0.20032	0.07311
21	25356	0.00001	0.00001	0.00001	0.00002	0.20031	0.06391
22	34185	0.00001	<0.00001	0.00001	0.00001	0.20003	0.09087
23	45087	0.00001	<0.00001	0.00001	0.00001	0.19990	0.12894
24	59559	<0.00001	<0.00001	0.00001	0.00001	0.19989	0.11610
25	81387	<0.00001	<0.00001	0.00001	0.00001	0.19975	0.21661

Table 8.4.: Listing of important quantities obtained by the adaptive scheme for the L-shaped domain and the sequential lamination model.

**Ellipsoidal perforations.** Figure 8.15 shows generated meshes and visualizations of the two-scale results for selected intermediate refinement steps. The refined interfaces are striking and clearly draw an outline of the trusses and the upper supporting structure. In later stages refinement also takes place within the dominating structures and the central bulk region becomes visible in the adaptive mesh. At some point a break in symmetry occurs, as was already observed for the uniform case in Section 6.2. It is probably caused by inaccuracies in the evaluation of the shape derivative for the microscopic cell problems. As the influence of single parameters on the cost functional decreases for increasingly fine cells, non-optimal optimization steps might get accepted. In the uniform setting we were able to partly counteract this issue by applying a scaling that was proportional to the uniform cell size. Naturally this is not possible anymore for adaptive meshes. Overall the obtained shapes match with results on uniform grids, cf. Figure 6.6. Only the small additional trusses that appeared on fine uniform meshes below the supporting structure are not present anymore. In fact they cannot be realized because the error estimate never predicts a need for refinement in those

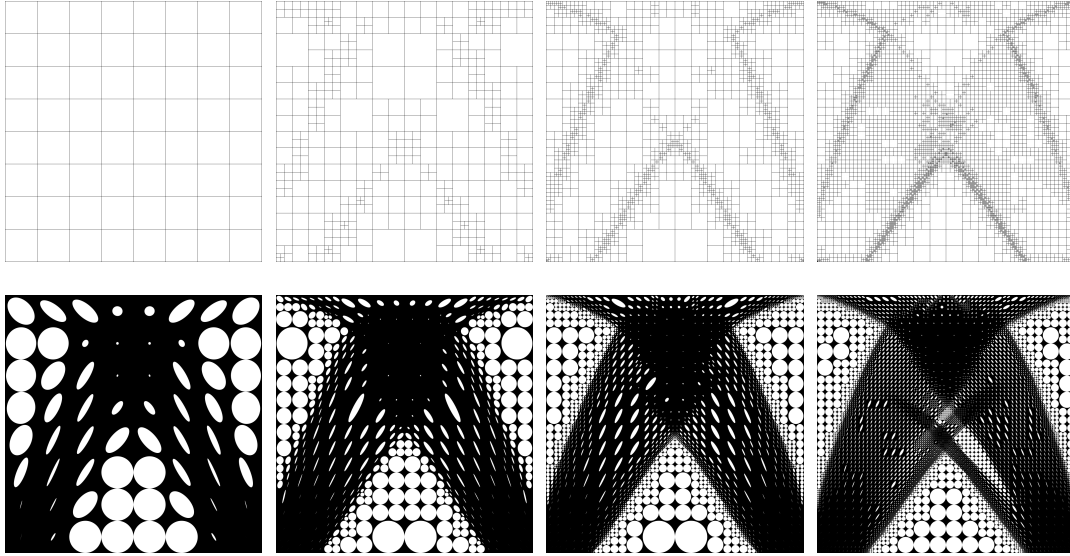


Figure 8.15.: Two-scale results after 0, 5, 10, and 18 refinement steps for the carrier plate scenario and one ellipsoidal perforation as the microstructure model. In the upper row the macroscopic mesh is shown. In the lower row a representative of the microstructure is drawn in each macroscopic cell.

regions, which are filled with as less material as possible. Still the adaptive strategy proves to be meaningful. After 7 refinement steps the adaptive mesh has 874 cells and the objective functional is below the value that was obtained on a uniform grid of level 7. Due to differences in the discretization of the microscopic problem, the values are not truly comparable, still the saving is significant.

In Table 8.5 we list figures of the error estimation in detail. Most conspicuous is that the objective functional increases after 10 refinement steps. Besides the already reported break in symmetry this is a clear indication that the results are not trustworthy at this stage anymore. In fact the cost value is close to the asymptotically determined, cf. Table 6.8, but as more and more cells fail to provide sound optimized shapes, the error indicators produce false values as well.

As an example for the spatial distribution of the error indicators during the sound phase of the algorithm we depict the situation after 6 refinement steps in Figure 8.16. Here we summed up the primal volume and edge residual, which are usually active within similar regions. We also summed up the control residual terms w. r. t. the scaling parameters of the ellipsoidal perforations. For elongated shapes one parameter corresponds to the dominant semiaxis, but the selection during the course of the algorithm is arbitrary. The visualization shows that the control residual terms w. r. t. the scaling parameters are active along the interfaces. The primal residual terms contribute there as well, but also at the lower corners, as seen previously. The control residual w. r. t. the rotation has less influence, which is expected as it does not account for a redistribution of material.

	$ \mathcal{M}_h $	$\sum_E \eta_E^{u^L}$	$\sum_E \eta_{\partial E}^{u^L}$	$\sum_E \frac{1}{2} \eta_E^{q_1}$	$\sum_E \frac{1}{2} \eta_E^{q_2}$	$\sum_E \frac{1}{2} \eta_E^{q_3}$	$\mathbf{J}^M$	$\frac{\sum_E \eta_E}{\mathbf{J}^M - \mathbf{J}_0^M}$
0	64	0.03653	0.02229	0.02719	0.00716	0.00198	2.41602	0.28230
1	94	0.03061	0.01599	0.01546	0.00422	0.00142	2.25959	0.37483
2	142	0.01549	0.00972	0.01310	0.00438	0.00128	2.23060	0.29003
3	232	0.01363	0.00943	0.00942	0.00300	0.00216	2.16069	0.46079
4	322	0.01160	0.00686	0.00742	0.00245	0.00167	2.14328	0.46670
5	454	0.00911	0.00529	0.00576	0.00196	0.00045	2.13068	0.43675
6	646	0.00625	0.00367	0.00457	0.00172	0.00033	2.10073	0.76103
7	874	0.00456	0.00258	0.00347	0.00132	0.00028	2.09635	0.70407
8	1183	0.00314	0.00199	0.00288	0.00106	0.00020	2.09157	0.73764
9	1573	0.00225	0.00134	0.00224	0.00079	0.00018	2.08141	2.83506
10	1969	0.00192	0.00105	0.00185	0.00093	0.01175	2.08187	6.13112

Table 8.5.: Listing of important quantities obtained by the adaptive scheme for the carrier plate scenario and one ellipsoidal perforation in the two-scale model.

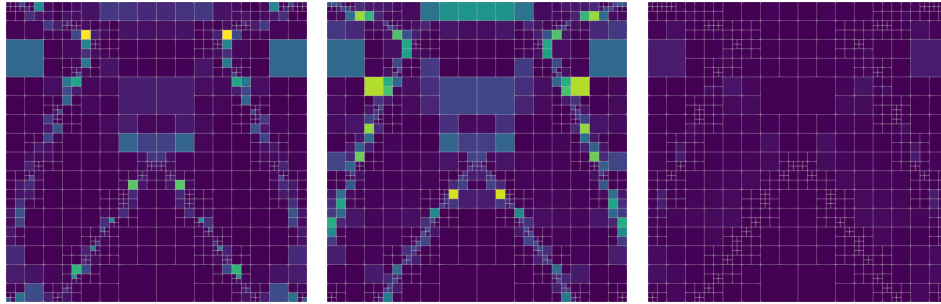



Figure 8.16.: Different terms in the estimated error after 6 refinement steps for the carrier plate scenario and one ellipsoidal perforation as microstructure model:  $\eta_E^{u^L} + \eta_{\partial E}^{u^L}$ ,  $\frac{1}{2}(\eta_E^{q_1} + \eta_E^{q_2})$ ,  $\eta_E^{q_3}$ , visualized using color map  with consistent ranges of mapped values.

**Rotating orthogonal rods.** We now turn toward the rotating orthogonal rods microstructure model. In Figure 8.17 we show generated meshes and visualizations of the two-scale results for selected intermediate refinement steps. The situation here is different from before. Overall the obtained shapes match with the results on uniform grids, cf. Figure 6.9. However distinct features in the refined meshed can be recognized only at later stages of the algorithm. Apart from the lower curved boundary of the upper supporting structure no sharp interfaces have formed. This is in accordance with earlier observations that the microstructure for this model varies rather smoothly. The adaptive scheme still aids in finding more optimal shapes. Regions with intermediate density, where the orientation of the perforations varies, receive refinement whereas regions with bulk or hardly any material do not. As an example we show the error indicators after 5 refinement steps in Figure 8.18 as done before. Consistent with the observation just described, marked cells are distributed throughout large parts of the working domain, which is especially different from the situation in Figure 8.16. In Table 8.5 we list



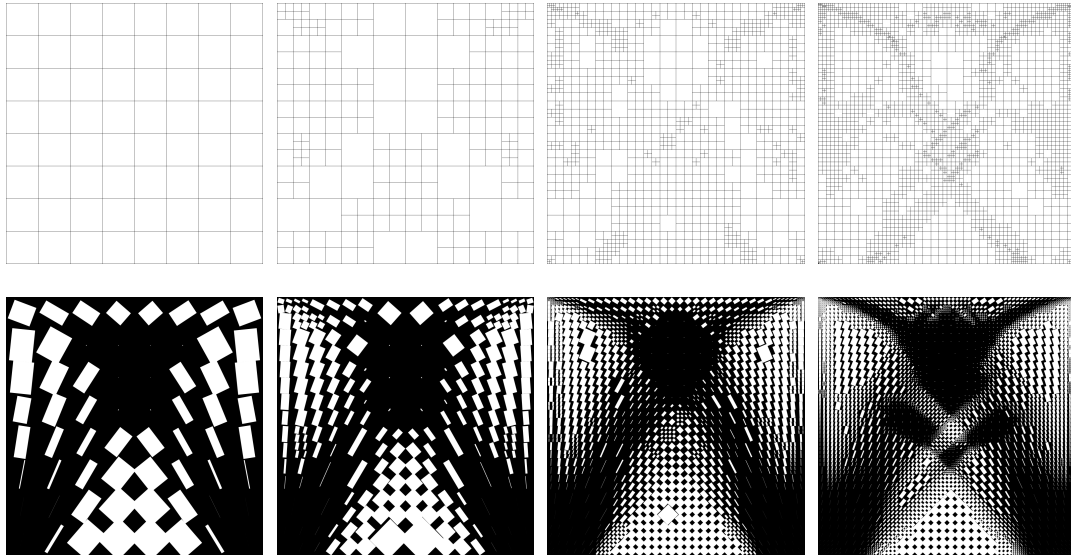


Figure 8.17.: Two-scale results after 0, 3, 9, and 13 refinement steps for the carrier plate scenario and rotating orthogonal rods as the microstructure model. In the upper row the macroscopic mesh is shown. In the lower row a representative of the microstructure is drawn in each macroscopic cell.

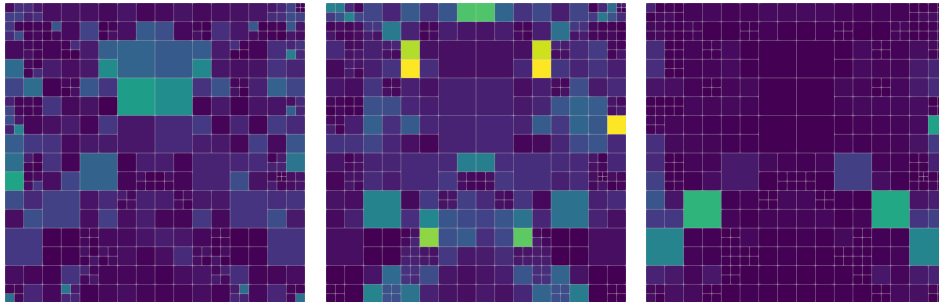



Figure 8.18.: Different terms in the estimated error after 5 refinement steps for the carrier plate scenario and rotating orthogonal rods as microstructure model:  $\eta_E^u + \eta_{\partial E}^u$ ,  $\frac{1}{2}(\eta_E^{q_1} + \eta_E^{q_2})$ ,  $\eta_E^{q_3}$ , visualized using color map  with consistent ranges of mapped values.

figures of the error estimation in detail. As before for the ellipsoidal perforations the objective function increases at some point. Also a break in symmetry can be observed. However, in contrast to all preceding examples, the cost never comes close to the asymptotic value of Table 6.8. Consequently the ratio in the last column of Table 8.5 becomes small. The error indicators still seem plausible but the shape is not correctly optimized anymore. On the whole the adaptive scheme seems to suffer more severely from numerical deficiencies, which could be attributed to the non-smooth boundary, cf. Remark 5.7, the coarse microscopic discretization,

	$ \mathcal{M}_h $	$\sum_E \eta_E^{u^L}$	$\sum_E \eta_{\partial E}^{u^L}$	$\sum_E \frac{1}{2} \eta_E^{q_1}$	$\sum_E \frac{1}{2} \eta_E^{q_2}$	$\sum_E \frac{1}{2} \eta_E^{q_3}$	$\mathbf{J}^M$	$\frac{\sum_E \eta_E}{\mathbf{J}^M - \mathbf{J}_0^M}$
0	64	0.03993	0.01756	0.02677	0.01526	0.00773	2.16324	0.34262
1	100	0.02724	0.01151	0.02639	0.01105	0.00565	2.04100	0.42905
2	148	0.01912	0.01020	0.01698	0.00708	0.00469	2.01734	0.34755
3	226	0.01179	0.00456	0.01398	0.09923	0.00426	1.95985	1.22084
4	229	0.01274	0.00606	0.01345	0.00612	0.00324	1.94581	0.43552
5	358	0.00859	0.00367	0.00840	0.00795	0.00268	1.93051	0.38979
6	493	0.00674	0.00270	0.00678	0.00406	0.00184	1.91493	0.34218
7	679	0.00424	0.00179	0.00516	0.00256	0.00128	1.91016	0.25050
8	973	0.00451	0.00160	0.00364	0.00244	0.00094	1.89196	0.31492
9	1273	0.00225	0.00085	0.00275	0.00958	0.00087	1.89822	0.33966
10	1276	0.00311	0.00113	0.00289	0.00185	0.00081	1.88629	0.27126
11	1753	0.00250	0.00097	0.00266	0.00177	0.00060	1.88267	0.26194
12	2356	0.00151	0.00060	0.00202	0.00115	0.00052	1.87748	0.21255
13	3349	0.00095	0.00036	0.00142	0.00082	0.00036	1.87994	0.13170
14	4570	0.00060	0.00021	0.00094	0.00060	0.00027	1.88510	0.07485
15	6085	0.00040	0.00013	0.00068	0.00038	0.00019	1.89392	0.04060

Table 8.6.: Listing of important quantities obtained by the adaptive scheme for the carrier plate scenario and rotating orthogonal rods in the two-scale model.

and the strongly varying scaling due to different cell sizes.

Summarizing the presented results, the derived goal-oriented error estimator can directly be applied to the numerical two-scale model. In case of the ellipsoidal perforations the results meet with expectations. Regions of high and low material density are sharply separated and the objective functional soon becomes near optimal. For the rotating orthogonal trusses however the adaptive scheme seems to suffer from numerical instabilities. Although the error indicators show meaningful values the objective functional falls short of the optimum.

## 8.4. Modeling error estimation

In this section we continue with error estimation for the numerical two-scale model. Bearing in mind that the ultimate goal is to approximate an optimal shape, the approach taken in the previous section is flawed. In particular the employed error estimate aims at minimizing the error  $|\mathbf{J}^M[q; u^*] - \mathbf{J}^M[q_h; u_h^*]|$ , which means that the target is an optimal shape within the class of the considered microstructure model. As expected, and seen from previously presented results, the investigated geometrically simple models can, however, never be optimal. Instead we need to consider the error  $|\mathbf{J}[\mathcal{O}^{\text{opt}}; u[\mathcal{O}^{\text{opt}}]] - \mathbf{J}^M[q_h; u_h^*]|$ , which includes both the *modeling error*, caused by the choice of the mechanically simple but non-optimal microstructure model, and the numerical discretization error. An appropriate adaptive scheme cannot be expected to fully cancel the error for decreasing mesh size, but allows to assess the remaining global modeling error and its spatial distribution.

With some rephrasing the previously obtained error estimate can be reused. Let  $C^L$  be an optimal tensor field, realized by the sequential lamination construction, and  $u^L$  the

associated elasticity solution. On the other hand let  $C_h^M$  be a discrete effective elasticity tensor field, obtained via numerical homogenization from the discrete two-scale model, and  $u_h^M$  the associated discrete solution. In the following we consider the full tensors  $C^L$ ,  $C_h^M$  as the controls  $q^L$ ,  $q_h^M$ , respectively. Using this notation the derivation in Section 8.1 remains valid. In particular the full primal residuals (8.2) now read

$$\begin{aligned}\eta_E^{u^M} &= \left| \int_E \operatorname{div} \{ C_h^M \varepsilon [u_h^M] \} \cdot (u^L - \vartheta_{u_h^*}) \, dx \right|, \\ \eta_{\partial E}^{u^M} &= \left| \int_{\partial E} j (C_h^M \varepsilon [u_h^M]) \cdot (u^L - \vartheta_{u_h^*}) \, da(x) \right|.\end{aligned}\tag{8.8}$$

For the control residual (8.4) observe that the elasticity tensors enter the Lagrangian linearly. The derivative w. r. t. the controls can therefore be directly given, resulting in

$$\eta_E^{q^M} = \left| \int_E (C^L - C^*[\vartheta_{q_h}]) \varepsilon [u_h^M] : \varepsilon [u_h^M] \, dx \right|.\tag{8.9}$$

Besides that, the remainder term (8.6) can be further evaluated. With  $e_u = u^L - u_h^M$  and  $e_q = C^L - C_h^M$  we get  $\frac{d^3}{ds^3} \mathcal{L}(q_h^M + se_{q^M}; u_h^M + se_{u^M}) = -6a^M(e_{q^M}; e_{u^M}, e_{u^M})$ , yielding

$$\mathcal{R} = \frac{1}{2} a^M(e_{q^M}; e_{u^M}, e_{u^M}).$$

As before differences involving the unknown continuous quantities  $C^L$ ,  $u^L$  need to be approximated for a practical numerical scheme. In contrast to the preceding sections the terms however stem from different material models and, as already seen, the individual outcomes from shape optimization are in general locally unrelated. For the purpose of illustration we consider a splitting of a potential primal weighting term

$$u^L - u_h^M = (u^L - u_h^L) + (u_h^L - u_h^M).\tag{8.10}$$

The first term on the right hand side could again be approximated using interpolation to higher order polynomials as done in Section 8.2.2, but for this the discrete solution  $u_h^L$  corresponding to the sequential lamination model would be needed. It could be computed from scratch on the same grid that was used to compute the solution  $u_h^M$  of the two-scale model. Solving another optimization problem in full detail would however impair the efficiency of our scheme, especially because the alternating algorithm is known to exhibit slow convergence. We therefore propose a truncated iteration, starting from stresses obtained for the two-scale model. To be precise we start with  $\sigma = C_h^M \varepsilon [u_h^M]$  and perform  $n$  iterations, obtaining  $u_{h,n}^L$ . Using this as an approximation for  $u_h^L$  is promising because the alternating algorithm typically shows a reasonable distribution of material already after few iterations. We claim that changes during later iterations are less significant and show some evidence in Figure 8.19. For this we did another run of the sequential lamination algorithm until convergence for the carrier plate scenario on an intermediate mesh of the adaptive scheme. The actual results will be discussed later. Here we evaluate the differences in the cost functional and the elasticity solution, between the truncated and the final result. A significant drop can be seen already in the early iterations. For our application we are in fact content with an approximation of the difference to the sequential lamination solution by trend and therefore consider the approach reasonable. Coming back to (8.10) we use  $u_h^L \approx u_{h,n}^L$ , which allows to directly evaluate the

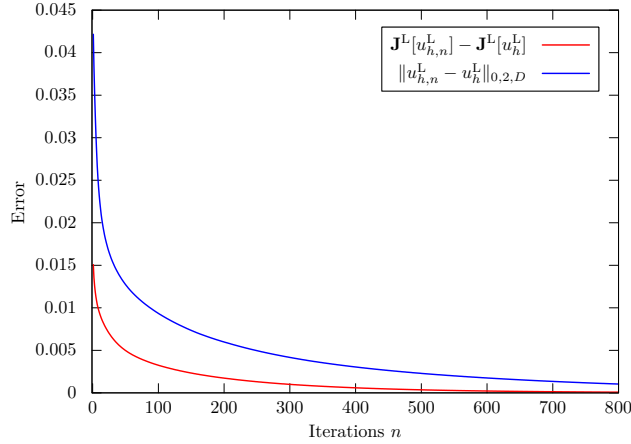


Figure 8.19.: Exemplary convergence behavior of the sequential lamination algorithm for the carrier plate scenario in terms of errors in the cost functional and the elasticity solution.

second term. For the first term interpolation to higher order polynomials is applied to the approximate solution, i. e.  $u^L \approx \mathcal{I}_h^{(4)} u_{h,n}^L$ . Practically the computation of the approximate solution is an intermediate step only and we directly evaluate the difference between  $\mathcal{I}_h^{(4)} u_{h,n}^L$  and  $u_h^M$ .

For the weighting term involving the effective elasticity tensors the situation is a little more complex. Here not only the continuous elasticity solution for the sequential lamination microstructure  $u^L$  comes into play, but also its corresponding optimal continuous tensor field  $C^L$ . As before we start from the elasticity tensor  $C_h^M$  and the associated stresses  $\sigma = C_h^M \varepsilon[u_h^M]$  obtained by the two-scale scheme. Using the truncated sequential lamination algorithm we obtain the approximation  $u_{h,n}^L$  and interpolate to higher order polynomials  $\mathcal{I}_h^{(4)} u_{h,n}^L$  on super patches. For this higher order solution we locally compute optimal elasticity tensors via the sequential lamination model. As they mutually depend on the stress and the strain we employ a Newton scheme as discussed in Section 8.2.2. This can be done at each quadrature point to approximate a continuously varying tensor field, cf. the discussion in Section 5.5.1. We summarize our approach in the following remark.

**Remark 8.12** (Approximation of local weights). To approximate the weighting terms for the primal and the control error indicator we first compute an approximation  $u_{h,n}^L$  of the elasticity solution for the sequential lamination microstructure. We start from stresses of the two-scale model and perform a small number  $n$  of iterations of the alternating algorithm. On every element  $E$  we consider a patch  $\mathcal{S}$  of four neighboring elements including  $E$  and proceed as follows.

- For the primal error indicator  $5 \times 5$  degrees of freedom stemming from all elements of the patch are used to construct a biquartic polynomial  $\mathcal{I}_h^{(4)} u_{h,n}^L$  on the patch. The interpolation is then compared to the two-scale solution.

$$\omega_E^{u^M} \approx \left\| \mathcal{I}_h^{(4)} u_{h,n}^L - u_h^M \right\|_{0,2,E}, \quad \omega_{\partial E}^{u^M} \approx \left\| \mathcal{I}_h^{(4)} u_{h,n}^L - u_h^M \right\|_{0,2,\partial E}$$

Practically we will evaluate the full residual terms (8.8).

- For the control error indicator corresponding stresses and effective elasticity tensors are locally computed from the interpolated solution using a Newton scheme. Then the elasticity tensors are compared.

$$\omega_E^C \approx \left\| C^L \left[ \mathcal{I}_h^{(4)} u_{h,n}^L \right] - C_h^M \left[ u_h^M \right] \right\|_{0,\infty,E}$$

Practically it is not reasonable to compare the elasticity tensors entry wise. For instance the sequential lamination construction always results in a rank deficiency, which needs to be compensated by a numerical regularization parameter. Instead it is more natural to consider the full residual term (8.9) and compare the respective elastic energy densities.

In the following we present results of the adaptive scheme steered by the derived modeling error estimate. We focus on rotating orthogonal rods as the microstructure model within the two-scale approach as it has proven to be closest to optimal shapes. As before the microscopic geometry is discretized by 12 points for each side of the outer and inner boundary. The Dörfler marking parameter is set to  $r = 0.4$ . For the approximation of the sequential lamination solution the truncated algorithm is run for  $k = 50$  iterations. We consider the scenarios of Section 8.2.3. As before we visualize the results by drawing the macroscopic domain subdivided into its square cells with a representative of the underlying microstructure in each cell.

**Carrier plate.** The first scenario is the carrier plate. In figures 8.20, 8.21, and 8.22 we show generated meshes, visualizations of the two-scale results, and the effective material density for selected intermediate refinement steps. The shape that was previously observed for this

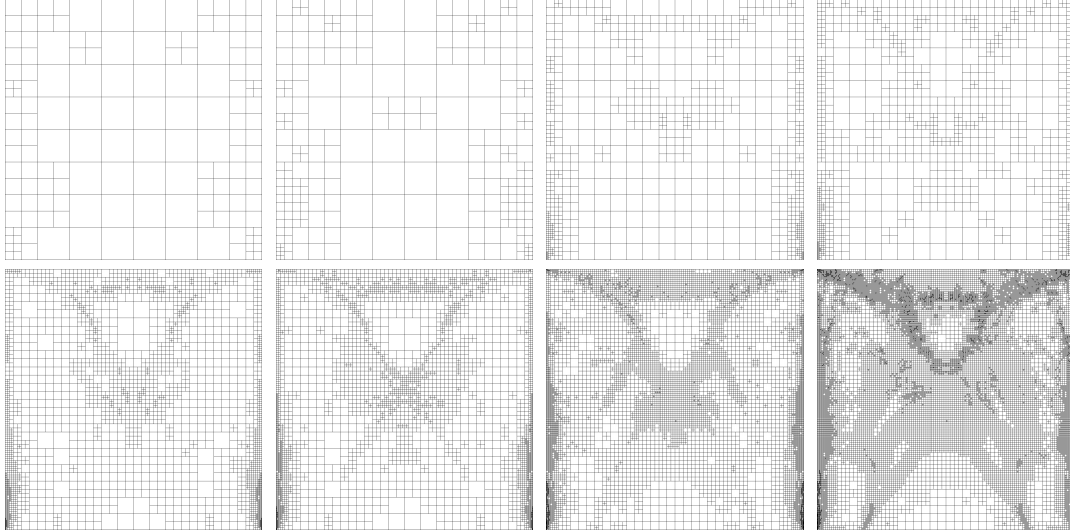


Figure 8.20.: Generated meshes after 2, 3, 6, 7, 9, 10, 12, and 14 refinement steps of the adaptive scheme using model error estimation for the carrier plate scenario and rotating orthogonal rods.

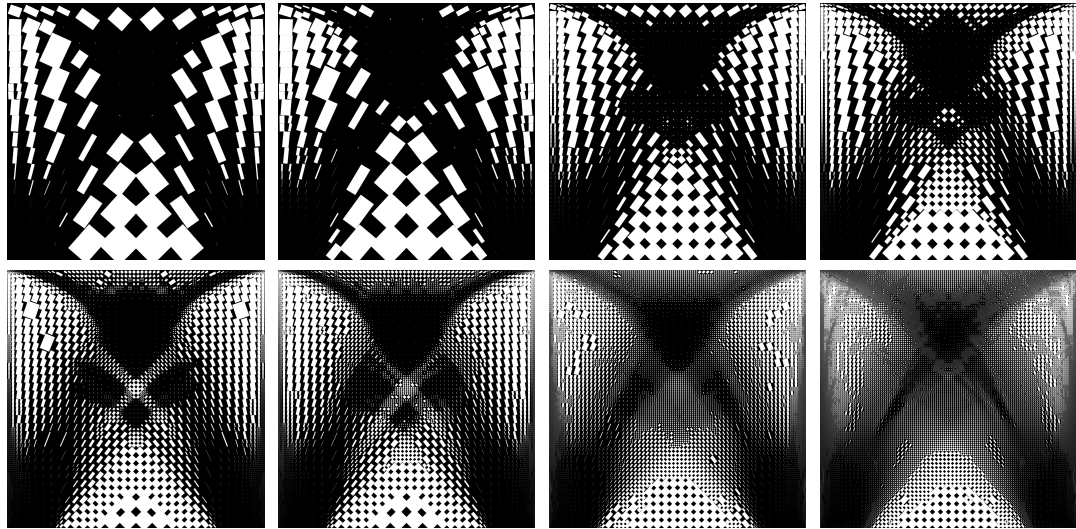


Figure 8.21.: Two-scale results after 2, 3, 6, 7, 9, 10, 12, and 14 refinement steps of the adaptive scheme using model error estimation for the carrier plate scenario and rotating orthogonal rods.

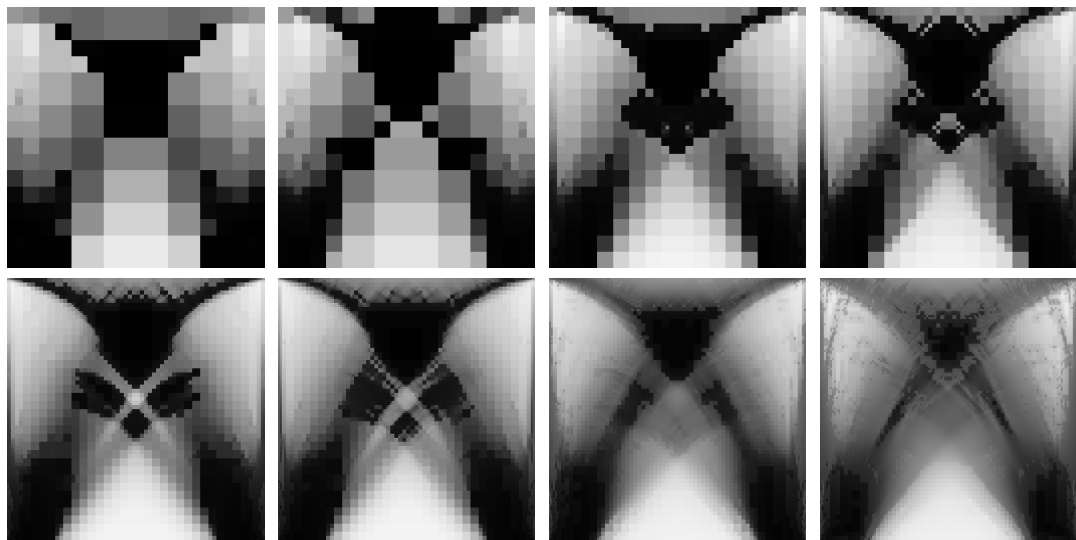


Figure 8.22.: Effective material density after 2, 3, 6, 7, 9, 10, 12, and 14 refinement steps of the adaptive scheme using model error estimation for the carrier plate scenario and rotating orthogonal rods.

scenario and microstructure model, with curved interfaces at the upper supporting structure, bulk parts in the upper center and lower corners, and a near void region in the lower center, is again recovered. When comparing to Figure 8.17, the mesh refinement however is different.

Here the upper interfaces are first formed near the central region, interfaces at the lower trusses become visible as well, and, overall, the break of symmetry is less severe. Table 8.7, which lists figures of the error estimation in detail, reveals that again the cost functional does not come close to the asymptotic value. In fact the best value after nine refinement step is still larger than in the preceding section, cf. Table 8.6. We examine the error indicators in

	$ \mathcal{M}_h $	$\sum_E \eta_E^{u^L}$	$\sum_E \eta_{\partial E}^{u^L}$	$\sum_E \frac{1}{2} \eta_E^{q^M}$	$\mathbf{J}^M$	$\frac{\sum_E \eta_E}{\mathbf{J}^M - \mathbf{J}_0^L}$
0	64	0.37190	0.21676	0.72643	2.16304	3.89684
1	100	0.10974	0.08996	0.49644	2.14281	2.29836
2	154	0.10728	0.08021	0.41047	2.02650	3.20490
3	262	0.05725	0.04534	0.35528	2.00626	2.73456
4	382	0.03040	0.03295	0.29010	1.99237	2.31847
5	598	0.02132	0.02462	0.21672	1.94141	2.58793
6	868	0.02216	0.02142	0.18847	1.93266	2.50205
7	1318	0.02034	0.02035	0.16594	1.90660	3.09896
8	2077	0.01844	0.01918	0.14089	1.90172	2.88868
9	3241	0.01852	0.02071	0.12824	1.89092	3.28367
10	5002	0.01958	0.02280	0.10735	1.89830	2.56470
11	7576	0.02195	0.02683	0.09668	1.90133	2.36862
12	11365	0.02528	0.03159	0.10013	1.91487	2.09491

Table 8.7.: Listing of important quantities obtained by the adaptive scheme using model error estimation for the carrier plate scenario and rotating orthogonal rods.

Figure 8.23. Throughout the run of the algorithm the control error indicator dominates the classical primal error estimate, cf. Table 8.7. As can be seen in Figure 8.23 it is active in regions where intermediate density is expected. This leads to the formation of interfaces toward areas of full and hardly any material, but also to even more refinement in the intermediate regions. In the first phase of the algorithm the shape thereby improves. The estimates decrease as well and the factor between estimated and real error, cf. last column of Table 8.7, stays within bounds. At some point additional structures from bulk material appear in the optimized shape. This can be seen after seven refinement steps in Figure 8.22. Initially this improves the costs and decreases the control error indicator, which reflects an averaged discrepancy between the two-scale model and an optimal shape in terms of the elastic energy density. The primal error estimates on the other hand start to increase only two steps later, due to the jumps. Later on the cost functional rises again. At this point optimization is not fully carried out anymore and the control error indicator starts to increase soon after. As before the scheme seems to suffer from numerical deficiencies.

The additionally built fine structures were already observed on uniform grids, see Figure 6.9. Their appearance indicates that the microscopic model is not able to capture a locally optimal shape. In fact the upper central part, where they first appear, is subject to shearing loads. Those require a genuine rank-2 sequential lamination construction and are less well sustained by the rotating rods microstructure, cf. Section 6.1.2.

**Remark 8.13** (Comparison of two-scale error estimation techniques). We claim that the modeling error approach is more profound with regard to optimal shapes. But, as just seen,

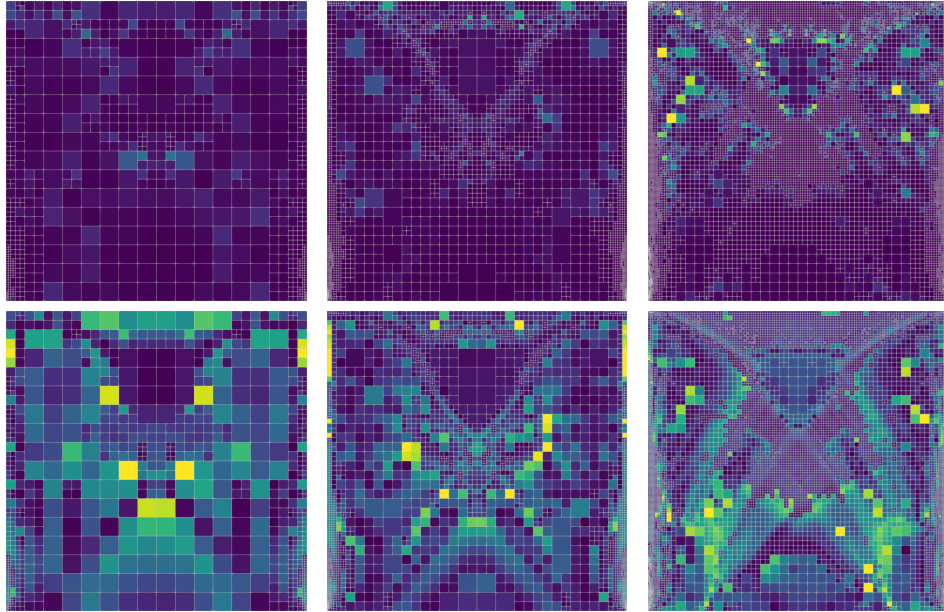



Figure 8.23.: Different terms in the modeling error estimate after 6, 9, and 12 refinement steps (left to right) for the carrier plate scenario and rotating orthogonal rods:  $\eta_E^u^L + \eta_{\delta E}^u^L$  and  $\frac{1}{2}\eta_E^q^M$  (top and bottom), visualized using color map  with consistent ranges of mapped values for each refinement step.

it does not yield better results than the straightforward application of the general error estimation in the preceding Section 8.3. This is not necessarily a shortcoming of the approach. In fact it aids in finding regions where there is a deficiency in the microscopic model. The resulting mesh refinement leads to the creation of fine-scale structures, which is the only means in the context of simplified geometric models, but undesirable in view of the two-scale approach with locally optimal microstructures. Only after that numerical difficulties impede the scheme. When comparing the spatial distribution of the error indicators in the respective figures 8.16 and 8.23, modeling error estimation seems to deliver a clearer picture, in particular with respect to separating the error due to the PDE solution and the controls. This might however also be attributed to the assessment of the control error in terms of the effective elastic energy density. It comprises all parameters of the microstructure model, in contrast to evaluating individual sensitivities as in the preceding section.

**Cantilever.** The next scenario is the cantilever. In figures 8.24, 8.25, and 8.26 we show generated meshes, visualizations of the two-scale results, and the effective material density for selected intermediate refinement steps. The adaptive scheme initially runs smoothly and familiar features of the cantilever shape are visible. Regions with full material are established at the left corners and along the upper and lower boundaries, as well as in the front where the loading attacks. Thick arcs with intermediate densities are formed in between. The microstructure aligns with the direction of the trusses and varies smoothly in between. Rather sharp interfaces emerge only at the front toward the region with full material and toward the



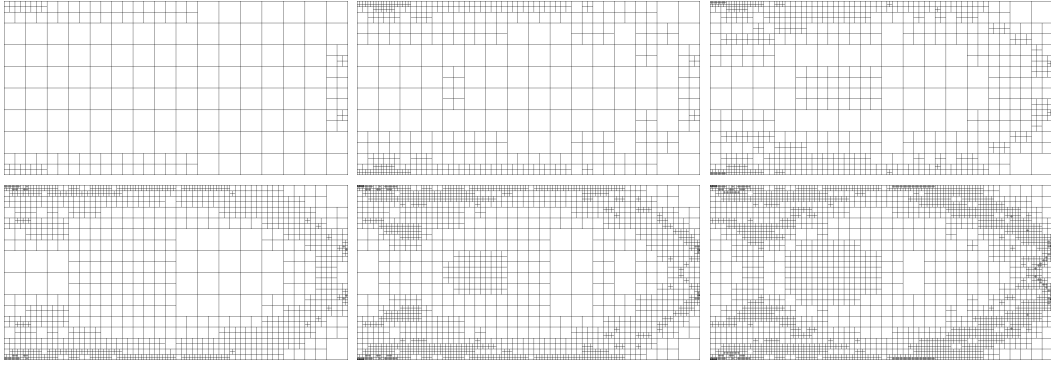


Figure 8.24.: Generated meshes after 2, 4, 5, 6, 7, and 8 refinement steps of the adaptive scheme using model error estimation for the cantilever scenario and rotating orthogonal rods.

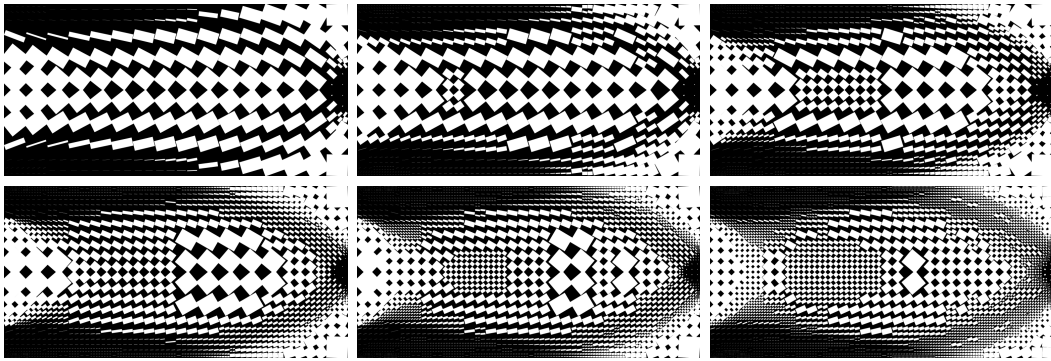


Figure 8.25.: Two-scale results after 2, 4, 5, 6, 7, and 8 refinement steps of the adaptive scheme using model error estimation for the cantilever scenario and rotating orthogonal rods.

corners where there is almost no material.

Regarding the error estimation we list details in Table 8.8 and show the spatial distribution for a selected intermediate step in Figure 8.27. As before the control error indicator is dominating throughout the run and is mainly active within regions of intermediate density. The objective functional decreases until after seven refinement steps. At this point some cells within the trusses are refined, where in the next step of the algorithm optimization is not carried out to full extent anymore, cf. Figure 8.26. As a consequence fluctuations of the effective density appear, whereas it is supposed to stay homogeneous. In the following both the costs and the error indicators start to grow. The optimal asymptotic value is not approached closely.

**Bridge.** The bridge scenario is considered next. In Figure 8.28 we show generated meshes, visualizations of the two-scale results, and the effective material density for selected intermediate refinement steps. The overall bridge shape is clearly visible. Regions with almost full material

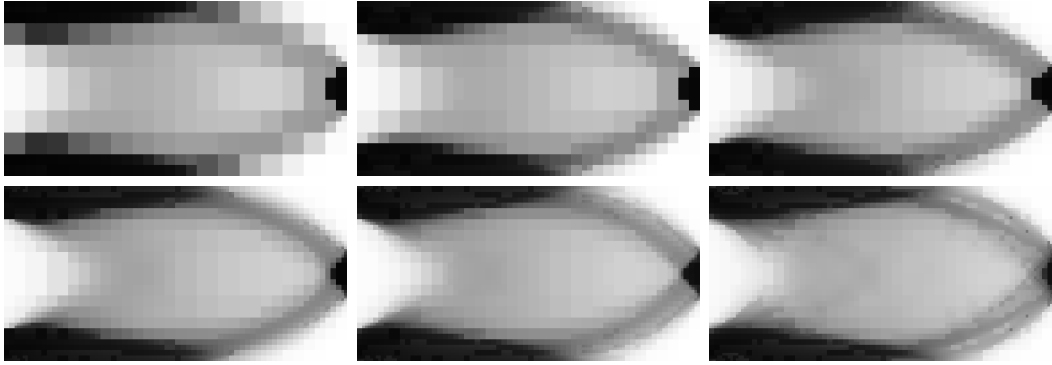


Figure 8.26.: Effective material density after 2, 4, 5, 6, 7, and 8 refinement steps of the adaptive scheme using model error estimation for the cantilever scenario and rotating orthogonal rods.

	$ \mathcal{M}_h $	$\sum_E \eta_E^{u^L}$	$\sum_E \eta_{\partial E}^{u^L}$	$\sum_E \frac{1}{2} \eta_E^{q^M}$	$\mathbf{J}^M$	$\frac{\sum_E \eta_E}{\mathbf{J}^M - \mathbf{J}_0^L}$
0	128	0.01524	0.00908	0.07064	0.24167	1.29182
1	158	0.00688	0.00452	0.05039	0.20831	1.53938
2	224	0.00434	0.00253	0.04229	0.19248	2.02236
3	362	0.00263	0.00184	0.03244	0.19132	1.59390
4	548	0.00263	0.00233	0.03040	0.18896	1.70111
5	902	0.00258	0.00275	0.02502	0.18073	2.41551
6	1508	0.00226	0.00278	0.02200	0.17729	2.96643
7	2357	0.00315	0.00356	0.01828	0.17615	3.13240
8	3593	0.00500	0.00611	0.02189	0.17761	3.68775
9	5333	0.00733	0.00909	0.02429	0.17946	3.69057

Table 8.8.: Listing of important quantities obtained by the adaptive scheme for the cantilever scenario and rotating orthogonal rods.

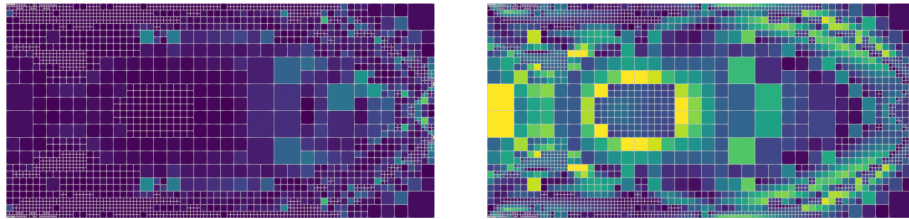



Figure 8.27.: Different terms in the modeling error estimate after 7 refinement steps for the cantilever scenario and rotating orthogonal rods:  $\eta_E^{u^L} + \eta_{\partial E}^{u^L}$  and  $\frac{1}{2} \eta_E^{q^M}$ , visualized using color map  with consistent range of mapped values.

are created where the loading acts and where the structure is fixated. Strong refinement occurs where the two types of boundary conditions meet in the lower corners. The spanned

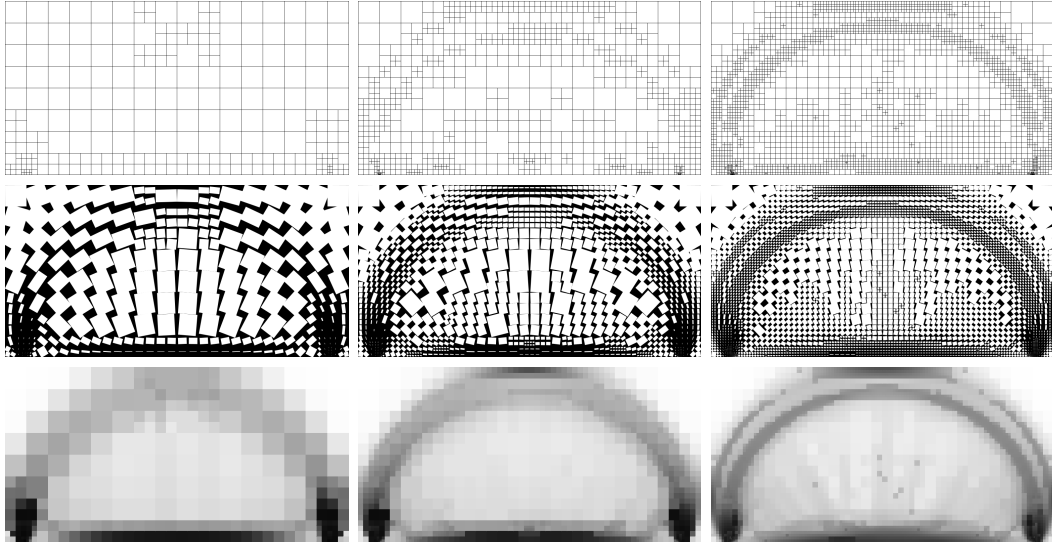


Figure 8.28.: Generated meshes, two-scale results, and effective material density after 3, 6, and 9 refinement steps for the bridge scenario and rotating orthogonal rods.

arc is of intermediate density and the microstructure within follows its path. Underneath the arc less material is used. The microstructure here depicts trusses that connect the arc to the floor. Thereby their orientation varies smoothly. In later stages of the algorithm the lower interface of the arc becomes more sharply resolved. This is different from the preceding examples, cf. figures 8.20 and 8.24. When looking at the spatial distribution of the error indicators in Figure 8.29 it becomes clear that the control error indicator is responsible. It

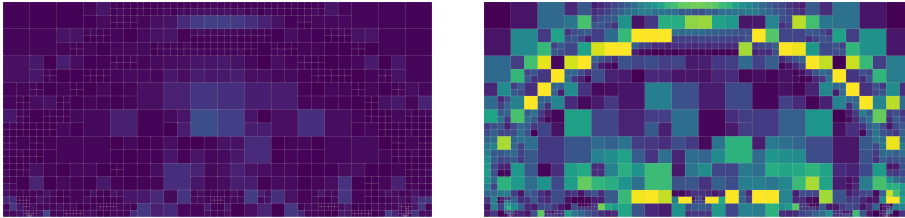



Figure 8.29.: Different terms in the modeling error estimate after 6 refinement steps for the bridge scenario and rotating orthogonal rods:  $\eta_E^{u^L} + \eta_{\partial E}^{u^L}$  and  $\frac{1}{2}\eta_E^{q^M}$ , visualized using color map  with consistent range of mapped values.

emphasized the discussed interface and the lower boundary, and is less spread out than before. This can be interpreted as a less severe deficiency of the two-scale model in this scenario. The construction can apparently better be realized by rank-1 lamination. Full details are listed in Table 8.9. The control error indicator dominates the primal indicator, which is initially high in the lower corners. A decrease in the cost functional and the indicators can be seen until after five refinement steps. Later on fluctuations in the so far homogeneous effective density appear, see Figure 8.28, and the costs and indicators rise. Again this must be attributed to

	$ \mathcal{M}_h $	$\sum_E \eta_E^u$	$\sum_E \eta_{\partial E}^u$	$\sum_E \frac{1}{2} \eta_E^q$	$\mathbf{J}^M$	$\frac{\sum_E \eta_E}{\mathbf{J}^M - \mathbf{J}_0^L}$
0	128	0.34209	0.39693	0.35527	0.92393	3.54671
1	137	0.15273	0.15309	0.38306	0.84661	3.78035
2	191	0.10004	0.11316	0.29093	0.79316	2.56143
3	263	0.05219	0.04898	0.24219	0.76323	2.86348
4	380	0.02626	0.02571	0.21399	0.74361	2.56739
5	575	0.02170	0.01965	0.22099	0.73552	1.56570
6	929	0.02097	0.02271	0.26207	0.73543	0.48351
7	1430	0.12674	0.17389	0.45120	0.85853	3.85990

Table 8.9.: Listing of important quantities obtained by the adaptive scheme for the bridge scenario and rotating orthogonal rods.

incomplete optimization. A tendency to build fine-scale structures is only seen in later steps.

**L-shaped domain.** The final scenario is the L-shaped domain. In Figure 8.30 we show generated meshes, visualizations of the two-scale results, and the effective material density for selected intermediate refinement steps. Regarding the volume distribution the overall shape is comparable to the results obtained via the sequential lamination construction, cf. Figure 8.13. The lower arc consists of nearly full material, whereas the upper part in the right quadrant is of intermediate density. Here the alignment of the microstructure can be clearly recognized, as in the bridge and cantilever scenarios before. In the lower inner part few material is used. A smoothly varying inclination of the microstructure can be seen as in the bridge scenario before. Interfaces are also visible in the generated adaptive meshes, especially toward the near void regions in the right and lower left corners. However refinement is stronger at the reentrant corner and the upper corners where different type of boundary conditions meet. In fact, the spatial distribution of the error indicators in Figure 8.31 shows that initially the primal error indicator has larger contributions than the control error indicator. In later stages the control indicator dominates, as seen before. It is active along the interfaces but also in the areas in between. Full details of the error estimation are listed in Table 8.10. The costs and indicators start to rise after eight and seven refinement steps, respectively. At this point the optimized shapes are not fully converged anymore and the mesh shows spurious overrefinement near the reentrant corner.

In conclusion a profound approach was presented that incorporates optimal shapes, realized by the sequential lamination construction, into the error estimation process. It is initially unclear if a shape resulting from a different modeling, which usually shows a different global volume distribution, is a suitable candidate for local comparisons. Yet the scheme performs well, with hardly increased computational cost. Interfaces are identified and resolved, but also homogeneous regions are refined. It was observed that this either happens where the microstructure varies smoothly or in regions where the two-scale model is actually outclassed by the superior sequential lamination technique. In the latter case fine-scale structures started to build up on the macroscale. In view of the two-scale approach this is undesired, but nevertheless the estimates aid in finding respective regions of interest.

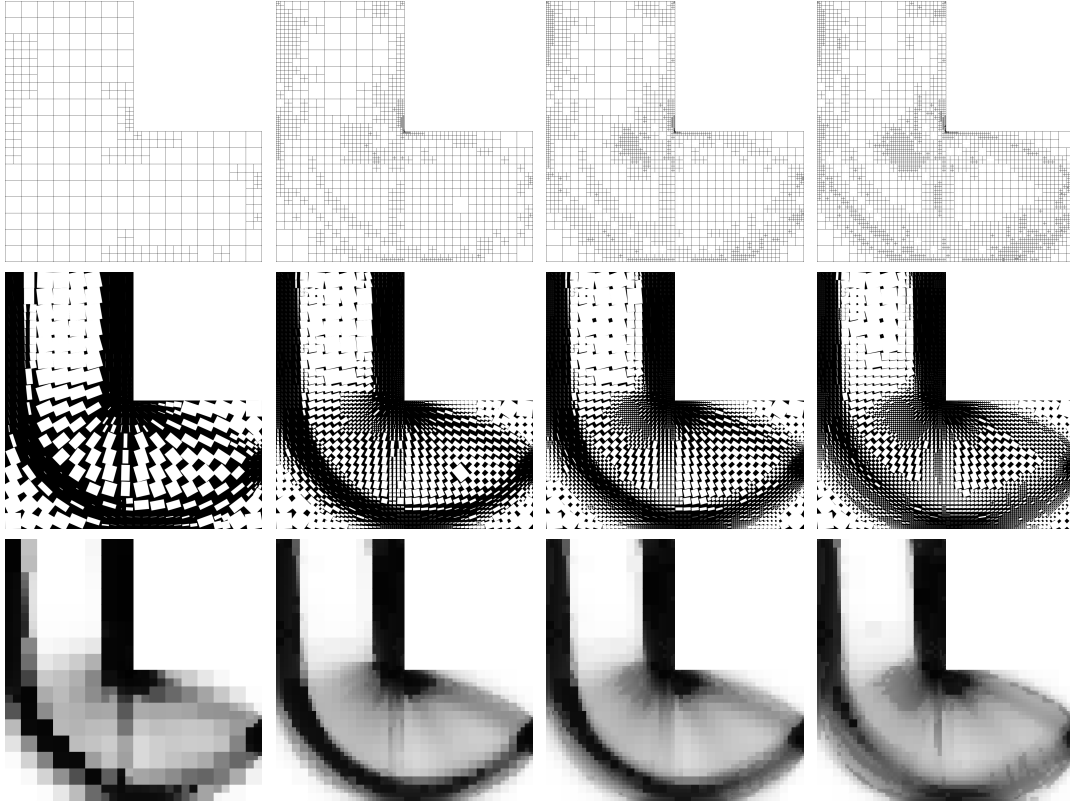


Figure 8.30.: Generated meshes, two-scale results, and effective material density after 2, 6, 7, and 8 refinement steps for the L-shaped domain and rotating orthogonal rods.

	$ \mathcal{M}_h $	$\sum_E \eta_E^{u^L}$	$\sum_E \eta_{\partial E}^{u^L}$	$\sum_E \frac{1}{2} \eta_E^{q^M}$	$\mathbf{J}^M$	$\frac{\sum_E \eta_E}{\mathbf{J}^M - \mathbf{J}_0^L}$
0	192	0.03245	0.03445	0.07295	0.28484	1.64872
1	240	0.01615	0.01706	0.05088	0.24597	1.83000
2	321	0.01020	0.01045	0.03592	0.22702	2.09511
3	474	0.00616	0.00651	0.03230	0.22132	2.11040
4	702	0.00428	0.00460	0.02644	0.21988	1.77868
5	1068	0.00248	0.00285	0.02399	0.21905	1.54039
6	1593	0.00411	0.00478	0.02138	0.21473	1.78013
7	2418	0.00471	0.00611	0.02211	0.21132	0.64246
8	3729	0.00779	0.01078	0.02916	0.21240	0.60986

Table 8.10.: Listing of important quantities obtained by the adaptive scheme for the L-shaped domain and rotating orthogonal rods.

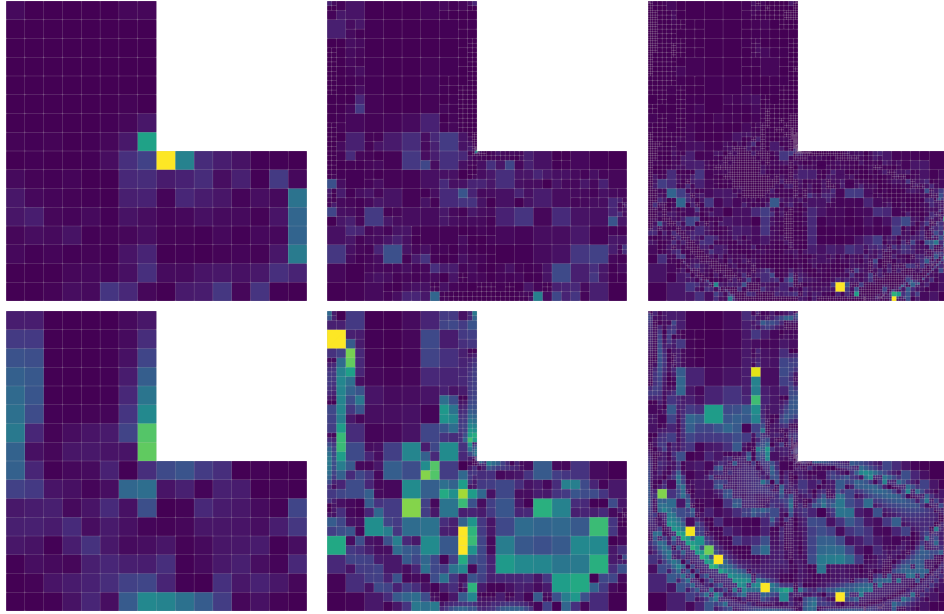



Figure 8.31.: Different terms in the modeling error estimate after 0, 4, and 8 refinement steps for the L-shaped domain and rotating orthogonal rods:  $\eta_E^u + \eta_{\partial E}^u$  and  $\frac{1}{2}\eta_E^q$ , visualized using color map  with consistent ranges of mapped values for each refinement step.

## 8.5. Conclusion

In this chapter the dual weighted residual approach was adopted to devise error estimation for the two-scale shape optimization model. It was derived on the basis of effective macroscopic elasticity tensors and could therefore directly be applied to the sequential lamination model as well. Although the considered compliance cost functional has a global nature and depends on the elasticity solution, the goal-oriented estimates provided significant benefit over the usual PDE estimates. In context of the sequential lamination model the parameter controlling the effective material density turned out crucial. Where the density changed rapidly interfaces were identified and sharply resolved. Overall the adaptive scheme performed well and robust. In context of the two-scale model parameters influencing the local volume fraction were found dominating as well. Resolution of interfaces however was less intense and refinement was observed in regions with homogeneous density as well. As an alternative approach, local comparisons to optimal sequential lamination microstructures were incorporated. The resulting modeling error estimates, expressed in terms of effective elastic energies, provided an even clearer picture. Refinement in homogeneous areas could be attributed to smoothly varying parameters, but also to regions where the simple microstructures were outclassed. The adaptive scheme initially performed well but was soon impeded by numerical issues preventing fully optimized microscopic geometries subsequently. Due to the different sizes of the cells, this could not be counteracted as in the deterministic context.

---

## CHAPTER 9

### Conclusion

---

MICROSTRUCTURES lie at the heart of this thesis. They can be observed in nature and they emerge in mathematical theory as well. Their appearance in classical solid-void-constructions is a manifestation of ill-posedness of the shape optimization problem and an associated weak convergence of the indicator function to a relaxed material density function. To make shape optimization numerically feasible, we devised a two-scale approach. The elasticity problem was formulated in a macroscopic setting, but its elastic properties stemmed from underlying locally periodic lattices on a distinct length scale, where classical shapes, made from geometrically simple perforations, were considered. Known concepts from shape and Lagrangian calculus were transferred to the two-scale setting and ultimately led to a finite dimensional constrained optimization problem.

**Discussion of results.** The devised numerical scheme was applied to synthetic benchmark, classical shape optimization, and stochastic optimization problems. From the outset the synthetic scenarios provided corner cases, where the optimized two-scale structures turned out suboptimal. As such, the method is not able to produce optimal microstructures in every situation. Instead its strength is the approximation of optimal shapes by simple structures, which besides result in realistic materials that could actually be manufactured. In practical applications the degree of underachievement is problem dependent, but the considered example showed a very small discrepancy only. Another feature is the versatile implementation, which easily allowed for ample comparisons of different models. Overall the numerical scheme turned out very robust, presumably due to the simple nature of the considered shapes. Local minima were encountered, but did not deteriorate the final outcomes significantly. Discretization of the perforations had a measurable influence, especially for geometries with non-smooth corners, but a good compromise between accuracy and efficiency was found. In the end the overall algorithmic realization proved to be efficient as well, due to extensive use of linearity and parallel computation of cell problems. An innovative extension is the storing of cell problem solutions for uniformly distributed samples of the parameter space. This could be done in a preparatory step, while the actual optimization run could make use of a lock-up table and interpolation. Hereby the performance became comparable to a single-scale simulation.

The method was applied in the context of stochastic programming and the aspired behavior was verified. In particular when telling apart the effects of the different stochastic cost functionals, the method proved very robust. Meaningful optimized results were obtained without any further intervention. The concept of stochastic dominance brought in a further perspective but also a suitable instrument to assess the performance of the two-scale materials. A single-scale benchmark shape was obtained by optimization and in the following a two-scale shape was found which was at least as well suited but required significantly less material.

Finally macroscopic grid adaptivity was added by deriving an error estimator in the two-scale context, following the dual weighted residual approach. This allowed to sharply mark out regions with fundamentally different elastic properties, as motivated by the introductory example. An application to the sequential lamination model was smooth and the obtained adaptive scheme proved efficient. In view of the considered examples, the cell count was reduced by almost two orders of magnitude when compared to uniform refinement. Also no overrefinement was observed, suggesting that the algorithm be efficient as well. When applied to two-scale shape optimization, the adaptive scheme initially worked just as well. In later stages numerical issues and incomplete optimization were encountered. Most likely they were caused by the different cell sizes in the adaptive mesh, leading to widely varying scaling of terms in the objective functional. Ultimately a direct comparison of the two-scale model to optimal materials realized by sequential lamination was incorporated into the error estimator. Due to the suboptimal shapes, the error could never reach zero, but it enabled a notion of modeling error estimation. For intermediate steps it was thereby possible to identify regions where the gap towards optimality was most prominent.

**Research perspective.** An extension of the two-scale model to *three spatial dimensions* suggests itself. Here it is important to realize that the presented theory of linearized elasticity and homogenization directly applies to the three dimensional setting. Thereby the macroscopic part of the model and the microscopic corrector problems can be set up straightforwardly. Especially the approximation (5.3) of the elastic energy density in the microstructured setting remains valid. Of course the computational complexity rises drastically but it is governed by the solving of the many cell problems and can thus be tackled using massive parallelization, thanks to the scalability.

Concerning the microscopic problem, it is important to realize that it is by no means restricted to solving full elasticity problems. Instead, any model lending itself to a good prediction of the reaction of the periodic lattice to macroscopic strains can be employed. For example in [396] a discrete *surrogate model* taking into account finitely many idealized elastic rods was used. Such an approach is computationally fast, even in a three dimensional setting. On the other hand more sophisticated models can be considered as well. In [397] a phase field approach is used. In the works by Barbarosie and Toader, as discussed in Section 5.3.3, a level set function is combined with successive insertions of small holes via the topological derivative and an additional rotation and skew of the unit cell. This brings a lot of flexibility for the shapes, but for corner cases, such as the pure shearing benchmark investigated in Section 6.1.2, the results do not necessarily improve.

On the algorithmic side, *parallelization* typically leaves room for improvement. The loop-up table approach turned out to be a powerful tool. It however suffered from the curse of dimensionality in case more than a few parameters were needed for the microstructure. In fact, the modeled microstructures turn the elasticity problem into a parametrized PDE where the elastic properties are drawn from a possibly high dimensional space. A major achievement would be a strategy allowing to select only a few instances, which are already sufficient to approximate nearby candidates. This is reminiscent of *sparse approximation* problems. For example [126] deals with higher order moments in stochastic PDEs and proves sufficient approximation capabilities for a low dimensional submanifold of the employed tensor product space of polynomials. The situation here is different as a single choice of parameters entails the solution of a microscopic PDE. In this regard, an approach based on adaptively



---

constructed sparse grids in the parameter space and hierarchical B-spline interpolation of the corresponding effective elasticity tensors has recently been presented in [399].

With regard to stochastic optimization, recent works have sufficiently shown that concepts from two-stage programming can be successfully applied to optimal control problems. In particular shape optimization had already been considered before and was extended to the two-scale setting here. Naturally further concepts like e. g. *stochastic dominance of third order* [417] or the *conditional value at risk* [348, 363] could be approached.

The introduction of error estimation made two important contributions. First, it enabled a goal-oriented and efficient adaptation of the macroscopic grid. Second, it allowed to quantify the modeling error. Just as for the macroscopic grid, the microscopic discretization could be adapted as well. While this is less common for the boundary element method used here, it is fully established for finite elements, which would be used in a microscopic phase field or level set approach. An extension of the error estimate to both scales is required, which we sketch in Appendix B.2. The estimated modeling error could be exploited to adapt the underlying type of microstructure. In an imaginable adaptive scheme a *cascade* of microstructure models with increasing complexity could be considered. It could e. g. range from single-scale, unphysical blending of elasticity tensors, as in the SIMP model, over microscopic perforations with fixed geometry, to freely evolving shapes based on phase fields and supported by microscopic grid adaptivity.



---

## APPENDIX A

### Adaptive schemes using triangular meshes

---

Before the decision was made to incorporate adaptive meshing into the QuocMesh library, a proof-of-concept study was conducted using a programming course code. Its implementation had been aimed at flexibility rather than performance. Thereby unstructured triangular grids were used and adaptivity was realized following a recursive bisection strategy. The alternating shape optimization algorithm for the sequential lamination model was implemented, as described in Section 5.5.4, with the exception of using quadratic finite elements on triangles. Also the dual weighted residual approach, as detailed in sections 8.1.1 and 8.2.2, was followed. In Figure A.1 we display obtained refined meshes and corresponding optimal density distributions for the carrier plate scenario. The results are very similar to those obtained with quadratic

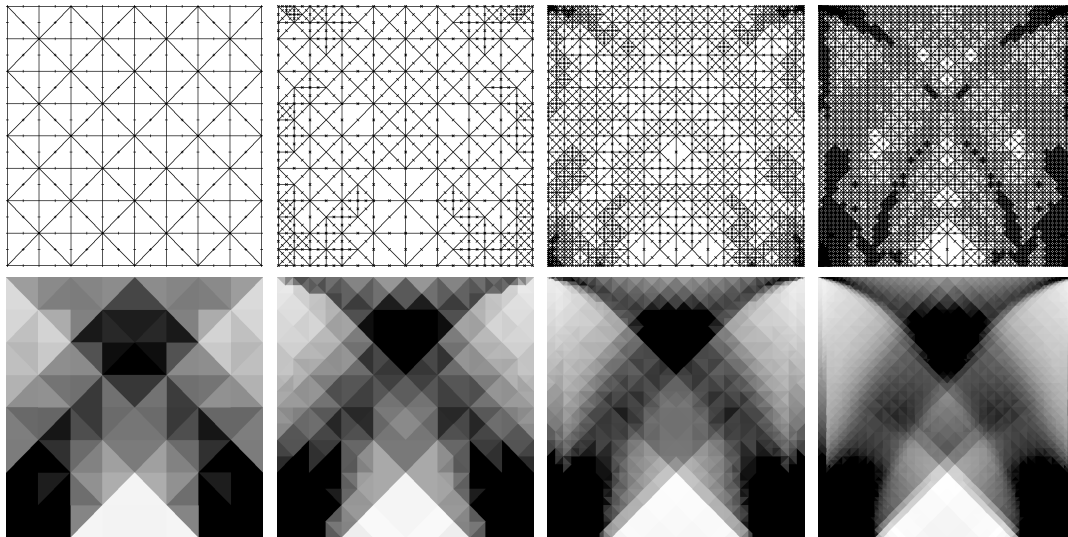


Figure A.1.: Generated meshes and optimal density in the sequential lamination model after 0, 6, 12, and 18 refinement steps of the adaptive scheme on triangular meshes for the carrier plate scenario.

mesh cells, cf. figures 8.2 and 8.3. In particular the already known macroscopic supporting structures can be recognized. Interfaces have been resolved by grid adaptivity, especially where curved outlines have been formed. An interesting observation is that the boundary of the mid lower, void area is not refined, in contrast to the situation in Figures 8.2. This is a fortuitous consequence of the isosceles right triangle shape. After some refinement steps the triangular

cells cover the area exactly, which is impossible with square cells.

The crux in this implementation was the approximation of weighting terms, as described in Section 8.2.2. Due to the unstructured mesh, an arbitrary triangle is not necessarily embedded into a super patch of uniformly shaped triangles, cf. the situation in Figure 8.1 and the sketch in Figure A.2. To begin with, we used global refinement of all triangles and let the alternating

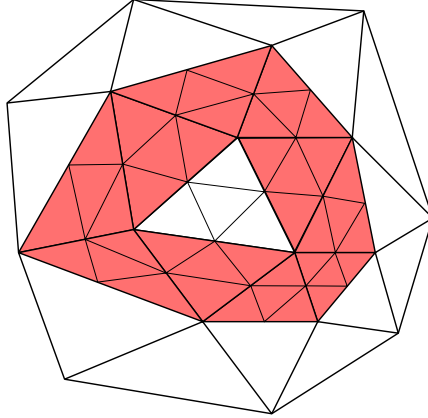


Figure A.2.: Sketch of unstructured triangular mesh. The 1-ring of the central element is highlighted in red. Thin lines indicate uniform refinement.

algorithm run again, starting from the prolonged solution on the actual grid. This allowed to compare current quantities to those obtained on a refined grid. Obviously this yields a better approximation of the weighting terms, compared to the finally used interpolation to higher order polynomials, cf. Remark 8.11. However it was computationally demanding and thus rendered the adaptive scheme infeasible. In this regard, managing the additional refinement was not an issue, as newly created elements were reused in the next steps anyway, either because they were selected for refinement or being used for computing the weighting terms again. Instead the runtime of the alternating algorithm was the limiting factor. First, it needed to be run for four times the number of degrees of freedom when compared to the actual problem. Second, it exhibited slow convergence towards the end and thus did not benefit much from the good initialization.

As an alternative strategy we tried to compute refined solutions on subsets of the global mesh only. In particular we considered 1-rings, i. e. the first layer of triangles, around an element, cf. Figure A.2. Only those elements were refined, the current solution on their outer boundary was imposed as boundary values, and the alternating algorithm was run. This could be realized in an efficient manner by refining the full mesh, assembling the required matrices only once, and using appropriate restrictions to the actual degrees of freedom when solving the subproblems. In the end, the approach turned out still too demanding. Although the subproblems were small, the slow convergence of the alternating algorithm prevailed in the overall scheme.

---

## APPENDIX B

### Variation of the two-scale functional

---

Computing variations of the introduced two-scale functionals is mostly a rephrasing of the single-scale setting presented in Section 4.1. Here we give the details.

#### B.1. Two-scale variational framework

The starting point is the two-scale elasticity problem in weak formulation

$$\begin{aligned}
 a^M(q; (u^*, \tilde{u}), (\vartheta^*, \tilde{\vartheta})) &= l(\vartheta^*) \quad \forall (\vartheta^*, \tilde{\vartheta}) \in H_{\Gamma_D}^1(D; \mathbb{R}^2) \times H_{\text{per},0}^1(\mathcal{Y}; \mathbb{R}^2) \quad \text{with} \quad (\text{B.1}) \\
 a^M(q; (u^*, \tilde{u}), (\vartheta^*, \tilde{\vartheta})) &:= \int_D \int_{\mathcal{Y}(x)} C(x, y) (\varepsilon_x[u^*] + \varepsilon_y[\tilde{u}]) : (\varepsilon_x[\vartheta^*] + \varepsilon_y[\tilde{\vartheta}]) \, dy \, dx, \\
 l(\vartheta^*) &:= \int_D f \cdot \vartheta^* \, dx + \int_{\Gamma_N} g \cdot \vartheta^* \, da(x).
 \end{aligned}$$

This is (5.6) with slightly adapted notation. For the time being, we consider an arbitrary cost functional  $\mathbf{J}^M[q; (u^*, \tilde{u})]$  depending on the solution of the two-scale elasticity problem and the parameters of the microscopic shapes. Following Section 4.1.2 we consider the Lagrangian

$$\mathcal{L}(q, (u^*, \tilde{u}), (p^*, \tilde{p})) := \mathbf{J}^M[q; (u^*, \tilde{u})] + a^M(q; (u^*, \tilde{u}), (p^*, \tilde{p})) - l(p^*). \quad (\text{B.2})$$

Computing the first variation in  $(p^*, \tilde{p})$  recovers the weak formulation of the two-scale problem (B.1), referred to as *primal* problem. The first variation in  $(u^*, \tilde{u})$  yields the two-scale *adjoint* problem

$$\mathbf{J}_{(u^*, \tilde{u})}^M[q; (u^*, \tilde{u})] (\vartheta^*, \tilde{\vartheta}) + a^M(q; (\vartheta^*, \tilde{\vartheta}), (p^*, \tilde{p})) = 0 \quad \forall (\vartheta^*, \tilde{\vartheta}). \quad (\text{B.3})$$

#### B.2. Error estimation

The error estimates derived in Chapter 8 were based on a macroscopic perspective with effective material properties stemming either from the optimal, analytical sequential lamination construction or the underlying, numerically optimized, periodic perforations. Thereby the microscopic model only entered implicitly when computing sensitivities of the macroscopic cost functional. Following Ohlberger [313] it is alternatively possible to derive an error estimate in closed form for both scales simultaneously. Starting from (B.2), the dual weighted residual approach is applied, similar to Section 8.1. The crucial point is to compute (8.1), which here reads

$$\begin{aligned}
 e_{\mathcal{L}} &= \frac{1}{2} \mathcal{L}_{(u^*, \tilde{u})}(q_h; (u_h^*, \tilde{u}_h), (p_h^*, \tilde{p}_h))(u^* - \vartheta_{u_h^*}, \tilde{u} - \vartheta_{\tilde{u}_h}) \\
 &\quad + \frac{1}{2} \mathcal{L}_{(p^*, \tilde{p})}(q_h; (u_h^*, \tilde{u}_h), (p_h^*, \tilde{p}_h))(p^* - \vartheta_{p_h^*}, \tilde{p} - \vartheta_{\tilde{p}_h}) \\
 &\quad + \frac{1}{2} \mathcal{L}_{,q}(q_h; (u_h^*, \tilde{u}_h), (p_h^*, \tilde{p}_h))(q - \vartheta_{q_h}) + \mathcal{R}
 \end{aligned} \quad (\text{B.4})$$

The second term is the primal problem (B.1), with a different test function. Using Green's first identity w. r. t.  $x$  and the macroscopic finite element partition  $\bar{\mathcal{O}} = \bigcup E$  yields

$$\begin{aligned}
 & \mathcal{L}_{,(p^*, \tilde{p})}(q_h; (u_h^*, \tilde{u}_h), (p_h^*, \tilde{p}_h))(p^* - \vartheta_{p_h^*}, \tilde{p} - \vartheta_{\tilde{p}_h}) \tag{B.5} \\
 &= \int_D \int_{\mathcal{Y}(x)} C(x, y) (\varepsilon_x[u_h^*] + \varepsilon_y[\tilde{u}_h]) : (\varepsilon_x[p^* - \vartheta_{p_h^*}] + \varepsilon_y[\tilde{p} - \vartheta_{\tilde{p}_h}]) \, dy \, dx \\
 & \quad - \int_{\Gamma_N} g \cdot (p^* - \vartheta_{p_h^*}) \, da(x) - \int_D f \cdot (p^* - \vartheta_{p_h^*}) \, dx \\
 &= - \sum_E \int_E \operatorname{div}_x \left\{ \int_{\mathcal{Y}(x)} C(x, y) (\varepsilon_x[u_h^*] + \varepsilon_y[\tilde{u}_h]) \, dy \right\} \cdot (p^* - \vartheta_{p_h^*}) \, dx \tag{I} \\
 & \quad + \sum_E \int_{\partial E} \left\{ \int_{\mathcal{Y}(x)} C(x, y) (\varepsilon_x[u_h^*] + \varepsilon_y[\tilde{u}_h]) \, dy \right\} n \cdot (p^* - \vartheta_{p_h^*}) \, da(x) \tag{II} \\
 & \quad - \sum_E \int_E f \cdot (p^* - \vartheta_{p_h^*}) \, dx \tag{III} \\
 & \quad - \sum_E \int_{\partial E \cap \Gamma_N} g \cdot (p^* - \vartheta_{p_h^*}) \, da(x) \tag{IV} \\
 & \quad + \int_D \int_{\mathcal{Y}(x)} C(x, y) (\varepsilon_x[u_h^*] + \varepsilon_y[\tilde{u}_h]) : \varepsilon_y[\tilde{p} - \vartheta_{\tilde{p}_h}] \, dy \, dx. \tag{V}
 \end{aligned}$$

By means of the results from homogenization there holds

$$\int_{\mathcal{Y}(x)} C(x, y) (\varepsilon_x[u_h^*] + \varepsilon_y[\tilde{u}_h]) \, dy = C^* \varepsilon_x[u_h^*] = \sigma_h,$$

cf. the terms on the left hand sides of (3.24) and (3.25). Thus (I) plus (III) reads

$$\sum_E \int_E (-\operatorname{div}_x \sigma_h - f) (p^* - \vartheta_{p_h^*}) \, dx,$$

and (II) plus (IV)

$$\sum_E \int_{\partial E} \sigma_h n \cdot (p^* - \vartheta_{p_h^*}) \, da(x) - \int_{\partial E \cap \Gamma_N} g \cdot (p^* - \vartheta_{p_h^*}) \, da(x).$$

These terms are the typical residual and jump discontinuity indicators on the macroscale. Term (V) contains microscopic cell problems for every macroscopic  $x \in D$ . In case the microscopic domain has a finite element partition  $\bar{\mathcal{Y}} = \bigcup Y$  as well, the expression can likewise be localized, now w. r. t.  $y$ , yielding

$$\begin{aligned}
 & - \int_D \sum_Y \int_Y \operatorname{div}_y \{C(x, y) (\varepsilon_x[u_h^*] + \varepsilon_y[\tilde{u}_h])\} \cdot (\tilde{p} - \vartheta_{\tilde{p}_h}) \, dy \, dx \\
 & + \int_D \sum_Y \int_{\partial Y} C(x, y) (\varepsilon_x[u_h^*] + \varepsilon_y[\tilde{u}_h]) n \cdot (\tilde{p} - \vartheta_{\tilde{p}_h}) \, da(y) \, dx.
 \end{aligned}$$

These terms are corresponding residual and jump discontinuity indicators on the microscale. They can be employed to steer grid adaptivity in each microscopic cell  $\mathcal{Y}(x)$ . Furthermore Ohlberger [313] suggests to use the integrated quantities over each cell as additional macroscopic indicators. They provide information on where the microscopic modeling is macroscopically underresolved. This is in the same vein as our modeling error approach in Section 8.4, which however was based on an estimated error in the objective functional and not an error in the PDE solution.

Our algorithmic realization uses the boundary element method on the microscale. In this situation (V) can be recast into the, analytically equivalent, boundary integral expression

$$\int_D \int_{\partial\mathcal{Y}(x)} C(x, y) (\varepsilon_x[u_h^*] + \varepsilon_y[\tilde{u}_h]) n \cdot (\tilde{p} - \vartheta_{\tilde{p}_h}) \, da(y),$$

cf. (3.11). Localization is then achieved by splitting the polygonal boundary  $\partial\mathcal{Y}$  into the line segments connecting the collocation points  $\xi_j \in \mathcal{N}_h$ . This is merely an example in analogy to the finite element setting. Although less popular, there is a rich theory for error estimation and adaptivity for the boundary element method as well, see e. g. the early reference [339] and the survey article [172]. The remaining terms in (B.4),  $\mathcal{L}_{,(u^*, \tilde{u})}$  and  $\mathcal{L}_{,q}$ , are problem dependent because of the included cost functional.

### B.3. Shape derivative

Computing the derivative of the cost functional w. r. t. the microscopic design parameters  $q$  in direction  $\beta$  initially leads to

$$\frac{d}{dq} \mathbf{J}^M[q; (u^*, \tilde{u})][q](\beta) = \mathbf{J}_{,q}^M[q; (u^*, \tilde{u})](\beta) + \mathbf{J}_{,(u^*, \tilde{u})}^M[q; (u^*, \tilde{u})]((u^*, \tilde{u}),_q[q](\beta)).$$

Following the steps in Section 4.1.3, the derivative of the PDE solution is eliminated using the adjoint solution of (B.3) and

$$\mathbf{J}_{,q}^M[q; (u^*, \tilde{u})](\beta) + a_{,q}^M(q; (u^*, \tilde{u}), (p^*, \tilde{p}))(\beta) - l_{,q}(p^*)(\beta) \quad (\text{B.6})$$

is obtained. In any case, the linear form contains macroscopic quantities only and hence the last term vanishes. Concerning the bilinear form  $a^M$ , the shape derivative w. r. t. the microscopic domain  $\mathcal{Y}$  has to be considered. Varying the parameters  $q$  varies the shape of the domain by virtue of the velocity field  $V[x; \beta]$  defined in (5.8). Thereby

$$\begin{aligned} & \frac{d}{dq} a^M(q; (u^*, \tilde{u}), (p^*, \tilde{p}))(\beta) = \\ & \int_D d\mathcal{Y}(x) \left( \int_{\mathcal{Y}(x)} C(x, y) (\varepsilon_x[u^*] + \varepsilon_y[\tilde{u}]) : (\varepsilon_x[p^*] + \varepsilon_y[\tilde{p}]) \, dy \right) (V[x; \beta]) \, dx = \\ & \int_D \int_{\partial\mathcal{Y}(x)} (V[x; \beta] \cdot n(y)) C(x, y) (\varepsilon_x[u^*] + \varepsilon_y[\tilde{u}]) : (\varepsilon_x[p^*] + \varepsilon_y[\tilde{p}]) \, dy \, dx \end{aligned}$$

is obtained, using Lemma 4.3.

## B.4. Application to the compliance functional

In Section 5.2.2 a variant of the compliance cost functional, cf. (4.12), was chosen, namely

$$-2 \mathbf{J}^M[q; (u^*, \tilde{u})] = -a^M(q; (u^*, \tilde{u}), (u^*, \tilde{u})) + 2l(u^*).$$

### B.4.1. Adjoint problem

For the choice of the compliance functional, the adjoint problem (B.3) reads

$$-2 a^M(q; (u^*, \tilde{u}), (\vartheta^*, \tilde{\vartheta})) + 2l(\vartheta^*) + a^M(q; (\vartheta^*, \tilde{\vartheta}), (p^*, \tilde{p})) = 0 \quad \forall (\vartheta^*, \tilde{\vartheta}).$$

Using the primal problem (B.1), this simplifies to

$$a^M(q; (\vartheta^*, \tilde{\vartheta}), (p^*, \tilde{p})) = 0 \quad \forall (\vartheta^*, \tilde{\vartheta}),$$

from which the trivial solution  $(p^*, \tilde{p}) = (0, 0)$  follows.

### B.4.2. Error estimates

Due to the vanishing adjoint solution, the Lagrangian (B.2) simplifies to

$$\mathcal{L}(q, (u^*, \tilde{u})) = -2 \mathbf{J}^M[q; (u^*, \tilde{u})].$$

To compute the error representation (B.4) there holds

$$\begin{aligned} \mathcal{L}_{,(u^*, \tilde{u})}(q_h; (u_h^*, \tilde{u}_h))(u^* - \vartheta_{u_h^*}, \tilde{u} - \vartheta_{\tilde{u}_h}) = \\ -2 (a^M(q; (u_h^*, \tilde{u}_h), (u^* - \vartheta_{u_h^*}, \tilde{u} - \vartheta_{\tilde{u}_h})) - l(u^* - \vartheta_{u_h^*})), \end{aligned}$$

which equals (B.5), except for the factor  $-2$  and the different test functions here. The error indicators derived above therefore almost coincide with those in (8.2). Furthermore there is

$$\mathcal{L}_{,q}(q_h; (u_h^*, \tilde{u}_h))(q - \vartheta_{q_h}) = (-a^M(q; (u_h^*, \tilde{u}_h), (u_h^*, \tilde{u}_h)) + 2l(u^*))_{,q} (q - \vartheta_{q_h}),$$

as handled for (8.4).

### B.4.3. Shape derivative

The derivative w. r. t. the microscopic design parameters (B.6) becomes

$$\begin{aligned} (-a^M(q; (u^*, \tilde{u}), (u^*, \tilde{u})) + 2l(u^*))_{,q}(\beta) = -a^M_{,q}(q; (u^*, \tilde{u}), (u^*, \tilde{u}))(\beta) = \\ - \int_D \int_{\partial \mathcal{Y}(x)} (V[x; \beta] \cdot n(y)) C(x, y) (\varepsilon_x[u^*] + \varepsilon_y[\tilde{u}]) : (\varepsilon_x[u^*] + \varepsilon_y[\tilde{u}]) \, dy \, dx, \end{aligned}$$

cf. (5.9).



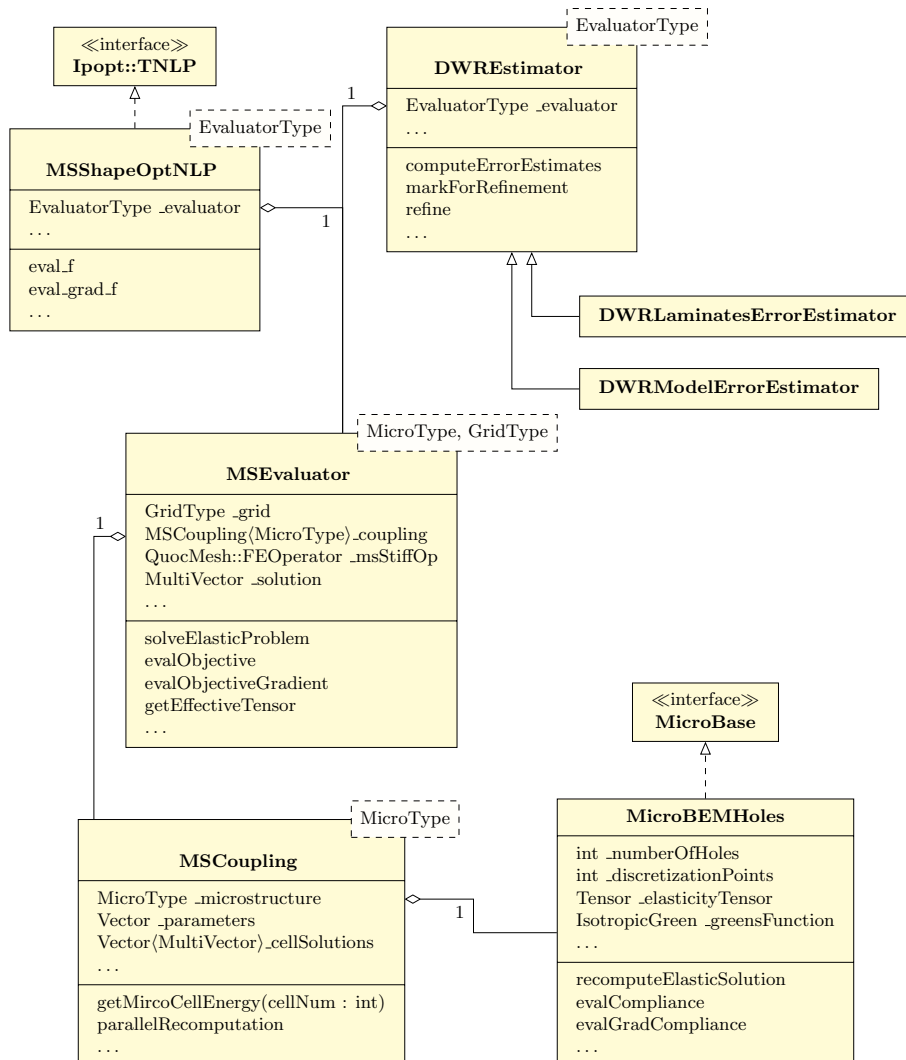
---

## APPENDIX C

### Software design

---

In the following a UML (*unified modeling language*) class diagram containing the most important building blocks of the C++ implementation for the simulation, optimization, and error estimation of the two-scale scheme is shown.





---

## Acknowledgements

---

I would like to express my personal gratitude to Prof. Dr. Martin Rumpf for giving me the opportunity to freely explore and develop the two-scale shape optimization framework, for continuously facilitating my work by giving key advice and providing resources of any kind, and for demonstrating a whole lot of patience.

I would further like to highlight the warm and productive atmosphere at the Hausdorff Center for Mathematics I could witness. I enjoyed the community, the international flair, the open doors, and the open-minded and enthusiastic attitude of my colleagues.

Financial support was provided by the German Research Foundation (DFG) through Priority Programme 1253 – *Optimization with Partial Differential Equations* and the Collaborative Research Centre 1060 – *The Mathematics of Emergent Effects*, which I highly appreciate.

Finally I would like to acknowledge the time and effort that so many individuals have put into developing freely available software. This work was carried out using solely open source software, such as Linux based operating systems and their tools, the GNU compiler collection, the Latex typesetting system and dozens of sophisticated packages, the GNU image manipulation program, the Inkscape vector graphics editor, the ParaView visualization software, and the Mozilla Firefox web browser, to name but a few. The importance of open access to knowledge and tools in research should never be underestimated.



---

## Bibliography

---

- [1] A. Abdulle and A. Nonnenmacher. “Adaptive finite element heterogeneous multiscale method for homogenization problems.” In: *Computer Methods in Applied Mechanics and Engineering* 200.37 (2011). Special Issue on Modeling Error Estimation and Adaptive Modeling, pp. 2710–2726. DOI: [10.1016/j.cma.2010.06.012](https://doi.org/10.1016/j.cma.2010.06.012) (cit. on p. 26).
- [2] A. Abdulle. “On A Priori Error Analysis of Fully Discrete Heterogeneous Multiscale FEM.” In: *Multiscale Modeling & Simulation* 4.2 (2005), pp. 447–459. DOI: [10.1137/040607137](https://doi.org/10.1137/040607137) (cit. on pp. 23, 26, 80, 81).
- [3] A. Abdulle. “Analysis Of A Heterogeneous Multiscale FEM For Problems In Elasticity.” In: *Mathematical Models and Methods in Applied Sciences* 16.04 (2006), pp. 615–635. DOI: [10.1142/S0218202506001285](https://doi.org/10.1142/S0218202506001285) (cit. on pp. 23, 81).
- [4] A. Abdulle and A. Nonnenmacher. “A posteriori error estimates in quantities of interest for the finite element heterogeneous multiscale method.” In: *Numerical Methods for Partial Differential Equations* 29.5 (2013), pp. 1629–1656. DOI: [10.1002/num.21769](https://doi.org/10.1002/num.21769) (cit. on pp. 26, 149).
- [5] A. Abdulle and C. Schwab. “Heterogeneous Multiscale FEM for Diffusion Problems on Rough Surfaces.” In: *Multiscale Modeling & Simulation* 3.1 (2005), pp. 195–220. DOI: [10.1137/030600771](https://doi.org/10.1137/030600771) (cit. on p. 81).
- [6] K. Abe, S. Kazama, and K. Koro. “A boundary element approach for topology optimization problem using the level set method.” In: *Communications in Numerical Methods in Engineering* 23 (2007), pp. 405–416. DOI: [10.1002/cnm.919](https://doi.org/10.1002/cnm.919) (cit. on p. 13).
- [7] D. Adalsteinsson and J. A. Sethian. “A fast level set method for propagating interfaces.” In: *Journal of Computational Physics* 118.2 (1995), pp. 269–277 (cit. on p. 13).
- [8] M. Ainsworth and J. T. Oden. *A posteriori Error Estimation in finite element analysis*. Wiley & Sons, 2000 (cit. on pp. 23, 27, 140).
- [9] M. Ainsworth and R. Rankin. “Guaranteed computable bounds on quantities of interest in finite element computations.” In: *International Journal for Numerical Methods in Engineering* 89.13 (2012), pp. 1605–1634. DOI: [doi.org/10.1002/nme.3276](https://doi.org/doi.org/10.1002/nme.3276) (cit. on pp. 25, 27).
- [10] J. Alexandersen and B. S. Lazarov. “Topology optimisation of manufacturable microstructural details without length scale separation using a spectral coarse basis preconditioner.” In: *Computer Methods in Applied Mechanics and Engineering* 290 (2015), pp. 156–182. DOI: [10.1016/j.cma.2015.02.028](https://doi.org/10.1016/j.cma.2015.02.028) (cit. on p. 29).
- [11] G. Allaire and S. Aubry. “On optimal microstructures for a plane shape optimization problem.” In: *Structural optimization* 17.2 (1999), pp. 86–94. DOI: [10.1007/BF01195933](https://doi.org/10.1007/BF01195933) (cit. on pp. 65, 68).

- [12] G. Allaire, E. Bonnetier, G. Francfort, and F. Jouve. “Shape Optimization by the Homogenization Method.” In: *Numerische Mathematik* 76 (1997), pp. 27–68 (cit. on pp. 17, 18, 28, 60, 61, 64, 65, 88, 89, 142).
- [13] G. Allaire and F. Jouve. “A level-set method for vibration and multiple loads structural optimization.” In: *Comput. Methods Appl. Mech. Engrg.* 194.30-33 (2005), pp. 3269–3290 (cit. on p. 28).
- [14] G. Allaire, F. Jouve, and H. Maillot. “Topology Optimization for Minimum Stress Design with the Homogenization Method.” In: *Struct Multidisc Optim* 28 (2004), pp. 87–98 (cit. on p. 17).
- [15] G. Allaire and R. V. Kohn. “Optimal design for minimum weight and compliance in plane stress using extremal microstructures.” In: *European J. Mech. A Solids* 12.6 (1993), pp. 839–878 (cit. on pp. 17, 61–65, 68).
- [16] G. Allaire. “Homogenization and two-scale convergence.” In: *SIAM J. Math. Anal.* 23.6 (1992), pp. 1482–1518. DOI: [10.1137/0523084](https://doi.org/10.1137/0523084) (cit. on pp. 44, 45).
- [17] G. Allaire. “Explicit lamination parameters for three-dimensional shape optimization.” In: *Control and Cybernetics* 23.3 (1994), pp. 309–326 (cit. on pp. 17, 65).
- [18] G. Allaire. *Shape optimization by the homogenization method*. Vol. 146. Applied Mathematical Sciences. New York: Springer-Verlag, 2002 (cit. on pp. 9, 62).
- [19] G. Allaire, S. Aubry, and F. Jouve. “Shape Optimization with General Objective Functions Using Partial Relaxation.” In: *Topology Optimization of Structures and Composite Continua*. Ed. by G. Rozvany and N. Olhoff. Vol. 7. NATO Science Series II: Mathematics, Physics and Chemistry. Kluwer Academic Publishers, 2000, pp. 239–249 (cit. on p. 17).
- [20] G. Allaire, S. Aubry, and F. Jouve. “Eigenfrequency optimization in optimal design.” In: *Computer Methods in Applied Mechanics and Engineering* 190.28 (2001), pp. 3565–3579. DOI: [10.1016/S0045-7825\(00\)00284-X](https://doi.org/10.1016/S0045-7825(00)00284-X) (cit. on p. 17).
- [21] G. Allaire, Z. Belhachmi, and F. Jouve. “The homogenization method for topology and shape optimization. Single and multiple loads case.” In: *Revue Européenne des Éléments Finis* 5.5-6 (1996), pp. 649–672. DOI: [10.1080/12506559.1996.10511241](https://doi.org/10.1080/12506559.1996.10511241) (cit. on p. 17).
- [22] G. Allaire and R. Brizzi. “A Multiscale Finite Element Method for Numerical Homogenization.” In: *Multiscale Modeling and Simulation* 4.3 (2005), pp. 790–812 (cit. on p. 22).
- [23] G. Allaire and C. Dapogny. “A linearized approach to worst-case design in parametric and geometric shape optimization.” In: *Math. Models Methods Appl. Sci.* 24.11 (2014), pp. 2199–2257. DOI: [10.1142/S0218202514500195](https://doi.org/10.1142/S0218202514500195) (cit. on p. 30).
- [24] G. Allaire and C. Dapogny. “A deterministic approximation method in shape optimization under random uncertainties.” In: *Journal of computational mathematics* 1 (2015), pp. 83–143. URL: [http://www.numdam.org/item/SMAI-JCM\\_2015\\_\\_1\\_\\_83\\_0](http://www.numdam.org/item/SMAI-JCM_2015__1__83_0) (cit. on p. 30).

- 
- [25] G. Allaire, P. Geoffroy-Donders, and O. Pantz. “Topology optimization of modulated and oriented periodic microstructures by the homogenization method.” en. In: *Computers & Mathematics with Applications* 78.7 (2019), pp. 2197–2229. DOI: [10.1016/j.camwa.2018.08.007](https://doi.org/10.1016/j.camwa.2018.08.007) (cit. on p. 19).
- [26] G. Allaire, F. de Gournay, F. Jouve, and A.-M. Toader. “Structural optimization using topological and shape sensitivity via a level set method.” eng. In: *Control and Cybernetics* 34.1 (2005), pp. 59–80. URL: <http://eudml.org/doc/209353> (cit. on p. 14).
- [27] G. Allaire, F. Jouve, and A.-M. Toader. “A level-set method for shape optimization.” In: *C. R. Acad. Sci. Paris, Série I* 334 (2002), pp. 1125–1130 (cit. on p. 13).
- [28] G. Allaire, F. Jouve, and A.-M. Toader. “Structural optimization using sensitivity analysis and a level-set method.” In: *Journal of computational physics* 194 (2004), pp. 363–393 (cit. on pp. 13, 14).
- [29] G. Allaire and R. V. Kohn. “Explicit optimal bounds on the elastic energy of a two-phase composite in two space dimensions.” In: *Quart. Appl. Math.* 51.4 (1993), pp. 675–699 (cit. on pp. 17, 63).
- [30] G. Allaire and R. V. Kohn. “Optimal bounds on the effective behavior of a mixture of two well-ordered elastic materials.” In: *Quart. Appl. Math.* 51.4 (1993), pp. 643–674 (cit. on pp. 17, 63–65).
- [31] G. Allaire and F. Murat. “Homogenization of the Neumann problem with nonisolated holes.” English. In: *Asymptotic Anal.* 7.2 (1993), pp. 81–95 (cit. on p. 46).
- [32] L. Ambrosio and G. Buttazzo. “An optimal design problem with perimeter penalization.” In: *Calculus of Variations and Partial Differential Equations* 1 (1993), pp. 55–69 (cit. on p. 10).
- [33] S. Amstutz, S. M. Giusti, A. A. Novotny, and E. A. de Souza Neto. “Topological derivative for multi-scale linear elasticity models applied to the synthesis of microstructures.” In: *International Journal for Numerical Methods in Engineering* 84.6 (2010), pp. 733–756. DOI: [10.1002/nme.2922](https://doi.org/10.1002/nme.2922) (cit. on p. 14).
- [34] S. Amstutz and H. Andrä. “A new algorithm for topology optimization using a level-set method.” In: *J. Comp. Phys.* 216 (2006), pp. 573–588 (cit. on pp. 14, 29).
- [35] S. Amstutz and M. Ciligot-Travain. “A Notion of Compliance Robustness in Topology Optimization.” In: *ESAIM: COCV* (2015). DOI: [10.1051/cocv/2014066](https://doi.org/10.1051/cocv/2014066) (cit. on p. 29).
- [36] M. Avellaneda and G. Milton. “Bounds on the effective elasticity tensor of composites based on two point correlations.” In: *Proceeding of the ASME Energy Technology Conference*. Ed. by D. Hui and T. Kozic. Vol. 24. American Society of Mechanical Engineers, 1989, pp. 89–93 (cit. on pp. 63, 66).
- [37] M. Avellaneda. “Optimal bounds and microgeometries for elastic two-phase composites.” In: *SIAM J. Appl. Math.* 47.6 (1987), pp. 1216–1228. DOI: [10.1137/0147082](https://doi.org/10.1137/0147082) (cit. on pp. 28, 63–66).

- [38] J.-F. Babadjian and M. Barchiesi. “A variational approach to the local character of G-closure: the convex case.” In: *Annales de l’Institut Henri Poincaré (C) Non Linear Analysis* 26.2 (2009), pp. 351–373. DOI: [10.1016/j.anihpc.2007.08.002](https://doi.org/10.1016/j.anihpc.2007.08.002) (cit. on p. 68).
- [39] I. Babuška and A. Miller. “The post-processing approach in the finite element method - Part 3: A posteriori error estimates and adaptive mesh selection.” In: *International Journal for Numerical Methods in Engineering* 20.12 (1984), pp. 2311–2324. DOI: [10.1002/nme.1620201211](https://doi.org/10.1002/nme.1620201211) (cit. on p. 25).
- [40] I. Babuška and W. C. Rheinboldt. “A-posteriori error estimates for the Finite Element method.” In: *International Journal for Numerical Methods in Engineering* 12.10 (1978), pp. 1597–1615. DOI: [10.1002/nme.1620121010](https://doi.org/10.1002/nme.1620121010) (cit. on p. 24).
- [41] I. Babuška and W. C. Rheinboldt. “Error estimates for adaptive finite element computations.” In: *SIAM J. Numer. Anal.* 15.4 (1978), pp. 736–754 (cit. on p. 24).
- [42] I. Babuška and C. Schwab. “A Posteriori Error Estimation for Hierarchic Models of Elliptic Boundary Value Problems on Thin Domains.” In: *SIAM Journal on Numerical Analysis* 33.1 (1996), pp. 221–246. DOI: [10.1137/0733013](https://doi.org/10.1137/0733013) (cit. on p. 25).
- [43] I. Babuška, T. Strouboulis, K. Copps, S. K. Gangaraj, and C. Upadhyay. *A-posteriori Error Estimation for Finite Element and Generalized Finite Element Method*. Tech. rep. TICAM Report 98-01. The University of Texas at Austin, 1998, pp. 1–41 (cit. on p. 25).
- [44] I. Babuška. “Homogenization and its Application. Mathematical and Computational Problems.” In: *Numerical Solution of Partial Differential Equations—III*. Ed. by B. Hubbard. Academic Press, 1976, pp. 89–116. DOI: [10.1016/B978-0-12-358503-5.50009-9](https://doi.org/10.1016/B978-0-12-358503-5.50009-9) (cit. on p. 22).
- [45] I. Babuška. “Solution of Interface Problems by Homgenization I.” In: *SIAM Journal on Mathematical Analysis* 7.5 (1976), pp. 603–634 (cit. on p. 16).
- [46] I. Babuška. “Solution of Interface Problems by Homgenization II.” In: *SIAM Journal on Mathematical Analysis* 7.5 (1976), pp. 635–645 (cit. on p. 16).
- [47] I. Babuška. “Solution of Interface Problems by Homgenization III.” In: *SIAM Journal on Mathematical Analysis* 8.6 (1977), pp. 923–937 (cit. on p. 16).
- [48] N. S. Bakhvalov and G. P. Panasenko. *Homogenisation: averaging processes in periodic media ; mathematical problems in the mechanics of composite materials*. Mathematics and its applications : Soviet series ; 36. Dordrecht u.a.: Kluwer, 1989 (cit. on p. 11).
- [49] J. M. Ball and R. D. James. “Fine phase mixtures as minimizers of energy.” In: *Arch. Ration. Mech. Anal.* 100 (1987), pp. 13–52 (cit. on p. 66).
- [50] W. Bangerth and R. Rannacher. *Adaptive Finite Element Methods for Differential Equations*. Lectures in Mathematics. Birkhäuser, 2003 (cit. on p. 25).
- [51] N. V. Banichuk. “Minimax approach to structural optimization problems.” In: *Journal of Optimization Theory and Applications* 20.1 (1976), pp. 111–127. DOI: [10.1007/BF00933350](https://doi.org/10.1007/BF00933350) (cit. on p. 28).
- [52] N. V. Banichuk. *Problems and Methods of Optimal Structural Design*. Ed. by E. J. Haug. Mathematical Concepts and Methods in Science and Engineering. Springer New York, 1983 (cit. on p. 9).



- 
- [53] N. V. Banichuk, F. J. Barthold, A. Falk, and E. Stein. “Mesh refinement for shape optimization.” In: *Structural optimization* 9.1 (1995), pp. 46–51. DOI: [10.1007/BF01742644](https://doi.org/10.1007/BF01742644) (cit. on p. 26).
- [54] N. V. Banichuk and P. Neittaanmäki. “On Structural Optimization with Incomplete Information.” In: *Mechanics Based Design of Structures and Machines* 35 (2007), pp. 75–95. DOI: [10.1080/15397730601184626](https://doi.org/10.1080/15397730601184626) (cit. on pp. 28, 29).
- [55] R. E. Bank and A. Weiser. “Some A Posteriori Error Estimators for Elliptic Partial Differential Equations.” In: *Mathematics of Computation* 44.170 (1985), pp. 283–301 (cit. on p. 24).
- [56] C. Barbarosie. “Shape optimization of periodic structures.” English. In: *Computational Mechanics* 30.3 (2003), pp. 235–246. DOI: [10.1007/s00466-002-0382-3](https://doi.org/10.1007/s00466-002-0382-3) (cit. on p. 20).
- [57] C. Barbarosie, S. Lopes, and A.-M. Toader. “A gradient-type algorithm for constrained optimization with applications to multi-objective optimization of auxetic materials.” 2017. URL: <https://arxiv.org/abs/1711.04863> (cit. on p. 81).
- [58] C. Barbarosie and S. Lopes. “A generalized notion of compliance.” In: *Comptes Rendus Mécanique* 339.10 (2011), pp. 641–648. DOI: [10.1016/j.crme.2011.07.002](https://doi.org/10.1016/j.crme.2011.07.002) (cit. on p. 58).
- [59] C. Barbarosie and A.-M. Toader. “Shape and topology optimization for periodic problems. I. The shape and the topological derivative.” In: *Struct. Multidiscip. Optim.* 40.1-6 (2010), pp. 381–391. DOI: [10.1007/s00158-009-0378-0](https://doi.org/10.1007/s00158-009-0378-0) (cit. on pp. 20, 79, 81, 82, 178).
- [60] C. Barbarosie and A.-M. Toader. “Shape and topology optimization for periodic problems. II. Optimization algorithm and numerical examples.” In: *Struct. Multidiscip. Optim.* 40.1-6 (2010), pp. 393–408. DOI: [10.1007/s00158-009-0377-1](https://doi.org/10.1007/s00158-009-0377-1) (cit. on pp. 13, 14, 20, 81, 90, 101, 102).
- [61] C. Barbarosie and A.-M. Toader. “Optimization of Bodies with Locally Periodic Microstructure.” In: *Mechanics of Advanced Materials and Structures* 19.4 (2012), pp. 290–301. DOI: [10.1080/15376494.2011.642939](https://doi.org/10.1080/15376494.2011.642939) (cit. on pp. 20, 79, 81).
- [62] C. Barbarosie and A.-M. Toader. “Optimization of bodies with locally periodic microstructure by varying the periodicity pattern.” In: *Netw. Heterog. Media* 9.3 (2014), pp. 433–451. DOI: [10.3934/nhm.2014.9.433](https://doi.org/10.3934/nhm.2014.9.433) (cit. on p. 82).
- [63] S. Bartels and C. Carstensen. “A convergent adaptive finite element method for an optimal design problem.” In: *Numer. Math.* 108.3 (2008), pp. 359–385. DOI: [10.1007/s00211-007-0122-x](https://doi.org/10.1007/s00211-007-0122-x) (cit. on p. 27).
- [64] M. Bebendorf. *Hierarchical Matrices: A Means to Efficiently Solve Elliptic Boundary Value Problems*. Vol. 63. Lecture Notes in Computational Science and Engineering (LNCSE). ISBN 978-3-540-77146-3. Springer-Verlag, 2008 (cit. on p. 91).
- [65] R. Becker, H. Kapp, and R. Rannacher. “Adaptive Finite Element Methods for Optimal Control of Partial Differential Equations: Basic Concept.” In: *SIAM J. Control Optim.* 39.1 (2000), pp. 113–132 (cit. on pp. 25, 137).

- [66] R. Becker and R. Rannacher. “A feed-back approach to error control in finite element methods: Basic analysis and examples.” In: *Computational Mechanics* 5 (1997), pp. 434–446 (cit. on pp. 25, 145).
- [67] R. Becker and R. Rannacher. “An optimal control approach to a posteriori error estimation in finite element methods.” In: *Acta Numer.* 10 (2001), pp. 1–102. DOI: [10.1017/S0962492901000010](https://doi.org/10.1017/S0962492901000010) (cit. on p. 25).
- [68] T. Belytschko, S. P. Xiao, and C. Parimi. “Topology optimization with implicit functions and regularization.” In: *International Journal for Numerical Methods in Engineering* 57.8 (2003), pp. 1177–1196. DOI: [10.1002/nme.824](https://doi.org/10.1002/nme.824) (cit. on p. 15).
- [69] A. Ben-Tal, M. Kočvara, A. Nemirovski, and J. Zowe. “Free material design via semidefinite programming: the multiload case with contact conditions.” In: *SIAM J. Optim.* 9 (1999), pp. 813–832 (cit. on p. 29).
- [70] A. Ben-Tal and A. Nemirovski. “Robust Convex Optimization.” In: *Mathematics of Operations Research* 23.4 (1998), pp. 769–805. DOI: [10.1287/moor.23.4.769](https://doi.org/10.1287/moor.23.4.769) (cit. on p. 27).
- [71] A. Ben-Tal, L. El-Ghaoui, and A. Nemirovski. *Robust Optimization*. Princeton and Oxford: Princeton University Press, 2009 (cit. on p. 27).
- [72] A. Ben-Tal and A. Nemirovski. “Robust optimization—methodology and applications.” In: *Math. Program.* 92.3, Ser. B (2002). ISMP 2000, Part 2 (Atlanta, GA), pp. 453–480. DOI: [10.1007/s101070100286](https://doi.org/10.1007/s101070100286) (cit. on p. 27).
- [73] M. P. Bendsøe. “Optimal shape design as a material distribution problem.” In: *Structural and Multidisciplinary Optimization* 1.4 (1989), pp. 193–202. DOI: [10.1007/BF01650949](https://doi.org/10.1007/BF01650949) (cit. on pp. 16, 19).
- [74] M. P. Bendsøe, J. M. Guedes, R. B. Haber, P. Pedersen, and J. E. Taylor. “An Analytical Model to Predict Optimal Material Properties in the Context of Optimal Structural Design.” In: *Journal of Applied Mechanics* 61.4 (1994), pp. 930–937. DOI: [10.1115/1.2901581](https://doi.org/10.1115/1.2901581) (cit. on p. 20).
- [75] M. P. Bendsøe and O. Sigmund. “Material interpolation schemes in topology optimization.” English. In: *Archive of Applied Mechanics* 69.9-10 (1999), pp. 635–654. DOI: [10.1007/s004190050248](https://doi.org/10.1007/s004190050248) (cit. on p. 19).
- [76] M. P. Bendsøe. “On Obtaining a Solution to Optimization Problems for Solid, Elastic Plates by Restriction of the Design Space.” In: *Journal of Structural Mechanics* 11.4 (1983), pp. 501–521. DOI: [10.1080/03601218308907455](https://doi.org/10.1080/03601218308907455) (cit. on p. 12).
- [77] M. P. Bendsøe, A. R. Díaz, and N. Kikuchi. “Topology and generalized layout optimization of elastic structures.” In: *Topology design of structures (Sesimbra, 1992)*. Vol. 227. NATO Adv. Sci. Inst. Ser. E Appl. Sci. Dordrecht: Kluwer Acad. Publ., 1993, pp. 159–205 (cit. on pp. 16, 18, 19).
- [78] M. P. Bendsøe and N. Kikuchi. “Generating optimal topologies in structural design using a homogenization method.” In: *Computer Methods in Applied Mechanics and Engineering* 71.2 (1988), pp. 197–224. DOI: [http://dx.doi.org/10.1016/0045-7825\(88\)90086-2](https://doi.org/http://dx.doi.org/10.1016/0045-7825(88)90086-2) (cit. on pp. 16–19, 21).

- 
- [79] M. P. Bendsøe and O. Sigmund. *Topology Optimization – Theory, Methods, and Applications*. 2nd ed. Springer Berlin Heidelberg, 2004, pp. XIV, 370. DOI: [10.1007/978-3-662-05086-6](https://doi.org/10.1007/978-3-662-05086-6) (cit. on pp. 9, 19, 86).
- [80] M. P. Bendsøe and C. A. M. Soares, eds. *Topology Design of Structures*. Springer Dordrecht, 1993. DOI: [10.1007/978-94-011-1804-0](https://doi.org/10.1007/978-94-011-1804-0) (cit. on p. 17).
- [81] A. Bensoussan, J.-L. Lions, and G. Papanicolaou. *Asymptotic analysis for periodic structures*. Studies in mathematics and its applications. North-Holland Pub. Co., 1978 (cit. on pp. 11, 40, 45).
- [82] D. J. Bergman. “Exactly Solvable Microscopic Geometries and Rigorous Bounds for the Complex Dielectric Constant of a Two-Component Composite Material.” In: *Phys. Rev. Lett.* 44 (19 1980), pp. 1285–1287. DOI: [10.1103/PhysRevLett.44.1285](https://doi.org/10.1103/PhysRevLett.44.1285) (cit. on p. 66).
- [83] J. R. Birge and F. Louveaux. *Introduction to Stochastic Programming*. New York: Springer, 1997 (cit. on p. 28).
- [84] L. Blank, H. Garcke, M. Hassan Farshbaf-Shaker, and V. Styles. “Relating phase field and sharp interface approaches to structural topology optimization.” In: *ESAIM: Control, Optimisation and Calculus of Variations* 20 (04 2014), pp. 1025–1058. DOI: [10.1051/cocv/2014006](https://doi.org/10.1051/cocv/2014006) (cit. on p. 15).
- [85] L. Blank et al. “Phase-field Approaches to Structural Topology Optimization.” In: *Constrained Optimization and Optimal Control for Partial Differential Equations*. Ed. by G. Leugering et al. Vol. 160. International Series of Numerical Mathematics. Springer Basel, 2012, pp. 245–256. DOI: [10.1007/978-3-0348-0133-1\\_13](https://doi.org/10.1007/978-3-0348-0133-1_13) (cit. on p. 15).
- [86] V. Bløasjö. “The Evolution of the Isoperimetric Problem.” In: *The American Mathematical Monthly* 112 (2005), pp. 526–566 (cit. on p. 1).
- [87] T. Borrvall and J. Petersson. “Topology optimization using regularized intermediate density control.” In: *Computer Methods in Applied Mechanics and Engineering* 190.37 (2001), pp. 4911–4928. DOI: [10.1016/S0045-7825\(00\)00356-X](https://doi.org/10.1016/S0045-7825(00)00356-X) (cit. on p. 19).
- [88] M. E. Botkin and J. A. Bennett. “Shape optimization of three-dimensional folded-plate structures.” In: *AIAA Journal* 23.11 (1985), pp. 1804–1810. DOI: [10.2514/3.9169](https://doi.org/10.2514/3.9169) (cit. on p. 12).
- [89] B. Bourdin and A. Chambolle. “Design-dependent loads in topology optimization.” In: *ESAIM Control Optim. Calc. Var.* 9 (2003), pp. 19–48 (cit. on p. 15).
- [90] B. Bourdin. “Filters in topology optimization.” In: *International Journal for Numerical Methods in Engineering* 50.9 (2001), pp. 2143–2158. DOI: [10.1002/nme.116](https://doi.org/10.1002/nme.116) (cit. on p. 19).
- [91] B. Bourdin and R. V. Kohn. “Optimization of structural topology in the high-porosity regime.” In: *J. Mech. Phys. Solids* 56.3 (2008), pp. 1043–1064. DOI: [10.1016/j.jmps.2007.06.002](https://doi.org/10.1016/j.jmps.2007.06.002) (cit. on p. 18).

- [92] J. F. Bourgat. “Numerical experiments of the homogenization method for operators with periodic coefficients.” In: *Computing Methods in Applied Sciences and Engineering*. Ed. by R. Glowinski, J. L. Lions, and I. Laboria. Vol. 704. Lecture Notes in Mathematics. Berlin, Heidelberg: Springer Berlin Heidelberg, 1977, pp. 330–356. DOI: [10.1007/BFb0063630](https://doi.org/10.1007/BFb0063630) (cit. on p. 16).
- [93] A. Braides and A. Defranceschi. *Homogenization of Multiple Integrals*. Oxford: Clarendon Press, 1998 (cit. on p. 11).
- [94] D. A. G. Bruggeman. “Berechnung verschiedener physikalischer Konstanten von heterogenen Substanzen. I. Dielektrizitätskonstanten und Leitfähigkeiten der Mischkörper aus isotropen Substanzen.” In: *Annalen der Physik* 416.7 (1935), pp. 636–664. DOI: [10.1002/andp.19354160705](https://doi.org/10.1002/andp.19354160705) (cit. on p. 63).
- [95] D. A. G. Bruggeman. “Berechnung verschiedener physikalischer Konstanten von heterogenen Substanzen. III. Die elastischen Konstanten der quasiisotropen Mischkörper aus isotropen Substanzen.” In: *Annalen der Physik* 421.2 (1937), pp. 160–178. DOI: [10.1002/andp.19374210205](https://doi.org/10.1002/andp.19374210205) (cit. on p. 64).
- [96] M. Buck, O. Iliev, and H. Andrä. “Multiscale finite element coarse spaces for the application to linear elasticity.” In: *Central European Journal of Mathematics* 11.4 (2013), pp. 680–701. DOI: [10.2478/s11533-012-0166-8](https://doi.org/10.2478/s11533-012-0166-8) (cit. on p. 22).
- [97] D. Bucur and G. Buttazzo. *Variational Methods in Shape Optimization Problems*. 1st ed. Vol. 65. Progress in Nonlinear Differential Equations and Their Applications. Birkhäuser Basel, 2005. DOI: [10.1007/b137163](https://doi.org/10.1007/b137163) (cit. on p. 9).
- [98] T. Burczyński and T. Adamczyk. “The application of the boundary element methods to optimal design of shape of the structure.” In: *Proc. 4th Conf. Meth.-Instr. of CAD*. 1983, pp. 83–92 (cit. on p. 13).
- [99] M. Burger. “A Framework for the Construction of Level Set Methods for Shape Optimization and Reconstruction.” In: *Interfaces and Free Boundaries* 5 (2003), pp. 301–329 (cit. on p. 13).
- [100] M. Burger, B. Hackl, and W. Ring. “Incorporating topological derivatives into level set methods.” In: *Journal of Computational Physics* 194.1 (2004), pp. 344–362 (cit. on p. 14).
- [101] M. Burger and R. Stainko. “Phase-Field Relaxation of Topology Optimization with Local Stress Constraints.” In: *SIAM Journal on Control and Optimization* 45.4 (2006), pp. 1447–1466 (cit. on p. 15).
- [102] G. Buttazzo and D. Aze. “Some remarks on the optimal design of periodically reinforced structures.” In: *ESAIM: M2AN* 23.1 (1989), pp. 53–61. DOI: [10.1051/m2an/1989230100531](https://doi.org/10.1051/m2an/1989230100531) (cit. on p. 11).
- [103] G. Buttazzo and G. Dal Maso. “Shape Optimization for Dirichlet Problems: Relaxed Formulation and Optimality Conditions.” In: *Applied Mathematics and Optimization* 23 (1991), pp. 17–49 (cit. on p. 10).
- [104] G. Buttazzo and G. Dal Maso. “An Existence Result for a Class of Shape Optimization Problems.” In: *Arch. Rational Mech. Anal.* 122 (1993), pp. 183–195 (cit. on p. 10).

- 
- [105] J. W. Cahn and J. E. Hilliard. “Free energy of a nonuniform system. I. Interfacial free energy.” In: *Journal of Chemical Physics* 28.2 (1958), pp. 258–267. DOI: [10.1063/1.1744102](https://doi.org/10.1063/1.1744102) (cit. on p. 14).
- [106] J. M. Cascon, C. Kreuzer, R. H. Nochetto, and K. G. Siebert. “Quasi-Optimal Convergence Rate for an Adaptive Finite Element Method.” In: *SIAM Journal on Numerical Analysis* 46.5 (2008), pp. 2524–2550. DOI: [10.1137/07069047X](https://doi.org/10.1137/07069047X) (cit. on p. 24).
- [107] J. Céa. “Conception optimale ou identification de formes, calcul rapide de la dérivée directionnelle de la fonction coût.” In: *Modélisation Math. Anal. Numér.* 20.3 (1986), pp. 371–402 (cit. on p. 57).
- [108] J. Céa, A. Gioan, and J. Michel. “Quelques résultats sur l’identification de domaines.” In: *CALCOLO* 10.3 (1973), pp. 207–232. DOI: [10.1007/BF02575843](https://doi.org/10.1007/BF02575843) (cit. on p. 12).
- [109] A. Chambolle. “A Density Result in Two-Dimensional Linearized Elasticity, and Applications.” In: *Archive for Rational Mechanics and Analysis* 167.3 (2003), pp. 211–233 (cit. on p. 10).
- [110] A. Chambolle and C. J. Larsen. “ $C^\infty$  regularity of the free boundary for a two-dimensional optimal compliance problem.” In: *Calculus of Variations and Partial Differential Equations* 18.1 (2003), pp. 77–94. DOI: [10.1007/s00526-002-0181-x](https://doi.org/10.1007/s00526-002-0181-x) (cit. on p. 10).
- [111] L. Chamoin and F. Legoll. “Goal-oriented error estimation and adaptivity in MsFEM computations.” In: *Computational Mechanics* 67.4 (2021), pp. 1201–1228. DOI: [10.1007/s00466-021-01990-x](https://doi.org/10.1007/s00466-021-01990-x) (cit. on p. 26).
- [112] F. R. Chang. *Stochastic Optimization in Continuous Time*. Cambridge: Cambridge University Press, 2004 (cit. on p. 28).
- [113] S. Chen and W. Chen. “A new level-set based approach to shape and topology optimization under geometric uncertainty.” English. In: *Structural and Multidisciplinary Optimization* 44.1 (2011), pp. 1–18. DOI: [10.1007/s00158-011-0660-9](https://doi.org/10.1007/s00158-011-0660-9) (cit. on p. 29).
- [114] S. Chen, W. Chen, and S. Lee. “Level set based robust shape and topology optimization under random field uncertainties.” English. In: *Structural and Multidisciplinary Optimization* 41.4 (2010), pp. 507–524. DOI: [10.1007/s00158-009-0449-2](https://doi.org/10.1007/s00158-009-0449-2) (cit. on p. 29).
- [115] Y. Chen, T. A. Davis, W. W. Hager, and S. Rajamanickam. “Algorithm 887: CHOLMOD, Supernodal Sparse Cholesky Factorization and Update/Downdate.” In: *ACM Trans. Math. Softw.* 35.3 (2008), 22:1–22:14. DOI: [10.1145/1391989.1391995](https://doi.org/10.1145/1391989.1391995) (cit. on p. 89).
- [116] A. H.-D. Cheng and D. T. Cheng. “Heritage and early history of the boundary element method.” In: *Engineering Analysis with Boundary Elements* 29.3 (2005), pp. 268–302. DOI: [10.1016/j.enganabound.2004.12.001](https://doi.org/10.1016/j.enganabound.2004.12.001) (cit. on p. 50).
- [117] K.-T. Cheng and N. Olhoff. “An investigation concerning optimal design of solid elastic plates.” In: *International Journal of Solids and Structures* 17.3 (1981), pp. 305–323. DOI: [10.1016/0020-7683\(81\)90065-2](https://doi.org/10.1016/0020-7683(81)90065-2) (cit. on pp. 11, 12).
- [118] G. P. Cherepanov. “Inverse problems of the plane theory of elasticity.” In: *Journal of Applied Mathematics and Mechanics* 38.6 (1974), pp. 915–931. DOI: [10.1016/0021-8928\(75\)90085-4](https://doi.org/10.1016/0021-8928(75)90085-4) (cit. on pp. 9, 66).

- [119] A. Cherkaev and R. Palais. “Optimal design of three-dimensional axisymmetric elastic structures.” In: *Structural optimization* 12.1 (1996), pp. 35–45. DOI: [10.1007/BF01270442](https://doi.org/10.1007/BF01270442) (cit. on p. 17).
- [120] A. V. Cherkaev and L. V. Gibiansky. “Coupled estimates for the bulk and shear moduli of a two-dimensional isotropic elastic composite.” In: *Journal of the Mechanics and Physics of Solids* 41.5 (1993), pp. 937–980. DOI: [10.1016/0022-5096\(93\)90006-2](https://doi.org/10.1016/0022-5096(93)90006-2) (cit. on p. 68).
- [121] A. Cherkaev. *Variational methods for structural optimization*. Vol. 140. Applied Mathematical Sciences. Springer-Verlag, New York, 2000, pp. xxvi+545. DOI: [10.1007/978-1-4612-1188-4](https://doi.org/10.1007/978-1-4612-1188-4) (cit. on p. 9).
- [122] A. Cherkaev and E. Cherkaev. “Principal Compliance and Robust Optimal Design.” In: *Journal of Elasticity* 72 (2003), pp. 71–98 (cit. on p. 29).
- [123] A. Cherkaev, Y. Grabovsky, A. Movchan, and S. Serkov. “The cavity of the optimal shape under the shear stresses.” In: 35 (1998), pp. 4391–4410 (cit. on p. 68).
- [124] A. Cherkaev and R. V. Kohn, eds. *Topics in the mathematical modelling of composite materials*. Boston, MA: Birkhäuser Boston Inc., 1997, pp. xiv+317 (cit. on p. 11).
- [125] A. V. Cherkaev, L. A. Krog, and I. Kucuk. “Stable optimal design of two-dimensional elastic structures.” In: *Control and Cybernetics* 27.2 (1998), pp. 265–282 (cit. on p. 28).
- [126] A. Chernov and C. Schwab. “Sparse p-version BEM for first kind boundary integral equations with random loading.” In: *Applied Numerical Mathematics* 59.11 (2009). Special Issue: Boundary Elements – Theory and Applications, BETA 2007 Dedicated to Professor Ernst P. Stephan on the Occasion of his 60th Birthday, pp. 2698–2712. DOI: [10.1016/j.apnum.2008.12.023](https://doi.org/10.1016/j.apnum.2008.12.023) (cit. on p. 178).
- [127] K. K. Choi and E. J. Haug. “Shape Design Sensitivity Analysis of Elastic Structures.” In: *Journal of Structural Mechanics* 11.2 (1983), pp. 231–269. DOI: [10.1080/03601218308907443](https://doi.org/10.1080/03601218308907443) (cit. on p. 12).
- [128] P. G. Ciarlet. *The finite element method for elliptic problems*. Studies in Mathematics and its Applications, Vol. 4. North-Holland Publishing Co., Amsterdam-New York-Oxford, 1978 (cit. on pp. 47, 49, 50, 86).
- [129] P. G. Ciarlet. *Mathematical elasticity. Vol. I*. Vol. 20. Studies in Mathematics and its Applications. Three-dimensional elasticity. North-Holland Publishing Co., Amsterdam, 1988 (cit. on pp. 31, 34, 35, 37, 38).
- [130] D. Cioranescu and J. S. J. Paulin. *Homogenization of reticulated structures*. Springer, 1999 (cit. on pp. 11, 40).
- [131] D. Cioranescu, A. Damlamian, and G. Griso. “Periodic unfolding and homogenization.” In: *Comptes Rendus Mathématique* 335.1 (2002), pp. 99–104. DOI: [10.1016/S1631-073X\(02\)02429-9](https://doi.org/10.1016/S1631-073X(02)02429-9) (cit. on p. 22).
- [132] D. Cioranescu and P. Donato. *An Introduction to Homogenization*. Oxford: Oxford University Press, 1999 (cit. on p. 11).
- [133] D. Cioranescu and J. S. J. Paulin. “Homogenization in open sets with holes.” In: *Journal of Mathematical Analysis and Applications* 71.2 (1979), pp. 590–607. DOI: [http://dx.doi.org/10.1016/0022-247X\(79\)90211-7](http://dx.doi.org/10.1016/0022-247X(79)90211-7) (cit. on p. 40).

- 
- [134] D. Clements and F. Rizzo. “A Method for the Numerical Solution of Boundary Value Problems Governed by Second-order Elliptic Systems.” In: *J. Inst. Maths. Applics* 22 (1978), pp. 197–202 (cit. on p. 50).
- [135] P. G. Coelho, P. R. Fernandes, J. M. Guedes, and H. C. Rodrigues. “A hierarchical model for concurrent material and topology optimisation of three-dimensional structures.” In: *Structural and Multidisciplinary Optimization* 35.2 (2008), pp. 107–115. DOI: [10.1007/s00158-007-0141-3](https://doi.org/10.1007/s00158-007-0141-3) (cit. on p. 20).
- [136] S. Conti, H. Held, M. Pach, M. Rumpf, and R. Schultz. “Shape optimization under uncertainty - a stochastic programming perspective.” In: *SIAM Journal on Optimization* 19.4 (2009), pp. 1610–1632. DOI: [10.1137/070702059](https://doi.org/10.1137/070702059) (cit. on pp. 13, 28, 117, 119).
- [137] S. Conti, B. Geihe, M. Lenz, and M. Rumpf. “A posteriori modeling error estimates in the optimization of two-scale elastic composite materials.” In: *ESAIM: Mathematical Modelling and Numerical Analysis* 52.4 (2018), pp. 1457–1476. DOI: [10.1051/m2an/2017004](https://doi.org/10.1051/m2an/2017004) (cit. on pp. 7, 110).
- [138] S. Conti, B. Geihe, M. Rumpf, and R. Schultz. “Two-Stage Stochastic Optimization Meets Two-Scale Simulation.” English. In: *Trends in PDE Constrained Optimization*. Ed. by G. Leugering et al. Vol. 165. International Series of Numerical Mathematics. Springer International Publishing, 2014, pp. 193–211. DOI: [10.1007/978-3-319-05083-6\\_13](https://doi.org/10.1007/978-3-319-05083-6_13) (cit. on pp. 4, 5, 123).
- [139] S. Conti, H. Held, M. Pach, M. Rumpf, and R. Schultz. “Risk Averse Shape Optimization.” In: *SIAM Journal on Control and Optimization* 49.3 (2011), pp. 927–947. DOI: [10.1137/090754315](https://doi.org/10.1137/090754315) (cit. on pp. 13, 28, 117, 123, 127, 136).
- [140] S. Conti, M. Lenz, N. Lüthen, M. Rumpf, and B. Zwicknagl. “Geometry of martensite needles in shape memory alloys.” In: *C. R. Math. Acad. Sci. Paris* 358.9-10 (2020), pp. 1047–1057. DOI: [10.5802/crmath.120](https://doi.org/10.5802/crmath.120) (cit. on p. 13).
- [141] S. Conti, M. Rumpf, and S. Simon. “Two-scale elastic shape optimization for additive manufacturing.” submitted. 2021. arXiv: [2111.14406](https://arxiv.org/abs/2111.14406) (cit. on p. 21).
- [142] B. Dacorogna. *Direct methods in the calculus of variations*. New York: Springer-Verlag, 1989 (cit. on p. 10).
- [143] M. Dambrine, C. Dapogny, and H. Harbrecht. “Shape Optimization for Quadratic Functionals and States with Random Right-Hand Sides.” In: *SIAM Journal on Control and Optimization* 53.5 (2015), pp. 3081–3103. DOI: [10.1137/15M1017041](https://doi.org/10.1137/15M1017041) (cit. on p. 28).
- [144] G. B. Dantzig. “Linear programming under uncertainty.” In: *Management Science* 1 (1955), pp. 197–206 (cit. on p. 27).
- [145] C. Dapogny et al. “Geometric Constraints for Shape and Topology Optimization in Architectural Design.” In: *Comput. Mech.* 59.6 (2017), pp. 933–965. DOI: [10.1007/s00466-017-1383-6](https://doi.org/10.1007/s00466-017-1383-6) (cit. on pp. 13, 72).
- [146] M. C. Delfour and J.-P. Zolésio. *Shapes and geometries*. Second. Vol. 22. Advances in Design and Control. Metrics, analysis, differential calculus, and optimization. Society for Industrial and Applied Mathematics (SIAM), Philadelphia, PA, 2011 (cit. on pp. 53–55).

- [147] K. Dems and Z. Mróz. “Variational approach by means of adjoint systems to structural optimization and sensitivity analysis I: Variation of material parameters within fixed domain.” In: *International Journal of Solids and Structures* 19.8 (1983), pp. 677–692. DOI: [10.1016/0020-7683\(83\)90064-1](https://doi.org/10.1016/0020-7683(83)90064-1) (cit. on p. 12).
- [148] K. Dems and Z. Mróz. “Variational approach by means of adjoint systems to structural optimization and sensitivity analysis II: Structure shape variation.” In: *International Journal of Solids and Structures* 20.6 (1984), pp. 527–552. DOI: [doi.org/10.1016/0020-7683\(84\)90026-X](https://doi.org/10.1016/0020-7683(84)90026-X) (cit. on p. 12).
- [149] D. Dentcheva and A. Ruszczyński. “Optimization with stochastic dominance constraints.” In: *SIAM J. Optim.* 14.2 (2003), 548–566 (electronic). DOI: [10.1137/S1052623402420528](https://doi.org/10.1137/S1052623402420528) (cit. on p. 28).
- [150] P. Destuynder and B. Métivet. “Explicit error bounds in a conforming finite element method.” In: *Mathematics of Computation* 68 (1999), pp. 1379–1396 (cit. on p. 24).
- [151] A. R. Díaz and M. P. Bendsøe. “Shape optimization of structures for multiple loading conditions using a homogenization method.” In: *Structural optimization* 4.1 (1992), pp. 17–22. DOI: [10.1007/BF01894077](https://doi.org/10.1007/BF01894077) (cit. on p. 17).
- [152] A. R. Díaz and N. Kikuchi. “Solutions to shape and topology eigenvalue optimization problems using a homogenization method.” In: *International Journal for Numerical Methods in Engineering* 35.7 (1992), pp. 1487–1502. DOI: [10.1002/nme.1620350707](https://doi.org/10.1002/nme.1620350707) (cit. on p. 17).
- [153] A. R. Díaz and R. Lipton. “Optimal material layout for 3D elastic structures.” In: *Structural optimization* 13.1 (1997), pp. 60–64. DOI: [10.1007/BF01198376](https://doi.org/10.1007/BF01198376) (cit. on p. 17).
- [154] A. R. Díaz and O. Sigmund. “Checkerboard patterns in layout optimization.” English. In: *Structural optimization* 10.1 (1995), pp. 40–45. DOI: [10.1007/BF01743693](https://doi.org/10.1007/BF01743693) (cit. on p. 19).
- [155] P. W. Dondl, B. Heeren, and M. Rumpf. “Optimization of the branching pattern in coherent phase transitions.” In: *C. R. Math. Acad. Sci. Paris* 354.6 (2016), pp. 639–644. DOI: [10.1016/j.crma.2016.03.013](https://doi.org/10.1016/j.crma.2016.03.013) (cit. on p. 12).
- [156] W. Dörfler. “A Convergent Adaptive Algorithm for Poisson’s Equation.” In: *SIAM J. Numer. Anal.* 33.3 (1996), pp. 1106–1124 (cit. on pp. 24, 141).
- [157] M. Dorobantu and B. Engquist. “Wavelet-Based Numerical Homogenization.” In: *SIAM Journal on Numerical Analysis* 35.2 (1998), pp. 540–559. URL: [www.jstor.org/stable/2587142](http://www.jstor.org/stable/2587142) (cit. on p. 23).
- [158] G. Duvaut. “Analyse fonctionnelle et mecanique des milieux continus. Application a l’etude des materiaux composites elastiques a structure periodique-homogeneisation.” In: *14th International Congress on Theoretical and Applied Mechanics (ICTAM), Delft, The Netherlands*. Ed. by W. T. Koiter. North-Holland Publishing Company, Amsterdam, 1976 (cit. on p. 11).
- [159] P. Duysinx and M. P. Bendsøe. “Topology optimization of continuum structures with local stress constraints.” In: *International Journal for Numerical Methods in Engineering* 43.8 (1998), pp. 1453–1478. DOI: [10.1002/\(SICI\)1097-0207\(19981230\)43:8<1453::AID-NME480>3.0.CO;2-2](https://doi.org/10.1002/(SICI)1097-0207(19981230)43:8<1453::AID-NME480>3.0.CO;2-2) (cit. on p. 17).



- 
- [160] J. Dvořák, J. Haslinger, and M. Miettinen. “Homogenization & optimal shape design-based approach in optimal material distribution problems. I: The scalar case.” In: *Advances in Mathematical Sciences and Applications* 9 (1999) (cit. on p. 20).
- [161] W. E and B. Engquist. “The heterogeneous multiscale methods.” In: *Commun. Math. Sci.* 1.1 (2003), pp. 87–132 (cit. on pp. 22, 80).
- [162] W. E and B. Engquist. “The Heterogeneous Multi-Scale Method for Homogenization Problems.” In: *Multiscale Methods in Science and Engineering*. Vol. 44. Lecture Notes in Computational Science and Engineering. Springer Berlin Heidelberg, 2005, pp. 89–110 (cit. on pp. 23, 80).
- [163] W. E, B. Engquist, and Z. Huang. “Heterogeneous Multiscale Method: A General Methodology for Multiscale Modeling.” In: *Physical Review B* 67.9 (2003), pp. 1–4. DOI: [10.1103/PhysRevB.67.092101](https://doi.org/10.1103/PhysRevB.67.092101) (cit. on pp. 22, 80).
- [164] W. E, P. Ming, and P. Zhang. “Analysis of the heterogeneous multiscale method for elliptic homogenization problems.” In: *J. Amer. Math. Soc.* 18.1 (2005), pp. 121–156 (cit. on pp. 23, 80, 81).
- [165] Y. R. Efendiev and T. Y. Hou. *Multiscale Finite Element Methods – Theory and Applications*. 1st ed. Surveys and Tutorials in the Applied Mathematical Sciences. Springer-Verlag New York, 2009, pp. XII, 234. DOI: [10.1007/978-0-387-09496-0](https://doi.org/10.1007/978-0-387-09496-0) (cit. on p. 22).
- [166] Y. R. Efendiev and X.-H. Wu. “Multiscale finite element for problems with highly oscillatory coefficients.” In: *Numerische Mathematik* 90.3 (2002), pp. 459–486. DOI: [10.1007/s002110100274](https://doi.org/10.1007/s002110100274) (cit. on p. 22).
- [167] A. Eichhorn and W. Römisch. “Polyhedral Risk Measures in Stochastic Programming.” In: *SIAM J. on Optimization* 16.1 (2005), pp. 69–95. DOI: <http://dx.doi.org/10.1137/040605217> (cit. on p. 28).
- [168] I. Ekeland and R. Témam. *Convex analysis and variational problems*. Philadelphia, PA, USA: Society for Industrial and Applied Mathematics, 1999 (cit. on pp. 10, 56).
- [169] H. Eschenauer, V. Kobelev, and A. Schumacher. “Bubble method for topology and shape optimization of structures.” English. In: *Structural optimization* 8.1 (1994), pp. 42–51. DOI: [10.1007/BF01742933](https://doi.org/10.1007/BF01742933) (cit. on p. 14).
- [170] J. D. Eshelby. “The force on an elastic singularity.” In: *Philosophical Transactions of the Royal Society of London A: Mathematical, Physical and Engineering Sciences* 244.877 (1951), pp. 87–112. DOI: [10.1098/rsta.1951.0016](https://doi.org/10.1098/rsta.1951.0016) (cit. on p. 66).
- [171] R. A. Feijó, A. A. Novotny, C. Padra, and E. O. Taroco. “The topological-shape sensitivity analysis and its applications in optimal design.” In: *Mecánica Computacional*. Ed. by S. R. Idelsohn, V. E. Sonzogni, and A. Cardona. Vol. XXI. 30. Santa Fe-Paraná, Argentina, 2002, pp. 2687–2711 (cit. on p. 14).
- [172] M. Feischl, T. Führer, N. Heuer, M. Karkulik, and D. Praetorius. “Adaptive Boundary Element Methods.” In: *Archives of Computational Methods in Engineering* 22.3 (2015), pp. 309–389. DOI: [10.1007/s11831-014-9114-z](https://doi.org/10.1007/s11831-014-9114-z) (cit. on pp. 24, 185).

- [173] J. Fish and V. Belsky. “Multi-grid method for periodic heterogeneous media Part 2: Multiscale modeling and quality control in multidimensional case.” In: *Computer Methods in Applied Mechanics and Engineering* 126.1 (1995), pp. 17–38. DOI: [10.1016/0045-7825\(95\)00812-F](https://doi.org/10.1016/0045-7825(95)00812-F) (cit. on p. 23).
- [174] J. Fish and V. Belsky. “Multigrid method for periodic heterogeneous media Part 1: Convergence studies for one-dimensional case.” In: *Computer Methods in Applied Mechanics and Engineering* 126.1 (1995), pp. 1–16. DOI: [10.1016/0045-7825\(95\)00811-E](https://doi.org/10.1016/0045-7825(95)00811-E) (cit. on p. 23).
- [175] W. H. Fleming and R. W. Rishel. *Deterministic and Stochastic Optimal Control*. New York: Springer, 1975 (cit. on p. 28).
- [176] I. Fonseca and S. Müller. “ $\mathcal{A}$ -quasiconvexity, lower semicontinuity, and Young measures.” English. In: *SIAM J. Math. Anal.* 30.6 (1999), pp. 1355–1390. DOI: [10.1137/S0036141098339885](https://doi.org/10.1137/S0036141098339885) (cit. on p. 61).
- [177] G. A. Francfort and J.-J. Marigo. “Revisiting brittle fracture as an energy minimization problem.” In: *J. Mech. Phys. Solids* 46.8 (1998), pp. 1319–1342. DOI: [10.1016/S0022-5096\(98\)00034-9](https://doi.org/10.1016/S0022-5096(98)00034-9) (cit. on p. 10).
- [178] G. A. Francfort and F. Murat. “Homogenization and optimal bounds in linear elasticity.” In: *Arch. Rational Mech. Anal.* 94.4 (1986), pp. 307–334. DOI: [10.1007/BF00280908](https://doi.org/10.1007/BF00280908) (cit. on pp. 62, 65).
- [179] G. Francfort, F. Murat, and L. Tartar. “Fourth-order moments of nonnegative measures on  $S^2$  and applications.” In: *Archive for Rational Mechanics and Analysis* 131.4 (1995), pp. 305–333. DOI: [10.1007/BF00380913](https://doi.org/10.1007/BF00380913) (cit. on p. 66).
- [180] J. Francú. “Homogenization of linear elasticity equations.” In: *Aplikace matematiky* 27.2 (1982), pp. 96–117 (cit. on p. 11).
- [181] S. Garreau, P. Guillaume, and M. Masmoudi. “The Topological Asymptotic for PDE Systems: The Elasticity Case.” In: *SIAM Journal on Control and Optimization* 39.6 (2001), pp. 1756–1778 (cit. on pp. 14, 59).
- [182] B. Geihe. “Formoptimierung perforierter elastischer Materialien.” Diploma thesis. Rheinische Friedrich-Wilhelms-Universität Bonn, 2009 (cit. on pp. 50, 51, 79, 88, 103).
- [183] B. Geihe. “Risikoaverse Formoptimierung hochaufgelöster perforierter elastischer Materialien.” Diploma thesis. Rheinische Friedrich-Wilhelms-Universität Bonn, 2014 (cit. on pp. 2, 91, 123).
- [184] B. Geihe, M. Lenz, M. Rumpf, and R. Schultz. “Risk averse elastic shape optimization with parametrized fine scale geometry.” In: *Mathematical Programming* 141.1-2 (2013), pp. 383–403. DOI: [10.1007/s10107-012-0531-1](https://doi.org/10.1007/s10107-012-0531-1) (cit. on pp. 4, 123).
- [185] B. Geihe and M. Rumpf. “A posteriori error estimates for sequential laminates in shape optimization.” In: *Discrete and Continuous Dynamical Systems - Series S* 9.5 (2016), pp. 1377–1392. DOI: [10.3934/dcdss.2016055](https://doi.org/10.3934/dcdss.2016055) (cit. on p. 6).
- [186] I. Gelfand and S. Fomin. *Calculus of variations*. Selected Russian publications in the mathematical sciences. Prentice-Hall, 1963 (cit. on p. 37).
- [187] P. Geoffroy-Donders, G. Allaire, and O. Pantz. “3-d topology optimization of modulated and oriented periodic microstructures by the homogenization method.” In: *J. Comput. Phys.* 401 (2020), pp. 108994, 30. DOI: [10.1016/j.jcp.2019.108994](https://doi.org/10.1016/j.jcp.2019.108994) (cit. on p. 19).

- 
- [188] M. Giacomini. “An Equilibrated Fluxes Approach to the Certified Descent Algorithm for Shape Optimization Using Conforming Finite Element and Discontinuous Galerkin Discretizations.” In: *Journal of Scientific Computing* 75.1 (2018), pp. 560–595. DOI: [10.1007/s10915-017-0545-1](https://doi.org/10.1007/s10915-017-0545-1) (cit. on p. 27).
- [189] M. Giacomini, O. Pantz, and K. Trabelsi. “Certified Descent Algorithm for shape optimization driven by fully-computable a posteriori error estimators.” In: *ESAIM: COCV* 23.3 (2017), pp. 977–1001. DOI: [10.1051/cocv/2016021](https://doi.org/10.1051/cocv/2016021) (cit. on p. 27).
- [190] L. V. Gibiansky and A. V. Cherkhaev. *Design of Composite Plates of Extremal Rigidity*. Tech. rep. see also GiCh97a. Ioffe Physicotechnical Institute, 1984 (cit. on pp. 11, 17, 63, 64).
- [191] L. V. Gibiansky and A. V. Cherkhaev. “Design of composite plates of extremal rigidity.” In: *Topics in the mathematical modelling of composite materials*. Vol. 31. Progr. Nonlinear Differential Equations Appl. Boston, MA: Birkhäuser Boston, 1997, pp. 95–137 (cit. on p. 63).
- [192] L. V. Gibiansky and A. V. Cherkhaev. “Microstructures of composites of extremal rigidity and exact bounds on the associated energy density.” In: *Topics in the mathematical modelling of composite materials*. Vol. 31. Progr. Nonlinear Differential Equations Appl. Boston, MA: Birkhäuser Boston, 1997, pp. 273–317 (cit. on p. 63).
- [193] L. Gibiansky and A. Cherkhaev. “Microstructures of composites of extremal rigidity and exact estimates of the associated energy density.” In: *Ioffe Physicotechnical Institute* 1115 (1987) (cit. on pp. 63–65).
- [194] J. Goodman, R. V. Kohn, and L. Reyna. “Numerical study of a relaxed variational problem from optimal design.” In: *Computer Methods in Applied Mechanics and Engineering* 57.1 (1986), pp. 107–127. DOI: [10.1016/0045-7825\(86\)90073-3](https://doi.org/10.1016/0045-7825(86)90073-3) (cit. on p. 16).
- [195] F. de Gournay, G. Allaire, and F. Jouve. “Shape and topology optimization of the robust compliance via the level set method.” In: *ESAIM Control Optim. Calc. Var.* 14 (2007), pp. 43–70 (cit. on p. 29).
- [196] Y. Grabovsky. “Bounds and extremal microstructures for two-component composites: a unified treatment based on the translation method.” In: *Proc. Roy. Soc. London Ser. A* 452.1947 (1996), pp. 919–944. DOI: [10.1098/rspa.1996.0046](https://doi.org/10.1098/rspa.1996.0046) (cit. on pp. 67, 68).
- [197] Y. Grabovsky and R. V. Kohn. “Microstructures minimizing the energy of a two phase elastic composite in two space dimensions. I. The confocal ellipse construction.” In: *J. Mech. Phys. Solids* 43.6 (1995), pp. 933–947. DOI: [10.1016/0022-5096\(95\)00016-C](https://doi.org/10.1016/0022-5096(95)00016-C) (cit. on pp. 66, 67).
- [198] Y. Grabovsky and R. V. Kohn. “Microstructures minimizing the energy of a two phase elastic composite in two space dimensions. II. The Vigdergauz microstructure.” In: *J. Mech. Phys. Solids* 43.6 (1995), pp. 949–972. DOI: [10.1016/0022-5096\(95\)00017-D](https://doi.org/10.1016/0022-5096(95)00017-D) (cit. on pp. 67, 68).
- [199] A. Grama, G. Karypis, and V. Kumar. *Introduction to Parallel Computing*. Addison-Wesley, 2003 (cit. on p. 112).

- [200] J. Greifstein and M. Stingl. “Simultaneous parametric material and topology optimization with constrained material grading.” In: *Structural and Multidisciplinary Optimization* 54.4 (2016), pp. 985–998. DOI: [10.1007/s00158-016-1457-7](https://doi.org/10.1007/s00158-016-1457-7) (cit. on p. 72).
- [201] J. P. Groen and O. Sigmund. “Homogenization-based topology optimization for high-resolution manufacturable microstructures.” In: *Internat. J. Numer. Methods Engrg.* 113.8 (2018), pp. 1148–1163. DOI: [10.1002/nme.5575](https://doi.org/10.1002/nme.5575) (cit. on pp. 18, 19).
- [202] J. Guedes, H. Rodrigues, and M. Bendsøe. “A material optimization model to approximate energy bounds for cellular materials under multiload conditions.” In: *Struct. Multidiscip. Optim.* 25.5 (2003), pp. 446–452. DOI: [10.1007/s00158-003-0305-8](https://doi.org/10.1007/s00158-003-0305-8) (cit. on p. 28).
- [203] X. Guo, K. Zhao, and M. Y. Wang. “Simultaneous shape and topology optimization with implicit topology description functions.” In: *Control and Cybernetics* 34.1 (2005), pp. 255–282 (cit. on p. 16).
- [204] M. E. Gurtin. “The Linear Theory of Elasticity.” In: *Linear Theories of Elasticity and Thermoelasticity: Linear and Nonlinear Theories of Rods, Plates, and Shells*. Ed. by C. Truesdell. Berlin, Heidelberg: Springer Berlin Heidelberg, 1973. Chap. 1, pp. 1–295. DOI: [10.1007/978-3-662-39776-3\\_1](https://doi.org/10.1007/978-3-662-39776-3_1) (cit. on pp. 68, 69).
- [205] R. Haber, C. Jog, and M. Bendsøe. “A new approach to variable-topology shape design using a constraint on perimeter.” English. In: *Structural optimization* 11.1-2 (1996), pp. 1–12. DOI: [10.1007/BF01279647](https://doi.org/10.1007/BF01279647) (cit. on p. 19).
- [206] W. Hackbusch and S. A. Sauter. “Composite Finite Elements for the approximation of PDEs on domains with complicated micro-structures.” In: *Numerische Mathematik* 75.4 (1997), pp. 447–472. DOI: [10.1007/s002110050248](https://doi.org/10.1007/s002110050248) (cit. on p. 13).
- [207] W. Hackbusch. *Integral Equations: Theory and Numerical Treatment*. Basel: Birkhäuser, 1995 (cit. on p. 51).
- [208] J. Hadamard. *Mémoire Sur Le Problème d’Analyse Relatif À l’Équilibre Des Plaques Élastiques Encastrées*. Mémoires présentés par divers savants à l’Académie des sciences de l’Institut de France: Éxtrait. Imprimerie nationale, 1908 (cit. on p. 12).
- [209] J. Hadar and W. R. Russell. “Rules for Ordering Uncertain Prospects.” In: *American Economic Review* 59.1 (1969), pp. 25–34. URL: <https://ideas.repec.org/a/aea/aecrev/v59y1969i1p25-34.html> (cit. on p. 28).
- [210] Z. Hashin and S. Shtrikman. “Note on a variational approach to the theory of composite elastic materials.” In: *Journal of the Franklin Institute* 271.4 (1961), pp. 336–341. DOI: [10.1016/0016-0032\(61\)90032-1](https://doi.org/10.1016/0016-0032(61)90032-1) (cit. on p. 63).
- [211] Z. Hashin and S. Shtrikman. “On some variational principles in anisotropic and nonhomogeneous elasticity.” In: *Journal of the Mechanics and Physics of Solids* 10.4 (1962), pp. 335–342. DOI: [10.1016/0022-5096\(62\)90004-2](https://doi.org/10.1016/0022-5096(62)90004-2) (cit. on p. 63).
- [212] Z. Hashin and S. Shtrikman. “A variational approach to the theory of the elastic behaviour of multiphase materials.” In: *J. Mech. Phys. Solids* 11 (1963), pp. 127–140 (cit. on p. 62).
- [213] Z. Hashin. “The elastic moduli of heterogeneous materials.” In: *Trans. ASME Ser. E. J. Appl. Mech.* 29 (1962), pp. 143–150 (cit. on p. 66).

- 
- [214] Z. Hashin. “Analysis of Composite Materials – A Survey.” In: *Journal of Applied Mechanics* 50.3 (1983), pp. 481–505. DOI: [10.1115/1.3167081](https://doi.org/10.1115/1.3167081) (cit. on p. 10).
- [215] J. Haslinger, A. Hillebrand, T. Kärkkäinen, and M. Miettinen. “Optimization of conducting structures by using the homogenization method.” In: *Structural and Multidisciplinary Optimization* 24.2 (2002), pp. 125–140. DOI: [10.1007/s00158-002-0223-1](https://doi.org/10.1007/s00158-002-0223-1) (cit. on p. 20).
- [216] J. Haslinger, M. Kočvara, G. Leugering, and M. Stingl. “Multidisciplinary Free Material Optimization.” In: *SIAM Journal on Applied Mathematics* 70.7 (2010), pp. 2709–2728 (cit. on p. 20).
- [217] J. Haslinger and R. A. E. Mäkinen. *Introduction to Shape Optimization*. Society for Industrial and Applied Mathematics, 2003. DOI: [10.1137/1.9780898718690](https://doi.org/10.1137/1.9780898718690) (cit. on p. 9).
- [218] J. Haslinger and P. Neittaanmäki. *Finite Element Approximation for Optimal Shape, Material and Topology Design*. 2nd. Wiley, 1996 (cit. on p. 9).
- [219] J. Haslinger and J. Dvořák. “Optimum composite material design.” In: *ESAIM: M2AN* 29.6 (1995), pp. 657–686. DOI: [10.1051/m2an/1995290606571](https://doi.org/10.1051/m2an/1995290606571) (cit. on p. 13, 20).
- [220] L. He, C.-Y. Kao, and S. Osher. “Incorporating topological derivatives into shape derivatives based level set methods.” In: *Journal of Computational Physics* 225.1 (2007), pp. 891–909 (cit. on p. 14).
- [221] H. Held. “Shape optimization under uncertainty from a stochastic programming point of view.” PhD thesis. Duisburg-Essen University, 2009. URL: <http://duepublico.uni-duisburg-essen.de/servlets/DozBibEntryServlet?mode=show&id=39066> (cit. on p. 118).
- [222] H. Held, R. Hemmecke, and D. L. Woodruff. “A decomposition algorithm applied to planning the interdiction of stochastic networks.” In: *Naval Research Logistics (NRL)* 52.4 (2005), pp. 321–328. DOI: [10.1002/nav.20079](https://doi.org/10.1002/nav.20079) (cit. on p. 28).
- [223] P. Henning and M. Ohlberger. “The Heterogeneous Multiscale Finite Element Method for Elliptic Homogenization Problems in Perforated Domains.” In: *Numerische Mathematik* 113, Issue 4 (2009), pp. 601–629 (cit. on p. 26).
- [224] P. Henning and M. Ohlberger. “Error control and adaptivity for heterogeneous multiscale approximations of nonlinear monotone problems.” In: *Discrete and Continuous Dynamical Systems - Series S* 8.1 (2015), pp. 119–150. DOI: [10.3934/dcdss.2015.8.119](https://doi.org/10.3934/dcdss.2015.8.119) (cit. on p. 26).
- [225] P. Henning, M. Ohlberger, and B. Schweizer. “An Adaptive Multiscale Finite Element Method.” In: *Multiscale Modeling & Simulation* 12.3 (2014), pp. 1078–1107. DOI: [10.1137/120886856](https://doi.org/10.1137/120886856) (cit. on p. 26).
- [226] D. Hilbert. “Über das Dirichletsche Prinzip.” In: *Mathematische Annalen* 59.1 (1904), pp. 161–186. DOI: [10.1007/BF01444753](https://doi.org/10.1007/BF01444753) (cit. on p. 10).
- [227] R. Hill. “The Elastic Behaviour of a Crystalline Aggregate.” In: *Proceedings of the Physical Society. Section A* 65.5 (1952), pp. 349–354. URL: <http://stacks.iop.org/0370-1298/65/i=5/a=307> (cit. on p. 62).

- [228] M. Hinze, R. Pinnau, M. Ulbrich, and S. Ulbrich. *Optimization with PDE Constraints*. 1st ed. Mathematical Modelling: Theory and Applications. Springer Dordrecht, 2009. DOI: [10.1007/978-1-4020-8839-1](https://doi.org/10.1007/978-1-4020-8839-1) (cit. on p. 9).
- [229] I. Hlaváček, A. Novotny, J. Sokołowski, and A. Źochowski. “On Topological Derivatives for Elastic Solids with Uncertain Input Data.” English. In: *Journal of Optimization Theory and Applications* 141.3 (2009), pp. 569–595. DOI: [10.1007/s10957-008-9490-3](https://doi.org/10.1007/s10957-008-9490-3) (cit. on p. 29).
- [230] V. H. Hoang and C. Schwab. “High-Dimensional Finite Elements for Elliptic Problems with Multiple Scales.” In: *Multiscale Modeling & Simulation* 3.1 (2005), pp. 168–194. DOI: [10.1137/030601077](https://doi.org/10.1137/030601077) (cit. on p. 22).
- [231] A. J. Hoffman and H. W. Wielandt. “The variation of the spectrum of a normal matrix.” In: *Duke Math. J.* 20 (1953), pp. 37–39 (cit. on p. 145).
- [232] T. Y. Hou and X.-H. Wu. “A Multiscale Finite Element Method for Elliptic Problems in Composite Materials and Porous Media.” In: *Journal of Computational Physics* 134 (1997), pp. 169–189. DOI: [10.1006/jcph.1997.5682](https://doi.org/10.1006/jcph.1997.5682) (cit. on p. 22).
- [233] T. Y. Hou, X.-H. Wu, and Z. Cai. “Convergence of a Multiscale Finite Element Method for Elliptic Problems with Rapidly Oscillating Coefficients.” In: *Math. Comp.* 68 (1999), pp. 913–943 (cit. on pp. 22, 73).
- [234] T. J. Hughes. “Multiscale phenomena: Green’s functions, the Dirichlet-to-Neumann formulation, subgrid scale models, bubbles and the origins of stabilized methods.” In: *Computer Methods in Applied Mechanics and Engineering* 127.1 (1995), pp. 387–401. DOI: [10.1016/0045-7825\(95\)00844-9](https://doi.org/10.1016/0045-7825(95)00844-9) (cit. on p. 23).
- [235] T. J. Hughes, G. R. Feijóo, L. Mazzei, and J.-B. Quincy. “The variational multiscale method—a paradigm for computational mechanics.” In: *Computer Methods in Applied Mechanics and Engineering* 166.1 (1998). Advances in Stabilized Methods in Computational Mechanics, pp. 3–24. DOI: [10.1016/S0045-7825\(98\)00079-6](https://doi.org/10.1016/S0045-7825(98)00079-6) (cit. on p. 23).
- [236] O. Jecker and A. Abdulle. “Numerical Experiments for Multiscale Problems in Linear Elasticity.” In: *Numerical Mathematics and Advanced Applications ENUMATH 2015*. Ed. by B. Karasözen, M. Manguoğlu, M. Tezer-Sezgin, S. Göktepe, and Ö. Uğur. Cham: Springer International Publishing, 2016, pp. 123–131. DOI: [10.1007/978-3-319-39929-4\\_13](https://doi.org/10.1007/978-3-319-39929-4_13) (cit. on p. 23).
- [237] E. D. Jensen. “Topological Structural Design using Genetic Algorithms.” PhD thesis. Purdue University, 1992 (cit. on p. 14).
- [238] P. D. L. Jensen, O. Sigmund, and J. P. Groen. “De-homogenization of optimal 2D topologies for multiple loading cases.” In: *Computer Methods in Applied Mechanics and Engineering* 399 (2022), p. 115426. DOI: [10.1016/j.cma.2022.115426](https://doi.org/10.1016/j.cma.2022.115426) (cit. on p. 28).
- [239] V. V. Jikov, S. M. Kozlov, and O. A. Oleinik. *Homogenization of differential operators and integral functionals*. Berlin: Springer-Verlag, 1994, pp. xii+570 (cit. on pp. 11, 68).
- [240] C. S. Jog, R. B. Haber, and M. P. Bendsøe. “A Displacement-Based Topology Design Method with Self-Adaptive Layered Materials.” In: *Topology Design of Structures*. Ed. by M. P. Bendsøe and C. A. M. Soares. Dordrecht: Springer Netherlands, 1993, pp. 219–238. DOI: [10.1007/978-94-011-1804-0\\_15](https://doi.org/10.1007/978-94-011-1804-0_15) (cit. on pp. 17, 18).

- [241] C. S. Jog and R. B. Haber. “Stability of finite element models for distributed-parameter optimization and topology design.” In: *Computer Methods in Applied Mechanics and Engineering* 130.3–4 (1996), pp. 203–226. DOI: [http://dx.doi.org/10.1016/0045-7825\(95\)00928-0](http://dx.doi.org/10.1016/0045-7825(95)00928-0) (cit. on p. 19).
- [242] C. Johnson and J. Pitkäranta. “Analysis of some mixed finite element methods related to reduced integration.” In: *Mathematics of Computation* 38.158 (1982), pp. 375–400. DOI: [10.2307/2007276](https://doi.org/10.2307/2007276) (cit. on p. 18).
- [243] F. Jouve and E. Bonnetier. “Checkerboard instabilities in topological shape optimization algorithms.” In: *Proceedings of the Conference on Inverse Problems, Control and Shape Optimization (PICOF'98), Carthage (1998)*. 1998 (cit. on pp. 18, 89).
- [244] P. Kall and S. Wallace. *Stochastic Programming*. Chichester: Wiley, 1994 (cit. on p. 28).
- [245] J. Kane and S. Saigal. “Design-sensitivity analysis of solids using BEM.” In: *Journal of Engineering Mechanics - ASCE* 114.10 (1988), pp. 1703–1722. DOI: [10.1061/\(ASCE\)0733-9399\(1988\)114:10\(1703\)](https://doi.org/10.1061/(ASCE)0733-9399(1988)114:10(1703)) (cit. on p. 13).
- [246] Y. Kantor and D. Bergman. “Improved rigorous bounds on the effective elastic moduli of a composite material.” In: *Journal of the Mechanics and Physics of Solids* 32.1 (1984), pp. 41–62. DOI: [10.1016/0022-5096\(84\)90004-8](https://doi.org/10.1016/0022-5096(84)90004-8) (cit. on p. 63).
- [247] G. Kharmanda, N. Olhoff, A. Mohamed, and M. Lemaire. “Reliability-based topology optimization.” In: *Structural and Multidisciplinary Optimization* 26.5 (2004), pp. 295–307. DOI: [10.1007/s00158-003-0322-7](https://doi.org/10.1007/s00158-003-0322-7) (cit. on p. 29).
- [248] N. Kikuchi, K. Y. Chung, T. Torigaki, and J. E. Taylor. “Adaptive finite element methods for shape optimization of linearly elastic structures.” In: *Computer Methods in Applied Mechanics and Engineering* 57.1 (1986), pp. 67–89. DOI: [10.1016/0045-7825\(86\)90071-X](https://doi.org/10.1016/0045-7825(86)90071-X) (cit. on p. 26).
- [249] N. Kogioso, W. Ahn, S. Nishiwaki, K. Izui, and M. Yoshimura. “Robust Topology Optimization for Compliant Mechanisms Considering Uncertainty of Applied Loads.” In: *Journal of Advanced Mechanical Design, Systems, and Manufacturing* 2.1 (2008), pp. 96–107. DOI: [10.1299/jamdsm.2.96](https://doi.org/10.1299/jamdsm.2.96) (cit. on p. 29).
- [250] R. V. Kohn and B. Wirth. “Optimal fine-scale structures in compliance minimization for a uniaxial load.” In: *Proceedings of the Royal Society of London A: Mathematical, Physical and Engineering Sciences* 470.2170 (2014) (cit. on p. 11).
- [251] R. V. Kohn and B. Wirth. “Optimal fine-scale structures in compliance minimization for a shear load.” In: *Communications in Pure and Applied Mathematics* (2015). to appear (cit. on p. 11).
- [252] R. V. Kohn and R. Lipton. “Optimal bounds for the effective energy of a mixture of isotropic, incompressible, elastic materials.” In: *Arch. Rational Mech. Anal.* 102.4 (1988), pp. 331–350. DOI: [10.1007/BF00251534](https://doi.org/10.1007/BF00251534) (cit. on pp. 63, 64).
- [253] R. V. Kohn and G. W. Milton. “On Bounding the Effective Conductivity of Anisotropic Composites.” In: *Homogenization and Effective Moduli of Materials and Media*. Ed. by J. L. Ericksen, D. Kinderlehrer, R. Kohn, and J.-L. Lions. New York, NY: Springer New York, 1986, pp. 97–125. DOI: [10.1007/978-1-4613-8646-9\\_5](https://doi.org/10.1007/978-1-4613-8646-9_5) (cit. on p. 63).

- [254] R. V. Kohn and G. Strang. “Optimal design and relaxation of variational problems. I.” In: *Comm. Pure Appl. Math.* 39.1 (1986), pp. 113–137. DOI: [10.1002/cpa.3160390107](https://doi.org/10.1002/cpa.3160390107) (cit. on pp. 10, 61).
- [255] R. V. Kohn and G. Strang. “Optimal design and relaxation of variational problems. II.” In: *Comm. Pure Appl. Math.* 39.2 (1986), pp. 139–182. DOI: [10.1002/cpa.3160390202](https://doi.org/10.1002/cpa.3160390202) (cit. on pp. 10, 61).
- [256] R. V. Kohn and G. Strang. “Optimal design and relaxation of variational problems. III.” In: *Comm. Pure Appl. Math.* 39.3 (1986), pp. 353–377. DOI: [10.1002/cpa.3160390305](https://doi.org/10.1002/cpa.3160390305) (cit. on pp. 9, 10, 59, 61).
- [257] S. M. Kozlov. “Averaging Differential Operators With Almost Periodic, Rapidly Oscillating Coefficients.” In: *Mathematics of the USSR-Sbornik* 35.4 (1979), pp. 481–498. DOI: [10.1070/sm1979v035n04abeh001561](https://doi.org/10.1070/sm1979v035n04abeh001561) (cit. on p. 11).
- [258] M. G. Larson and A. Målqvist. “Adaptive Variational Multiscale Methods Based on A Posteriori Error Estimation: Duality Techniques for Elliptic Problems.” In: *Multiscale Methods in Science and Engineering*. Ed. by B. Engquist, O. Runborg, and P. Lötstedt. Berlin, Heidelberg: Springer Berlin Heidelberg, 2005, pp. 181–193. DOI: [10.1007/3-540-26444-2\\_9](https://doi.org/10.1007/3-540-26444-2_9) (cit. on p. 26).
- [259] M. Lenz. “Modellierung und Simulation des effektiven Verhaltens von Grenzflächen in Metalllegierungen.” PhD thesis. University Bonn, 2007. URL: <http://nbn-resolving.de/urn:nbn:de:hbz:5N-12741> (cit. on pp. 50, 51, 88, 92).
- [260] J. L. Lions. *Optimal Control of Systems Governed by Partial Differential Equations*. 1st ed. Grundlehren der mathematischen Wissenschaften. Springer Berlin, Heidelberg, 1971 (cit. on p. 9).
- [261] R. Lipton. “On the effective elasticity of a two-dimensional homogenised incompressible elastic composite.” In: *Proceedings of the Royal Society of Edinburgh: Section A Mathematics* 110.1-2 (1988), pp. 45–61. DOI: [10.1017/S0308210500024847](https://doi.org/10.1017/S0308210500024847) (cit. on p. 63).
- [262] R. Lipton. “A saddle-point theorem with application to structural optimization.” In: *Journal of Optimization Theory and Applications* 81.3 (1994), pp. 549–568. DOI: [10.1007/BF02193100](https://doi.org/10.1007/BF02193100) (cit. on p. 17).
- [263] R. Lipton. “Composites with symmetry and their extremal properties.” In: *International Journal of Solids and Structures* 31.24 (1994), pp. 3407–3417. DOI: [10.1016/0020-7683\(94\)90023-X](https://doi.org/10.1016/0020-7683(94)90023-X) (cit. on p. 17).
- [264] R. Lipton. “Optimal bounds on effective elastic tensors for orthotropic composites.” In: *Proceedings of the Royal Society of London. Series A: Mathematical and Physical Sciences* 444.1921 (1994), pp. 399–410. DOI: [10.1098/rspa.1994.0028](https://doi.org/10.1098/rspa.1994.0028) (cit. on p. 17).
- [265] R. Lipton. “Design of functionally graded composite structures in the presence of stress constraints.” In: *International Journal of Solids and Structures* 39.9 (2002), pp. 2575–2586. DOI: [10.1016/S0020-7683\(02\)00129-4](https://doi.org/10.1016/S0020-7683(02)00129-4) (cit. on pp. 17, 18).
- [266] K. A. Lurie. “On the optimal distribution of the resistivity tensor of the working substance in a magnetohydrodynamic channel.” In: *Journal of Applied Mathematics and Mechanics* 34.2 (1970), pp. 255–274. DOI: [10.1016/0021-8928\(70\)90139-5](https://doi.org/10.1016/0021-8928(70)90139-5) (cit. on p. 11).



- [267] K. A. Lurie and A. V. Cherkaev. “Exact estimates of conductivity of composites formed by two isotropically conducting media taken in prescribed proportion.” In: *Proceedings of the Royal Society of Edinburgh: Section A Mathematics* 99.1–2 (1984), pp. 71–87. DOI: [10.1017/S030821050002597X](https://doi.org/10.1017/S030821050002597X) (cit. on p. 62).
- [268] K. A. Lurie and A. V. Cherkaev. “G-closure of a set of anisotropically conducting media in the two-dimensional case.” In: *Journal of Optimization Theory and Applications* 42.2 (1984), pp. 283–304. DOI: [10.1007/BF00934300](https://doi.org/10.1007/BF00934300) (cit. on p. 62).
- [269] K. A. Lurie and A. V. Cherkaev. “Effective characteristics of composite materials and the optimal design of structural elements.” In: *Adv. in Mech.* 9.2 (1986), pp. 3–81 (cit. on p. 11).
- [270] K. A. Lurie, A. V. Cherkaev, and A. V. Fedorov. “Regularization of optimal design problems for bars and plates, part 1.” In: *Journal of Optimization Theory and Applications* 37.4 (1982), pp. 499–522. DOI: [10.1007/BF00934953](https://doi.org/10.1007/BF00934953) (cit. on p. 11).
- [271] K. A. Lurie, A. V. Cherkaev, and A. V. Fedorov. “Regularization of optimal design problems for bars and plates, part 2.” In: *Journal of Optimization Theory and Applications* 37.4 (1982), pp. 523–543. DOI: [10.1007/BF00934954](https://doi.org/10.1007/BF00934954) (cit. on p. 11).
- [272] J. E. Marsden and T. J. R. Hughes. *Mathematical foundations of Elasticity*. Prentice–Hall, Englewood Cliffs, 1983 (cit. on pp. 31, 35).
- [273] K. Marti. *Stochastic Optimization Methods*. Berlin: Springer, 2005 (cit. on p. 28).
- [274] A.-M. Matache, I. Babuška, and C. Schwab. “Generalized p-FEM in homogenization.” In: *Numerische Mathematik* 86.2 (2000), pp. 319–375. DOI: [10.1007/PL00005409](https://doi.org/10.1007/PL00005409) (cit. on p. 22).
- [275] A.-M. Matache and C. Schwab. “Homogenization via p-FEM for problems with microstructure.” In: *Applied Numerical Mathematics* 33.1–4 (2000), pp. 43–59. DOI: [http://dx.doi.org/10.1016/S0168-9274\(99\)00069-0](http://dx.doi.org/10.1016/S0168-9274(99)00069-0) (cit. on p. 22).
- [276] A.-M. Matache. “Sparse Two-Scale FEM for Homogenization Problems.” In: *Journal of Scientific Computing* 17.1 (2002), pp. 659–669. DOI: [10.1023/A:1015187000835](https://doi.org/10.1023/A:1015187000835) (cit. on p. 22).
- [277] A.-M. Matache and C. Schwab. “Generalized FEM for Homogenization Problems.” In: *Multiscale and Multiresolution Methods*. Ed. by T. J. Barth, T. Chan, and R. Haimes. Berlin, Heidelberg: Springer Berlin Heidelberg, 2002, pp. 197–237 (cit. on p. 22).
- [278] A.-M. Matache and C. Schwab. “Two-Scale FEM for Homogenization Problems.” In: *Mathematical Modelling and Numerical Analysis* 36.4 (2002), pp. 537–572. DOI: [10.1051/m2an:2002025](https://doi.org/10.1051/m2an:2002025) (cit. on p. 22).
- [279] K. Matsui and K. Terada. “Continuous approximation of material distribution for topology optimization.” In: *International Journal for Numerical Methods in Engineering* 59.14 (2004), pp. 1925–1944. DOI: [10.1002/nme.945](https://doi.org/10.1002/nme.945) (cit. on p. 19).
- [280] K. Maute. “Topology Optimization under Uncertainty.” In: *Topology Optimization in Structural and Continuum Mechanics*. Ed. by G. I. N. Rozvany and T. Lewiński. Vienna: Springer Vienna, 2014, pp. 457–471. DOI: [10.1007/978-3-7091-1643-2\\_20](https://doi.org/10.1007/978-3-7091-1643-2_20) (cit. on p. 28).
- [281] J. C. Maxwell. *A Treatise on Electricity and Magnetism*. 1st Edition. Oxford: Clarendon Press, 1873 (cit. on p. 10).

- [282] E. J. McShane. “Necessary conditions in generalized-curve problems of the calculus of variations.” In: *Duke Mathematical Journal* 7.1 (1940), pp. 1–27. DOI: [10.1215/S0012-7094-40-00701-3](https://doi.org/10.1215/S0012-7094-40-00701-3) (cit. on p. 10).
- [283] A. Michell. “LVIII. The limits of economy of material in frame-structures.” In: *Philosophical Magazine Series 6* 8.47 (1904), pp. 589–597. DOI: [10.1080/14786440409463229](https://doi.org/10.1080/14786440409463229) (cit. on pp. 11, 68).
- [284] G. W. Milton. “Bounds on the complex dielectric constant of a composite material.” In: *Applied Physics Letters* 37.3 (1980), pp. 300–302. DOI: [10.1063/1.91895](https://doi.org/10.1063/1.91895) (cit. on p. 66).
- [285] G. W. Milton. *The Theory of Composites*. Cambridge University Press, 2002 (cit. on p. 10).
- [286] G. W. Milton, M. Briane, and D. Harutyunyan. “On the possible effective elasticity tensors of 2-dimensional and 3-dimensional printed materials.” en. In: *Mathematics and Mechanics of Complex Systems* 5.1 (2017), pp. 41–94. DOI: [10.2140/memocs.2017.5.41](https://doi.org/10.2140/memocs.2017.5.41) (cit. on p. 21).
- [287] G. W. Milton and A. V. Cherkaev. “Which Elasticity Tensors are Realizable?” In: *Journal of Engineering Materials and Technology* 117.4 (1995), pp. 483–493. DOI: [10.1115/1.2804743](https://doi.org/10.1115/1.2804743) (cit. on p. 20).
- [288] G. W. Milton and R. V. Kohn. “Variational bounds on the effective moduli of anisotropic composites.” In: *Journal of the Mechanics and Physics of Solids* 36.6 (1988), pp. 597–629. DOI: [http://dx.doi.org/10.1016/0022-5096\(88\)90001-4](http://dx.doi.org/10.1016/0022-5096(88)90001-4) (cit. on p. 63).
- [289] P. Ming and X. Yue. “Numerical methods for multiscale elliptic problems.” In: *Journal of Computational Physics* 214.1 (2006), pp. 421–445. DOI: [10.1016/j.jcp.2005.09.024](https://doi.org/10.1016/j.jcp.2005.09.024) (cit. on p. 23).
- [290] L. Modica and S. Mortola. “Un esempio di  $\Gamma^-$ -convergenza.” In: *Boll. Un. Mat. Ital. B (5)* 14.1 (1977), pp. 285–299 (cit. on p. 15).
- [291] R. C. Morgan and I. Babuška. “An approach for constructing families of homogenized equations for periodic media. Part I: An integral representation and its consequences.” In: *SIAM J. Math. Anal.* 22 (1991), pp. 1–15 (cit. on p. 22).
- [292] R. C. Morgan and I. Babuška. “An approach for constructing families of homogenized equations for periodic media. Part II: Properties of the kernel.” In: *SIAM J. Math. Anal.* 22 (1991), pp. 16–33 (cit. on p. 22).
- [293] P. Morin, R. Nochetto, M. Pauletti, and M. Verani. “Adaptive SQP Method for Shape Optimization.” English. In: *Numerical Mathematics and Advanced Applications 2009*. Ed. by G. Kreiss, P. Lötstedt, A. Målqvist, and M. Neytcheva. Springer Berlin Heidelberg, 2010, pp. 663–673. URL: [http://dx.doi.org/10.1007/978-3-642-11795-4\\_71](http://dx.doi.org/10.1007/978-3-642-11795-4_71) (cit. on p. 27).
- [294] P. Morin, R. H. Nochetto, M. S. Pauletti, and M. Verani. “Adaptive finite element method for shape optimization.” In: *ESAIM: Control, Optimisation and Calculus of Variations* 18 (04 2012), pp. 1122–1149. DOI: [10.1051/cocv/2011192](https://doi.org/10.1051/cocv/2011192) (cit. on p. 27).
- [295] P. Morin, R. H. Nochetto, and K. G. Siebert. “Data Oscillation and Convergence of Adaptive FEM.” In: *SIAM Journal on Numerical Analysis* 38.2 (2000), pp. 466–488. DOI: [10.1137/S0036142999360044](https://doi.org/10.1137/S0036142999360044) (cit. on p. 24).

- 
- [296] A. Müller and D. Stoyan. *Comparison Methods for Stochastic Models and Risks*. Wiley, 2002 (cit. on pp. 28, 130).
- [297] F. Murat and L. Tartar. “Calcul des variations et homogénéisation.” In: *Homogenization methods: theory and applications in physics (Bréau-sans-Nappe, 1983)*. Vol. 57. Collect. Dir. Études Rech. Élec. France. Paris: Eyrolles, 1985, pp. 319–369 (cit. on pp. 11, 62, 64).
- [298] F. Murat. “Un contre-exemple pour le problème du contrôle dans les coefficients.” In: *CR Acad. Sci. Paris Sér. AB 273* (1971), A708–A711 (cit. on pp. 9, 59).
- [299] F. Murat. “Contre-exemples pour divers problèmes où le contrôle intervient dans les coefficients.” In: *Annali di Matematica Pura ed Applicata* 112.1 (1977), pp. 49–68. DOI: [10.1007/BF02413475](https://doi.org/10.1007/BF02413475) (cit. on pp. 9, 59).
- [300] F. Murat and J. Simon. “Etude De Problème D’Optimal Design.” In: *Proceedings of the 7th IFIP Conference on Optimization Techniques: Modeling and Optimization in the Service of Man, Part 2*. London, UK, UK: Springer-Verlag, 1976, pp. 54–62. URL: <http://dl.acm.org/citation.cfm?id=646301.758961> (cit. on p. 12).
- [301] F. Murat and L. Tartar. “Calculus of variations and homogenization.” In: *Topics in the mathematical modelling of composite materials*. Vol. 31. Progr. Nonlinear Differential Equations Appl. Boston, MA: Birkhäuser Boston, 1997, pp. 139–173 (cit. on p. 64).
- [302] F. Murat and L. Tartar. “H-Convergence.” In: *Topics in the Mathematical Modelling of Composite Materials*. Ed. by A. Cherkaev and R. Kohn. Boston, MA: Birkhäuser Boston, 1997, pp. 21–43. DOI: [10.1007/978-1-4612-2032-9\\_3](https://doi.org/10.1007/978-1-4612-2032-9_3) (cit. on pp. 45, 46).
- [303] N. Muskhelishvili. *Some Basic Problems of the Mathematical Theory of Elasticity*. Groningen-Holland: P. Noordhoff, 1953 (cit. on p. 66).
- [304] N. Neuss, W. Jäger, and G. Wittum. “Homogenization and multigrid.” In: *Computing* 66 (2001), pp. 1–26 (cit. on p. 23).
- [305] H. T. Ngoan. “Convergence of the solutions of boundary value problems for a sequence of elliptic equations.” In: *Uspekhi Mat. Nauk* 32.3(195) (1977), pp. 183–184 (cit. on p. 11).
- [306] G. Nguetseng. “A General Convergence Result for a Functional Related to the Theory of Homogenization.” In: *SIAM Journal on Mathematical Analysis* 20.3 (1989), pp. 608–623. DOI: [10.1137/0520043](https://doi.org/10.1137/0520043) (cit. on p. 44).
- [307] R. H. Nochetto, A. Veiser, and M. Verani. “A safeguarded dual weighted residual method.” In: *IMA Journal of Numerical Analysis* 29.1 (2008), pp. 126–140. DOI: [10.1093/imanum/drm026](https://doi.org/10.1093/imanum/drm026) (cit. on pp. 25, 149).
- [308] A. N. Norris. “Optimal orientation of anisotropic solids.” In: *The Quarterly Journal of Mechanics and Applied Mathematics* 59.1 (2005), pp. 29–53. DOI: [10.1093/qjnam/hbi030](https://doi.org/10.1093/qjnam/hbi030) (cit. on p. 69).
- [309] A. A. Novotny and J. Sokołowski. *Topological Derivatives in Shape Optimization*. Berlin, Heidelberg: Springer Berlin Heidelberg, 2013. DOI: [10.1007/978-3-642-35245-4](https://doi.org/10.1007/978-3-642-35245-4) (cit. on p. 14).
- [310] J. T. Oden and S. Prudhomme. “Goal-oriented error estimation and adaptivity for the finite element method.” In: *Comput. Math. Appl.* 41.5-6 (2001), pp. 735–756. DOI: [10.1016/S0898-1221\(00\)00317-5](https://doi.org/10.1016/S0898-1221(00)00317-5) (cit. on pp. 25, 27).

- [311] J. T. Oden and K. S. Vemaganti. “Adaptive Modeling of Composite Structures: Modeling Error Estimation.” In: *International Journal for Computational Civil and Structural Engineering* 1 (2000), pp. 1–16 (cit. on p. 26).
- [312] J. T. Oden and K. S. Vemaganti. “Estimation of local modeling error and goal-oriented adaptive modeling of heterogeneous materials. I. Error estimates and adaptive algorithms.” In: *J. Comput. Phys.* 164.1 (2000), pp. 22–47. DOI: [10.1006/jcph.2000.6585](https://doi.org/10.1006/jcph.2000.6585) (cit. on p. 26).
- [313] M. Ohlberger. “A posteriori error estimates for the heterogeneous multiscale finite element method for elliptic homogenization problems.” In: *SIAM Multiscale Mod. Simul.* 4.1 (2005), pp. 88–114 (cit. on pp. 26, 81, 183, 185).
- [314] O. A. Oleinik, A. S. Shamaev, and G. A. Yosifian. *Mathematical Problems in Elasticity and Homogenization*. Studies in Mathematics and its Applications. Amsterdam: North-Holland, 1992 (cit. on pp. 11, 40).
- [315] N. Olhoff, M. P. Bendsøe, and J. Rasmussen. “CAD-Integrated Structural Topology and Design Optimization.” In: *Shape and Layout Optimization of Structural Systems and Optimality Criteria Methods*. Ed. by G. I. N. Rozvany. Vienna: Springer Vienna, 1992, pp. 171–197. DOI: [10.1007/978-3-7091-2788-9\\_11](https://doi.org/10.1007/978-3-7091-2788-9_11) (cit. on p. 18).
- [316] S. J. Osher and F. Santosa. “Level Set Methods for Optimization Problems Involving Geometry and Constraints I. Frequencies of a Two-density Inhomogeneous Drum.” In: *J. Comput. Phys.* 171.1 (2001), pp. 272–288. DOI: [10.1006/jcph.2001.6789](https://doi.org/10.1006/jcph.2001.6789) (cit. on p. 13).
- [317] S. J. Osher and J. A. Sethian. “Fronts propagating with curvature-dependent speed: algorithms based on Hamilton-Jacobi formulations.” In: *J. Comput. Phys.* 79.1 (1988), pp. 12–49. DOI: [10.1016/0021-9991\(88\)90002-2](https://doi.org/10.1016/0021-9991(88)90002-2) (cit. on p. 13).
- [318] M. Pach. “Risikoaverse Formoptimierung - Risikomaße und stochastische Ordnungen.” Dissertation. Universität Duisburg-Essen, 2014. URL: <http://duepublico.uni-duisburg-essen.de/servlets/DocumentServlet?id=33727> (cit. on p. 130).
- [319] O. Pantz and K. Trabelsi. “A Post-Treatment of the Homogenization Method for Shape Optimization.” In: *SIAM Journal on Control and Optimization* 47.3 (2008), pp. 1380–1398. DOI: [10.1137/070688900](https://doi.org/10.1137/070688900) (cit. on p. 18).
- [320] M. Paraschivoiu, J. Peraire, and A. T. Patera. “A posteriori finite element bounds for linear-functional outputs of elliptic partial differential equations.” In: *Computer Methods in Applied Mechanics and Engineering* 150.1 (1997). Symposium on Advances in Computational Mechanics, pp. 289–312. DOI: [0.1016/S0045-7825\(97\)00086-8](https://doi.org/0.1016/S0045-7825(97)00086-8) (cit. on p. 25).
- [321] B. Paul. *Prediction of Elastic Constants of Multiphase Materials*. Vol. 218. 1960, pp. 36–4 (cit. on p. 62).
- [322] G. Pavliotis and A. Stuart. *Multiscale Methods – Averaging and Homogenization*. 1st ed. Texts in Applied Mathematics. Springer-Verlag New York, 2008, pp. XVIII, 310. DOI: [10.1007/978-0-387-73829-1](https://doi.org/10.1007/978-0-387-73829-1) (cit. on p. 39).
- [323] P. Pedersen. “On optimal orientation of orthotropic materials.” English. In: *Structural optimization* 1.2 (1989), pp. 101–106. DOI: [10.1007/BF01637666](https://doi.org/10.1007/BF01637666) (cit. on pp. 17, 69, 95).

- 
- [324] T. Pennanen. “Epi-convergent discretizations of multistage stochastic programs.” In: *Mathematics of Operations Research* 30 (2005), pp. 245–256 (cit. on p. 28).
- [325] P. Penzler, M. Rumpf, and B. Wirth. “A Phase-Field Model for Compliance Shape Optimization in Nonlinear Elasticity.” In: *ESAIM: Control, Optimisation and Calculus of Variations* 18.1 (2012), pp. 229–258. DOI: [10.1051/cocv/2010045](https://doi.org/10.1051/cocv/2010045) (cit. on pp. 15, 58).
- [326] J. Petersson. “Some convergence results in perimeter-controlled topology optimization.” In: *Computer Methods in Applied Mechanics and Engineering* 171.1 (1999), pp. 123–140. DOI: [10.1016/S0045-7825\(98\)00248-5](https://doi.org/10.1016/S0045-7825(98)00248-5) (cit. on p. 19).
- [327] J. Petersson and O. Sigmund. “Slope constrained topology optimization.” In: *International Journal for Numerical Methods in Engineering* 41.8 (1998), pp. 1417–1434. DOI: [10.1002/\(SICI\)1097-0207\(19980430\)41:8<1417::AID-NME344>3.0.CO;2-N](https://doi.org/10.1002/(SICI)1097-0207(19980430)41:8<1417::AID-NME344>3.0.CO;2-N) (cit. on p. 19).
- [328] C.-M. Pfeiler and D. Praetorius. “Dörfler marking with minimal cardinality is a linear complexity problem.” In: *Mathematics of Computation* 89 (2020), pp. 2735–2752. DOI: [10.1090/mcom/3553](https://doi.org/10.1090/mcom/3553) (cit. on pp. 24, 141).
- [329] G. C. Pflug and W. Römisch. *Modeling, Measuring and Managing Risk*. World Scientific, Singapore, 2007 (cit. on p. 28).
- [330] O. Pironneau. “Optimal shape design for elliptic systems.” English. In: *System Modeling and Optimization*. Ed. by R. Drenick and F. Kozin. Vol. 38. Lecture Notes in Control and Information Sciences. Springer Berlin Heidelberg, 1982, pp. 42–66. DOI: [10.1007/BFb0006123](https://doi.org/10.1007/BFb0006123) (cit. on p. 12).
- [331] O. Pironneau. *Optimal shape design for elliptic systems*. 1st ed. Scientific Computation. Springer Berlin Heidelberg, 1984. DOI: [10.1007/978-3-642-87722-3](https://doi.org/10.1007/978-3-642-87722-3) (cit. on p. 9).
- [332] W. Prager and J. L. Synge. “Approximations in elasticity based on the concept of function space.” In: *Quarterly of Applied Mathematics* 5 (1947), pp. 241–269 (cit. on pp. 23, 24).
- [333] A. Prékopa. *Stochastic Programming*. Dordrecht: Kluwer, 1995 (cit. on p. 28).
- [334] S. Prudhomme and J. T. Oden. “On goal-oriented error estimation for elliptic problems: application to the control of pointwise errors.” In: *Comput. Methods Appl. Mech. Engrg.* 176.1-4 (1999). New advances in computational methods (Cachan, 1997), pp. 313–331. DOI: [10.1016/S0045-7825\(98\)00343-0](https://doi.org/10.1016/S0045-7825(98)00343-0) (cit. on p. 25).
- [335] M. Ptashnyk and B. Seguin. “Periodic Homogenization and Material Symmetry in Linear Elasticity.” In: *Journal of Elasticity* 124.2 (2016), pp. 225–241. DOI: [10.1007/s10659-015-9566-x](https://doi.org/10.1007/s10659-015-9566-x) (cit. on p. 69).
- [336] J. P. Quirk and R. Saposnik. “Admissibility and Measurable Utility Functions.” In: *The Review of Economic Studies* 29.2 (1962), pp. 140–146. DOI: [10.2307/2295819](https://doi.org/10.2307/2295819) (cit. on p. 28).
- [337] U. Raitums. “The extension of extremal problems connected with a linear elliptic equation.” In: *Dokl. Akad. Nauk SSSR* 243.2 (1978), pp. 281–283 (cit. on p. 11).
- [338] U. Raitums. “On the Local Representation of G-Closure.” In: *Archive for Rational Mechanics and Analysis* 158.3 (2001), pp. 213–234. DOI: [10.1007/PL00004244](https://doi.org/10.1007/PL00004244) (cit. on p. 68).

- [339] E. Rank. “A-posteriori error estimates and adaptive refinement for some boundary integral element methods.” In: *Proc. Int. Conf. on Accuracy Estimates and Adaptive Refinements in Finite Element Computations ARFEC, Lisbon*. 1984 (cit. on pp. 24, 185).
- [340] S. I. Repin. “A posteriori error estimation for nonlinear variational problems by duality theory.” In: *Journal of Mathematical Sciences* 99.1 (2000). Translated from *Zapiski Nauchnykh Seminarov POMI*, Vol. 243, 1997, pp. 201–214., pp. 927–935. DOI: [10.1007/BF02673600](https://doi.org/10.1007/BF02673600) (cit. on p. 24).
- [341] S. I. Repin. “A posteriori error estimation for variational problems with uniformly convex functionals.” In: *Math. Comp.* 69.230 (2000), pp. 481–500 (cit. on pp. 24, 27).
- [342] S. I. Repin. *A Posteriori Estimates for Partial Differential Equations*. Radon Series on Computational and Applied Mathematics. Wal, 2008 (cit. on p. 23).
- [343] A. Reuss. “Berechnung der Fließgrenze von Mischkristallen auf Grund der Plastizitätsbedingung für Einkristalle.” In: *ZAMM - Journal of Applied Mathematics and Mechanics / Zeitschrift für Angewandte Mathematik und Mechanik* 9.1 (1929), pp. 49–58. DOI: [10.1002/zamm.19290090104](https://doi.org/10.1002/zamm.19290090104) (cit. on p. 62).
- [344] D. Reynolds, J. McConnachie, P. Bettess, W. C. Christie, and J. W. Bull. “Reverse adaptivity — a new evolutionary tool for structural optimization.” In: *International Journal for Numerical Methods in Engineering* 45.5 (1999), pp. 529–552. DOI: [10.1002/\(SICI\)1097-0207\(19990620\)45:5<529::AID-NME599>3.0.CO;2-2](https://doi.org/10.1002/(SICI)1097-0207(19990620)45:5<529::AID-NME599>3.0.CO;2-2) (cit. on p. 14).
- [345] M. Riis and R. Schultz. “Applying the Minimum Risk Criterion in Stochastic Recourse Programs.” In: *Comput. Optim. Appl.* 24.2-3 (2003), pp. 267–287 (cit. on p. 28).
- [346] U. T. Ringertz. “On finding the optimal distribution of material properties.” In: *Structural optimization* 5.4 (1993), pp. 265–267. DOI: [10.1007/BF01743590](https://doi.org/10.1007/BF01743590) (cit. on p. 20).
- [347] R. T. Rockafellar, S. Uryasev, and M. Zabarankin. “Generalized deviations in risk analysis.” In: *Finance and Stochastics* 10.1 (2006), pp. 51–74. URL: <http://ideas.repec.org/a/spr/finsto/v10y2006i1p51-74.html> (cit. on p. 28).
- [348] R. T. Rockafellar and S. Uryasev. “Optimization of Conditional Value-at-Risk.” In: *Journal of Risk* 2 (2000), pp. 21–41 (cit. on p. 179).
- [349] H. Rodrigues, J. M. Guedes, and M. P. Bendsøe. “Hierarchical optimization of material and structure.” In: *Structural and Multidisciplinary Optimization* 24.1 (2002), pp. 1–10. DOI: [10.1007/s00158-002-0209-z](https://doi.org/10.1007/s00158-002-0209-z) (cit. on p. 20).
- [350] W. Römisch and R. Schultz. “Multistage stochastic integer programming: an introduction.” In: *Online Optimization of Large Scale Systems*. Ed. by M. Grötschel, S. O. Krumke, and J. Rambau. Springer, 2001, pp. 581–600 (cit. on p. 28).
- [351] M. P. Rossow and J. E. Taylor. “A Finite Element Method for the Optimal Design of Variable Thickness Sheets.” In: *AIAA Journal* 11 (11 1973), pp. 1566–1569. DOI: [10.2514/3.50631](https://doi.org/10.2514/3.50631) (cit. on p. 19).
- [352] G. I. N. Rozvany, M. Zhou, and W. Gollub. “Continuum-type optimality criteria methods for large finite element systems with a displacement constraint. Part II.” In: *Structural optimization* 2.2 (1990), pp. 77–104. DOI: [10.1007/BF01745456](https://doi.org/10.1007/BF01745456) (cit. on p. 12).

- 
- [353] G. I. N. Rozvany, M. Zhou, M. Rotthaus, W. Gollub, and F. Spengemann. “Continuum-type optimality criteria methods for large finite element systems with a displacement constraint. Part I.” In: *Structural optimization* 1.1 (1989), pp. 47–72. DOI: [10.1007/BF01743809](https://doi.org/10.1007/BF01743809) (cit. on p. 12).
- [354] G. I. N. Rozvany et al. “Least-weight design of perforated elastic plates—I/II.” In: *International Journal of Solids and Structures* 23.4 (1987), pp. 521–550. DOI: [10.1016/0020-7683\(87\)90016-3](https://doi.org/10.1016/0020-7683(87)90016-3) (cit. on p. 16).
- [355] G. I. N. Rozvany. *Structural Design via Optimality Criteria*. 1st ed. Mechanics of Elastic and Inelastic Solids. Springer Dordrecht, 1989. DOI: [10.1007/978-94-009-1161-1](https://doi.org/10.1007/978-94-009-1161-1) (cit. on p. 12).
- [356] N. Rumigny, P. Papadopoulos, and E. Polak. “On the use of consistent approximations in boundary element-based shape optimization in the presence of uncertainty.” In: *Comput. Methods Appl. Mech. Engrg.* 196 (2007), pp. 3999–4010 (cit. on p. 29).
- [357] A. Ruszczyński and A. Shapiro. *Handbooks in Operations Research and Management Sciences, 10: Stochastic Programming*. Amsterdam: Elsevier, 2003 (cit. on p. 28).
- [358] A. Ruszczyński and A. Shapiro. “Optimization of Convex Risk Functions.” In: *Math. Oper. Res.* 31.3 (2006), pp. 433–452. DOI: <http://dx.doi.org/10.1287/moor.1050.0186> (cit. on p. 28).
- [359] L. A. Schmit. “Structural Design by Systematic Synthesis.” In: *2nd Conference on Electronic Computation, Pittsburgh PA*. 1960 (cit. on p. 12).
- [360] O. Schmitt, J. Friederich, and P. Steinmann. “Manufacturing constraints in parameter-free shape optimization.” In: *PAMM* (Erlangen, Germany). Erlangen, Germany: Wiley, 2014, pp. 787–788. DOI: [10.1002/pamm.201410376](https://doi.org/10.1002/pamm.201410376) (cit. on p. 72).
- [361] R. Schultz. “Stochastic programming with integer variables.” In: *Mathematical Programming* 97 (2003), pp. 285–309 (cit. on p. 28).
- [362] R. Schultz and S. Tiedemann. “Risk Aversion via Excess Probabilities in Stochastic Programs with Mixed-Integer Recourse.” In: *SIAM J. on Optimization* 14.1 (2003), pp. 115–138. DOI: <http://dx.doi.org/10.1137/S1052623402410855> (cit. on p. 28).
- [363] R. Schultz and S. Tiedemann. “Conditional Value-at-Risk in Stochastic Programs with Mixed-Integer Recourse.” In: *Math. Program.* 105.2-3 (2006), pp. 365–386 (cit. on p. 179).
- [364] A. Schumacher. “Topologieoptimierung von Bauteilstrukturen unter Verwendung von Lochpositionierungskriterien.” PhD thesis. Universität – Gesamthochschule Siegen, 1996 (cit. on p. 14).
- [365] F. Schury, M. Stingl, and F. Wein. “Efficient two-scale optimization of manufacturable graded structures.” In: *SIAM Journal on Scientific Computing* 34.6 (2012), B711–B733 (cit. on p. 21).
- [366] G. P. Sendeckyj. *Mechanics of Composite Materials*. 1st ed. Vol. 2. Composite materials. Academic Press, 1974 (cit. on p. 10).
- [367] J. A. Sethian and A. Wiegmann. “Structural Boundary Design via Level Set and Immersed Interface Methods.” In: *Journal of Computational Physics* 163.2 (2000), pp. 489–528. DOI: [10.1006:jcph.2000.6581](https://doi.org/10.1006/jcph.2000.6581) (cit. on p. 13).

- [368] M. Shaked and G. Shanthikumar. *Stochastic Orders*. 1st ed. Springer New York, 2007, pp. XVI, 474. DOI: [10.1007/978-0-387-34675-5](https://doi.org/10.1007/978-0-387-34675-5) (cit. on p. 28).
- [369] A. Shapiro, D. Dentcheva, and A. Ruszczyński. *Lectures on Stochastic Programming*. Philadelphia: SIAM-MPS, 2009 (cit. on p. 28).
- [370] O. Sigmund and J. Petersson. “Numerical instabilities in topology optimization: A survey on procedures dealing with checkerboards, mesh-dependencies and local minima.” English. In: *Structural optimization* 16.1 (1998), pp. 68–75. DOI: [10.1007/BF01214002](https://doi.org/10.1007/BF01214002) (cit. on p. 19).
- [371] O. Sigmund. “Materials with prescribed constitutive parameters: An inverse homogenization problem.” In: *International Journal of Solids and Structures* 31.17 (1994), pp. 2313–2329. DOI: [10.1016/0020-7683\(94\)90154-6](https://doi.org/10.1016/0020-7683(94)90154-6) (cit. on p. 20).
- [372] O. Sigmund. “A new class of extremal composites.” In: *Journal of the Mechanics and Physics of Solids* 48.2 (2000), pp. 397–428. DOI: [10.1016/S0022-5096\(99\)00034-4](https://doi.org/10.1016/S0022-5096(99)00034-4) (cit. on p. 68).
- [373] J. Simon. “Differentiation with Respect to the Domain in Boundary Value Problems.” In: *Numerical Functional Analysis and Optimization* 2.7-8 (1980), pp. 649–687. DOI: [10.1080/01630563.1980.10120631](https://doi.org/10.1080/01630563.1980.10120631) (cit. on p. 12).
- [374] J. Sokołowski and A. Żochowski. “Optimality Conditions for Simultaneous Topology and Shape Optimization.” In: *SIAM J. Control Optim.* 42 (2003), pp. 1198–1221 (cit. on p. 14).
- [375] J. Sokołowski and J.-P. Zolésio. *Introduction to shape optimization*. Shape sensitivity analysis. Berlin: Springer-Verlag, 1992 (cit. on p. 9).
- [376] J. Sokołowski and A. Żochowski. “On the Topological Derivative in Shape Optimization.” In: *SIAM J. Control Optim.* 37.4 (1999), pp. 1251–1272 (cit. on pp. 14, 59).
- [377] J. Sokołowski and A. Żochowski. “Topological Derivatives Of Shape Functionals For Elasticity Systems.” In: *Mechanics of Structures and Machines* 29.3 (2001), pp. 331–349. DOI: [10.1081/SME-100105654](https://doi.org/10.1081/SME-100105654) (cit. on p. 14).
- [378] C. Somigliana. “Sopra l’equilibrio di un corpo elastico isotropo.” In: *Il Nuovo Cimento (1877-1894)* 3 (1885), 17: 140–148, 272–276, 18: 161–166, 19: 84–90, 20: 278–282, 181–185 (cit. on p. 51).
- [379] S. Spagnolo. “Sulla convergenza di soluzioni di equazioni paraboliche ed ellittiche.” In: *Annali della Scuola Normale Superiore di Pisa - Classe di Scienze* 22.4 (1968), pp. 571–597. URL: <http://eudml.org/doc/83472> (cit. on p. 46).
- [380] C. Stangl. “Strukturoptimierung mit IPOPT im deterministischen und stochastischen Fall.” Diploma thesis. University of Duisburg-Essen, 2008 (cit. on p. 88).
- [381] E. Stein and S. Ohnibus. “Coupled model- and solution-adaptivity in the finite-element method.” In: *Computer Methods in Applied Mechanics and Engineering* 150.1 (1997). Symposium on Advances in Computational Mechanics, pp. 327–350. DOI: [10.1016/S0045-7825\(97\)00082-0](https://doi.org/10.1016/S0045-7825(97)00082-0) (cit. on p. 24).
- [382] E. Stein and S. Ohnibus. “Anisotropic discretization- and model-error estimation in solid mechanics by local Neumann problems.” In: *Computer Methods in Applied Mechanics and Engineering* 176.1 (1999), pp. 363–385. DOI: [10.1016/S0045-7825\(98\)00345-4](https://doi.org/10.1016/S0045-7825(98)00345-4) (cit. on p. 26).



- 
- [383] M. Steinbach. “Tree-sparse convex programs.” In: *Mathematical Methods of Operations Research* 56 (2002), pp. 347–376 (cit. on p. 28).
- [384] O. Steinbach. *Numerische Näherungsverfahren für elliptische Randwertprobleme: Finite Elemente und Randelemente*. German. Wiesbaden: B. G. Teubner, 2003 (cit. on pp. 50, 51).
- [385] M. Stingl, M. Kočvara, and G. Leugering. “A New Non-linear Semidefinite Programming Algorithm with an Application to Multidisciplinary Free Material Optimization.” In: *Optimal Control of Coupled Systems of Partial Differential Equations*. Ed. by K. Kunisch, J. Sprekels, G. Leugering, and F. Tröltzsch. Basel: Birkhäuser Basel, 2009, pp. 275–295 (cit. on p. 20).
- [386] M. Stingl, M. Kočvara, and G. Leugering. “A Sequential Convex Semidefinite Programming Algorithm with an Application to Multiple-Load Free Material Optimization.” In: *SIAM Journal on Optimization* 20.1 (2009), pp. 130–155. DOI: [10.1137/070711281](https://doi.org/10.1137/070711281) (cit. on pp. 20, 28, 29).
- [387] M. Stolpe and K. Svanberg. “Modelling topology optimization problems as linear mixed 0-1 programs.” In: *International Journal for Numerical Methods in Engineering* 57.5 (2003), pp. 723–739. DOI: [10.1002/nme.700](https://doi.org/10.1002/nme.700) (cit. on pp. 14, 15).
- [388] P. Suquet. “Une méthode duale en homogénéisation : application aux milieux élastiques.” In: *Journal de Mécanique Théorique et Appliquée* (1982), pp. 79–98 (cit. on pp. 11, 61).
- [389] K. Suzuki and N. Kikuchi. “A homogenization method for shape and topology optimization.” In: *Computer Methods in Applied Mechanics and Engineering* 93.3 (1991), pp. 291–318. DOI: [10.1016/0045-7825\(91\)90245-2](https://doi.org/10.1016/0045-7825(91)90245-2) (cit. on p. 16).
- [390] V. Šverák. “On optimal shape design.” In: *Journal de Mathématiques Pures et Appliquées* 72 (1993) (cit. on p. 10).
- [391] A. Takezawa, S. Nii, M. Kitamura, and N. Kogiso. “Topology optimization for worst load conditions based on the eigenvalue analysis of an aggregated linear system.” In: *Comput. Methods Appl. Mech. Engrg.* 200.25-28 (2011), pp. 2268–2281. DOI: [10.1016/j.cma.2011.03.008](https://doi.org/10.1016/j.cma.2011.03.008) (cit. on p. 29).
- [392] L. Tartar. “Estimations fines des coefficients homogénéisés.” In: *Ennio De Giorgi colloquium (Paris, 1983)*. Vol. 125. Res. Notes in Math. Boston, MA: Pitman, 1985, pp. 168–187 (cit. on pp. 62, 64, 66).
- [393] L. Tartar. “Problemes de Controle des Coefficients Dans des Equations aux Derivees Partielles.” In: *Control Theory, Numerical Methods and Computer Systems Modelling*. Ed. by A. Bensoussan and J. L. Lions. english translation MuTa97b. Berlin, Heidelberg: Springer Berlin Heidelberg, 1975, pp. 420–426 (cit. on p. 11).
- [394] L. Tartar. “Estimations of homogenized coefficients.” In: *Topics in the mathematical modelling of composite materials*. Vol. 31. Progr. Nonlinear Differential Equations Appl. Boston, MA: Birkhäuser Boston, 1997, pp. 9–20 (cit. on p. 64).
- [395] S. Tiedemann. *Risk Measures with Preselected Tolerance Levels in Two-Stage Stochastic Mixed-Integer Programming*. Cuvillier Verlag Göttingen, 2005 (cit. on p. 28).
- [396] S. Tölkes. “Ein Stabmodell der zweiskaligen elastischen Formoptimierung.” Diploma thesis. Rheinische Friedrich-Wilhelms-Universität Bonn, 2011 (cit. on p. 178).

- [397] S. Tölkes. “Numerical methods in stochastic and two-scale shape optimization.” PhD thesis. Rheinische Friedrich-Wilhelms-Universität Bonn, 2018. URL: <https://hdl.handle.net/20.500.11811/7556> (cit. on pp. 20, 178).
- [398] F. Tröltzsch. *Optimale Steuerung partieller Differentialgleichungen*. 2nd ed. 1. Auflage 2005. Vieweg & Teubner Verlag Wiesbaden, 2009. DOI: [10.1007/978-3-8348-9357-4](https://doi.org/10.1007/978-3-8348-9357-4) (cit. on p. 9).
- [399] J. Valentin, D. Hübner, M. Stingl, and D. Pflüger. “Gradient-Based Two-Scale Topology Optimization With B-Splines on Sparse Grids.” In: *SIAM Journal on Scientific Computing* 42.4 (2020), B1092–B1114 (cit. on pp. 21, 179).
- [400] K. S. Vemaganti. “Modelling error estimation and adaptive modelling of perforated materials.” In: *Internat. J. Numer. Methods Engrg.* 59.12 (2004), pp. 1587–1604. DOI: [10.1002/nme.929](https://doi.org/10.1002/nme.929) (cit. on p. 26).
- [401] K. S. Vemaganti and J. T. Oden. “Estimation of local modeling error and goal-oriented adaptive modeling of heterogeneous materials. II. A computational environment for adaptive modeling of heterogeneous elastic solids.” In: *Comput. Methods Appl. Mech. Engrg.* 190.46-47 (2001), pp. 6089–6124. DOI: [10.1016/S0045-7825\(01\)00217-1](https://doi.org/10.1016/S0045-7825(01)00217-1) (cit. on p. 26).
- [402] R. Verfürth. *A Review of a posteriori error estimation and adaptive mesh-refinement techniques*. Chichester, Stuttgart: Wiley, B.G.Teubner, 1996 (cit. on p. 23).
- [403] S. Vigdergauz. “Energy-minimizing inclusions in a planar elastic structure with macroisotropy.” In: *Structural optimization* 17.2 (1999), pp. 104–112. DOI: [10.1007/BF01195935](https://doi.org/10.1007/BF01195935) (cit. on p. 67).
- [404] S. Vigdergauz. “Integral equation of the inverse problem of the plane theory of elasticity.” In: *Journal of Applied Mathematics and Mechanics* 40.3 (1976), pp. 518–522. DOI: [10.1016/0021-8928\(76\)90046-0](https://doi.org/10.1016/0021-8928(76)90046-0) (cit. on p. 67).
- [405] S. Vigdergauz. “Three-dimensional grained composites of extreme thermal properties.” In: *Journal of the Mechanics and Physics of Solids* 42.5 (1994), pp. 729–740. DOI: [10.1016/0022-5096\(94\)90040-X](https://doi.org/10.1016/0022-5096(94)90040-X) (cit. on p. 67).
- [406] S. Vigdergauz. “Two-Dimensional Grained Composites of Extreme Rigidity.” In: *Journal of Applied Mechanics* 61.2 (1994), pp. 390–394. URL: <http://appliedmechanics.asmedigitalcollection.asme.org/article.aspx?articleid=1411269> (cit. on pp. 67, 68).
- [407] M. Vohralík. “Guaranteed and Fully Robust a posteriori Error Estimates for Conforming Discretizations of Diffusion Problems with Discontinuous Coefficients.” In: *Journal of Scientific Computing* 46.3 (2011), pp. 397–438. DOI: [10.1007/s10915-010-9410-1](https://doi.org/10.1007/s10915-010-9410-1) (cit. on p. 25).
- [408] W. Voigt. “Ueber die Beziehung zwischen den beiden Elasticitätsconstanten isotroper Körper.” In: *Annalen der Physik* 274.12 (1889), pp. 573–587. DOI: [10.1002/andp.18892741206](https://doi.org/10.1002/andp.18892741206) (cit. on p. 62).
- [409] A. Wächter. “An Interior Point Algorithm for Large-Scale Nonlinear Optimization with Applications in Process Engineering.” Phd Thesis. Carnegie Mellon University, 2002 (cit. on p. 88).

- [410] A. Wächter and L. T. Biegler. “On the Implementation of a Primal-Dual Interior Point Filter Line Search Algorithm for Large-Scale Nonlinear Programming.” In: *Mathematical Programming* 106.1 (2006), pp. 25–57 (cit. on p. 88).
- [411] S. W. Wallace and W. T. Ziemba. *Applications of Stochastic Programming*. Vol. MPS-SIAM Series on Optimization. Philadelphia: SIAM and MPS, 2005 (cit. on p. 28).
- [412] L. Walpole. “On bounds for the overall elastic moduli of inhomogeneous systems — I.” In: *Journal of the Mechanics and Physics of Solids* 14.3 (1966), pp. 151–162. DOI: [10.1016/0022-5096\(66\)90035-4](https://doi.org/10.1016/0022-5096(66)90035-4) (cit. on p. 62).
- [413] F. Wang, B. S. Lazarov, and O. Sigmund. “On projection methods, convergence and robust formulations in topology optimization.” In: *Structural and Multidisciplinary Optimization* 43.6 (2011), pp. 767–784. DOI: [10.1007/s00158-010-0602-y](https://doi.org/10.1007/s00158-010-0602-y) (cit. on p. 29).
- [414] M. Y. Wang, X. Wang, and D. Guo. “A level set method for structural topology optimization.” In: *Computer methods in applied mechanics and engineering* 192 (2003), pp. 227–246 (cit. on p. 13).
- [415] M. Y. Wang and S. Zhou. “Phase field: a variational method for structural topology optimization.” In: *Comput. Model. Eng. Sci.* 6 (2004), pp. 547–566 (cit. on p. 15).
- [416] P. Wei and M. Y. Wang. “A piecewise constant level set method for structural topology optimization.” In: *7th World Congress on Structural and Multidisciplinary Optimization*. 2007, 1659?–1668 (cit. on p. 16).
- [417] G. A. Whitmore. “Third-Degree Stochastic Dominance.” In: *The American Economic Review* 60.3 (1970), pp. 457–459. URL: <http://www.jstor.org/stable/1817999> (cit. on pp. 28, 179).
- [418] O. Wiener. *Abhandlungen der mathematisch-physikalischen Klasse der königlichen sächsischen Gesellschaft der Wissenschaften*. Tech. rep. 6. Physikalisches Institut, Universität Leipzig, 1912 (cit. on pp. 62, 63).
- [419] W. Wollner. “Goal-Oriented Adaptivity for Optimization of Elliptic Systems subject to Pointwise Inequality Constraints: Application to Free Material Optimization.” In: *PAMM* 10.1 (2010), pp. 669–672. URL: <http://dx.doi.org/10.1002/pamm.201010325> (cit. on p. 27).
- [420] Y. Xie and G. Steven. “A simple evolutionary procedure for structural optimization.” In: *Computers & Structures* 49.5 (1993), pp. 885–896. DOI: [http://dx.doi.org/10.1016/0045-7949\(93\)90035-C](http://dx.doi.org/10.1016/0045-7949(93)90035-C) (cit. on p. 14).
- [421] T. Yamada, K. Izui, S. Nishiwaki, and A. Takezawa. “A topology optimization method based on the level set method incorporating a fictitious interface energy.” In: *Computer Methods in Applied Mechanics and Engineering* 199.45-48 (2010), pp. 2876–2891. DOI: <http://dx.doi.org/10.1016/j.cma.2010.05.013> (cit. on p. 16).
- [422] R. Yang and C. Chuang. “Optimal topology design using linear programming.” In: *Computers & Structures* 52.2 (1994), pp. 265–275. DOI: [http://dx.doi.org/10.1016/0045-7949\(94\)90279-8](http://dx.doi.org/10.1016/0045-7949(94)90279-8) (cit. on p. 19).
- [423] L. C. Young. “Generalized Surfaces in the Calculus of Variations.” In: *Annals of Mathematics* 43.1 (1942), pp. 84–103 (cit. on p. 10).

- [424] L. Young. *Lecture on the Calculus of Variations and Optimal Control Theory*. AMS Chelsea Publishing Company Series. AMS Chelsea Publishing, 1980. URL: <https://books.google.de/books?id=F3mZOY-FUi4C> (cit. on p. 10).
- [425] X. Zhao, S. Mao, and Z.-C. Shi. “Adaptive Quadrilateral and Hexahedral Finite Element Methods with Hanging Nodes and Convergence Analysis.” In: *Journal of Computational Mathematics* 28.5 (2010), pp. 621–644. DOI: [10.4208/jcm.1001-m3006](https://doi.org/10.4208/jcm.1001-m3006) (cit. on p. 24).
- [426] B. Zhu, M. Skouras, D. Chen, and W. Matusik. “Two-Scale Topology Optimization with Microstructures.” en. In: *ACM Transactions on Graphics* 36.5 (2017), pp. 1–16. DOI: [10.1145/3095815](https://doi.org/10.1145/3095815) (cit. on p. 21).
- [427] O. C. Zienkiewicz and J. S. Campbell. “Shape optimization and sequential linear programming.” In: *Optimum Structural Design*. Ed. by R. Gallagher and O. Zienkiewicz. New York: Wiley, 1973, pp. 109–126 (cit. on p. 12).
- [428] O. C. Zienkiewicz and J. Z. Zhu. “A simple error estimator and adaptive procedure for practical engineering analysis.” In: *International Journal for Numerical Methods in Engineering* 24.2 (1987), pp. 337–357. DOI: [10.1002/nme.1620240206](https://doi.org/10.1002/nme.1620240206) (cit. on pp. 24, 27).
- [429] A. Źochowski. “Optimal Perforation Design in 2-Dimensional Elasticity.” In: *Mechanics of Structures and Machines* 16.1 (1988), pp. 17–33. DOI: [10.1080/08905458808960251](https://doi.org/10.1080/08905458808960251) (cit. on p. 16).
- [430] T. I. Zohdi, J. Oden, and G. J. Rodin. “Hierarchical modeling of heterogeneous bodies.” In: *Computer Methods in Applied Mechanics and Engineering* 138.1 (1996), pp. 273–298. DOI: [10.1016/S0045-7825\(96\)01106-1](https://doi.org/10.1016/S0045-7825(96)01106-1) (cit. on p. 25).
- [431] J.-P. Zolésio. “Identification de domaines par deformations.” MA thesis. Nice University, 1979 (cit. on p. 12).
- [432] J.-P. Zolésio. “The Material Derivative (or Speed) Method for Shape Optimization.” In: *Optimization of distributed parameter structures*. NATO ASI series. Series E, Applied sciences 50. Alphen aan den Rijn, The Netherlands: Sijthoff & Noordhoff Inter National Publishers, 1981, pp. 1089–1151 (cit. on p. 12).
- [433] J. Zowe, M. Kočvara, and M. P. Bendsøe. “Free material optimization via mathematical programming.” In: *Mathematical Programming* 79.1 (1997), pp. 445–466. DOI: [10.1007/BF02614328](https://doi.org/10.1007/BF02614328) (cit. on p. 27).